Quantum Back-Action Evasion in a Hybrid Spin-Optomechanical System

Møller, Christoffer Bo

Publication date:
2018

Document version
Publisher's PDF, also known as Version of record

Quantum Back-Action Evasion in a Hybrid Spin-Optomechanical System

Christoffer Møller

Ph.D. Thesis

Quantum Back-Action Evasion in a Hybrid Spin-Optomechanical System

Christoffer Bo Møller

This thesis has been submitted to the PhD School of Science at the University of Copenhagen.

Danish Center for Quantum Optics

Niels Bohr Institute
Faculty of Science
University of Copenhagen
Denmark

January 2018

Principle Supervisor: Prof. Eugene Simon Polzik

Ph.D. Committee

External:
Assoc. Prof. Philipp Treutlein (University of Basel, Switzerland)
Prof. Markus Aspelmeyer (University of Vienna, Austria)

Local:
Assoc. Prof. Ferdinand Kuemmeth (Niels Bohr Institute)

Submission date: January 21, 2018
Defense date: February 22, 2018

Abstract

This thesis reports the construction of a hybrid setup consisting of an optomechanical system in and an atomic spin ensemble capable of quantum back-action evading measurements of mechanical motion by use of an itinerant optical field.

The optomechanical system consists of a highly stressed, $500\,\mu m \times 500\,\mu m \times 60\,nm$, SiN membrane placed in the middle of an unresolved, high finesse, one-sided optical cavity. This cavity is placed in a cryostat operated at 4.4 K. The motion of the dielectric membrane modulates the cavity resonance frequency, and thus the light field populating the cavity. This couples the light degrees of freedom with the motion of the mechanics allowing a sensitive read out of mechanical motion by interrogation of the light quadratures output from the cavity. The limit of the sensitivity with which this motion can be read out, without disturbing the system, is set by the quantum back-action introduced by the probing light onto the mechanical motion.

The significant influence of the quantum back-action on the motion of the mechanics is initially demonstrated by a $(-3.18 \pm 0.18)\,dB$ (equivalent to $(53 \pm 2)\,\%$ below shot noise) observed ponderomotive squeezing. Correcting for detection efficiency and additional classical laser noise gives an ideal squeezing of $-8.6\,dB$ (equivalent to 86 % below shot noise). The squeezed light noise occurs as a result of a projection of the optically transduced mechanical motion onto the optical quadrature, whose quantum correlations were the drive for the motion in the first place.

Using an atomic spin ensemble pumped to its most energetic state, we realize an oscillator with an effective negative mass. Using the motion of this oscillator as a reference allows for the evasion of back-action on the mechanical oscillator. The spin ensemble consists of a vapour cell with 10^9 spin polarized cesium atoms confined to a micro-channel of length $300\,\mu m \times 300\,\mu m \times 10\,mm$ coated with a spin preserving layer. The cell is placed in a magnetically controlled environment allowing for precise control of the oscillator frequency and spin direction. The spins are coupled to an optical probe via the Faraday effect and read out in transmission before being filtered and directed towards the optomechanical setup.

Measuring the output optical phase quadrature from this cascaded hybrid system allows for measurements of mechanical displacement with enhanced sensitivity in the relevant regime where the mechanical displacement sensitivity is overwhelmed by the added noise caused by the quantum back-action. This quantum back-action

is demonstrated to be evaded by $-1.8\,\mathrm{dB}$ (equivalent to a $(-34 \pm 5)\,\%$ reduction) and is well understood by a detailed theoretical hybrid model. The model provides further insight into how to significantly boost back-action evasion in such a hybrid system.

Demonstrating an optically linked hybrid system consisting of two quantum enabled subsystems, capable of significant back-action evasion, lays the foundation for generating Einstein-Podolsky-Rosen entanglement between the two.

Sammenfatning

Denne afhandling omhandler konstruktionen af et hybridsetup, bestående af et optomekanisk system, samt et atomart spin-ensemble, som ved hjælp af en optisk forbindelse tillader en kvantetilbagekoblingsundvigende måling af mekanisk bevægelse.

Det optomekaniske system består af en $500\,\mu m \times 500\,\mu m \times 60\,nm$ SiN-membran under højt stress, placeret i midten af et uopløst, høj-finesse, ensidet optisk kavitet. Kaviteten er placeret i en kryostat der opereres ved $4.4\,K$. Bevægelsen af den dielektriske membran modulerer kavitetens resonansfrekvens, og dermed det optiske felt i kaviteten. Dette kobler lysets frihedsgrader med bevægelsen af mekanikken, hvilket tillader præcise udlæsninger af den mekaniske bevægelse ved måling af lyskvadraturerne udsendt fra kaviteten. Grænsen for følsomheden hvormed bevægelsen kan udlæses uden at forstyrre systememet sættes af kvantetilbagekoblingen forårsaget af det undersøgende lys på den mekaniske bevægelse.

Denne væsentlige påvirkning fra kvantetilbagekoblingen på bevægelsen af mekaniken demonstreres indledningsvis igennem $(-3.18 \pm 0.18)\,dB$ (ækvivalent til $(53 \pm 2)\,\%$ under haglstøjsniveau) observeret ponderomotorisk klemning. Såfremt der korrigeres for detektionseffiktivitet, og klassisk laserstøj, udregnes en ideel klemning på $-8.6\,dB$ (ækvivalent til $86\,\%$ under haglstøjsniveau). Det klemte lys opstår som et resultat af projektionen af den optisk transducerede mekaniske bevægelse på den optiske kvadratur, hvis kvantefluktuationer var den dominerende drivkraft for bevægelsen i første omgang.

Vha. et atomart spinensemble pumpet til den mest energirige tilstand realiserer vi en oscillator med en effektiv negativ masse. Ved at benytte bevægelsen af denne oscillator som reference, tillades undvigelse af tilbagekobling på den mekaniske oscillator. Spinensemblet består af en gascelle med 10^9 spinpolariserede cæsium-atomer, begrænset til en mikrokanal med størrelsen $300\,\mu m \times 300\,\mu m \times 10\,mm$ som er belagt med et spinbevarende lag. Cellen er placeret i et magnetisk kontrolleret miljø, hvilket tillader præcis kontrol af oscillatorens frekvens og spinnets retning. Spinnene er koblet til en optisk undersøgelsesstråle igennem Faraday-effekten, som udlæses i transmission før den filtreres og sendes imod det optomekaniske setup.

Måling af den udsendte optiske fasekvadratur fra dette sekventielle hybridsystem tillader måling af den mekaniske forskydning med øget sensitivitet i det relevante regime, hvor den mekaniske forskydningssensitivitet overskygges af den tilføjede støj

fra kvantetilbagekobling. Denne kvantetilbagekobling demonstreres undveget med 1.8 dB (ækvivalent til $(34 \pm 5)\,\%$ reduktion), og er velforstået igennem en detaljeret teoretisk model for hybridsystemet. Modellen giver yderligere indsigt i hvordan en væsentligt øget tilbagekoblingsunvigelse kan opnåes i et hybridsystem som dette.

Demonstration af et optisk forbundet hybridsystem, bestående af to kvantebegrænsede undersystemer, som udviser væsentlig tilbagekoblingsundvigelse lægger grunden for frembringelsen af Einsten-Podolsky-Rosen-sammenfiltring af de to undersystemer.

Acknowledgements

No man is an island, entire of itself;
every man is a piece of the continent,
a part of the main.

John Donne

It is hard to convey in mere words the joy, privilege, and gratitude I feel for those who helped me along the windy road of the last 4 years at QUANTOP. Especially for those who also helped me get here in the first place. In particular our group leader Eugene Polzik for giving me the opportunity and means to contribute to our field of physics, and hopefully science in general. For mentoring by example, demonstrating stoicism in times of experimental hardship, and maintaining a clear vision (appropriately updated) of the path ahead throughout. But, perhaps most of all, for fostering an incredibly productive and (I suspect) uniquely friendly and warm work environment. For this experience, and more, I am forever grateful.

Likewise, I want to thank Albert Schliesser whose excitement and energy were contagious, and expectations relentlessly motivating. I am incredibly fortunate to have spent 2 years working with, and learning from you as team leader of the membrane lab, and I am extremely pleased that you now, so deservedly, have your own thriving group. I took your idiom on experimental practice, stretching high for goals on a solid foundation, to heart and will continue to apply it.

When I first interviewed for the PhD position, I spent time with Eugene and Albert discussing the various problems faced at the time. However, the most memorable moments, besides my last minute haphazard talk of course, were the hours spent together with William Nielsen in the lab. He was working on some Labview program and I was meant to help. In classic William fashion he brought me up to speed and made me feel as though I was contributing, even though I most certainly was not. We ended up working directly together for 2 years and I learned much of what I know – and what I should have known – directly from him. This is particularly true in the delightful art of programming and his love for open source software pushed, not just me, but the entire lab to adopt Python as the primary programming language of choice. The related infrastructure he helped build is a useful tool to current – and undoubtedly future – students.

Alongside William, ever present and equally brilliant, was the incredibly moti-

vated Yeghishe Tsaturyan. His work ethic and dedication is incredibly contagious and, I think, single-handedly makes the membrane lab the hardest working of all Eugenes labs. His passion for optomechanics, and compassion for fellow scientists, makes him indispensable as a coworker and as a friend. I cannot thank you enough Yeghishuhi!

In the original membrane lab, when I started, were also Tolga Bağci, Andreas Næsby Rasmussen, Anders Simonsen, Andreas Barg and Willi Carlsen all of whom I thank for their warm welcome into our dungeon. In particular Willi Carlsen, whom I not only worked with alongside William, but also shared an office and many laughs with for a good year. A real pleasure.

The lab has since lost and attracted members. Notably the addition of Rodrigo Thomas (PhD) and Georgios Vasilakis (Post Doc), from another one of Eugene's labs, as permanent residents of the membrane outer dungeon was a big step. The discussions we had as a trio were incredibly rewarding and entertaining. The ever vocal and brilliant Georgios helped shape and matured my scientific thinking, and approach, to what it is today. As you became a father and family called, Rodrigo and I were left to fend for ourselves with only brief returns of our beloved Greek demigod. Together we pushed our experiment incredibly far and in doing so developed a (hopefully) lasting bond! To Georgios I note that you did not *have* to leave, you simply *chose* to. And dear Rodriga, may you run fast and far with the wind in your back! Also, don't forget to massage the bandwidth.

Indespensible at, and characteristic of, QUANTOP is the German power duo of Jörg Müller and Jürgen Appel, without which our experiment, along with countless others, would surely be terribly afflicted by some technical problem. Their combined practical and theoretical quantum optics knowledge is a priceless resource and a deep pleasure to tap into whether through discussions, problem solving or general conversation. It is, thus, an honour and a privilege to have recently begun working with Jürgen on our experiment directly!

On the theoretical side, this work would not have happened were it not for the heavyweight of Klemens Hammerer. Formerly his emissary, the now locally bound Emil Zeuthen deserves untold praise for his previous and continued work on our theoretical quandaries. He and Xinyao Huang have recently helped illuminate the path forward, and I, for one, have learnt so much from our discussions!

To the honorary members of the "Membrane plus Rodrigo" gang who should not go unmentioned: Yannick Seis, Ivan Galinskiy, Massimiliano Rossi and Junxin Chen I wish you all the fortitude necessary to take a day off and go travelling. Just don't forget me! There are countless more people from Eugenes labs, Alberts new group, our "rivals" at Peter Lodahls photonics group, and elsewhere, who have, and continue to make, my time at NBI so pleasurable. I wish you all the best of luck and cake every day!

At the university at large I would like to thank the mechanical workshop for the high quality work and advice provided regarding technical developments. In

particular the now retired Erik Grønbæk and his successor Thomas Hedegaard for all the work that went into designing the mechanical components of our experiment. Likewise at the electronic workshop I would like to especially thank Henrik Bertelsen who made the detectors (that, of course, Jürgen had designed) used for detecting all the quantum schmauntum stuff in this thesis. Similarly, gratitude is extended towards Axel Boisen and Jimmy Hansen whos skill in fixing electronic equipment have saved unimaginable amounts of time and mo ney. On the IT side of things Björn Nilsson deserves special credit for being incredibly helpful and available. Our now retired institute caretaker, Bjarne Bønsøe, was also incredibly resourceful in solving numerous practical problems as well as locating various hidden treasures throughout the labyrinth of our institute. Last, but not least, our amazing group secretary Charlotte Hviid who helped me through all things PhD related.

On the home front I would never have been able to do any of this without the support of my partner, Marta. For all your incredible encouragement and unfailing assistance throughout these years, dziękuję bardzo! To my friends and family, who I now look forward to seeing again, thank you for your patience and support.

I would also like to thank the creators and maintainers of free software. In particular the big three: LaTeX, Python and Inkscape, without which this thesis would be unrecognizable. Equally commendable are the incredible contributors to Stack Exchange and Stack Overflow; the Jörg and Jürgens of programming. Similarly adding to the visual appeal of this work is the cover art, courtesy of Bastian Leonhardt Strube and Mads Vadsholt.

To those who helped me through the writing process, especially those last minute heroes (you know who you are!) who helped me shove this thesis across the finish line, I am unspeakably grateful! And, finally, to the students who now follow in my stead, Christoffer Østfeldt in particular, I wish you high Qs and great success! Head the wisdom hanging above your new (my old) office desk, which reads:

Work hard,
Get results,
No mistakes.

Ironed perler beads

A brief history
of a time well spent

If at first you don't succeed,
try two more times so that your
failure is statistically significant.

Mitchell Moffit & Gregory Brown

The work presented in this thesis represents the latest development in the long term goal aimed at entangling two fundamentally different systems; a mechanical resonator and an atomic spin ensemble. This ambitious project, facilitated by the "hybrid " overall system, has numerous fundamental aspects of interest as well as useful practical applications in the field of quantum optics, and sensing in general. The idea originated as a somewhat natural extension of the entanglement already demonstrated between two spin ensembles in Eugenes Polziks group in Julsgaard et al. (2001). Through discussions with Peter Zoller and his then postdoc Klemens Hammerer, the idea began to take shape. Once Markus Aspelmeyer was brought in as the expert in experimental optomechanics, it all culminated in the joint proposal Hammerer et al. (2009).

Now the technical challenges were all that had to be overcome; easier said than done! In Eugenes group in particular, an optomechancial subgroup had only just been formed in 2008. It was run by team leader Koji Usami and had been maturing quickly. Promising initial results together with Dalziel Wilson (on the membrane side) and Hanna Krauter (on the spin ensemble side) showed that the desired experiment for entangling the two systems would be at the limit of what was possible, but not beyond! In 2012 Eugene was looking to strengthen the optomechanical effort and brought in Albert Schliesser as assistant professor in 2013 to lead the optomechanical subgroup. I visited shortly thereafter and started as a research assistant for a few months before beginning my Ph.D. in January 2014.

By this time the physical platform of the optomechanical system had been determined. The exact details of its design however, were still to be decided. From there it had to be built and brought into the quantum regime. I started working on this with William Nielsen, a fellow PhD student, with the clear goal of ultimately bringing the optomechanics subgroup into the quantum regime. In parallel the performance of the mechanical device specifically was being developed and im-

proved by Yeghishe Tsaturyan and Andreas Barg with their early efforts published in Tsaturyan et al. (2014). Initially our efforts lie in detecting sub-poissonian light noise statistics through an inherently quantum optomechanical interaction known as ponderomotive squeezing. We measured the first hints of $\sim 2\,\%$ squeezing in early spring of 2015. By the middle of autumn we had improved this to a $\sim 16\,\%$ effect, unequivocally ushering in quantum optomechanics at NBI. This work is published in Nielsen et al. (2016) and the fruits of our effort were elegantly documented in the PhD thesis of Nielsen (2016).

Following the optomechanical entrance into the quantum regime, I began working specifically on the hybrid experiment in the summer of 2015. For this, a new dedicated, optomechanical system was built, specifically tailored to the requirements of the hybrid system, and using the knowledge acquired from our original design. Working towards this ambitious goal a new (dream) team was assembled. Rodrigo Thomas, Georgios Vasilakis and Kasper Jensen had already been working on a suitable, quantum enabled, atomic system. So, together with Albert and I on the optomechanical side, we all began integrating our two experiments, with Eugene directly leading the hybrid (dream) team. Worth noting are a few milestones reached along the way. Initially, our two systems were optically linked by a 100 m path length interferometer since the experimental infrastructure to address both systems were physically located in two different labs. The first major milestone was when the experiments were physically joined in holy matrimony after which the atoms moved in with the mechanics in June 2015.

We then began measuring back-action evasion of large amounts of added pulsed classical noise. This added noise was gradually reduced until we could eventually demonstrate the evasion of added pulsed classical noise on the scale equivalent to ~ 10 units of optical shot noise in the spring of 2016. By the middle of summer we had improved and on July 24 we could demonstrate the evasion on the order of just a few units of optical vacuum noise. This milestone is described in section 6.3.4.

Fast forward to November 22, 2016 when the quantum back-action associated with the optical shot noise was demonstrably evaded for the first time. The results of more detailed measurements throughout December have since been published in Møller et al. (2017) and are detailed in section 6.4. The work presented in this thesis describes the underlying machinery and part of the labour that led to these fruits.

Since the this publication, very significant improvements to both subsystems and the optical link that comprise the hybrid system have been completed, while some are still under way. These include the implementation of a new generation of improved mechanical resonators by Tsaturyan et al. (2017), a more quantum enabled spin ensemble, and severely reduced optical losses. These technical improvements, combined with a matured experimental understanding, are currently paving the road for progress to march through. Hybrid entanglement is now within reach.

Published work

Peer reviewed journal articles

Andreas Barg, Yeghishe Tsaturyan, Erik Belhage, William H. P. Nielsen, Christoffer B. Møller, and Albert Schliesser.
Measuring and imaging nanomechanical motion with laser light. *Applied Physics B*, 123(1):8, December 2016.
URL https://doi.org/10.1007/s00340-016-6585-7

William H. P. Nielsen, Yeghishe Tsaturyan, Christoffer B. Møller, Eugene S. Polzik, and Albert Schliesser.
Multimode optomechanical system in the quantum regime. *Proceedings of the National Academy of Sciences*, 114(1):62-66, December 2016.
URL http://www.pnas.org/content/114/1/62.abstract

Christoffer B. Møller, Rodrigo A. Thomas, Georgios Vasilakis, Emil Zeuthen, Yeghishe Tsaturyan, Mikhail Balabas, Kasper Jensen, Albert Schliesser, Klemens Hammerer, and Eugene S. Polzik.
Quantum back-action-evading measurement of motion in a negative mass reference frame. *Nature*, 547(7662):191–195, July 2017.
URL http://dx.doi.org/10.1038/nature22980

Conference Proceedings

Rodrigo A. Thomas, Christoffer B. Møller, Georgios Vasilakis, Emil Zeuthen, Yeghishe Tsaturyan, Kasper Jensen, Albert Schliesser, Klemens Hammerer, and Eugene S. Polzik.
Quantum Back Action Evading Measurements in a Spin-Mechanics Hybrid System.
CLEO, JTh4G.5, 2017.
URL http://www.osapublishing.org/abstract.cfm?URI=CLEO_AT-2017-JTh4G.5

Yeghishe Tsaturyan, William H.P. Nielsen, Christoffer B. Møller, Andreas Barg, Junxin Chen, Yannick Seis, Eugene S. Polzik and Albert Schliesser.
Multimode Quantum Optomechanics with Ultra-coherent Nanomechanical Resonators.
CLEO, FW4F.5, 2017.
URL http://www.osapublishing.org/abstract.cfm?URI=CLEO_QELS-2017-FW4F.5

Heisenberg, Schrödinger and Ohm are in a car. They get pulled over. Heisenberg is driving and the cop asks him "Do you know how fast you were going?". "No, but I know exactly where I am" Heisenberg replies. The cop says "You were doing 55 in a 35." Heisenberg throws up his hands and shouts "Great! Now I'm lost!"

The cop thinks this is suspicious and orders him to pop open the trunk. He checks it out and says "Do you know you have a dead cat back here?". "Well we do now!" shouts Schrödinger. The cop moves to arrest them. Ohm resists.

Contents

List of Figures

List of Tables

Chapter 1

Introduction

Before we begin discussing the details of what is covered in this thesis, let us consider a measurement limitation imposed by the Heisenberg uncertainty principle. This example, following Polzik and Hammerer (2015), will motivate the key elements of this work.

1.1 Motivational example

Let us consider a generic quantum harmonic oscillator with canonical position and momentum $\hat{q}(t), \hat{p}(t)$ respectively, and a mass $m > 0$. As this oscillator undergoes harmonic motion at its natural frequency Ω, the position varies in time according to

$$\hat{q}(t) = \hat{q}(0)\cos(\Omega t) + \frac{\hat{p}(0)}{m\Omega}\sin(\Omega t). \tag{1.1}$$

A measurement of the position with uncertainty $\Delta\hat{q}$, imposes an associated uncertainty in the conjugate variable, the momentum, of $\Delta\hat{p}$. This is the Heisenberg uncertainty principle, $\Delta\hat{q}\Delta\hat{p} \geq \hbar/2$, and is a consequence of the non-commutative nature of the canonical operators, $[\hat{q}, \hat{p}] = i\hbar$.

This uncertainty in the momentum will, as the oscillator undergoes harmonic motion according to eq. (1.1), translate into an accumulation of uncertainty regarding the position. This means that the phase space trajectory of the oscillator cannot be tracked for arbitrary times with arbitrary precision. Such tracking is, for example, desirable for sensing purposes and this "quantum back-action" of the measurement sets a limit to the precision of such sensing.

To circumvent the accumulation of noise we envision introducing an auxiliary oscillator with position and momentum $\hat{q}_0(t)$, $\hat{p}_0(t)$ respectively, and the same natural frequency Ω. For this oscillator we will match the magnitude of the mass, but allow it to be both positive and *negative*, i.e. $m_0 = \pm m$. If we consider the position of our original oscillator with respect to this auxiliary oscillator we find that

$$\hat{q}(t) - \hat{q}_0(t) = (\hat{q}(0) - \hat{q}_0(0))\cos(\Omega t) + \frac{\hat{p}(0) \mp \hat{p}_0(0)}{m\Omega}\sin(\Omega t). \tag{1.2}$$

Using the auxiliary oscillator as a (quantum) reference frame, we will see below that measuring the relative position is not necessarily afflicted by the accumulation of "quantum back-action" noise, depending on the sign of the auxiliary systems mass.

In the case of two identical, traditional, positive mass oscillators ($m_0 = m$), the relative position, as seen in eq. (1.2), depends on non-commuting relative variables $\hat{q}(0) - \hat{q}_0(0)$ and $\hat{p}(0) - \hat{p}_0(0)$, which are bound according to Heisenberg's uncertainty principle. However, when the auxiliary system has a negative mass $m_0 = -m$, the relative position depends on the summed momenta variable $\hat{p}(0) + \hat{p}_0(0)$ with which it commutes,

$$[\hat{q} - \hat{q}_0, \hat{p} + \hat{p}_0] = 0. \tag{1.3}$$

Thus simultaneous knowledge of the relative position and the summed momenta is allowed, unconstrained by Heisenberg's uncertainty principle.

As this point you may be worried that Mr. Heisenberg is being made a fool. However, rest assured, the overall system has four degrees of freedom and we have simply chosen two combinations, which do not commute, and are thus unconstrained by his uncertainty principle. Uncertainty is still being accumulated, but in variables dynamically uncoupled from the relative variables of interest. This is a feature only available in the case of a negative auxiliary mass system.

In practice one gains knowledge of, say, the position of an oscillator by way of a measurement. This thesis is all about measuring the harmonic motion of a mechanical oscillator, without the uncertainty (back-action) imposed by the measurement affecting the evolution of the system. To do this we introduce an oscillator with a negative mass reference oscillator and measure their relative motion by way of an itinerant optical field.

The relative position $(\hat{q} - \hat{q}_0)$ and summed momenta $(\hat{p} + \hat{p}_0)$ are known as EPR variables. A simultaneous measurement of these can project the total system into an arbitrary well defined state, whose sum of the variances of these EPR variables is less than the sum of all the individual system variable variances. Such a state is entangled and is, as the acronym may have given away, those originally considered by Einstein, Podolsky and Rosen in their famous challenge to the theory of quantum mechanics in Einstein et al. (1935). Thus the ability to avoid the measurement back-action is intimately related to the generation of EPR entanglement of the two oscillators.

1.2 Approach

The main system of interest will be the aforementioned mechanical oscillator and our auxiliary system, with the ability to realize an effective "negative" mass, will be an atomic spin oscillator. This thesis outlines our progress towards realizing back-action free measurements of mechanical motion as just described, and as mentioned, such measurements also naturally lead towards entanglement of the two physically

different and distant quantum systems. This ambitious goal, proposed nearly a decade ago by Hammerer et al. (2009), is simultaneously of high fundamental and practical interest. The use of such a hybrid system presents both novel behavior and a valuable quantum information tool.

The two individual systems emerge from well established fields in quantum optics, namely atomic spin physics and optomechanics. The former emerged from the scientific study of the light-matter interactions, which has led to early advancements of *Quantum Mechanics*. The latter grew out of a desire to understand the limits facing the technically challenging interferometric approach to studying gravitational waves predicted by the other contemporary giant of physics, *General Relativity*.

We begin by discussing the fields of optomechanics and atomic spins in general terms along with similar efforts in building hybrid systems consisting of the two.

1.3 Brief background

We make use of two specific platforms for studying the interaction of light and matter: atomic spins and a micro-mechanical resonator. In the following subsection, we briefly review the use of atomic spin ensembles, optomechanical devices, and hybrid systems insofar as they are relevant to this work. For a broader and more comprehensive overview the following resources are recommended. For atomic ensembles see the review of Hammerer et al. (2010), whilst for optomechanical systems the review of Aspelmeyer et al. (2014). Hybrid systems are particularly numerous and diverse in their realizations. Resources for their overview involving predominantly mechanical oscillators and atomic systems are discussed in the previously stated references as well as in Treutlein et al. (2014); Wallquist et al. (2009).

A fairly recent and brief editorial, Schleier-Smith (2016), outlines of the motivations behind the drive for hybrid systems. These motivations can be bluntly boiled down and explained as follows. No single platform is able to provide all the desired functionalities of emerging quantum technologies. The desire is, thus, to merge useful aspects of various systems in order to meet and improve the performance of crucial tasks, such as precision sensing and quantum communication. Additionally, coupling hybrid systems leads to novel behavior that may further our fundamental understanding of quantum mechanics.

For both the atomic and mechanical systems a so called quantum non-demolition measurement can be realized. Such a measurement may result in a back-action free estimation of a single system variable. This was first discussed by Caves et al. (1980); Braginsky et al. (1980) and has been realized by a variety of groups and in a plethora of systems. Recently, ideas to go beyond the limitation of single variable quantum back-action free measurement have surfaced. In the context of cavity optomechanics notable works include Tsang and Caves (2012); Polzik and Hammerer (2015), as well as the proposal of Hammerer et al. (2009), which this thesis is specifically motivated by.

1.3.1 Atomic spins

Atoms are inherently quantum. Studying their behavior has a rich history of advancing the field of physics, not least from our institute which bears the name of one early pioneer. Similarly quantum is light, and its interaction with atoms helped develop quantum mechanics and eventually led to a new field separate from atomic physics and optics. This field of quantum optics has traditionally focused on light-matter coupling through the experimentally rather challenging platform of cavity quantum electro-dynamics.

In the last two decades, a new direction of atom-light interactions has emerged as a feasible platform. The logic is to trade off a rather strong coupling to a single atom (or atoms) for a weaker interaction with a large ensemble. By confining a large number of atoms in a small region of space, research groups are now able to realize a whole host of different interaction types as well as high interaction strengths.

One such platform is atomic spin ensembles where the collective spin components of a large ensemble of Alkali atoms interact with light via the Faraday effect. This platform is particularly well suited for precision metrology, particularly with respect to sensing magnetic fields, as described in Budker and Romalis (2007); Budker and Kimball (2013). Notable groups include Mike Romalis' at Princeton, which use a Potassium (K) vapour for precision magnetometry Kominis et al. (2003); Savukov et al. (2006), Morgan Mitchell's group at ICFO[1], which uses a cold Rubidium (Rb) ensemble Wolfgramm et al. (2010); Koschorreck et al. (2010); Sewell et al. (2012), and of course by Eugene Polzik's group here at NBI[2], which uses a Cesium vapour, most recently with Jensen et al. (2016).

These efforts all share the same limit to precision metrology; namely the effect of the measurement back-action on the system. Thus, it should come as no surprise that all have studied ways to surpass this limitation. In Mike Romalis' group they looked into a stroboscopic QND measurements of a single atomic spin quadrature, while piling the back-action noise into the conjugate quadrature Vasilakis et al. (2011). Morgan Mitchell's group recently showed sensitivity improvements to spin degrees of freedom beyond classical limits by sidestepping the traditional Heisenberg uncertainty relation. They map the back-action from two spin variables into an unmeasured third quadrature, see Colangelo et al. (2017).

Eugene Polzik's group also demonstrated stroboscopic back-action evasion in one quadrature in Vasilakis et al. (2015). Furthermore, entanglement assisted back-action evasion, improving senstivity, was demonstrated in Wasilewski et al. (2010). This scheme made use of two spin ensembles projected by a Bell-measurement into an Einstein-Podolsky-Rosen (EPR) entangled state Julsgaard et al. (2001). Subsequently this entanglement was further demonstrated in the steady state regime

[1]The Institute of Photonic Sciences, The Barcelona Institute of Science and Technology, Barcelona, Spain.

[2]Niels Bohr Institute, University of Copenhagen, Copenhagen, Denmark.

Krauter et al. (2011). In such a system a measurement of two precessing spin quadratures can be unbounded by the Heisenberg uncertainity relation as the back-action is directed into irrelevant spin quadratures of the joint system.

1.3.2 Optomechanics

Optomechanics, although no longer a new field, has matured drastically in the last decades. The field deals with the interaction between light (often enhanced by a cavity) and a mechanically compliant oscillator. This coupling is traditionally mediated by the radiation pressure force, which fundamentally has quantum fluctuations governed by light statistics itself. These quantum fluctuations impose a fundamental limit, caused by the random back-action of the light, on the sensitivity to mechanical motion, were first considered in the early days by Vladimir Braginsky, Anatoly Manukin and Farid Khalili in Braginskii and Manukin (1977); Braginsky et al. (1992). A partial workaround is that of quantum non-demolition measurements as described by Braginsky et al. (1980) and Caves et al. (1980).

Fast forward a few decades, skipping important theoretical insights and experimental developments, we enter the current era where the aforementioned intrinsic quantum fluctuations of light play a crucial role. In particular, in 2008 the group of Dan Stamper-Kurn at Berkley[3] observed the radiation pressure back-action on a collective mechanical mode of an ultracold gas ensemble of Rb atoms held in an optical cavity, see Murch et al. (2008). This was subsequently repeated in 2013 by Cindy Regal's group in JILA[4] by Purdy et al. (2013a), with a more traditional solid state mechanical oscillator embedded in an optical cavity (like the one employed in this work).

Competing with the radiation pressure quantum back-action effect is the influx of noise from the thermal environment of the mechanical oscillator – thus why an isolated ultracold atomic ensemble beat out much larger and hotter solid state devices. The ever present struggle against thermal noise reached a milestone in 2010 where, aided by a dilution refrigerator held at 35 mK, Andrew Cleland's group at Santa Barbara[5] prepared a microwave frequency micromechanical resonator in its quantum ground state, see O'Connell et al. (2010).

This regime was subsequently reached by others in 2011 by use of laser cooling, notably Oskar Painter's group at Caltech[6][7] by Chan et al. (2011) and in Konrad Lehnert's group at JILA[8] by Teufel et al. (2011). The former took a microwave fre-

[3]University of California at Berkeley, California, USA.

[4]A joint institute between the National Institute of Standards and Technology and the University of Colorado at Boulder, Colorado, USA.

[5]Santa Barbara, University of California, California, USA.

[6]California Institute of Technology, Pasadena, California, USA.

[7]With the help of Markus Aspelmeyer's group at the Vienna Center for Quantum Science and Technology, University of Vienna, Vienna, Austria.

[8]In conjuction with Raymond Simmonds at National Institute of Standards and Technology,

quency mechanical oscillator from a much higher[9] initial temperature to the ground state, while the latter brought a much lower frequency[10] mechanical device to the quantum ground state starting from the 20 mK dilution fridge environment. The laser sideband cooling technique is a manifestation of an effect known as dynamical back-action known from the early days of Braginsky and is discussed in section 4.1.4. While the limits of this cooling technique were not known in these early days, they were soon discovered by Caves (1980) to be given by the quantum back-action of light. Cooling to this limit was recently demonstrated in Cindy Regal's group by Peterson et al. (2016a).

As the control of mechanical oscillators continued to grow, new techniques and schemes were developed. In a particularly strong analogy with the electromagnetically induced transparency (EIT) effect present for atoms, the optomechanical equivalent was demonstrated in Tobias Kippenberg'as group at EPFL[11] by Weis et al. (2010) and in Oskar Painter's group by Safavi-Naeini et al. (2011). This effect is known as optomechanically induced transparency (OMIT) and is discussed in section 4.3.

The effects of the radiation pressure quantum back-action on the motion of the mechanics, while at once being a limit to measurement sensitivity, can also be used to generate squeezed light. This was demonstrated by Brooks et al. (2012a) in Dan Stamper-Kurn's group and followed, once again, by the solid state mechanical oscillators in Oskar Painter's and Cindy Regal's groups by Safavi-Naeini et al. (2013); Purdy et al. (2013b). This effect is further discussed in section 4.4.

This regime of detecting squeezed light is an important milestone as it necessitates two (typically) important features of a quantum optomechanical experiment. First, the mechanical oscillator must be influenced significantly, as compared to thermal noise, by the quantum fluctuations of light, i.e. the quantum back-action. Secondly, the detection efficiency for the quantum behavior must not be prohibitively large. We, as shown by Nielsen et al. (2016), have recently joined the set of experimenters worldwide operating in this – quite non-trivial – regime by detecting significant squeezing of light for a multitude of mechanical modes simultaneously.

For mechanics it is the motional degrees of freedom that are of interest and are measured. Just as was the case for the atomic ensembles in section 1.3.1, the measurement sensitivity is eventually limited by the quantum back-action. Thus, it should come as no surprise that many of the aforementioned groups are looking into evading it! Early on, using traditional positive mass mechanical oscillators the back-action can be evaded in the case of two detuned oscillators, but only in a narrow bandwidth. This was shown by Caniard et al. (2007) in Antoine Heidmann's

Boulder, Colorado, USA.

[9] Almost 600 times higher.

[10] Lower by a factor of about 600!

[11] Ecole Polytechnique Fédérale de Lausanne, Lausanne, Switzerland.

group at LKB[12] and the effect is also observed here in[13] fig. 6.21. Another trick to improve measurement sensitivity was demonstrated in Cindy Regal's group by Kampel et al. (2017) using correlations between the optical quadratures through a technique known as variational readout.

A quantum back-action free measurement of a single quadrature on a single mechanical oscillator was proprosed by Clerk et al. (2008) implementing a two tone drive based on a scheme first developed by Braginsky et al. (1980). Keith Schwab's group at Caltech implemented this idea in the microwave domain to great effect, see Suh et al. (2014).

Not content with evasion limited to a single mechanical quadrature, a broadband back-action evading scheme was proposed by Woolley and Clerk (2013) implementing a two tone drive of cavity mode addressing two mechanical oscillators. This scheme further attracted experimentalists. Dan Stamper-Kurn's group added another ultracold atomic ensemble to their optical cavity and observed a cavity mediated coupling between the two mechanical oscillators driven by the quantum back-action in Spethmann et al. (2015). Again, in the microwave domain, Mika Sillanpää's group at Aalto[14] demonstrated quantum back-action evasion of the collective quadratures of two uncoupled mechanical oscillators in Ockeloen-Korppi et al. (2016) paving the way for entanglement between the two, which is currently under review, see the pre-print by Ockeloen-Korppi et al. (2017).

1.3.3 Hybrid systems

Since our hybrid system is comprised of an optically linked Cs vapour spin ensemble and a micro-mechanical oscillator in a cavity, see Møller et al. (2017), we will restrict our focus to hybrid systems employing similar subsystems[15]. Employing a hybrid system provides an alternative route towards back-action evading measurements, entanglement and much more – in this case richer due to the fundamentally different nature of the subsystems. This approach should be seen as complementary to, but distinct from, the single system efforts described in sections 1.3.1 and 1.3.2. Central to back-action evasion proposal on which our scheme is based, Hammerer et al. (2009), and other discussed here, is the ability of the atomic spin ensemble to be realized in an effective negative mass configuration, as we will see in section 5.10.

On a similar trajectory is Philipp Treutlein's group in Basel[16] who early on demonstrated an ultracold Rb ensemble optically linked and coupled to a micro-mechanical oscillator in Camerer et al. (2011). Recently they added a cavity for

[12] Laboratoire Kastler Brossel, École Normale Supérieure, Paris, France.

[13] Albeit for a positive mass spin and mechanical oscillator. Nonetheless, the physics is the same.

[14] Aalto University, Greater Helsinki, Finland.

[15] We, thus, neglect atomic like systems such as colour centers and quantum dots, as well as mechanics related systems like electro-optomechanics and plasmonic optomechanics.

[16] University of Basel, Basel, Switzerland.

the mechanics and demonstrated a large (factor of ~ 460) sympathetic cooling of the mechanical motion in Jöckel et al. (2014). Further utilization of the atoms as a spin ensemble, by manipulation of the internal states, provides yet another degree of freedom. This may allow a pursuit of entanglement and quantum back-action evasion akin to our own.

Similarly, Dan Stamper-Kurn's group has recently shown in a pre-print, that they are able to orient their ultracold Rb cloud as a spin ensemble in the negative mass configuration, and couple it to the center of mass motion of the same cloud by way of interaction with an optical cavity mode. Their coupling gives rise to an instability Kohler et al. (2017), which drives correlations between the quadratures of the system. Further improvements may see this system's utility extend to the quantum regime.

1.4 Overview of thesis structure

This thesis follows the typical structure of a main body of work detailing the essential concepts necessary for appreciation and discussion of results. Some details related to these concepts or results are long winded or too technical to warrant inclusion in the main body. These can thus be found in appendices. The first two appendices, namely appendices A and B, which discuss Fourier analysis, power spectral densities and optical detection methods, provides enough background to hopefully understand the mathematical language spoken throughout this thesis. If not already familiar concepts, I would recommend starting with those prior to approaching the main body.

1.4.1 Main body

In chapter 2 we will introduce and review some important results for the "third half" of our hybrid system, namely the optical field linking them. The traditional amplitude and phase quadratures of light will be discussed, as they are relevant for the optomechanical system. Similarly some polarization quadratures will be discussed as they are important for the spin system. We then consider the dynamics of a Fabry-Pérot cavity, the fundamental behaviour of which is crucial in understanding the more complicated optomechanical dynamics. Finally the quantum Heisenberg-Langevin approach to treating dissipation quantum mechanically is introduced and applied to the Fabry-Pérot cavity as an example.

In chapter 3 we will first introduce the basic dynamics of membrane resonators and see how we may reduce the real world 3D nature of such a device to an effectively 1D harmonic oscillator. We will see how the more realistic case of a damped mechanical harmonic oscillator is treated and behaves. The importance of the mechanical Q factor is explained followed by a brief overview of the mechanisms which, in practice, limit it and methods by which to enhance it. This is followed by a

description of the phononic bandgap shielded membrane resonators that form the mechanical workhorse in our optomechanical experiments.

Next, in chapter 4, we will discuss the canonical cavity optomechanical system and the well known effect of dynamical back-action, which modifies the mechanical susceptibility. Then we discuss how the quantum back-action disturbance of a probing optical field disturbs the mechanical motion. We then discuss our practical realization of the optomechanical interaction using a membrane-in-the-middle approach. From here we show that we realize a quantum optomechanical system, where the quantum back-action disturbance dominants the thermal noise. This quantum back-action produces correlations between the optical quadratures, which is measured as an ponderomotive squeezing in the detected optical amplitude quadrature. These results are akin to the results we published in Nielsen et al. (2016) and display stronger correlations, both observed and inferred. Also discussed are the interesting effect of optomechanically induced transparency as well as a few practical considerations regarding the operation of our system.

In chapter 5 we introduce our realization of a spin system based on an ensemble of cesium atoms. The basic atomic structure of cesium is discussed followed by the crucial coupling to external magnetic fields. A basic theoretical model that allows the basic dynamics of the systems interaction with a probing light field is then derived. This is followed by a more detailed description. The regime in which we can prepare this spin ensemble as an effective harmonic oscillator, able to display both a positive and negative effective mass, is then outlined. The relevant mechanisms for the quantum behavior are then discussed followed by a few effects not captured by the simple model. Finally a few practical considerations are discussed.

In chapter 6 we finally get to the real meat of the thesis, where we take our light from chapter 2 and use it to link the optomechanical system of chapter 4 with the spin system of chapter 5. We first discuss the idea, first laid out in the motivational example of section 1.1, of back-action evasion in the simple QND case. We then discuss the experimental details of how we optically address the atomic spin and optomechanical systems in a cascaded fashion to realize a unified hybrid system.

Back-action evading measurements in the domain of pulsed disturbances are then discussed and evasion on the single noise quanta level subsequently demonstrated. Continuous quantum back-action evasion in the steady state regime is then discussed. This is facilitated by a more detailed model addressing the implications of operating the optomechanical cavity detuned from resonance. We then, with a detailed theory at our disposal, demonstrate the significant evasion of the quantum back-action! This is done first in the case where the spin and mechanical systems are degenerate, and subsequently for the non-degenerate case. This latter case offers us the largest demonstration of quantum back-action cancellation observed.

In chapter 7 we briefly summarize the key results of this thesis before discussing the future prospects of entanglement generation which naturally follow these results. To wrap up the thesis, we discuss some quite significant improvements implemented

since the experiments described in this work, as well as possible improvements, which may shape the future hybrid experiment.

1.4.2 Appendices

First off, in appendix A we describe the Fourier transform, its digital implementation, and the construction of a power spectral density. These form the back-bone of how we describe, measure, and view the most important results of this work.

Secondly, in appendix B, we discuss the types of detection used to measure the optical quadratures relevant for the atomic spins, optomechanical, and hybrid system. Also briefly discussed is how they relate to the mathematical constructs of appendix A used to analyze them. Lastly, how losses affect the propagation and detection of quantum correlations is discussed.

In appendix C we describe a general approach to measure the fraction of an oscillators response, which is due to the quantum back-action of light as compared to everything else. This is an important instrument to measure the degree to which quantum back-action dominates a systems behavior.

In appendix D we describe briefly the basics of Gaussian optics, free space and in a cavity, as it is relevant for discussions of loss and limitations of the mechanical and atomic systems.

Then in appendix E we describe the useful mathematical tool of transforming into a rotating frame as well as state a handful of useful algebraic relations.

In appendix F we detail an effective operator formalism used specifically to describe the effective spontaneous emission damping rate caused by a large probe field for the spin ensemble. This framework also provides a useful language and foundation on which, a more general and inclusive atomic model may be built.

In appendix G we detail some theoretical results needed for section 6.3. These results relate to the description of an oscillators response to a pulsed optical force. These is necessary for the discussion of the near quantum results of section 6.3.

Lastly, in appendix H, we derive the general optomechanical model used to describe the most important results of section 6.4. Also shown is a very useful approximation for understanding the quantum back-action evasion in the unresolved, but red detuned optomechanical regime.

Chapter 2

Light

Almost all experiments described in this thesis utilize laser light in one way or another. Laser light is particularly well suited for both probing and linking our quantum systems for multiple reasons. Firstly, the systems of interest couple to light degrees of freedom, thus enabling us to learn about our quantum systems by subsequent interrogation of the light. Secondly, optical detectors and various well established techniques allow for this interrogation to be done very efficiently. Thirdly, light from a laser can be spectrally very well defined and monochromatic as far as our quantum systems (the end users) are concerned. Finally, laser light has large coherence times, and thus can be used over large distances allowing us to link our distant quantum systems.

Light has various degrees of freedom depending on which modes of the field one considers and their relative phases. This will be explored in the following sections. Its basic behaviour will also serve as an introductory example to the quantum harmonic oscillator and its dynamics. It will also help introduce some notation, necessary concepts and relations.

The electromagnetic (light) field will, in general, be composed of various modes of different wave-vectors $\boldsymbol{k}$, frequencies ω_k and polarizations. For simplicity, let us here consider quantizing this field in a finite confined space with perfectly conducting boundaries. Furthermore, let us consider just a single mode of angular frequency ω and described by the creation and annihilation operators $\hat{a}(t)$, $\hat{a}^\dagger(t)$ at some time t. The field satisfies the bosonic commutation relations given by

$$\left[\hat{a}(t), \hat{a}^\dagger(t')\right] = \delta(t - t'), \tag{2.1a}$$

$$\left[\hat{a}^\dagger(t), \hat{a}^\dagger(t')\right] = [\hat{a}(t), \hat{a}(t')] = 0, \tag{2.1b}$$

and evolves according to the field Hamiltonian given by

$$\hat{\mathcal{H}} = \hbar\omega \left(\hat{a}^\dagger(t)\hat{a}(t) + 1/2\right), \tag{2.2}$$

where $\hat{a}^\dagger(t)\hat{a}(t) = \hat{n}(t)$ is the operator describing the number of photons in the field. The constant term of $\hbar\omega/2$ is the ground state energy of the field given by the field frequency and the reduced Planck constant $\hbar$.

In this Heisenberg picture operators explicitly depend on time and the states do not. The evolution an operator $\hat{\mathcal{O}}(t)$ is given by the Heisenberg equation

$$\dot{\hat{\mathcal{O}}}(t) \equiv \frac{\mathrm{d}}{\mathrm{d}t}\hat{\mathcal{O}}(t) = \frac{i}{\hbar}\left[\hat{\mathcal{H}}, \hat{\mathcal{O}}(t)\right]. \tag{2.3}$$

The field operator $\hat{a}$ thus has a time evolution given by $\hat{a}(t) = \hat{a}(0)e^{-i\omega t}$. Let us write down the electric field of this mode quantized along the z-direction. Each spatial mode contains two allowed polarizations. For simplicity we consider only a single polarization mode of a single spatial mode. If the polarization mode is linearly aligned with the x-direction, the electric field can, from Christopher Gerry (2005), be written as

$$\hat{\boldsymbol{E}}(t) = \boldsymbol{e}_x\mathcal{E}_x\left(\hat{a}(t) + \hat{a}^\dagger(t)\right) = \boldsymbol{e}_x\mathcal{E}_x\left(\hat{a}(0)e^{-i\omega t} + \hat{a}^\dagger(0)e^{i\omega t}\right), \tag{2.4}$$

where $\mathcal{E}$ roughly describes the resultant electric field per photon.

The time correlations of the field of mean excitation $\bar{n} = \langle\hat{n}(t)\rangle$ are typically useful quantities. These are given by

$$\langle\hat{a}^\dagger(t)\hat{a}(t')\rangle = \bar{n}\delta(t-t'), \tag{2.5a}$$
$$\langle\hat{a}(t)\hat{a}^\dagger(t')\rangle = (\bar{n}+1)\delta(t-t'), \tag{2.5b}$$
$$\langle\hat{a}(t)\hat{a}(t')\rangle = \langle\hat{a}^\dagger(t)\hat{a}^\dagger(t')\rangle = 0. \tag{2.5c}$$

Similarly useful are the correlations expressed in the Fourier domain, discussed in appendix A, which read

$$\langle\hat{a}(\Omega)\hat{a}^\dagger(\Omega')\rangle = (\bar{n}+1)\delta(\Omega-\Omega'), \tag{2.6}$$
$$\langle\hat{a}^\dagger(\Omega)\hat{a}(\Omega')\rangle = \bar{n}\delta(\Omega-\Omega'). \tag{2.7}$$

In the following we will describe degrees of freedom for these light modes and subsequently for radiative modes not confined in space. As will become clear later on, the observables associated with these light degrees of freedom provide us with information about the light field, and can be used as probes of the mechanical and atomic spin system.

2.1 Optical phase quadratures

Inspecting eq. (2.4) we see that the electric field is proportional to the real part of $\hat{a}$. If we were to write out the magnetic field, it would be proportional to the imaginary component of $\hat{a}$. These components of the field operator $\hat{a}$ can be thought of as the dimensionless generalized position and momentum of the light field, and behave as such. These can be defined as

$$\hat{X}(t) \equiv \frac{1}{\sqrt{2}}\left(\hat{a}(t) + \hat{a}^\dagger(t)\right), \tag{2.8a}$$
$$\hat{Y}(t) \equiv \frac{i}{\sqrt{2}}\left(\hat{a}^\dagger(t) - \hat{a}(t)\right). \tag{2.8b}$$

These are known as quadrature phase operators[1] and indeed oscillate at ω as would be expected from a traditional harmonic oscillator. This is seen by explicitly writing out the time dependence as in eq. (2.4), namely

$$\hat{X}(t) = \hat{X}(0)\cos\omega t + \hat{Y}(0)\sin\omega t, \tag{2.9a}$$
$$\hat{Y}(t) = \hat{Y}(0)\cos\omega t - \hat{X}(0)\sin\omega t. \tag{2.9b}$$

These operators describe canonically conjugate variables with the canonical commutation relations for a quantum harmonic oscillator that we shall see manifested throughout this work. These relations are,

$$\left[\hat{X}(t), \hat{Y}(t')\right] = i\delta(t-t'), \tag{2.10a}$$
$$\left[\hat{X}(t), \hat{X}(t')\right] = \left[\hat{Y}(t), \hat{Y}(t')\right] = 0. \tag{2.10b}$$

Just like a traditional harmonic oscillator, as we will see in chapter 3, we find that the Hamiltonian of eq. (2.2) can be re-expressed as

$$\hat{\mathcal{H}}(t) = \frac{\hbar\omega}{2}\left(\hat{X}^2(t) + \hat{Y}^2(t)\right). \tag{2.11}$$

These non-commuting quadratures also obey the classic Heisenberg uncertainty relation, which limits instantaneous knowledge of both to arbitrary precision,

$$\mathrm{Var}\left[\hat{X}(t)\right]\mathrm{Var}\left[\hat{Y}(t')\right] \geq \left|\frac{1}{2i}\langle\left[\hat{X}(t), \hat{Y}(t')\right]\rangle\right|^2 \tag{2.12}$$
$$\geq 1/4, \quad \text{for vacuum and } t = t'. \tag{2.13}$$

The statistics of these quadratures of light depend on the underlying quantum state. We will predominantly be concerned with the "most classical" quantum state of light, namely the coherent state, as it is a useful approximation to the state produced at the output of our laser sources on relevant time scales. This coherent state is defined by the property $\hat{a}\,|\alpha\rangle = \alpha\,|\alpha\rangle$ and has noise equivalent to that of vacuum[2] corresponding to a variance of $\mathrm{Var}(\hat{X}) = \mathrm{Var}(\hat{Y}) = 1/2$. This vacuum noise is also known as shot noise. This coherent state has mean amplitude $|\alpha|$ and phase ϕ, which is illustrated in phase space in fig. 2.1 along with the vacuum state.

The amplitude of the coherent field is given by the mean number of photons in the field. From fig. 2.1 it is clear that the uncertainty in phase, $\Delta\phi$, of the state is reduced for ever larger coherent states, i.e. $\Delta\phi \propto 1/|\alpha|$. This also enhances the phase sensitivity.

As will become clear in section 4.1, these quadratures, $\hat{X}$ and $\hat{Y}$, couple to the mechanical degrees of freedom. The vacuum noise of $\hat{X}$ will act as a driving force,

[1] so called because they are 90 deg out of phase - thus in "quadrature".

[2] Thus why this state is also known as displaced vacuum, i.e. the vacuum state displaced by a large mean field α.

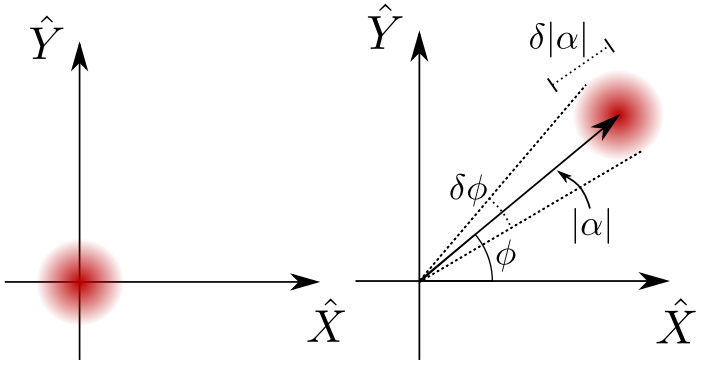

Figure 2.1: **Vacuum and coherent optical field in phase space.** The vacuum state (**left**) has zero mean amplitude and a spread given by the ground state variance of 1/2 in each quadrature. A coherent state (**right**) has a mean amplitude of α and a phase between the quadratures of ϕ. The amplitude and phase sensitivities are shown as $\delta\phi$ and $\delta|\alpha|$.

while the quadrature $\hat{Y}$ will inscribe the motional information and its shot noise will determine the sensitivity to this motion above the lights coherent state vacuum noise. The trade-off between the improved sensitivity, scaling with $1/|\alpha|$, and the driving force of $\hat{X}$, scaling with $|\alpha|$, leads to the standard quantum limit.

Just as in eqs. (2.5) and (2.6), we can also look at the correlation functions of these Hermitian quadrature operators. We find that

$$\langle \hat{Y}(t)\hat{Y}(t')\rangle = \langle \hat{X}(t)\hat{X}(t')\rangle = \left(\bar{n} + \frac{1}{2}\right)\delta(t-t'), \tag{2.14a}$$

$$\langle \hat{Y}(\Omega)\hat{Y}(\Omega')\rangle = \langle \hat{X}(\Omega)\hat{X}(\Omega')\rangle = \left(\bar{n} + \frac{1}{2}\right)\delta(\Omega-\Omega'). \tag{2.14b}$$

where the optical quadratures in the Fourier domain are given by

$$\hat{X}(\Omega) = \frac{1}{\sqrt{2}}\left(\hat{a}^\dagger(-\Omega) + \hat{a}(\Omega)\right), \tag{2.15a}$$

$$\hat{Y}(\Omega) = \frac{i}{\sqrt{2}}\left(\hat{a}^\dagger(-\Omega) - \hat{a}(\Omega)\right). \tag{2.15b}$$

Most often in this work the relevant case is when the field is in the vacuum state with $\bar{n} = 0$. The variance of 1/2 for each quadrature as just discussed is also seen in the power spectral density, discussed in appendix A, of the optical quadratures. These will be

$$S_{YY}(\Omega) = S_{XX}(\Omega) = 1/2, \tag{2.16}$$

and are spectrally white. This shot noise level sets the standard noise floor in quantum limited measurements of these quadratures. In practice these quadratures contain frequency dependent noise and looking at the power spectral density of an optical quadrature as a function of Fourier frequency is commonly referred to as a spectrum. The noise is typically additional to the shot noise of eq. (2.16), but may in certain cases through an interaction with a system, interfere destructively with the shot noise and create spectral regions of sub-poissonian light statistics. We will see this in explicitely in section 4.4.

2.2 Polarization states

2.2.1 Free space description

Previously we simply stated results for the electromagnetic field quantized in a finite volume. This gives rise to discrete allowed wave-vectors, of which we just considered a single mode. Now we wish to talk about fields in free space. We, thus, take our finite boundary conditions and let them tend to infinity. This leads to a continuum of allowed wave-vectors, k and thus radiation modes $\hat{a}(k)$. If we restrict ourselves to a single polarization degree of freedom and quantize the field only along a single direction, say z, then the full continuum hamiltonian for the radiation field is given by

$$\hat{\mathcal{H}}_L = \int \hbar ck \left(\hat{a}^\dagger(k)\hat{a}(k) + 1/2\right) \mathrm{d}k. \tag{2.17}$$

Considering both the time and spatial dynamics of a continuum mode is elegantly summarized in Julsgaard (2003, App. C.). Consider the very relevant case where we have an interaction between a light field and some system given by the Hamiltonian $\hat{\mathcal{H}}_{\text{int}}$. The field $\hat{a}(z,t)$ is defined in every point in space and time, and its evolution in real space[1] is then given by

$$\left(\frac{\partial}{\partial t} + c\frac{\partial}{\partial z}\right)\hat{a}(z,t) = \frac{i}{\hbar}\left[\hat{\mathcal{H}}_{\text{int}}, \hat{a}(z,t)\right] \tag{2.18}$$

where the spatial evolution term comes from the evolution of the field according to $\hat{\mathcal{H}}_L$.

These field operators $\hat{a}(z,t)$ are defined as the Fourier transforms of the reciprocal space operators $\hat{a}(k)$. From eq. (2.17) the term $\hat{a}^\dagger(k)\hat{a}(k)\,\mathrm{d}k$ can be interpreted as the photon number within the wavevector slice $k \to k + \mathrm{d}k$. Thus, in "real space" $\hat{a}^\dagger(z)\hat{a}(z)\,\mathrm{d}z$ is the number of photons in some region of space bounded by z and $z + \mathrm{d}z$. For free space modes it is often most useful to talk about photon fluxes at a particular point in space, say before and after an interaction with some system. It is, thus, sensible to define a field operator,

$$\hat{a}(t) = \sqrt{c}\,\hat{a}(z,t). \tag{2.19}$$

where the added factor of c normalizes the operator such that $\hat{a}^\dagger(t)\hat{a}(t)$ now describes the photon flux at some point z.

2.2.2 Stokes vectors

Classically a light field with different polarization components can be fully described by what are known as Stokes vectors. These vectors span a 4D space of polarization

[1] as opposed to reciprocal k-space.

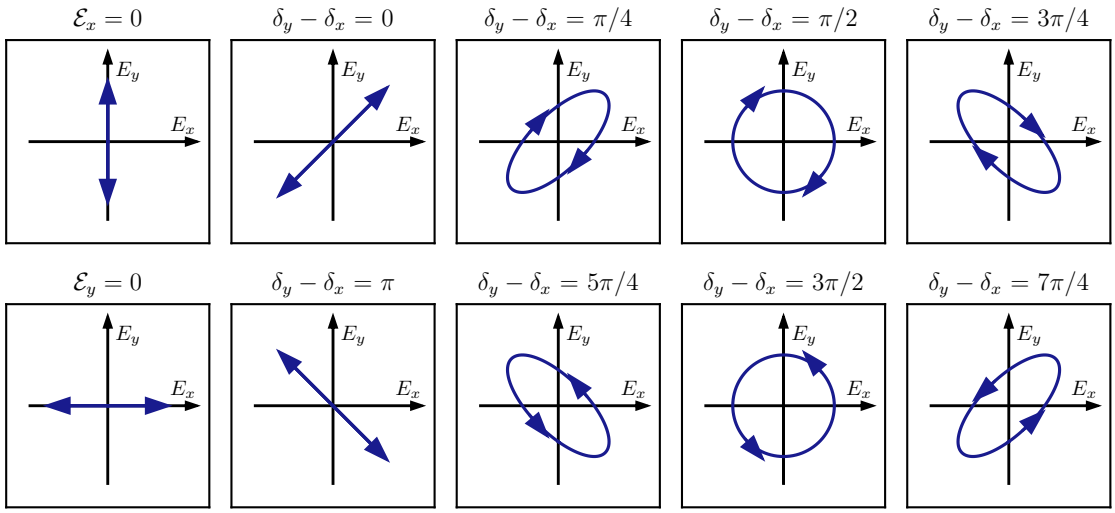

Figure 2.2: **Polarization ellipse examples.** Examples of polarization types visualized by the polarization ellipse described by eq. (2.21). We describe the examples going left to right with $\mathcal{E}_x = \mathcal{E}_y$ unless otherwise stated. **First column:** Linearly polarized light along y (top) and x (bottom). **Second column:** Linearly polarized light along 45° (top) and −45° (bottom). **Third and fifth column:** Elliptically polarized right (top) and left (bottom) handed light. **Fourth column:** Circularly polarized right (top) and left (bottom) handed light.

states, which are exhaustively covered in great detail in Goldstein (2003). Normalizing these vectors yields three vectors spanning the interior of a unit sphere. Here we will simply give a quick classical introduction and then state the results as they pertain to our needs.

Suppose a plane wave, monochromatic light field traveling along z is composed of polarization components along two orthogonal directions x and y. If we consider the electric field of this wave at a particular point in space we can write,

$$\boldsymbol{E}(t) = \boldsymbol{e}_x \underbrace{\mathcal{E}_x \cos(\omega t + \delta_x)}_{E_x} + \boldsymbol{e}_y \underbrace{\mathcal{E}_y \cos(\omega t + \delta_y)}_{E_y}, \tag{2.20}$$

where we have E_x and E_y as the electric field components along the x and y direction respectively. Notice that the polarization components may have a relative phase between them given by $\delta = \delta_y - \delta_x$. The allowed configurations of these polarization components is given by what is known as the polarization ellipse

$$\frac{E_x^2(t)}{\mathcal{E}_x^2} + \frac{E_y^2(t)}{\mathcal{E}_y^2} - \frac{2E_x(t)E_y(t)}{\mathcal{E}_x\mathcal{E}_y}\cos(\delta) = \sin^2(\delta). \tag{2.21}$$

This ellipse describes the electric field in the transverse plane and is a convenient way to visualize the polarization state of the light. A selection of polarization configurations are shown in fig. 2.2. The particular polarization state is simply defined by relative phase shift between the two polarization components as well as their magnitude. We distinguish between three distinct polarization types each described by two degenerate states. These are,

- Linearly polarized light along the horizontal axis x and vertical axis y (pictorially $\leftrightarrow$ and $\updownarrow$),
- Linearly polarized light oriented at $\pm 45°$ w.r.t the x axis, (pictorially $\nearrow$ and $\nwarrow$)
- Left and right handed circularly polarized light (LHCP, RHCP) around the direction of propagation, (pictorially $\circlearrowleft$ and $\circlearrowright$).

The polarization states are neatly summarized by the famous classical Stokes polarization parameters, which together provide a complete description of any polarization state. More on their classical derivation, description and use can be found in Goldstein (2003).

We are interested in a quantum analogue of these vectors. If we write our quantized electric field component of the light in a form reminiscent of eq. (2.20) we get,

$$\hat{\boldsymbol{E}}(z,t) = \mathcal{E}_x \boldsymbol{e}_x \left(\hat{a}_x e^{i\phi_x(t)} + \hat{a}_x^\dagger e^{-i\phi_x(t)}\right) + \mathcal{E}_y \boldsymbol{e}_y \left(\hat{a}_y e^{i\phi_y(t)} + \hat{a}_y^\dagger e^{-i\phi_y(t)}\right) \tag{2.22}$$

where we have written the time dependence of a mode $\hat{a}_i$ out in its phase $\phi_i(t) = kz - \omega t + \delta_i$. With this definition in mind, we define the quantum analogs of the Stokes vectors, for a field traveling along the z direction, as

$$\hat{S}_0(z,t) = \frac{1}{2}\left(\hat{a}_x^\dagger \hat{a}_x + \hat{a}_y^\dagger \hat{a}_y\right) = \frac{1}{2}\left(\hat{n}_x + \hat{n}_y\right), \tag{2.23a}$$

$$\hat{S}_x(z,t) = \frac{1}{2}\left(\hat{a}_x^\dagger \hat{a}_x - \hat{a}_y^\dagger \hat{a}_y\right) = \frac{1}{2}\left(\hat{n}_x - \hat{n}_y\right), \tag{2.23b}$$

$$\hat{S}_y(z,t) = \frac{1}{2}\left(\hat{a}_x^\dagger \hat{a}_y + \hat{a}_y^\dagger \hat{a}_x\right) = \frac{1}{2}\left(\hat{n}_{+45} - \hat{n}_{-45}\right), \tag{2.23c}$$

$$\hat{S}_z(z,t) = \frac{1}{2i}\left(\hat{a}_x^\dagger \hat{a}_y - \hat{a}_y^\dagger \hat{a}_x\right) = \frac{1}{2}\left(\hat{n}_R - \hat{n}_L\right), \tag{2.23d}$$

where we have omitted writing the time and space dependence of the field operators. We can always perform the normalization to photon fluxes of eq. (2.19) for the Stokes vectors

$$\hat{S}_i(t) = c\hat{S}_i(z,t), i \in \{0,x,y,z\}, \tag{2.24}$$

so that we may talk about the operators in terms of photon fluxes at a particular point in space.

These Stokes operators of eq. (2.23d) are expressed in the linearly horizontal and vertical basis. Notice that in this basis $\hat{S}_x$ is the difference in the photon number flux operators of polarizations aligned to this basis. Similarly, if we rotate basis into that of $\pm 45°$ or R, L we find that $\hat{S}_y$ and $\hat{S}_z$ express differences in the amount of ± 45 deg polarized light and RCHP vs LCHP polarized light, respectively. The

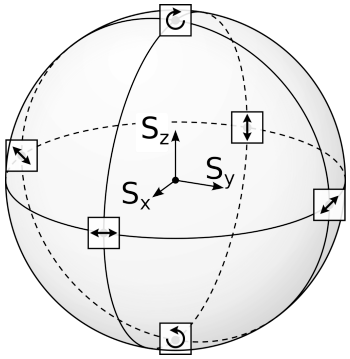

Figure 2.3: **Poincare sphere.** The Stokes components $\hat{S}_j,\ j \in \{x, y, z\}$ span the polarization space, which can be visualized as tracing out a sphere of radius $\hat{S}_0$. This sphere is useful in representing the polarization of a light field. Figure is a modified version of Geek3 (2014).

total number flux of excitations of the field is characterized by $\hat{S}_0$ in any basis, since $\hat{n}_x + \hat{n}_y = \hat{n}_{45} + \hat{n}_{-45} = \hat{n}_R + \hat{n}_L$. The details of these transformations are given in eq. (2.25) below. The operators in these rotated bases are defined by the following basis vectors

$$\boldsymbol{e}_{45,-45} = \frac{(\boldsymbol{e}_x \pm \boldsymbol{e}_y)}{\sqrt{2}}, \tag{2.25a}$$

$$\boldsymbol{e}_{L,R} = \frac{(\boldsymbol{e}_x \pm i\boldsymbol{e}_y)}{\sqrt{2}}. \tag{2.25b}$$

As we shall see in section 5.5, these Stokes operators present the natural language through which the atomic spins and light will communicate. There are strong analogies between the Stokes operators $\hat{S}_i$ presented here (and in particular the approximation presented below in section 2.2.3) and the atomic spin operators $\hat{J}_i$ of eq. (5.23) (where $i \in \{0, x, y, z\}$). An example of this is that they both obey the angular momentum commutation relations of (here written for the Stokes operators)

$$\left[\hat{S}_j, \hat{S}_k\right] = i\epsilon_{jkl}\hat{S}_l, \tag{2.26a}$$

$$\left[\hat{S}_0, \hat{S}_j\right] = 0,\ \ j \in \{x, y, z\}, \tag{2.26b}$$

$$\hat{S}_0\left(\hat{S}_0 + 1\right) = \hat{S}_x^2 + \hat{S}_y^2 + \hat{S}_z^2. \tag{2.26c}$$

where the tensor ϵ_{jkl} is the usual anti-symmetric Levi-Civita symbol.

Analogous to how one may represent the states of a two-level spin 1/2 particle on the Bloch sphere, the Stokes operators describing the polarization state may be represented on the Poincare sphere shown in fig. 2.3. By construction we can use the intrastructure of the Pauli matrices defined for the Bloch sphere to define the Stokes vectors. Exactly how is described in appendix B.4.

From eq. (2.18) it follows that these Stokes operators evolve according to the some interaction Hamiltonian as

$$\left(\frac{\partial}{\partial t} + c\frac{\partial}{\partial z}\right)\hat{S}(z,t) = \frac{i}{\hbar}\left[\hat{\mathcal{H}}_{\text{int}}, \hat{S}(z,t)\right]. \tag{2.27}$$

The interacting medium, we will eventually be considering, is an atomic ensemble contained within a region of 10 mm in length meaning that light travels through it in 33 ps. The dynamics of interest in the atomic ensemble will be on a timescale on the order of $\sim 1\,\mu$s, which is much slower. We will be concerned with observing of the effect of the atom-light interaction by measuring the light polarization quadratures and will, therefore, be concerned with variations on the latter timescale. Thus, for the evolution of the Stokes operators we may in practice neglect the effects of field retardation ($\partial/\partial t$ term) and simply write

$$c\partial_z \hat{S}(z,t) \equiv c\frac{\partial}{\partial z}\hat{S}(z,t) \approx \frac{i}{\hbar}\left[\hat{\mathcal{H}}_{\text{int}}, \hat{S}(z,t)\right]. \tag{2.28}$$

If we say that the region the atoms are confined to is between $z = 0$ and $z = L$, then we can write these input-output relations for all the light polarization quadratures as

$$\hat{S}_k^{\text{in}}(t) \equiv \hat{S}_k(z=0,t), \tag{2.29a}$$
$$\hat{S}_k^{\text{out}}(t) \equiv \hat{S}_k(z=L,t), \tag{2.29b}$$

for $k \in \{x, y, z\}$.

In practice we need to do polarimetry to measure these light polarization quadratures. The procedure and logic to do this is described in appendix B.3 and essentially involves manipulating the light field by use of polarizers and phase retarders, and detecting appropriate fields with balanced detectors.

2.2.3 Effective quadrature operators

Suppose we have a large coherent state linearly polarized along x. We can then treat this field component classically and write $\hat{a}_x \to i\alpha$, where $\alpha \in \mathbb{R}$ and the phase is chosen without the loss of generality. If the remaining component in the field $\hat{a}_y$ is small, then keeping only terms to first order in it, our Stokes vectors can be re-written as,

$$\hat{S}_x \to S_x = \frac{\alpha^2}{2}, \tag{2.30a}$$
$$\hat{S}_y = \frac{i\alpha}{2}\left(\hat{a}_y^\dagger - \hat{a}_y\right), \tag{2.30b}$$
$$\hat{S}_z = -\frac{\alpha}{2}\left(\hat{a}_y + \hat{a}_y^\dagger\right). \tag{2.30c}$$

In light of the notation introduced in section 2.1 it is clear that we can express $\hat{S}_y$ and $\hat{S}_z$ from eq. (2.30) above as effective quadratures of the y polarization mode. Defining quadratures

$$\hat{X} \equiv \frac{\hat{S}_z}{\sqrt{S_x}}, \tag{2.31a}$$
$$\hat{Y} \equiv -\frac{\hat{S}_y}{\sqrt{S_x}}, \tag{2.31b}$$

we obtain the canonical commutation relation of $\left[\hat{X}, \hat{Y}\right] = i$ already seen in eq. (2.10). Thus, by having a strong field, linearized along x, the orthogonal polarization components form a convenient effective harmonic oscillator.

Furthermore, on a practical level, realizing quantum limited performance of these quadratures is not very demanding on a typical laser. Using of a high extinction polarizer can easily produce light with sufficiently clean, for our purposes, polarization quadratures.

As we shall see in chapter 5 these polarization quadratures couple to the degrees of freedom of the spin system. Being able to relate these general polarization quadratures to the classic effective amplitude and phase optical phase quadratures is important for the mapping required to link the spin and optomechanical systems in chapter 6.

2.3 Fabry-Pérot cavity

The Fabry-Pérot resonator is one of the simplest interferometers available. In its purest form it consists of just two parallel reflecting boundaries. In this section we will consider the basics of such a device where both these boundaries consist of mirrors.

2.3.1 Classical basics

The basic dynamics of a cavity can be summarized in the following way. Suppose a plane wave input described by electric field E_{in} impinges on a mirror of field reflection and transmission amplitudes (r_1, t_1). Part of the field will be reflected and the remaining (in the absence of losses) will be transmitted. Once transmitted the field meets another mirror with field reflection and transmission amplitudes (r_2, t_2). Clearly, part of the field will be reflected and met by the first mirror once more, this is the field E_2. Thus a circulating field is generated that can build up if the counter propagating fields constructively interfere. This process can be thought of as the field having an effective roundtrip gain proportional to r_1 and r_2, as will be seen shortly. The fields relevant to the description of the cavity are illustrated in fig. 2.4, and their relation to each other are given by the following relations,

$$E_{\text{refl}} = it_1 e^{ikL} E_2 + r_1 E_{\text{in}}, \tag{2.32a}$$
$$E_1 = it_1 E_{\text{in}} + r_1 e^{ikL} E_2, \tag{2.32b}$$
$$E_2 = r_2 e^{ikL} E_1, \tag{2.32c}$$
$$E_{\text{out}} = it_2 e^{ikL} E_1. \tag{2.32d}$$

The field E_1 encapsulates the relevant dynamic. It is the sum of the transmitted input field itE_{in} and the reflected field having completed a roundtrip $r_1 e^{ikL} E_2$. This can, thus, be thought of as the ("circulating") intracavity field. The relative power

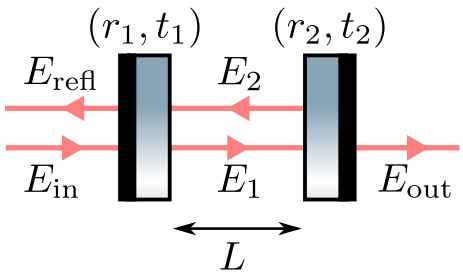

Figure 2.4: **Basic Fabry-Pérot cavity.** The input E_{in} and reflected E_{refl} fields are seen on the left. In the middle, the counter propagating fields E_1 and E_2 fill the cavity of length L. The output field is given by E_{out}. The mirrors themselves have amplitude reflection and transmission coefficients $(r_i, t_i),\ i \in \{1, 2\}$.

of the input and intracavity fields will be given by

$$\frac{|E_1|^2}{|E_{\text{in}}|^2} = \frac{t_1^2}{1 - r_1 r_2 e^{2ikL}} \equiv g t_1^2 \tag{2.33}$$

$$= \frac{T_1}{\left(1 - \sqrt{R_1 R_2}\right)^2 + 4\sin^2(kL)}, \tag{2.34}$$

where the enhancement for constructive interference, $\sin^2(kL) = 0$, is evident. This requirement is simply for the accumulated roundtrip phase $2kL = n2\pi,\ n \in \mathbb{Z}$. When this is the case the intracavity field is enhanced by a factor $|g| = \left(1 - \sqrt{R_1 R_2}\right)^{-1}$, which in principle can be arbitrarily high as the reflectivities of the mirrors are increased. The intracavity field of eq. (2.34) is plotted in fig. 2.5 where resonances and an enhancement of the input power are apparent for the above mentioned choice of roundtrip phase. The spacing between the consecutive longitudinal modes is given by the free spectral range (FSR) and the width of the resonances are given by the cavity bandwidth κ. The ratio of these two define the cavity finesse $\mathcal{F}$

$$\mathcal{F} \equiv \frac{\text{FSR}}{\kappa/2\pi}, \tag{2.35}$$

which is a useful quantity providing a numerical intuition for the sharpness of the cavity enhancement features seen in fig. 2.5.

An FSR simply corresponds to an additional 2π in roundtrip phase. We can change this phase by either altering the cavity length by δL or by changing the input field frequency by $\delta\nu$. The FSRs[1] corresponding to these are,

$$\text{FSR}_{\delta L} = \frac{\lambda}{2}, \tag{2.36a}$$

$$\text{FSR}_{\delta\nu} = 1/\tau_{RT} = \frac{c}{2L}, \tag{2.36b}$$

where we further define the cavity round-trip time $\tau_{RT} \equiv \frac{2L}{c}$.

[1] note the $\text{FSR}_{\delta\nu}$ is not in angular units. This convention is used throughout this thesis.

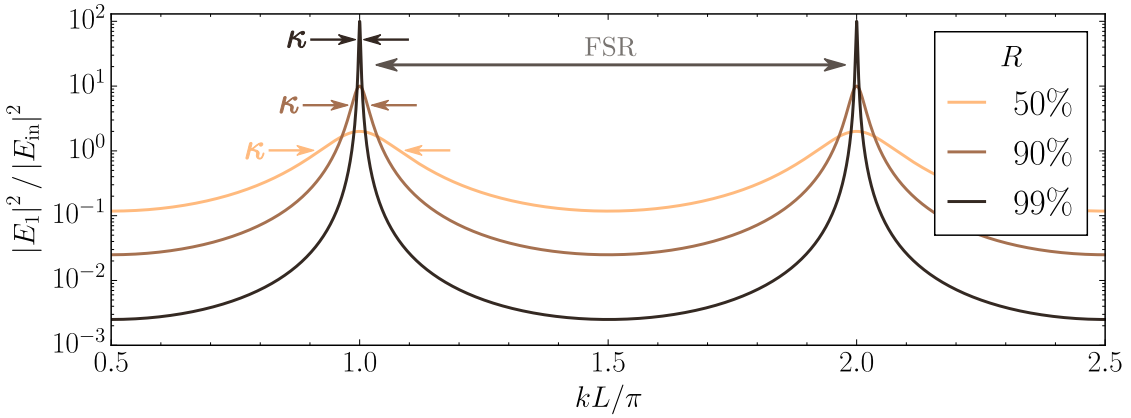

Figure 2.5: **Cavity resonances.** Intracavity field for variable round trip phase $2kL$. Symmetric cavity consisting of mirrors with a power reflectivity of $R = R_1 = R_2$. Periodic cavity enhancements (resonances) of the input power every 2π multiple of the roundtip phase. Resonance spacing is a free spectral range (FSR) and the width (FWHM) of these resonances is the cavity linewidth κ.

The FSR is a parameter independent of mirror reflectivities, as is it constitutes a statement about the roundtrip phase. The cavity bandwidth κ, however, is related to the amplitude of the roundtrip gain. Thus, it does depend on the mirror choice, as we shall soon see.

What is not reflected need not be transmitted. In general optical losses are present and can be characterized by a power loss of δ_i. The power transmission and reflections for each mirror i are related by energy conservation through $R_i + T_i = 1 - \delta_i$, which allow us to define a round trip power loss of

$$\delta_{\mathrm{RT}} = \delta_0 + (1 - R_1) + (1 - R_2) \tag{2.37a}$$

$$= T_1 + T_2 + \delta_0 + \delta_1 + \delta_2 = T_1 + T_2 + \delta_L \tag{2.37b}$$

characterizing the fractional power returned per round trip of the cavity. Above δ_0 characterizes additional loss not associated with the mirrors and δ_L simply describes all power losses not associated with a transmission. This round trip loss is unsurprisingly related to the cavity enhancement. In the limit where the transmission and added losses are small compared to the reflection, they are related via $|g| = 2/\delta_{\mathrm{RT}}$.

In general, one can relate the cavity finesse[2] eq. (2.35) to the total roundtrip (RT) loss of eq. (2.37) via Ismail et al. (2016)

$$\mathcal{F} = \frac{\pi}{2}\left[\arcsin\left(\frac{1 - \sqrt{\delta_{\mathrm{RT}}}}{2\sqrt[4]{\delta_{\mathrm{RT}}}}\right)\right]^{-1} \approx \frac{2\pi}{\delta_{\mathrm{RT}}}, \tag{2.38}$$

where the approximation is very good for small roundtrip losses[3].

[2] so called Lorentzian finesse.

[3] only a $\sim 10\,\%$ error at $\delta_{\mathrm{RT}} = 20\,\%$.

Looking back at eq. (2.34) and fig. 2.5, and assuming a small roundtrip loss $\delta_{\mathrm{RT}} \ll 1$, the resonant power enhancement can be cast in terms of the cavity finesse[4],

$$\frac{|E_1|^2}{|E_{\mathrm{in}}|^2} \approx \frac{4T_1}{\delta_{\mathrm{RT}}^2} \approx 4\eta_1 \frac{\mathcal{F}}{2\pi}. \tag{2.39}$$

Here we have introduced another important parameter, namely the coupling efficiency η, characterizing the efficiency of coupling a field through a given port. It measures how large a fraction of the total cavity round trip loss is given by said port. This is both of practical and fundamental importance. Practically, it determines how large an input field is needed to reach a desired intracavity field. Fundamentally, it acts both as a limited detection efficiency[5], as well as a measure of the importance of the vacuum fluctuations entering from a given port.

For a general port $i \in (1, 2)$ we have an in/out-coupling efficiency

$$\eta_i = T_i/\delta_{\mathrm{RT}} = \kappa_i/\kappa. \tag{2.40}$$

Here we have used the fact that total angular loss rate of the cavity κ is, in general, linearly composed of many component loss rates κ_i via,

$$\kappa = \delta_{\mathrm{RT}}/\tau_{\mathrm{RT}} = \kappa_1 + \kappa_2 + \kappa_{\mathrm{ex}} \tag{2.41}$$

$$\kappa_{1,2} = \frac{T_{1,2}}{\tau_{\mathrm{RT}}}, \tag{2.42}$$

where $\kappa_{1,2}$ are due to the transmissions of mirrors 1 and 2. The remaining term $\kappa_{ex} = \delta_L/\tau_{\mathrm{RT}}$ in an additional loss term that describes all remaining loss.

2.3.2 Classical input-output

To get a idea of how this intracavity field evolves with time let us consider the field E_1 on the time scale of a roundtrip, τ_{RT}. From eq. (2.32) we see that

$$E_1(t + \tau_{\mathrm{RT}}) = it_1 E_{\mathrm{in}}(t) + r_1 r_2 e^{2ikL} E_1(t). \tag{2.43}$$

We can approximate the time evolution by noting that the round trip time is very fast compared to the dynamics of interest in the cavity, i.e.

$$\dot{E}_1(t) \approx \frac{E_1(t + \tau_{\mathrm{RT}}) - E_1(t)}{\tau_{\mathrm{RT}}} \tag{2.44}$$

$$\approx \left(i\Delta - \frac{\kappa}{2}\right) E_1 + \frac{it_1}{\tau_{\mathrm{RT}}} E_{\mathrm{in}} \tag{2.45}$$

$$= \left(i\Delta - \frac{\kappa}{2}\right) E_1 + \sqrt{\kappa_1} \frac{E_{\mathrm{in}}}{\tau_{\mathrm{RT}}}, \tag{2.46}$$

[4] notice that for typical parameters the enhancement is roughly given by $\mathcal{F}$.

[5] If only one output port is observed

where we assumed that the mirror reflectance $r_{1,2} \approx 1$ and that laser frequency $\omega_L = k/c$ are close[6] to the cavity resonance ω_c. The difference between these two frequencies is known as the detuning

$$\Delta \equiv \omega_L - \omega_c. \tag{2.47}$$

Since $\kappa_1 = \frac{t_1^2}{\tau_{\mathrm{RT}}}$, we have written $\sqrt{\kappa_1} = \frac{it_1}{\sqrt{\tau_{\mathrm{RT}}}}$ for didactic purposes. Had we chosen a different convention[7] for the amplitude transmission and reflection coefficients, we would have found the same evolution equation, but without the awkward complex unit.

If we Fourier transform eq. (2.46) we find that the intracavity power, is simply the input enhanced by a Lorentzian of κ (FWHM) centered on $\Omega = \Delta$, i.e.

$$\frac{|E_1(\Omega)|^2}{|E_{\mathrm{in}}(\Omega)|^2 / \tau_{\mathrm{RT}}} = \frac{\kappa_1}{(\kappa/2)^2 + (\Delta - \Omega)^2}. \tag{2.48}$$

Whenever the cavity finesse is high the cavity lineshape is well approximated by a Lorentzian. In this regime we recover the power enhancement of eq. (2.39) when $\Delta = \Omega = 0$, as expected.

Now let's see what we may learn about the intracavity field E_1 by measuring E_{refl}. If we look at the reflected field, and make the same approximations, we find that

$$\frac{E_{\mathrm{refl}}}{\sqrt{\tau_{\mathrm{RT}}}} \approx r_1 \frac{E_{\mathrm{in}}}{\sqrt{\tau_{\mathrm{RT}}}} - \sqrt{\kappa_1} E_1. \tag{2.49}$$

This is known as an input-output equation and describes how, and at what rate, information is gathered about the intracavity field. Had we looked at the output port 2 of the cavity we would have found that the field leaks out with a rate of $\sqrt{\kappa_2}$. Thus, in general the efficiency of a port i to collect the information pertaining to the intracavity field is given by $\eta_i = \kappa_i/\kappa$ of eq. (2.40).

This efficiency can, almost at will, be conveniently tailored for cavities. As we shall shortly see, in the quantum context it is often the case that you wish one port to be highly overcoupled, i.e. $\eta \approx 1$. For classical fields you occasionally want quite the opposite. For a cavity probed in transmission we find

$$\frac{|E_{\mathrm{out}}(\Omega)|^2}{|E_{\mathrm{in}}(\Omega)|^2} = \frac{\kappa_1 \kappa_2}{(\kappa/2)^2 + (\Delta - \Omega)^2} \tag{2.50}$$

$$= \frac{4T_1 T_2}{\delta_{\mathrm{RT}}} = 4\eta_1\eta_2, \ \Delta = \Omega = 0. \tag{2.51}$$

From which we note one of many useful features. If the cavity has no additional loss, then $\eta_1\eta_2 = \eta_1(1 - \eta_1)$. If we choose $\eta_1 = 1/2$, also known as critical coupling,

[6] $\Delta/\mathrm{FSR} \ll 1$

[7] this is done to be consistent with previous work Jayich et al. (2008), Nielsen (2016)

and probe on resonance $\Delta = 0$ we will get $|E_{\text{out}}(0)|^2 = |E_{\text{in}}(0)|^2$. Thus, the DC power will be transmitted. However noise at sideband (SB) frequencies $\Omega \neq 0$ will be suppressed by the cavity Lorentzian. This is a way to filter a laser with classical noise at SB frequencies.

Looking at the reflected field, on resonance we similarly find that in the low loss limit,

$$\frac{|E_{\text{refl}}(\Omega)|^2}{|E_{\text{in}}(\Omega)|^2} = |1 - 2\eta_1|^2, \ \Delta = \Omega = 0, \tag{2.52}$$

from which it is clear that for critical coupling, no light is reflected back. This is a consequence of the light reflected destructively interfering with the light transmitted from the cavity in the reflected port.

2.3.3 Practical considerations

Cavity geometry

In practice, the cavity input optical spatial modes are not plane waves but rather Gaussian, see appendix D.1 for their most basic description. The mirrors can, therefore, not both be flat to form a stable high finesse resonator. In fact, to form a stable resonator there are certain requirements, detailed in appendix D.3, which must be fulfilled. For this work we make use of a stable plano-concave cavity geometry. Their are infinitely many spatial modes allowed in such a cavity and they are given by eq. (D.3.31). Of interest to us is the fundamental TEM_{00} mode as this allows for the highest optomechanical coupling as described in section 4.5.2.

Achieving high finesse

Furthermore, achieving high finesse is easier said than done. In practice one cannot make the mirror reflectivities arbitrarily close to 1, although one can through considerable effort actually get .99999, which is remarkably close, by use of a distributed Bragg reflector. The conventional technique for optical mirrors, such as the ones made use of in this work, involves depositing a coating consisting of alternating layers of high and low index of refraction. This forms an effective high optical impedance in a narrow frequency band, whose center is defined by the thickness of the layers.

The limit to achievable finesse arises due to parasitic losses, which also limit the attainable degree of overcoupling as well as the reachable intracavity power as the fraction of light not reflected is shared between transmission and loss. As this loss begins to dominate the transmission, less light is admitted with diminishing returns from the (slightly) increasing finesse.

Achieving the aforementioned incredible reflections of $1 - R \simeq 1\,\text{ppm}$ requires tremendous skill and effort with respect to the coating itself. It additionally puts strict requirements on the optical substrates the coatings are placed upon. At these

1 ppm levels, controlling various imperfections, which lead to scattering and absorption, becomes very relevant.

For example, the fraction of scattered light S at a wavelength λ probing a large flat region of rms surface roughness δ is given by

$$S = 1 - \exp\left[-\left(\frac{4\pi\delta}{\lambda}\right)^2\right] \approx \left(\frac{4\pi\delta}{\lambda}\right)^2, \tag{2.53}$$

where the approximation is good in the typical case of small surface roughness $\delta \ll \lambda$.

This means that achieving a scatter of < 1 ppm at 852 nm requires a surface roughness of about $\delta = 0.7$ Å over a large region of the mirror probed by the cavity mode. Needless to say, making optical substrates achieving these levels of polish is difficult, but surprisingly (though barely) feasible. The larger the required clear aperture region is, however, the more challenging.

For this reason the specifics of the desired cavity modes and their extent may conflict with a desire for a high finesse (low loss) cavity. In particular the cavity spot size is often restricted by the amount of tolerable loss. This may be due to a limited region of the mirror coating being low loss, or, in our case typically, an opaque Silicon frame holding a membrane. The loss from these simple cases be estimated using the results of appendix D.2 and are useful in considerations of membrane geometries designs.

2.4 Quantum Heisenberg-Langevin equation

It seems natural to extend the field description above to the quantum domain. However, fundamental to the classical interpretation is that the field in the cavity leaks out and is "lost" to the environment. Treating this loss on the quantum mechanical level is non-trivial, but can be done in a rather intuitive sense as we shall see.

Central to describing this dissipation is the idea of a reservoir (bath[1]) to which your system is coupled. It is through this coupling that the system decays by leaking into the bath. The fluctuation-dissipation theorem demands that the bath also leaks into the system. The effect of this is a fluctuating driving term, referred to as the Langevin force. This fluctuating force also ensures that the commutation relations of eq. (2.1) are conserved in the presence of loss.

In the short exposition we will follow the approach described in Gardiner and Collett (1985); Lukin (2005). In doing so, we will assume that this bath is an infinite reservoir with no memory, i.e. a delta correlated in time. This is of course not true in general, but is a good model so long as the characteristic time scale of the bath is much shorter than that of cavity decay, which is the case for all the oscillators we will consider. This type of reservoir is known as Markovian.

[1] These are used interchangeably, but refer to one and the same.

Suppose we wish to describe the dynamics of a system S coupled to a reservoir R, then the full Hamiltonian will be given by

$$\hat{\mathcal{H}} = \hat{\mathcal{H}}_{\mathrm{S}} + \hat{\mathcal{H}}_{\mathrm{S\text{-}R}} + \hat{\mathcal{H}}_{\mathrm{R}}, \tag{2.54}$$

where $\hat{\mathcal{H}}_{\mathrm{S\text{-}R}}$ describes the system–reservoir interaction. The evolution of an operator $\hat{\mathcal{O}}_\mu$ is then given by,

$$\frac{\mathrm{d}}{\mathrm{d}t}\hat{\mathcal{O}}_\mu = \frac{i}{\hbar}\left[\hat{\mathcal{H}}_{\mathrm{S}}, \hat{\mathcal{O}}_\mu\right] + \frac{i}{\hbar}\left[\hat{\mathcal{H}}_{\mathrm{S\text{-}R}}, \hat{\mathcal{O}}_\mu\right] + \frac{i}{\hbar}\left[\hat{\mathcal{H}}_{\mathrm{R}}, \hat{\mathcal{O}}_\mu\right]. \tag{2.55}$$

We will in this thesis only be interested in the dynamics of system operators, and thus we can disregard $\hat{\mathcal{H}}_{\mathrm{R}}$ in the following discussion.[2]

We can, in general, write the system–reservoir Hamiltonian in terms of system and reservoir operators $\hat{S}$ and $\hat{R}$, respectively, as

$$\hat{\mathcal{H}}_{\mathrm{S\text{-}R}} = -(\hat{R}^\dagger \hat{S} + \hat{R}\hat{S}^\dagger). \tag{2.56}$$

From here we can solve the evolution equation of eq. (2.55) for a general system operator $\mathcal{O}_\mu$ and get the general quantum Heisenberg-Langevin equation given by

$$\frac{\mathrm{d}}{\mathrm{d}t}\hat{\mathcal{O}}_\mu = \hat{d}_\mu + \hat{f}_\mu, \tag{2.57}$$

$$\hat{d}_\mu = \frac{i}{\hbar}\left[\hat{\mathcal{H}}_{\mathrm{sys}}, \hat{\mathcal{O}}_\mu\right] + \text{decay}. \tag{2.58}$$

Here $\hat{d}_\mu$ represents the evolution of the field operator as determined by the system Hamiltonian $\hat{\mathcal{H}}_{\mathrm{sys}}$ and the decay. The Langevin force is a stochastic force with $\langle \hat{f}_\mu \rangle = 0$ and correlation function given by

$$\langle \hat{f}_\mu \hat{f}_\nu \rangle = 2D_{\mu\nu}\delta(t - t'). \tag{2.59}$$

We can evaluate the correlation function by application of the fluctuation dissipation theorem, which, assuming the bath is Markovian, is given by the generalized Einstein equation of

$$2D_{\mu\nu} = \frac{\mathrm{d}}{\mathrm{d}t}\langle \hat{\mathcal{O}}_\mu \hat{\mathcal{O}}_\nu \rangle - \langle \hat{\mathcal{O}}_\mu \hat{d}_\nu \rangle - \langle \hat{d}_\mu \hat{\mathcal{O}}_\nu \rangle. \tag{2.60}$$

Since the reservoir is simultaneously the drain into which the system mode $\hat{S}$ decays, and the source of the stochastic driving Langevin force $\hat{f}$, we can express the reservoir operator $\hat{R}$ in terms of these as

$$\hat{R}(t) = i\hbar\left(\frac{\gamma}{2}\hat{S} + \hat{f}(t)\right) \tag{2.61}$$

[2]Reservoir engineering is an interesting topic in its own right. In optomechanics, to pick an example, it may be used to facilitate a two-mode squeezed states between two mechanical oscillators as described in Woolley and Clerk (2014).

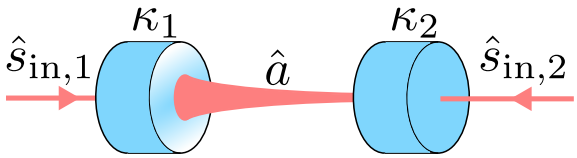

Figure 2.6: **Quantum cavity description.** Input modes $\hat{s}_{\mathrm{in,j}}$ couple through ports j to force the intracavity field $\hat{a}$. Drawn are only input modes from the cavity ports labeled $j = 1, 2$. In general, loss in the cavity not due to transmission through the mirrors constitutes yet another port, which although not illustrated would be in addition to 1 and 2.

where γ is the power decay rate of the system mode $\hat{S}$ into reservoir $\hat{R}$.

We can write down the Heisenberg-Langevin equation of motion for a general system operator $\hat{\mathcal{O}}$ as

$$\frac{\mathrm{d}}{\mathrm{d}t}\hat{\mathcal{O}} = \frac{i}{\hbar}\left[\hat{\mathcal{H}}_{\mathrm{S}}, \hat{\mathcal{O}}\right] + \left(\frac{\gamma}{2}\hat{S}^{\dagger} + \hat{f}^{\dagger}\right)\left[\hat{\mathcal{O}}, \hat{S}\right] - \left[\hat{\mathcal{O}}, \hat{S}^{\dagger}\right]\left(\frac{\gamma}{2}\hat{S} + \hat{f}\right). \tag{2.62}$$

This Heisenberg-Langevin evolution equation allows us to describe the evolution and dissipation of a cavity or mechanical mode quantum mechanically. Both of these will also serve as an excellent illustration of the quantum Heisenberg-Langevin equation in action!

2.5 Quantum description cavity modes

2.5.1 Cavity Evolution

Using the classical system as a guide, we now wish to map into the language of the Heisenberg-Langevin approach described in section 2.4. The setup is illustrated in fig. 2.6. We can easily identify the fields outside the cavity entering through port $j \in (1, 2)$ as reservoirs whose operators we can write as $i\hbar\sqrt{\eta_j\kappa}\,\hat{s}_{\mathrm{in,j}}(t)$. The prefactors are added in anticipation of a result akin to that of the classical evolution found in eq. (2.46). The system operator is of course the cavity operator, $\hat{a}$ and thus we can write out the Hamiltonian as,

$$\hat{\mathcal{H}} = \hat{\mathcal{H}}_{\mathrm{S}} + \hat{\mathcal{H}}_{\text{S-R}} + \hat{\mathcal{H}}_{\mathrm{R}}, \tag{2.63a}$$

$$\hat{\mathcal{H}}_S = \hat{\mathcal{H}}_{\mathrm{cav}} = \hbar\omega_c\hat{a}^{\dagger}(t)\hat{a}(t), \tag{2.63b}$$

$$\hat{\mathcal{H}}_{\text{S-R}} = \hat{\mathcal{H}}_{\mathrm{drive}} = -i\hbar\sum_j \sqrt{\eta_j\kappa}\left(\hat{s}_{\mathrm{in,j}}(t)\hat{a}^{\dagger}(t) - \hat{s}^{\dagger}_{\mathrm{in,j}}(t)\hat{a}(t)\right), \tag{2.63c}$$

$$\hat{\mathcal{H}}_{\mathrm{R}} = \hat{\mathcal{H}}_{\mathrm{laser}} = \sum_j \hbar\omega_{\mathrm{L,j}}\hat{s}^{\dagger}_{\mathrm{in,j}}(t)\hat{s}_{\mathrm{in,j}}(t). \tag{2.63d}$$

The time dependent, Heisenberg picture, field operators in eq. (2.63) evolve on the time scale of their optical frequency which is typically much faster than the timescales of interest here. Any such slowly varying residual can be isolated from the fast optical dynamics if we move into a rotating frame at the laser and input

field frequencies. Doing so we find these residual slowly varying operators and a simplified Hamiltonian of

$$\hat{\mathcal{H}} = \hat{\mathcal{H}}_{\mathrm{S}} + \hat{\mathcal{H}}_{\text{S-R}} + \hat{\mathcal{H}}_{\mathrm{R}}, \tag{2.64a}$$

$$\hat{\mathcal{H}}_S = \hat{\mathcal{H}}_{\mathrm{cav}} = -\Delta \hat{a}^\dagger \hat{a} - \frac{i\kappa}{2} \hat{a}^\dagger \hat{a}, \tag{2.64b}$$

$$\hat{\mathcal{H}}_{\text{S-R}} = \hat{\mathcal{H}}_{\mathrm{drive}} = i\hbar \sum_j \sqrt{\eta_j \kappa} \left(\hat{s}^\dagger_{\mathrm{in,j}} \hat{a} - \hat{s}_{\mathrm{in,j}} \hat{a}^\dagger \right), \tag{2.64c}$$

$$\hat{\mathcal{H}}_{\mathrm{R}} = 0. \tag{2.64d}$$

This is done by a unitary transformation, the procedure which is described in appendix E.1. The operator needed to construct the unitary matrix is $\hat{A} = \hbar\omega_{\mathrm{L}} \hat{a}^\dagger(t)\hat{a}(t)t + \sum_j \hbar\omega_{\mathrm{L,j}} \hat{s}^\dagger_{\mathrm{in,j}}(t)\hat{s}_{\mathrm{in,j}}(t)$. Going forward we adopt a slightly sloppy, but more readable, notation for the subsequent operators now in the rotating frame. This choice is also described in appendix E.1.

If we now solve for the evolution of the cavity mode $\hat{a}$ according to the Hamiltonian of eq. (2.64) according to eq. (2.55) adding the mode damping, or by applying eq. (2.62) using $\hat{S} = \hat{a}$ and $\hat{f} = \sum_j \sqrt{\eta_j \kappa}\, \hat{s}_{\mathrm{in,j}}$, we get

$$\dot{\hat{a}} = \left(i\Delta - \frac{\kappa}{2} \right) \hat{a} + \sum_j \sqrt{\eta_j \kappa}\, \hat{s}_{\mathrm{in,j}}. \tag{2.65}$$

This is the Heisenberg-Langevin equation for the cavity mode. It is, by construction, clearly of the classic form given by eq. (2.58). Furthermore, eq. (2.65) is reminiscent of the classical result of eq. (2.46). If the input modes were comprised of large mean fields then we recover this classical result.

This is often the case as the input fields are typically a coherent field from a laser with a large mean field and quantum fluctuations on top. In the case of a coherent tone this is the typical description and is indeed referred to as "displaced vacuum", see fig. 2.1. Such a scenario would also give rise to a large intracavity mean field. We thus cast the fields $\hat{a}$ and $\hat{s}_{\mathrm{in,j}}$ as

$$\hat{a} = \bar{a} + \delta\hat{a}, \tag{2.66}$$

$$\hat{s}_{\mathrm{in,j}} = \bar{s}_{\mathrm{in,j}} + \delta\hat{s}_{\mathrm{in,j}}. \tag{2.67}$$

We thus get two equations of motion, one for the mean field, and one for the quantum fields. These are given by

$$\dot{\bar{a}} = \left(i\Delta - \frac{\kappa}{2} \right) \bar{a} + \sum_j \sqrt{\eta_j \kappa}\, \bar{s}_{\mathrm{in,j}}, \tag{2.68}$$

$$\dot{\delta\hat{a}} = \left(i\Delta - \frac{\kappa}{2} \right) \delta\hat{a} + \sum_j \sqrt{\eta_j \kappa}\, \delta\hat{s}_{\mathrm{in,j}}. \tag{2.69}$$

Where eq. (2.68) reproduces the classical heuristic result of eq. (2.46) in the case of a single input. We simply identify $\bar{s}_{\mathrm{in}} = E_{\mathrm{in}}/\tau_{\mathrm{RT}}$ and $\bar{a} = E_1$. This also lets us

notice that these fields are defined differently. The input modes $\hat{s}_{\mathrm{in,j}}$ describe photon fluxes whereas the intracavity field describes a photon number[1].

Suppose we consider the effect of having just one input, $j = 1$, and we consider the steady state case $\dot{\bar{a}} = 0$, then

$$\bar{n} \equiv |\bar{a}|^2 = \frac{\eta_1 \kappa}{\Delta^2 + (\kappa/2)^2} \frac{P_{\mathrm{in}}}{\hbar\omega_L}, \tag{2.70}$$

$$P_{\mathrm{in}} \equiv |\bar{s}_{\mathrm{in},1}|^2 \hbar\omega_L, \tag{2.71}$$

which if we consider the cavity on resonance and compare to the input power, gives

$$\frac{P_{\mathrm{circ}}}{P_{\mathrm{in}}} = \frac{\hbar\omega_L \bar{n}/\tau_{\mathrm{RT}}}{P_{\mathrm{in}}} = 4\eta_1 \frac{\mathcal{F}}{2\pi}. \tag{2.72}$$

This is just as we found in eq. (2.39). In this case we cast circulating power in terms of the intracavity field on the timescale of the roundtrip time.

The main difference between the classical argument and the quantum one is, that you will always have vacuum leaking in from both ports in proportion to the ports coupling efficiency η_j and the cavity loss κ. Notice that in eq. (2.69) the input modes play the role of the thermal Langevin force of the eq. (2.58), where $\delta\hat{s}_{\mathrm{in,j}} = \hat{f}_j/\sqrt{\eta_j\kappa}$. Expressing the correlation functions of these we find the expected delta-correlated bath as a result of the commutation relations of the reservoir modes,

$$\langle \hat{s}_{\mathrm{in,j}}(t)\hat{s}^\dagger_{\mathrm{in,j}}(t')\rangle = (\bar{n}_j(\omega) + 1)\,\delta(t - t'), \tag{2.73a}$$

$$\langle \hat{s}^\dagger_{\mathrm{in,j}}(t)\hat{s}_{\mathrm{in,j}}(t')\rangle = \bar{n}_j(\omega)\delta(t - t'), \tag{2.73b}$$

where $\bar{n}_j(\omega) = \langle \hat{s}^\dagger_{\mathrm{in,j}}\hat{s}_{\mathrm{in,j}}\rangle$ is the mean occupation of at a particular frequency ω. This occupation is given by the bosonic thermal occupation of

$$n(\omega) = \frac{1}{\exp(\hbar\omega/k_BT) - 1} \to \begin{cases} \frac{k_BT}{\hbar\omega}, & \text{for } k_BT \gg \hbar\omega \\ 0, & \text{for } k_BT \ll \hbar\omega \end{cases} \tag{2.74}$$

where T is the temperature of the bath. For the optical frequencies relevant to this work, the mean occupation is absolutely negligible[2]. However for experiments utilizing microwave sources at say 1 GHz, you would already have a mean thermal occupation of 1 at 70 mK. Thus why most microwave quantum optomechanics experiments are done in a dilution refrigeration environment.

Our cavities will have decay rates of < 100 MHz, which is very small compared to the optical frequencies ~ 350 THz used to probe. This can be characterized by the cavity Q-factor, similarly defined to the mechanical Q-factor of eq. (3.40) as $Q_{\mathrm{cav}} = \omega_c/\kappa$, which is $> 10^6$. Thus, we can to a very good approximation say that the optical thermal occupation is spectrally flat across the cavity bandwidth.

[1] This makes good sense in the classical picture too. The input field is a traveling wave, thus, best described by an input power, whereas the intracavity field is a standing wave best described by its energy.

[2] $n(852\,\mathrm{nm}) \sim 10^{-26}$ at $T = 300\,\mathrm{K}$.

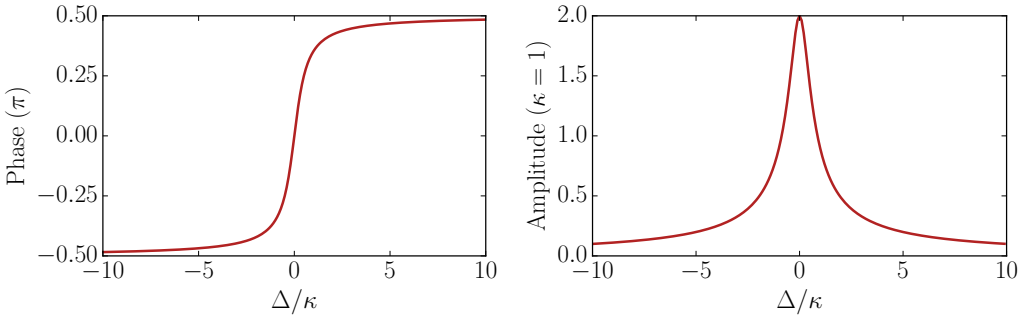

Figure 2.7: **Intracavity field phase and amplitude.** Intracavity field phase (**left**) and amplitude (**right**) as a function of cavity detuning. The field is given by eq. (2.76) and the phase is measured relative to the input field $\bar{s}_{\text{in}}$. For the amplitude plot we set $\kappa = 1$ and $\bar{s}_{\text{in}} = 1$.

2.5.2 Cavity input-output

Just as we saw in section 2.5.1, the quantum equations of motion can be motivated from the classical. So we write the input-output equations of the cavity in direct analogy to the classical result of eq. (2.49) as

$$\hat{s}_{\text{out,j}}(t) = \hat{s}_{\text{in,j}}(t) - \sqrt{\eta_j \kappa}\,\hat{a}. \tag{2.75}$$

These input-output relations can also be used to derive the steady state mean reflected and transmitted field equations of eqs. (2.51) and (2.52) as is easily checked by squaring the eq. (2.77) and eq. (2.78). If we consider a single input, with coupling efficiency η, and mean input field $\bar{s}_{\text{in}}$, then

$$\bar{a} = \frac{\sqrt{\eta\kappa}}{(\kappa/2) - i\Delta}\bar{s}_{\text{in}}, \tag{2.76}$$

$$\bar{s}_{\text{refl}} = \bar{s}_{\text{in}} - \sqrt{\eta\kappa}\,\bar{a}, \tag{2.77}$$

$$\bar{s}_{\text{trans}} = -\sqrt{(1-\eta)\kappa}\,\bar{a}. \tag{2.78}$$

The amplitude and phase of the mean intracavity field $\bar{a}$ relative to the input field $\bar{s}$ is shown in fig. 2.7. The transmitted field $\bar{s}_{\text{trans}}$ has the same relative phase but a different amplitude as is clear from eq. (2.78).

Unlike the intracavity or transmitted field, the phase of the reflected field $\bar{s}_{\text{refl}}$ depends on the coupling efficiency η since there is an interference with the light immediately reflected. In the regime of $\eta > 1/2$ the reflected field is always π phase shifted on resonance as is seen in fig. 2.8. The returned power is also shown and varies with the coupling efficiency.

Cavity coupling regimes

Three regimes present themselves from the perspective of the reflected field. For $\eta > 1/2$ we are "overcoupled" and see a large contribution from the intracavity

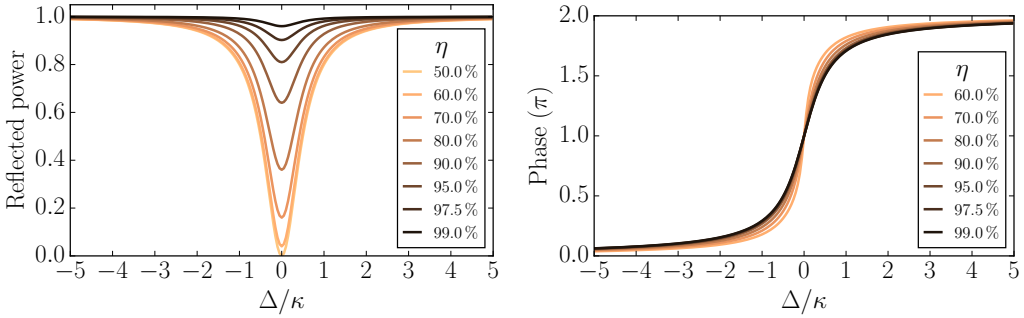

Figure 2.8: **Reflected power and phase.** The mean field reflected power (**left**) and phase (**right**) relative to the input field as function of cavity detuning as described by eq. (2.77). In both cases the overcoupling η of the cavity is varied.

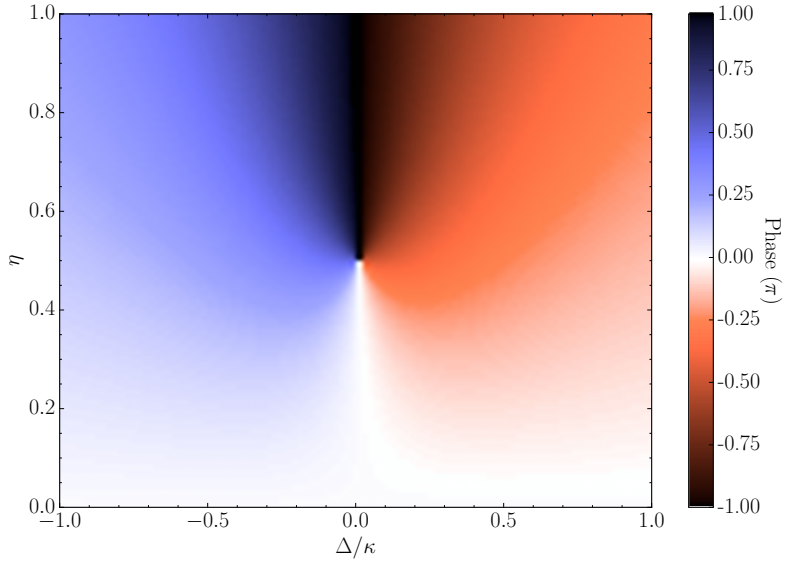

Figure 2.9: **Reflected field phase for variable overcoupling.** Reflected field phase of eq. (2.77) as a function of cavity detuning Δ and cavity overcoupling η. The phase wraps around at π (black) for visual ease.

field. When $\eta = 1/2$ we are critically coupled[3], and all input power is lost in the cavity (to the transmitted port or elsewhere). Finally there is the undercoupled regime of $\eta < 1/2$. The phase of the reflected field for all these conditions can be seen in fig. 2.9.

From the quantum perspective it is clear from eqs. (2.77) and (2.78) that the coupling efficiency η effectively sets the limit for the detection efficiency of the intracavity field. This loss will mask the quantum correlations of the intracavity field as seen in e.g. the sub-poissonian light statistics observed in section 4.4. Thus, for many quantum optics experiments the overcoupled regime is preferable.

For the scheme of quantum back-action evasion in section 6.2 the cavity is probed in reflection, and we wish to measure both the intracavity field as well as the input field. In this case the highly overcoupled regime is preferable and we can write

[3]Also known as impedance matched

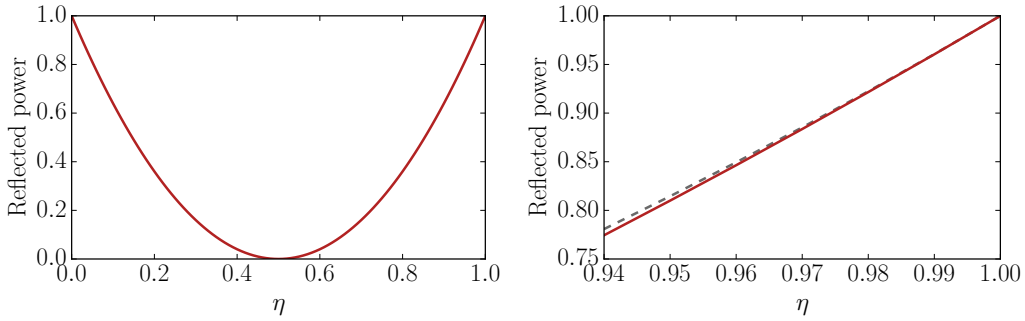

Figure 2.10: **On resonance reflected power.** Reflected power (red curve) on cavity resonance according to eq. (2.79). **Left:** Varying the overcoupling from the undercoupled regime of $\eta < 1/2$, through the critical coupling $\eta = 1/2$ into the overcoupled regime $\eta = 1/2$. **Right:** Closer view at the highly overcoupled regime. Here the reflected power goes as $\approx \eta^4$ and the approximation of the exact η^4 dependence (dashed grey line) is very good within the typically relevant regime of $\eta > 95\,\%$.

$\eta = (1 - \epsilon) \approx 1$, where $\epsilon \ll 1$ is a power loss. The detection efficiency of the input field reflected off the cavity (on resonance, $\Delta = 0$ for simplicity), is

$$\frac{|\bar{s}_{\text{refl}}|^2}{|\bar{s}_{\text{in}}|^2} = (1 - 2\eta)^2 \approx (1 - 4\epsilon) \approx \eta^4. \tag{2.79}$$

The on resonance reflected power of eq. (2.79) is shown in fig. 2.10 and can be compared to the power loss of fig. 2.8. Clearly, if the cavity is operated detuned, as turned out to be desirable in results to be discussed in chapter 6, this loss can be reduced.

Phase of reflected field

We will be concerned with the effect of these phase rotations on the quadrature operators. The input-output relations of eq. (2.75) are trivially extended to that of field amplitude and phase quadrature operators, defined by eq. (2.8), such that

$$\begin{pmatrix} \hat{X}_{\text{out,j}}(t) \\ \hat{Y}_{\text{out,j}}(t) \end{pmatrix} = \begin{pmatrix} \hat{X}_{\text{in,j}}(t) \\ \hat{Y}_{\text{in,j}}(t) \end{pmatrix} - \sqrt{\eta_j \kappa} \begin{pmatrix} \hat{X}_{\text{cav}} \\ \hat{Y}_{\text{cav}} \end{pmatrix}, \tag{2.80}$$

where $\hat{X}_{\text{cav}}$, $\hat{Y}_{\text{cav}}$ are a cavity amplitude and phase quadratures. Supposing again that we have only a single input they are predictably related to their input via

$$\begin{pmatrix} \hat{X}_{\text{cav}} \\ \hat{Y}_{\text{cav}} \end{pmatrix} = \begin{pmatrix} \cos(\theta) & \sin(\theta) \\ -\sin(\theta) & \cos(\theta) \end{pmatrix} \begin{pmatrix} \hat{X}_{\text{in}} \\ \hat{Y}_{\text{in}} \end{pmatrix}, \tag{2.81}$$

where the rotation by $\theta = \text{Arg}(\bar{a}/\bar{s}_{\text{in}})$ is the phase rotation of the input field by the cavity. It is given by,

$$\tan(\theta) = \frac{\Delta}{\kappa/2}, \tag{2.82}$$

which is shown in fig. 2.7. For detunings comparable to the cavity half-bandwidth this rotation is very significant. In fact when $|\Delta| = \kappa/2$ the intracavity quadratures will be an equal mix of the input amplitude and phase quadratures. In the far detuned regime of $|\Delta| \gg \kappa/2$ the roles are completely swapped, such that the intracavity amplitude quadrature is simply given by the input phase quadrature, and vice versa. The quadrature rotation will be important once the mechanical oscillator is introduced to the cavity.

The reflected field quadratures can likewise be viewed as rotated inputs given by

$$\hat{\boldsymbol{X}}_{\text{out}} = \boldsymbol{R}^{\intercal}(\phi)\hat{\boldsymbol{X}}_{\text{in}}, \tag{2.83}$$

$$\boldsymbol{R}(\phi) \equiv \begin{pmatrix} \cos(\phi) & -\sin(\phi) \\ \sin(\phi) & \cos(\phi) \end{pmatrix}, \tag{2.84}$$

where ϕ is shown in fig. 2.9 and is given by

$$\tan(\phi) = \frac{-2\eta x}{x^2 + (1 - 2\eta)}, \; x = \frac{\Delta}{\kappa/2}. \tag{2.85}$$

Notice that for $\eta \approx 1$ and $\Delta \ll \kappa/2$ the reflected field simply acquires the phase shift $\phi \approx 2\theta = \Delta/\kappa$, i.e. getting the same small rotation going in and out of the cavity. In eq. (2.84) we have written the input and output quadratures in vector form where

$$\hat{\boldsymbol{X}}_{\text{in,out}} = \begin{pmatrix} \hat{X}_{\text{in,out}} \\ \hat{Y}_{\text{in,out}} \end{pmatrix}. \tag{2.86}$$

Chapter 3

Mechanics

Integral to the work of this thesis is the behavior and description of a traditional mechanical harmonic oscillator. It forms the oscillator, originally discussed in the motivational example of section 1.1, the motion of which we wish to measure as precisely as possible. Experimentally we chose a highly stressed, $\sim 60\,\mathrm{nm}$ thick and $\sim 500\,\mu\mathrm{m}$ wide, stoichiometic silicon nitride[1] membrane to be this canonical oscillator. This choice is made due to its very low optical as well as mechanical losses, a crucial resource in the quantum limited sensing.

The extreme $\sim 10^4$ aspect ratio between the membrane side length and its thickness, as well the high stress, is why we call it a membrane and suggest that the dynamics of thin plates are applicable to describe their behavior. This membrane and the larger Si device supporting it can be seen in fig. 3.8 and is the membrane used for the results presented later in section 4.4 and chapter 6.

In this chapter we will start off by describing membranes as stressed thin plates. We will then see how such a device can be treated as a effectively 1D damped harmonic oscillator and then discuss its quantized equations of motion.

The importance of the mechanical quality factor (a measure of the mechanical dissipation) will then be highlighted followed by a discussion of the various losses which impact it. Finally we will discuss the physical implementation of our membrane device and its fabrication. We will conclude by reflecting on the past, present and future generation of membrane devices used.

3.1 Membranes

3.1.1 Simple description

Consider a thin plate of uniform density ρ and isotropic in-plane stress σ a sketch of which is shown in fig. 3.1. For small out of plane deviations $w(x, y, t)$ of the membrane from equilibrium at $z = 0$ we can naively postulate a generic wave equation

[1] Although the chemical composition is Si_3N_4 we will simply write SiN throughout this work.

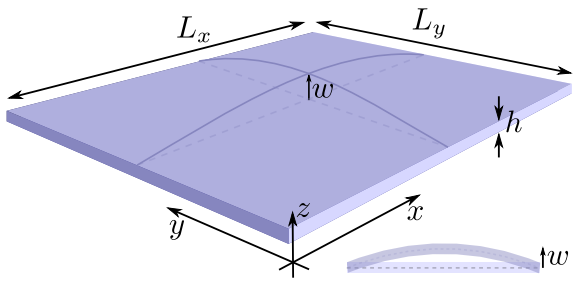

Figure 3.1: **Membrane sketch** Sketch of a thin plate of height h and side lengths of L_x and L_y. The effect of an out of plane displacement w is shown by the curved solid blue lines over the dashed equilibrium values. The inset to the right shows a profile view of an example of out of place displacement.

to describe the motion. It will be given by

$$\nabla^2 w = \frac{1}{c^2}\ddot{w}, \tag{3.1a}$$

$$c^2 \equiv \sigma/\rho, \tag{3.1b}$$

where the speed of sound c is given by the Newton-Laplace equation.

If we enforce the boundary conditions of zero out of plane displacement at the edges of the membrane and assume a separable solution of the form

$$w(x, y, t) = q(t)\phi(x, y), \tag{3.2}$$

we find that the displacement will spatially be determined by (given a suitable choice of origin)

$$\phi_{mn}(x, y) = \sin(mk_x x)\sin(nk_y y), \ \{m, n\} \in \mathbb{Z} \tag{3.3a}$$

$$k_x = \frac{\pi}{L_x}, \ k_y = \frac{\pi}{L_y}. \tag{3.3b}$$

The allowed wave-vectors mk_x and nk_y are quantized by the boundary conditions of

$$\phi_{mn}(0, 0) = \phi_{mn}(L_x, 0) = \phi_{mn}(L_x, L_y) = \phi_{mn}(0, L_y) = 0, \tag{3.4}$$

where L_x and L_y are the membrane dimensions along x and y respectively.

As perhaps could be expected the quantized wave-vectors result in a mode dependent time evolution of amplitude q_{mn}. For each mode these are given by

$$q_{mn}(t) = q_{mn}(0)\cos(\Omega_{mn} t) \tag{3.5}$$

where Ω_{mn} is the angular mode frequency. This solution assumes an initial arbitrary phase choice of $\dot{q}_{mn}(0) = 0$. In general, the motion will of course be a superposition of all modes with each their own phase. However, we will in practice be concerned with individual modes and thus this complication is omitted.

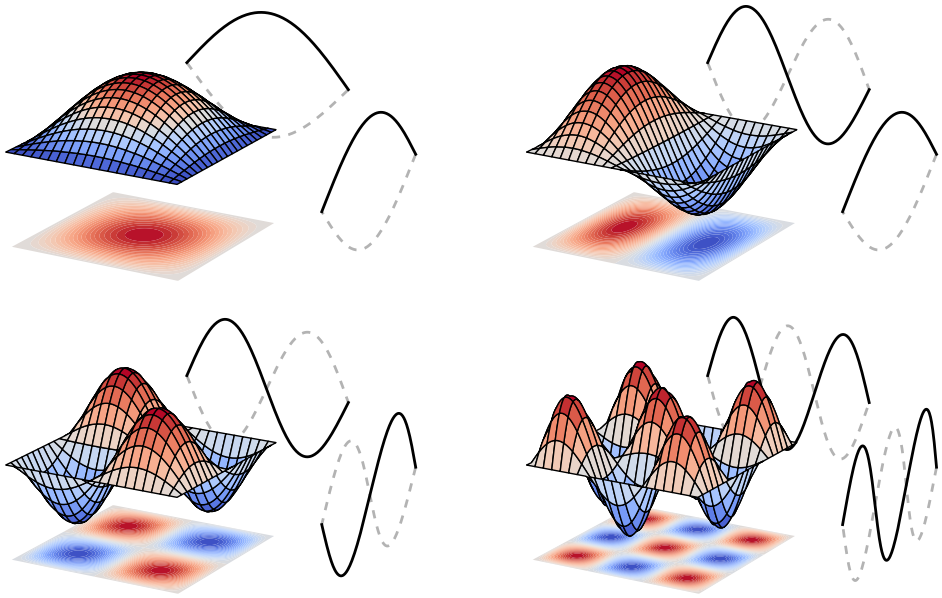

Figure 3.2: **Membrane mode examples.** A snapshot of simplistic motion (meshed sheet) for a selection of membrane modes characterized by mode numbers (m, n) according to eq. (3.2). Going left to right and top to bottom we have (1,1), (1,2), (2,2) and (3,3). For each, red is considered maximum displacement whereas blue is minimal. The black lines show the profile of motion along the x and y axis of the membrane at maximum displacement. The dashed grey lines shown the same but with a phase lag of π. Below each membrane is a 2D displacement map.

A selection of the spatial modes allowed eq. (3.3) are shown in fig. 3.2. From the profiles of the modes along the x or y direction it is clear that the mode indexes m and n denote the number of antinodes along these axes respectively.

The angular frequency of these modes are given by

$$\Omega_{mn} = c\sqrt{(mk_x)^2 + (nk_y)^2} = \pi c\sqrt{\frac{m^2}{L_x^2} + \frac{n^2}{L_y^2}}, \tag{3.6}$$

which for a square membrane of $L = L_x = L_y$ simplifies to,

$$\Omega_{mn} = \Omega_{11}\sqrt{\frac{m^2 + n^2}{2}}, \ \Omega_{11} = \frac{\sqrt{2}\pi c}{L}, \tag{3.7}$$

where Ω_{11} is the membranes fundamental frequency. The membranes used in this work[1], described in section 3.10, have a fundamental mode frequency of about 0.8 MHz. Furthermore, in chapters 4 and 6 we will be working with the $(1, 2)$ mode which has a frequency of about 1.3 MHz.

[1]Stress from fabrication is $\sigma = 1\,\text{GPa}$ and stoichiometric SiN has a density of $\rho = 3200\,\text{kg/m}^3$, Pierson (2000).

3.1.2 Detailed description

The simplistic wave equation of eq. (3.1) turns out to be an excellent approximation to the actual dynamics of the membranes under consideration. The full expression for a small out of plane displacement w of a membrane of uniform thickness h is given by Landau L.D. (1986); Leissa (1993)

$$-\frac{\partial^2}{\partial x_\beta^2}\left(D_{\alpha\beta}\frac{\partial^2}{\partial x_\alpha^2}\right)w + h\frac{\partial}{\partial x_\beta}\left(\sigma_{\alpha\beta}\frac{\partial}{\partial x_\alpha}\right)w = \rho\ddot{w},\ \alpha,\beta\in\{x,y\}, \tag{3.8}$$

where the Einstein summation convention is implied and h is the membrane thickness as shown in fig. 3.1. $D_{\alpha\beta}$ is known as the flexural rigidity and $\sigma_{\alpha\beta}$ the stress, both given along a particular axis denoted by the subscripts. For the membranes of interest in this work, which are based on amorphous SiN, we can reasonably assume that the density and tension are isotropic, i.e. $D_{\alpha\beta} = D$ and $\sigma_{\alpha\beta} = \sigma$. Thus, we can simplify eq. (3.8) to

$$-\frac{D}{\sigma h}\nabla^4 w + \nabla^2 w = \frac{1}{c^2}\ddot{w}, \tag{3.9}$$

where $\nabla^4 \equiv \nabla^2(\nabla^2)$ is the biharmonic operator and c is the speed of sound as defined in eq. (3.1).

The additional term in eq. (3.9) can be understood by considering the now modified dispersion relation. If we consider a square membrane with[2] wavevector $k = k_x = k_y$, and frequency Ω_{mn}, for simplicity we see that[3]

$$\Omega_{mn}^2 = \left(m^2+n^2\right)k^2\left(1+\frac{D}{h\sigma}\left(m^2+n^2\right)k^2\right)c^2 \equiv k_{\text{eff},mn}^2 c^2 \tag{3.10}$$

The effect is clearly an increased effective wavevector $k_{\text{eff},mn}$, which leads to an increased energy cost $\propto k^2$. This can be associated with the curvature of a given mode, which is proportional to the second spatial derivative – thus k^2.

Since this effect is related to the bending of a structure one would naively expect it to depend on the materials Youngs modulus E and Poisson ratio ν. It should also scale with the thickness as the bending cost associated with a thicker base should be higher for a given k (which is independent of thickness). In fact the flexural rigidity is defined as,

$$D \equiv \frac{Eh^3}{12\left(1-\nu^2\right)}. \tag{3.11}$$

We can quantify the impact of this additional term via the modification is has on the dispersion relation. Had we considered the impact more generally we would have found the relevant dimensionless parameter for a given mode (m,n) to be

$$R_{m,n} = \frac{D}{\sigma h}\left(m^2+n^2\right)k^2 \propto \left(\frac{h}{L}\right)^2. \tag{3.12}$$

[2]The extension is trivial to different side lengths is trivial.

[3]Fourier transforming we simply have $\frac{\mathrm{d}}{\mathrm{d}x} \to i(mk_x)$ and $\frac{\mathrm{d}}{\mathrm{d}t} \to i\Omega_{mn}$. See eq. (A.1.7).

In this work we will generally be concerned with low order modes, $m, n \sim 1$, where $R \sim 10^{-5}$. Indeed we would need to make our membranes 10 times larger or work with modes of $m, n \sim 10$ for this even to be $\sim$ ‰ effect. Thus, the approximation originally made in eq. (3.1) and the derived expressions are excellent approximations for our purposes here.

Furthmore, there are no real benefits to the work here in making the membranes thicker. In fact, due to the current advances of Tsaturyan et al. (2017), thinner membranes are a likely choice for future endeavours.

3.2 Effective 1D harmonic oscillator

It is often useful to recast the general 3D dynamics of eq. (3.9) into an effective 1D harmonic oscillator. This will be especially useful for this work as we will eventually only probe the membrane motion at a point. The modes of this effective 1D oscillator will effective masses of m_{eff}, which may be different from the physical mass of the entire membrane m_{phys}.

For our simple geometry we can approximate this effective mass by considering the solution to eq. (3.1). From the separable solution of eq. (3.2) we can integrate the potential energy contribution of each oscillating mass element comprising the entire volume V of the membrane. This gives the total potential energy of a given mode (m, n) as

$$U_{mn}(t) = \frac{1}{2}\Omega_{mn}^2 \int w^2(x, y, t)\, \mathrm{d}V \tag{3.13}$$

$$= \frac{1}{2}\frac{\rho L_x L_y h}{4}\Omega_{mn}^2 q^2(t), \tag{3.14}$$

which evidently doesn't depend on which mode number is being considered.

We can compare this potential to that of a traditional 1D harmonic oscillator of mass m and displacement $x(t)$ with potential energy[1] $U_{mn} = \frac{1}{2}m_{mn}\Omega_{mn}^2 x^2(t)$. Doing so, we identify that we can assign our 3D membrane the effective 1D mass of

$$m_{\text{eff}} = \frac{\rho L_x L_y h}{4} = \frac{1}{4}m_{\text{phys}}, \tag{3.15}$$

While the effective mass for a rectangular membrane is independent of the mode index, this is not true in general. The effective mass of axisymmetric modes of circular membranes decreases for higher mode numbers (more radial anti-nodes) as is shown and discussed in Wilson (2012).

We can also define an effective spring constant $K_{\text{eff},mn}$, which is related to the eigenmode frequencies through the dispersion relation of eq. (3.10) as,

$$\Omega_{\text{eff},mn} = k_{\text{eff},mn}c = \sqrt{\frac{K_{\text{eff},mn}}{m_{\text{eff},mn}}}. \tag{3.16}$$

[1] An unfortunate case of notation. m_{mn} is the mass m of mode (m, n) written as a subscript.

We can, thus, write down a 1D simple harmonic oscillator equation of motion for the membrane in the absence of any driving force or damping as

$$m_{\text{eff}}\ddot{q}_{mn}(t) + K_{\text{eff},mn}q_{mn}(t) = 0. \tag{3.17}$$

3.2.1 Galerkin's Method

For more complicated mechanical structure, we can, in general, calculate the effective mass and spring constant using Galerkin's method Schmid et al. (2016). This approach is readily implemented in finite-element modeling of non-trivial geometries, making it possible to define effective parameters for more complicated membrane designs. This is particularly important for the designs of new membranes which are based on Tsaturyan et al. (2017).

With Galerkin's method the effective parameters can be calculated via integrating the normalized spatial mode function $\phi(x, y)$ as follows

$$m_{\text{eff},mn} = \rho \int \phi_{mn}^2 \, \mathrm{d}V, \tag{3.18a}$$

$$K_{\text{eff},mn} = \sigma \int \left(\frac{D}{\sigma h} \phi_{mn} \nabla^4 \phi_{mn} - \phi_{mn} \nabla^2 \phi_{mn} \right) \mathrm{d}V, \tag{3.18b}$$

which for the standard square membrane of fig. 3.1 reproduces the results of eqs. (3.15) and (3.16).

Note that the effective spring constant is related to the effective wave-vector by

$$K_{\text{eff},mn} = (m_{\text{eff},mn}c^2)k_{\text{eff},mn}. \tag{3.19}$$

We can write eq. (3.18a) in a more suitable fashion for use in finite element modeling. Also allowing the density ρ to vary with position ($\boldsymbol{r}$) we have

$$m_{\text{eff}} = \int \rho(\boldsymbol{r}) \left(\frac{|\boldsymbol{Q}(\boldsymbol{r})|}{|\boldsymbol{Q}(\boldsymbol{r})|_{\max}} \right)^2 \mathrm{d}V, \tag{3.20}$$

where the mode displacements $\boldsymbol{Q}$ are integrated over the entire structure of volume V.

3.3 Damped harmonic oscillator

So far we have said nothing about the forces and interactions that invariably damp the motion of any real world membrane. These will show up in our effective 1D harmonic oscillator equation eq. (3.17) under the collective umbrella of an effective dissipation rate γ_m. This effective damping rate will contain contributions from many different sources of various origins. A selection of the damping mechanisms will be discussed later in this chapter.

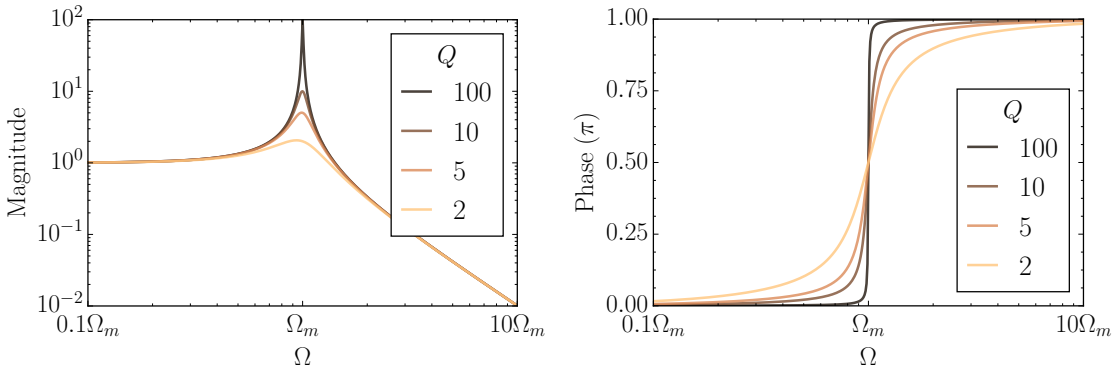

Figure 3.3: **Magnitude and phase of a damped harmonic oscillator.**Susceptibility $\chi(\Omega)$, eq. (3.23), for a unit mass damped harmonic oscillator of different damping rates given relative to mechanical frequency by $Q = \Omega_m/\gamma_m$. **Left:** Magnitude $|\chi(\Omega)|$, **Right:** Phase $\mathrm{Arg}(\chi(\Omega))$.

Let us assess the impact this damping has on the mechanical oscillator by consider just a single mode of the effective 1D oscillator. Suppose the mode has frequency Ω_M, viscous damping rate[1] γ_M and a mass[2] m. If the mode is subject to an external force F_{ext} then the displacement $q(t)$ will obey the damped harmonic oscillator equation of

$$\ddot{q}(t) + \gamma_M \dot{q} + \Omega_M^2 q = F_{\mathrm{ext}}/m. \tag{3.21}$$

Consider now this motion in the Fourier domain[3]. Here the motion of q at a Fourier frequency Ω is given by,

$$q(\Omega) = \chi(\Omega) F(\Omega), \tag{3.22}$$

$$\chi(\Omega) \equiv \frac{m^{-1}}{\Omega_M^2 - \Omega^2 + i\Omega\gamma_M}, \tag{3.23}$$

where the susceptibility $\chi(\Omega)$ has been introduced and is shown in fig. 3.3 for various γ_M. It is clear that χ becomes sharper for smaller γ_M and is centered on the resonance frequency. The oscillator's response near the resonance frequency is enhanced whilst the off-resonant response remains unchanged. At very low frequencies (DC) the response is m^{-1}/Ω_M^2 and for Fourier frequencies $\Omega \gg \Omega_M$ we have $-m^{-1}/\Omega^2$. From these off resonance limits it is also clear that the phase of the oscillators response goes from in phase to completely out of phase as we cross the resonance.

3.4 Equations of motion

Now, suppose that we take this effective 1D harmonic oscillator and quantize its motion. We, thus, have the following system Hamiltonian, omitting the time depen-

[1] γ_M is the rate at which mechanical power decays.
[2] This is, of course, the effective mass but for simplicity we henceforth drop this qualifier.
[3] $\frac{\mathrm{d}}{\mathrm{d}t} \to i\Omega$ with our definition of the Fourier transform.

dence for simplicity,

$$\hat{\mathcal{H}} = \frac{\hat{p}^2}{2m} + \frac{1}{2} m \Omega_m^2 \hat{q}^2. \tag{3.24}$$

The position $\hat{q}$ and momentum $\hat{p}$ operators for a particular mode are described by an underlying field operator $\hat{b}$, which obeys the boson commutation relations of eq. (2.1). Just like in section 2.1 they describe the real and imaginary components of $\hat{b}$, i.e.

$$\hat{q} = x_{\text{zpf}} \left(\hat{b} + \hat{b}^\dagger \right), \tag{3.25}$$

$$\hat{p} = p_{\text{zpf}} i \left(\hat{b}^\dagger - \hat{b} \right). \tag{3.26}$$

We have introduced the zero-point motion, which is simply the variance of the mechanical oscillator in the ground state, e.g. $\text{Var}(\hat{q}) = \langle 0 | \hat{q}^2 | 0 \rangle = x_{\text{zpf}}^2$ (similarly for the momentum). These quantities are given by

$$x_{\text{zpf}} = \sqrt{\frac{\hbar}{2m\Omega_m}}, \tag{3.27}$$

$$p_{\text{zpf}} = m \Omega_m x_{\text{zpf}}, \tag{3.28}$$

and represent a natural scale by which we may reference mechanical motion. For a 1 MHz mode this ground state temperature[1] is around 25 µK. This is a useful order of magnitude to keep in mind when considering a required cooling power to reach the ground state regime.

These zero point motions also allow us to define dimensionless mechanical quadrature operators,

$$\hat{Q} \equiv \frac{1}{\sqrt{2}} \left(\hat{b} + \hat{b}^\dagger \right) = \frac{\hat{q}}{\sqrt{2}\, x_{\text{zpf}}}, \tag{3.29a}$$

$$\hat{P} \equiv \frac{i}{\sqrt{2}} \left(\hat{b}^\dagger - \hat{b} \right) = \frac{\hat{p}}{\sqrt{2}\, p_{\text{zpf}}}, \tag{3.29b}$$

exactly as with light as defined in eq. (2.10). Thus, they also obey the same canonical commutation relations. We can now write the Hamiltonian of eq. (3.24) in terms of these dimensionless operators – just like for light in eq. (2.2) – as,

$$\hat{\mathcal{H}} = \frac{\hbar \Omega_m}{2} \left(\hat{Q}^2 + \hat{P}^2 \right) = \hbar \Omega_m (\hat{b}^\dagger \hat{b} + 1/2). \tag{3.30}$$

The amount of excitations in the mode is given by the phonon number operator $\hat{n}_m = \hat{b}^\dagger \hat{b}$.

If we look back at eq. (3.21) we see that membrane is, in fact, technically a resonator. That is, it needs a driving force for any motion to exist[2]. This external driving force in the absence of any other coupling is the thermal environment.

[1] For some temperature T we can say $k_B T = \frac{1}{2} \hbar \Omega_m$.

[2] Throughout this thesis we will, nonetheless, refer to it as an oscillator.

The inescapably ever finite coupling to this bath gives rise to input driving fluctuations and also the dissipation of mechanical energy as dictated by the fluctuation-dissipation theorem. We can model this bath as composed of independent harmonic oscillators whose position are coupled by a spring[3] to our system. In the language of section 2.4, this system-reservoir interaction can be described by the Hamiltonian Ford et al. (1988)

$$\hat{\mathcal{H}}_{\text{S-R}} = \sum_j \frac{\hat{p}_j^2}{2m_j} + \frac{k_j}{2}\left(\hat{q}_j - \hat{q}\right). \tag{3.31}$$

This has the canonical form of eq. (2.56), where $\hat{R} = \hat{b}_j + \hat{b}$ and $\hat{S} = \hat{b}$.

Looking at eq. (3.21) it is easy to motivate our quantum Heisenberg-Langevin equations. They are given by

$$\dot{\hat{Q}} = \Omega_m \hat{P} \tag{3.32a}$$

$$\dot{\hat{P}} = -\Omega_m \hat{Q} - \gamma_m \hat{P} + \hat{F} \tag{3.32b}$$

where the first follows from the $\dot{\hat{q}} = \hat{p}/m$. The second is simply eq. (3.21) with an external Langevin force $\hat{F}$. As the dissipation occurs in only one mechanical quadrature the input fluctuations also only appear in this quadrature (at twice the rate). Often the rotating wave approximation is employed where losses (and thus input fluctuations) are shared among the two quadratures equally.

In the case of coupling to the mechanical thermal bath only, this Langevin force is a thermal force $\hat{F}^{\text{th,in}}$ with coupling rate $\sqrt{2\gamma}$, i.e.

$$\hat{F} = \sqrt{2\gamma}\,\hat{F}^{\text{th,in}}. \tag{3.33}$$

This thermal force has a correlation function given by Giovannetti and Vitali (2001) of

$$\begin{aligned}\langle \hat{F}^{\text{th,in}}(t)\hat{F}^{\text{th,in}}(t')\rangle &= \int_{-\infty}^{\infty} e^{i\Omega(t-t')}\left(\coth\left(\frac{\hbar\Omega}{2k_B T_{\text{bath}}}\right)+1\right)\frac{\mathrm{d}\Omega}{2\pi} \\ &\approx (\bar{n}_{\text{bath}} + 1/2)\delta(t-t').\end{aligned} \tag{3.34}$$

The approximation is made for a bath with a high mean occupancy ($k_B T \gg \hbar\Omega_m$)[4] and we have treated the bath as effectively Markovian. This is justified as the thermal bath time scale is on the order of $\hbar/(k_B T) \sim 2\,\text{ps}$ at $T = 4\,\text{K}$, whereas the typical decay time scales relevant for this work are $1/\gamma_m > 1\,\text{s}$.

For these dimensionless operators it is more suitable to define a dimensionless susceptibility (dimensionfull one defined in eq. (3.23)) as

$$\chi(\Omega) = \frac{\Omega_m}{\Omega_m^2 - \Omega^2 + i\Omega\gamma_m}. \tag{3.35}$$

[3] with constant $k_j = m_j\Omega_j$

[4] $\coth(x) = \frac{1}{x} + \frac{x}{3} + \ldots$

Under this definition we have for the relation, in the Fourier domain, for the dimensionless position operator

$$\hat{Q}(\Omega) = \chi(\Omega)\hat{F}(\Omega) \tag{3.36}$$

in nice analogy with the dimensionfull expression of eq. (3.22).

The coupling to the thermal bath is synonymous with dissipation. As will be described shortly in section 3.5.2 we are typically interested in the case where this dissipation is very small, $\gamma_M \ll \Omega_M$. Thus, we will often be interested in the response near resonance, i.e. around $\Omega \approx \Omega_m$ where the response is the greatest. In this regime we can make the following useful approximation,

$$\chi(\Omega) \approx \frac{1/2}{(\Omega_m - \Omega) + i\gamma_m/2} = \frac{L(\Omega)}{\gamma_m}, \tag{3.37}$$

where the response approximates that of the complex Lorentzian $L(\Omega)$ defined as

$$L(\Omega, \Omega_m, \gamma_m) \equiv \frac{\gamma_m/2}{(\Omega_m - \Omega) + i(\gamma_m/2)}. \tag{3.38}$$

Care should be taken when using the Lorentzian approximation since the full susceptibility of eq. (3.35) has a flat low frequency response as well as a two poles ($\Omega = \pm\Omega_m$). The Lorentzian approximation of eq. (3.37) is very useful, but does not caption these two features. An important result to bare in mind is the integral over the susceptibility, which gives

$$\int_{-\infty}^{\infty} |\chi(\Omega)|^2 \frac{\mathrm{d}\Omega}{2\pi} = \frac{1}{2\gamma_m}. \tag{3.39}$$

The integral over the approximate susceptibility eq. (3.37) falls a factor of 2 short since it is missing a negative frequency pole.

3.5 Mechanical quality factor

3.5.1 Basic description

When considering the susceptibility it is natural to cast the damping rate relative to the resonance frequency. This quantity is known as the Q factor and is defined as

$$Q \equiv 2\pi \frac{U}{\Delta U} \approx \frac{\Omega_m}{\gamma_m}, \tag{3.40}$$

where the approximation is valid in the regime of low damping. This dimensionless quantity is defined by the ratio of the total energy stored U to that lost per oscillation ΔU. From this perspective three distinct regimes emerge, namely the overdamped ($Q < 1/2$), critically damped ($Q = 1/2$) and underdamped ($Q > 1/2$) regimes. Each

are interesting in their own right, but only the underdamped case will be relevant for describing the mechanical oscillator. In this regime the system undergoes many oscillations before being significantly damped. The importance of this regime can be understood as follows.

A mode with higher Q dissipate less stored energy per oscillation cycle. As this dissipative loss is due to a coupling with the environment it entails a non-unitary evolution of motion. This is (typically) undesirable and the Q, as we shall see shortly in section 3.5.2, will set the relevant time scale for which quantum behavior should be expected.

Since contributions to the total damping rate add linearly, thus, contributions to the Q add in parallel. We may further differentiate between internal and external sources of loss, writing

$$Q^{-1} = \sum_i Q_{\mathrm{int},i}^{-1} + \sum_i Q_{\mathrm{ext},i}^{-1}, \tag{3.41}$$

This is typically done as the former is set by the material (and its quality) used whereas the latter is a consequence environmental factors, which in principle can be manipulated by a crafty experimentalist. We will explore a few relevant cases of both types of loss shortly.

3.5.2 Importance of Q

The importance of a high quality factor membrane for our quantum optics ambitions can be seen from the following simple consideration. To realize a useful quantum harmonic oscillator its dynamics must not be significantly disturbed on the timescale of a single coherent mechanical oscillation by unwanted noise sources.

Suppose this noise source is the thermal reservoir at temperature T_{bath}. The mean number of thermal phonons in the reservoir at the mechanical frequency Ω_m is given by eq. (2.74), and in the limit of large bath temperature, is

$$\bar{n}_{\mathrm{bath}} = \frac{k_B T_{\mathrm{bath}}}{\hbar \Omega_m}. \tag{3.42}$$

The rate at which you interact with this bath is proportional to the coupling rate (the decay rate) γ_m times the number of available quanta $\bar{n}_{\mathrm{bath}}$. This is known as the decoherence rate,

$$\gamma_{\mathrm{dec}}^{\mathrm{th}} = \gamma_m(\bar{n}_{\mathrm{bath}} + 1/2) \approx \gamma_m \bar{n}_{\mathrm{bath}}, \tag{3.43}$$

where the bath vacuum contribution of $1/2$ is often dwarfed by the mean occupation $\bar{n}_{\mathrm{bath}}$. If the bath is in the ground state then the decoherence rate is simply the decay rate, namely γ_m. As we have already assumed that the mean bath occupation is very large (which is always a good assumption in this thesis) we can safely neglect this additional contribution in what follows.

A minimum of a single coherent oscillation requires $\gamma_{\mathrm{dec}}^{\mathrm{th}} < \Omega$, which is usually expressed as the $Q - f$ product (Q times mechanical frequency f)

$$Qf > \frac{k_B T_{\mathrm{bath}}}{2\pi\hbar} \approx 5\,\mathrm{THz}, \text{ for } T_{\mathrm{bath}} = 300\,\mathrm{K}. \tag{3.44}$$

The amount by which one's system is above (or below) this sets the amount (or fraction) of coherent oscillations possible given no other decoherence sources. Achieving just a single coherent oscillation at room temperature has proved very difficult for the SiN membranes in general. A membrane with a $Q \sim 10\,\mathrm{M}$ and a frequency of 1 MHz just barely makes one coherent oscillation at room temperature.

This is one of the main reasons why experiments are typically operated in a cryogenic environments, in our case at a temperature of $T \sim 10\,\mathrm{K}$. At this reduced temperature the bath occupation is significantly lower, by $\sim 1/30$, and the Q is increased by a factor[1] ~ 3. This results in ~ 100 times more coherent oscillations overall. In the future however, with much higher Q systems becoming available, room temperature quantum operation may become feasible.

3.5.3 Measuring Q

The quality factor is typically measured in the time or Fourier domain depending on the situation. For low Q modes the Fourier domain is easiest as the decay time is fast, and thus spectrally broad. This makes the mechanical linewidth easy to estimate from Lorentzian fits of a power spectral density proportional to the mechanical displacement.

For high Q modes a ringdown technique is typically employed. Here the membrane mode is excited, either by optical or physically driving, far out of the equilibrium with the thermal bath. Turning off this added drive the subsequent return to equilibrium occurs as exponential decay with a time constant related to the mode Q.

Suppose the drive boosts the amplitude to some large value A. If we then turn off the drive and neglect the thermal driving force in this large amplitude limit, the motional amplitude will decay according to

$$q(t) = A\sin(\Omega_m t + \phi)e^{-\gamma_m t/2}. \tag{3.45}$$

Suppose this motion is linearly transduced into, say, an optical quadrature, as is described in section 4.2, and then detected. The detected signal, proportional to the mechanical motion, can then be analysed, e.g. by a lock-in amplifier as in our case, and the decay of the signal power at the membrane frequency Ω_m can be measured. The timescale of the decay yields the quality factor as the membrane frequency is known. An example of such an exponential ringdown is seen in fig. 3.4.

[1] This is a fact universally true amongst amorphous materials.

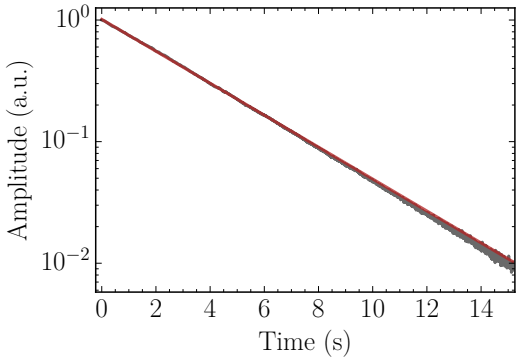

Figure 3.4: **Mechanical ringdown example.** The membrane used for the results of chapter 6 is cryogenically cooled to near 4 K, and the $(1, 2)$ mode is excited to a large amplitude, and then observed as the ringing down as vibrational energy is lost. Shown is not the power but the amplitude (square root of power) which decays only half as fast. Grey points are data, blue line is an exponential fit. From many such measurements we can extract a mechanical quality factor of $Q = 13 \times 10^6$ for this membrane mode.

3.6 Zener's loss model

In general, many solid materials are anelastic, i.e. exhibiting both viscous and elastic behaviour, with no lasting deformation. Their behaviour is practically differentiated by their response to an externally applied force (stress). When the local stress σ changes this affects the material strain ϵ and deformation occurs. If the strain occurs in phase with the stress the system is said to be purely elastic (this is of course unrealistic) and if the strain responds $\pi/2$ out of phase we identify it as purely viscous. As already alluded to, in general the strain will lag by an amount δ that depends on how viscous compared to elastic the material is. Suppose we modulate the stress at frequency Ω and look at the Young's modulus[1]

$$E \equiv \frac{\sigma}{\epsilon} = \frac{\sigma_0 e^{i\Omega t}}{\epsilon_0 e^{i(\Omega t - \delta)}} \tag{3.46}$$

$$= \frac{\sigma_0}{\epsilon_0}\left(\cos(\delta) + i\sin(\delta)\right) = E_1 + iE_2. \tag{3.47}$$

Thus, we can model the anelasticity via a complex Young's modulus. One can show Schmid et al. (2016, Chapter 2.3) that the retarded response, due to a finite viscous damping, is related to the quality factor of eq. (3.40) by

$$Q^{-1} = \frac{E_2}{E_1} = \tan(\delta) \tag{3.48}$$

$$\approx \delta, \ \delta \ll 1. \tag{3.49}$$

The factor $\tan(\delta)$ is typically referred to as a "loss tangent" and is inversely related to the quality factor by definition Marc André Meyers (2008, Chapter 2), $\tan(\delta) \equiv$ energy loss/energy stored.

[1] Typically defined as $\frac{\text{stress}}{\text{strain}}$.

For any standard linear solid[2] we can write a general rate equation relating the stress and strain. Suppose we kept the material under a constant stress (or strain) and let the strain (or stress) relax. This would occur on a time scale given by τ_σ (or τ_ϵ). This rate equation would have the following form,

$$\sigma + \tau_\epsilon \dot{\sigma} \propto \epsilon + \tau_\sigma \dot{\epsilon}. \tag{3.50}$$

This equation is perhaps most useful to use when the strain and stress are modulated at some frequency Ω due to for example the membrane oscillating at $\Omega = \Omega_m$. In that case one can show, see Zener (1948), that

$$Q^{-1} = \tan(\delta) = \frac{\Omega\left(\tau_\sigma - \tau_\epsilon\right)}{1 + \Omega^2 \tau_\sigma \tau_\epsilon} \tag{3.51}$$

$$= \Delta \frac{\Omega\bar{\tau}}{1 + \left(\Omega\bar{\tau}\right)^2}, \tag{3.52}$$

$$\Delta = \frac{\tau_\sigma - \tau_\epsilon}{\bar{\tau}},\ \bar{\tau} = \sqrt{\tau_\sigma \tau_\epsilon}. \tag{3.53}$$

This is known as the Zener model and is peaked when the oscillation frequency coincides with the time scale τ. The overall scale of the loss is given by Δ, not to be confused with the cavity detuning. The limits can be understood in the following way. For oscillations much faster than this timescale the system has no time to relax, thus resulting in lower loss than the on-resonant case. Conversely, for oscillations much slower than this timescale the system is always relaxed and in equilibrium, thus lower loss.

In general, there may be multiple time scales due to multiple relaxation mechanisms. These will result in multiple loss peaks known as Debye peaks. We will see this model used to characterize relevant loss mechanisms now.

3.7 Intrinsic loss mechanisms

Thermoelastic damping

Thermoelastic damping (TED), as the name suggests, is the loss caused by spatially inhomogenous heating caused by deformation. If we consider a membrane of density ρ as an example we can picture this mechanism as follows. Undergoing oscillations there are regions of compression and tension. Depending on the sign of the coefficient of thermal expansion (CTE) α the local temperature will rise or fall in these regions. Temperature gradients are, thus, formed from which heat will irreversibly flow leading to a diffusion of the mechanical energy and effectively loss.

For small excitations the local temperature variations are negligible compared to the ambient bulk temperature T. The relevant time scale for this mechanism was

[2] as the following model is known as.

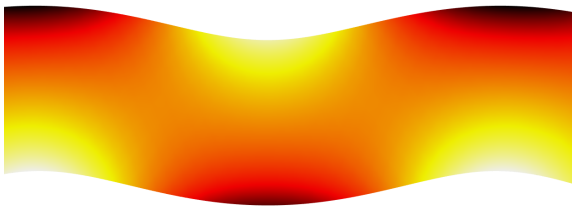

Figure 3.5: **Illustration of thermoelastic damping.** The (widely exaggerated) motion of a 2D slab of material leads to areas of compression which heat up (darker regions) and regions of expansion which cool down (lighter regions). The diffusion of heat diffuses out the mechanical motional energy ultimately a source of mechanical energy loss.

worked out by Zener (1937, 1938) and is given by

$$\tau_{\mathrm{TED}} = \frac{h^2}{\pi^2 D}, \tag{3.54}$$

$$\alpha_{th} \equiv \frac{\kappa}{\rho c_p}, \tag{3.55}$$

where α_{th} is the thermal diffusivity, which is the relevant inertia of the heat conduction equation (written here without an internal source of heat),

$$\dot{T} = \alpha_{th} \nabla^2 T. \tag{3.56}$$

For a 60 nm thick SiN membrane the time scale $\tau_{\mathrm{TED}} \sim 0.2\,\mathrm{ns}$ (5 GHz) is much faster than the modes of interest which oscillate on the time scale of 1 us (1 MHz). This timescale becomes quadratically shorter for thinner membranes. The thermal diffusivity α_{th} is related to the heat conductivity κ and the specific heat capacity c_p by

$$\alpha_{th} = \frac{\kappa}{\rho c_p}. \tag{3.57}$$

The scale of this damping will be related to the amount of expansion, which will be proportional to α, T and E_1. It is given by

$$\Delta_{\mathrm{TED}} = \frac{T E_1 \alpha_{\mathrm{CTE}}^2}{\rho c_p}. \tag{3.58}$$

This loss can of course also be viewed in light of the Zener model with amplitude and characteristic time scales given by eqs. (3.54) and (3.58) respectively.

A derivation of thermoelastic loss can be done from first principles in absence of stress, as is by Lifshitz and Roukes (2000). They consider the thermoelastic effect of the on the flexural rigitidy in conjuction with the heat equation of eq. (3.56). The result is given by

$$Q^{-1}_{\mathrm{TED,LR}} = \Delta_{\mathrm{TED}} g(\xi), \tag{3.59}$$

$$g(\xi) = \left(\frac{6}{\xi} - \frac{6}{\xi^3} \frac{\sin(\xi) + \sinh(\xi)}{\cos(\xi) + \cosh(\xi)} \right), \quad \xi = \sqrt{\frac{\Omega h^2}{2\alpha_{th}}}. \tag{3.60}$$

which predicts the similar losses as the aforementioned Zener model.

The scale of the thermoelastic damping is clearly proportional to the coefficient of thermal expansion. For some materials the coefficient changes sign with temperature (e.g. Silicon and Sapphire), and it generally decreases in amplitude for reduced temperatures. Thus, one can eliminate this damping contribution present in such a material by choosing the temperature where $\alpha_{\mathrm{CTE}} = 0$ or reduce it by cooling. For applications where this loss is the limiting source of noise, this is seriously considered. Materials with a zero-crossing near room temperature are even available, e.g. Zerodur (lithium-aluminosilicate glass-ceramic) and Invar (Nickel-Iron alloy).

Akhiezer damping

Whilst one can to some degree engineer one's way around TED damping, the mechanism behind Akheizer damping is more difficult to escape. This damping is also known as phonon-phonon interaction loss.

At its heart it is an interaction between sound waves and thermal phonons. Thus why, this loss mechanism is also refered to as a phonon-phonon loss. As explained by Braginsky et al. (1985, Chapter 2), if the sound wavelength is much larger than the phonon mean free path, one can consider the sound wave as locally perturbing the local phonon frequencies. This happens by the material lattice being deformed. This displaces the phonons from the equilibrium of the Planck distribution. Phonon-phonon scattering events reestablish thermal equilibrium, but at the expense of sound wave energy diffusion. The link between a locally deformed lattice and vibrational energy is described by the thermodynamic Grüneisen parameter γ_G.

The effect can also be thought of in terms of a change of temperature as the local lattice deforms. A contraction (say) leads to increased phonon frequencies, and thus a locally higher temperature. Thus, the timescale for this mechanism depends on the thermal diffusivity $\alpha_t h$ and some notation of the propagation speed of phonons, here characterized by the Debye velocity v_D. The timescale is given by Braginsky et al. (1985, Chapter 2)

$$\tau_{\mathrm{Akhiezer}} = \frac{3\alpha_t h}{v_D^2}, \tag{3.61}$$

which for our SiN membranes will be on the order of 5 fs (20 THz). The Debye velocity is given by,

$$\frac{3}{v_D^3} = \frac{2}{v_t^3} + \frac{1}{v_l^3}. \tag{3.62}$$

For low stress SiN membranes this speed is very close to that of the speed of sound[1], i.e. $v_D \approx v = \sqrt{E/\rho}$.

[1] This of course depends on the exact material parameters but is on the order of a few percent. For the theoretically expected transverse and longitudinal sound velocities of thin film, low stress SiN see Ma et al. (2017)

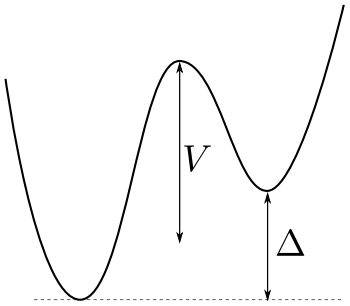

Figure 3.6: **Two level system (TLS) model.** This double well potential is representative of the two stable configurations of a local defect in an amorphous material. The potential difference between the minima is given by Δ and the barrier height (from midway between the two minima) is given by V.

The scale of the loss is given by

$$\Delta_{\text{Akhiezer}} = \frac{C_p T \rho \gamma_G^2}{E}, \tag{3.63}$$

and together with eq. (3.61) and the Zener model provide a good order of magnitude estimate for the resultant loss.

Although the discussion for Akhiezer damping is typically framed for materials with a crystalline lattice, this mechanism is also present in amorphous SiN. This is due to the (inevitable present) local structure. This structure is described in Wang et al. (1996) where they also review lattice defects present in SiN. This is the origin of the next considered internal loss mechanism, two level defects.

Two level systems (TLS)

The behaviour of amorphous solids a cryogenic temperatures has been a subject of intense study over the past few decades. The seemingly universal behaviour among "glassy" materials (at temperatures above a few Kelvin) has also recently been observed in Silicon Nitride string resonators in the context of cavity optomechanics Faust et al. (2014). The temperature dependence of the quality factor in amorphous materials is well captured by a so-called two-level system (TLS) model. The loss of elastic energy is ascribed to a distribution of local defects[2] in the material, each with two stable configuration described by an asymmetric double-well potential, see fig. 3.6 and Vacher et al. (2005) for an overview of the theory. The activation energies, V, are typically on the order of several hundred Kelvin Faust et al. (2014), suggesting that a single MHz frequency phonon cannot excite such a two-level system on its own. Indeed, Faust et al. (2014) have suggested a scattering process where a TLS is excited by a scattering process involving a resonator phonon and a high-energy bulk phonon. This irreversible process thus results in loss of elastic energy. At

[2]Beyond defects found in crystalline materials (vacancies, substitutional defects, dislocations, etc.), it's worth noting that amorphous solid have order in smaller regions (so called "grains"), the interfaces between which are filled with various defects.

lower bath temperatures the rate of TLS excitations is reduced. This is responsible for the observed factor of $2.5-3$ increase in Q observed for our membranes as they are cooled from room temperature to 4 K.

3.8 Dissipation dilution

The intrinsic loss mechanisms described briefly in section 3.7 all set a limit on the highest attainable quality factor for an untensioned thin plate resonator. Thankfully (and the reason why we use it) SiN can be highly stressed, which results in an increased stored mechanical energy U, whilst leaving the intrinsic loss of mechanical energy ΔU unaffected. Thus from eq. (3.40) it follows that this leads to a higher quality factor.

Consider the case of thermoelastic loss described in section 3.7. In the presence of an additional stress the damping is reduced significantly as was shown by Zwickl (2011); Chakram et al. (2014), the former of which derives the expression[1]

$$Q_{\mathrm{TED}}^{-1} = \frac{\Omega^2 E_1 h^2 \rho}{12(1-\nu)^2\sigma^2} Q_{\mathrm{TED,LR}} = \lambda^2 \frac{\pi^2\left(m^2+n^2\right)}{4} Q_{\mathrm{TED,LR}}. \tag{3.64}$$

In the last step we simply write out the membrane frequency $\Omega = \Omega_{mn}$ according to eq. (3.7). It is thus clear that adding a stress σ reduces thermoelastic loss by a "dilution factor" λ given by

$$\lambda = \sqrt{\frac{4D}{\sigma h}} = \frac{h}{L}\sqrt{\frac{E}{3\sigma(1-\nu^2)}}. \tag{3.65}$$

Within the optomechanics community this was first observed in Verbridge et al. (2006, 2007) and the above explanation provided by Schmid and Hierold (2008) shortly thereafter. In practice, this dissipation dilution means a higher Q by an amount α, i.e.

$$Q_{\mathrm{intrinsic}} \to \alpha Q_{\mathrm{intrinsic}}. \tag{3.66}$$

The amount of dilution in general depends on material parameters, the mode frequency and the specifics of the structure under consideration. However, for a square membrane clamped at the edges, such as discussed in section 3.1.2, this dilution is given by Yu et al. (2012) to be

$$\alpha^{-1} = \lambda\left(\underbrace{1}_{\text{edge}} + \underbrace{\lambda\frac{\pi^2\left(m^2+n^2\right)}{4}}_{\text{sine}}\right) = \underbrace{\lambda}_{\text{edge}} + \underbrace{\lambda^2\frac{\pi^2\left(m^2+n^2\right)}{4}}_{\text{sine}}. \tag{3.67}$$

[1] Here rewritten in terms of our thermoelastic scale factor Δ_{TED} from eq. (3.58).

Notice that the dilution of eq. (3.67) has two contributing components. The first is term ("edge") derives from the bending near the edge of the membrane where it is clamped to the surrounding structure. The second ("sine") term comes from the sinusoidal bending of the modes, described in eq. (3.3).

Note that dissipation dilution works better for bigger and thinner membranes that are highly stressed. The SiN membranes used in this work, see section 3.10, have a thickness and size chosen for reasons besides the dissipation dilution, see section 4.5, and are stressed to roughly 1 GPa, an appreciable fraction of the total yield stress of (6.4 ± 0.6) GPa Kaushik et al. (2005). This gives a typical dilution factor of $\lambda \approx \alpha^{-1} \approx 10^{-4}$.

Fundamentally, the dilution is really an increase in elongation energy (stress) compared to the bending energy. So when the bending energy becomes comparable, e.g. for large mode numbers, the dilution wears off. As we are interested in the low order modes the increase in $Q_{\text{intrinsic}}$ is to a very good approximation given by $1/\lambda$. This means that the dilution will be limited by the "edge" contribution. However, for a new generation of membranes this limiting "edge" term can be heavily suppressed by a "soft clamping" technique described in Tsaturyan et al. (2017).

As can be seen from eq. (3.67), upon removal of the edge term, the dilution scales with the square of the dilution factor, suggesting a $(L/h)^2$ scaling of the quality factor. Surface effects, however, modify the scaling which is shown by Tsaturyan et al. (2017) to have the following dependence

$$Q \propto \frac{L^2}{h}. \tag{3.68}$$

3.9 External loss mechanisms

Beyond the intrinsic mechanisms that lead to loss are external sources, a few of which will now be discussed. An excellent overview of these, and several others, can be found in Schmid et al. (2016).

Gas damping

Lets first consider the loss resulting from embedding a membrane in a surrounding medium. If the dimensions of the membrane are smaller than the mean free path of the medium constituents, then the damping will be of a ballistic nature. Achieving higher vacuum is often exponentially more difficult it is useful to quantify the amount of this ballistic gas damping with vacuum pressure.

We assume that the gas behaves like an ideal gas at pressure P proportional to the gas temperature T by

$$P = \rho_{\text{gas}} \frac{R}{M_{\text{gas}}} T, \tag{3.69}$$

where the gas has density ρ_{gas} and molar mass M_{gas}. R is the universal gas constant.

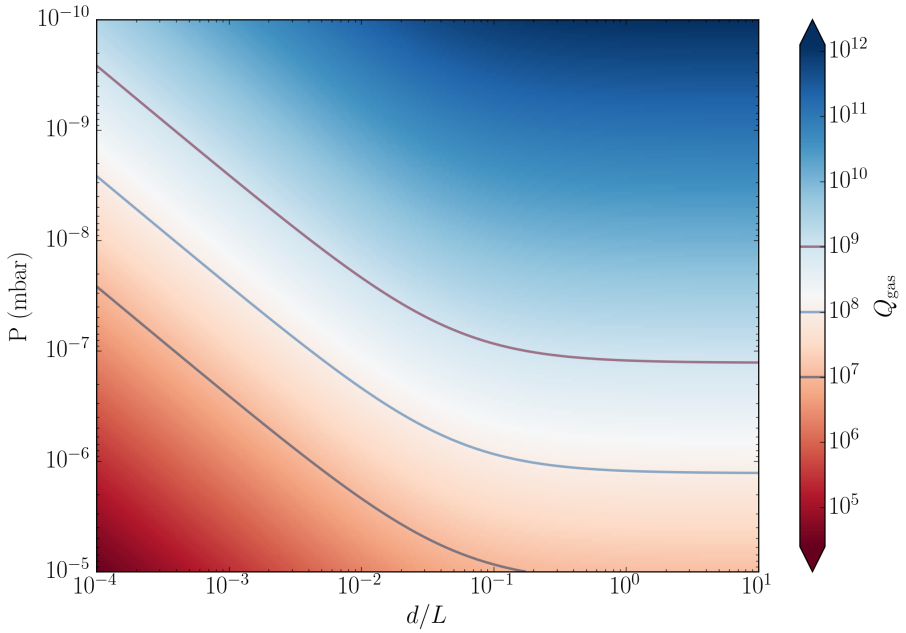

Figure 3.7: **Q limit due to gas damping.** Limit to the mechanical quality factor posed by gas damping, according to eq. (3.73). The two regimes derive from the relative importance of squeeze film damping versus ballistic damping.

In the presence of such a surrounding medium it can be shown that the resultant ballistic gas damping is given by Bao et al. (2002)

$$Q_{\mathrm{B}} = \frac{\rho h \Omega_{mn}}{4} \sqrt{\frac{\pi}{2\rho_{\mathrm{gas}} P_{\mathrm{gas}}}} \tag{3.70}$$

$$= \frac{\rho h \Omega_{mn}}{4} \sqrt{\frac{\pi}{2}} \sqrt{\frac{RT}{M_{\mathrm{gas}}}} \frac{1}{P}. \tag{3.71}$$

This is of course just an approximation as the membrane is typically not the only object in the environment. In general, the geometry of the immediate environment can be shown the influence the effect of the gas damping. A very relevant case is that of the membrane being placed close to a flat surface (e.g. a mirror).

The gas between these two surfaces results in an enhanced damping, the contribution of which is known as squeeze-film damping. If the membrane has a side length L and is a distance d from a parallel surface then the additional damping experienced will be given by Bao et al. (2002)

$$Q_{\mathrm{SF}} = \frac{32}{\beta} \frac{d}{L} Q_{\mathrm{B}}, \tag{3.72}$$

where β is a factor taking into account the geometry of the membrane surface. In the case of a rectangular membrane we have $\beta = \pi/2$.

The total gas damping is the inverse sum of these two effects,

$$Q_{\mathrm{gas}} = Q_D \left(1 + \frac{\beta}{32} \frac{L}{d}\right)^{-1}, \tag{3.73}$$

and is shown in fig. 3.7. It is clear that squeeze-film damping is an effect that is mostly relevant for membranes in rather close proximity to another surface $d \sim L/20$ compared to the general scale of the membrane structure. This is not a problem for the assemblies realized in this work, but present a very real concern if one wishes to engineer a stucture with our macroscopic membranes ($\sim 0.5\,\mathrm{mm}$) on the scale of a typical NIR wavelength $\lambda \sim 1\,\mu\mathrm{m}$.

Clamping losses (phonon tunneling)

Mounting conditions typically have a high impact on the quality factor of an object. This is because mounting conditions affect the amount of mechanical energy radiated into the environment. To see this, consider the membrane (m) in profile (1D) and notice that a wave traveling towards the boundary with the substrate (s) will be completely reflected in the case of a perfectly rigid interface. In fact, if the boundary is completely soft (or free) the wave is also reflected. This is an important point which we shall shortly see.

In practice, the interface is not perfectly rigid, and we can attribute to it some finite impedance to motion $Z_s = \rho_s c_s$. The membrane itself has some impedance $Z_m = \rho_m c_m$ and the reflected wave amplitude will be proportional to

$$R = \frac{Z_m - Z_s}{Z_m + Z_s} = \frac{1-\eta}{1+\eta}, \tag{3.74}$$

where we introduced $\eta \equiv Z_s/Z_m$ as a useful measure of the ratio of the two impedances. Clearly for $\eta = 0$ or ∞ no power is transmitted as stated previously. Any transmitted wave energy can essentially be considered to be lost and will, thus reduce the resonator Q. This is also commonly referred to as phonon tunneling or radiation loss, see Wilson-Rae (2008).

The impact on Q can be found by a more careful analysis of the coupling between membrane and continuum substrate modes, as has been done by Wilson-Rae (2008); Wilson-Rae et al. (2011). It was found that the Q depends on an overlap integral between the stress and displacement fields of the modes, as well as a spectral overlap. In the case most relevant here, namely a highly stressed membrane, substrate and a thin square membrane the result can be approximated by[1] Villanueva and Schmid (2014)

$$Q_{\text{clamping}} \approx 1.5\beta \left(\frac{\rho_s}{\rho_m}\right)^2 \eta^3 \frac{m^2 n^2}{(m^2+n^2)^{3/2}} \frac{L}{h}, \tag{3.75}$$

$$\eta \approx \sqrt{\frac{E_s \rho_s}{\sigma_m \rho_m}} = Z_s/Z_m. \tag{3.76}$$

This result demonstrates that a high impedance mismatch η is preferable, and that higher order modes will be (linearly for $m = n$) less limited. The fundamental

[1] Here we re-write this slightly to fit with the heuristic discussion above.

$(1,1)$ mode for common membrane parameters this loss limits the Q to $\sim 10\,\mathrm{M}$, for optimal mounting conditions. Unfortunately one often does not wish to work with the lowest order modes, $(1,1)$ included, which have proved extremely sensitive to the specifics of how the overall structure is supported, an effect quantified by the experimental catch-all β. This was first systematically considered by Wilson in Wilson et al. (2009) and Wilson (2012, Chapter 4) where, perhaps unsurprisingly in hindsight, minimal contact was found to be preferable.

Practically, contact is required and often desired due to other concerns like stability and thermalization in a cold environment. Luckily, this issue can be addressed in a much more systematic fashion, by means of phononic crystal structuring of the silicon substrate.

3.10 Phononic bandgap shielded membrane resonators

If we consider eq. (3.76) once more we see that the impedance mismatch η is of critical importance. A way to, in effect, increase this is by a periodic array of alternating high and low impedance regions. The effect of this patterning is to create a mechanical "Bragg mirror", i.e. to boost the reflection of an incident mechanical wave. While a reflection on an interface is given by the impedance mismatch via eq. (3.74), if the interface consists of N alternating high and low impedance regions then the impedance mismatch is boosted to η^N, thus, reflecting more. This principle is used in making low loss (high finesse) optical cavities where an alternating stack of high and low index (and thus impedance) materials can realize incredibly low loss.

Physically these high and low impedance regions are realized by suspending the membrane by a mesh of alternating high and low mass regions in a Silicon support structure, see fig. 3.8. This structure is known as a phononic crystal and the periodic structure modifies the dispersion relations and creates a bandgap. This bandgap is key, as it leads to a suppression of radiated mechanical energy for modes of frequency inside the bandgap since their motion is suppressed in the phononic structure. The phononic bandgap reduces the amount of elastic energy lost to the substrate modes, which are strongly coupled to the environment. Furthermore, since the membrane rests on a small silicon defect, with a sparse mode spectrum, which further reduces the probability of a spectral, as well as spatial, overlap between a membrane mode and a (silicon) defect mode, see Yu et al. (2014); Tsaturyan et al. (2014).

If the structure is chosen with care, the phononic bandgap can be large (compared to the central frequency) as seen in fig. 3.8 and in a useful region with respect to membrane modes of interest. Since the suppression of elastic waves scales exponentially with the number of unit cells, only a few unit cells are sufficient for this structure to offer sizeable advantages, as shown in Tsaturyan et al. (2014).

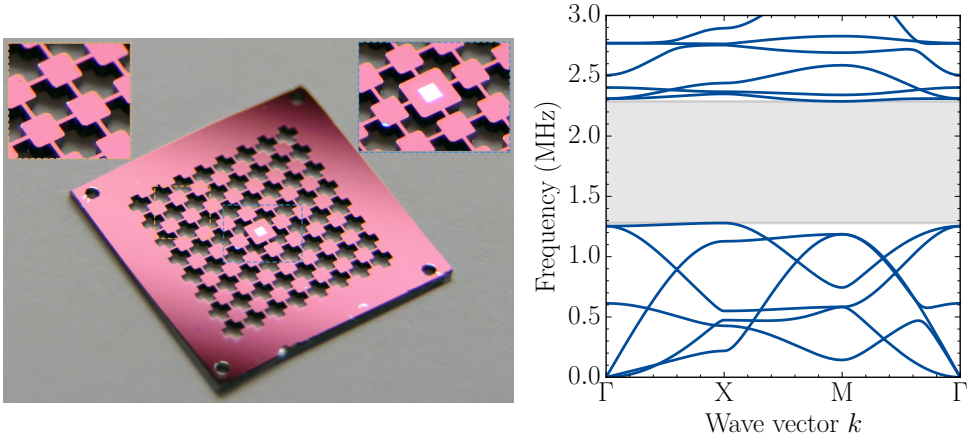

Figure 3.8: **2D phononic crystal shielded membrane. Left:** A picture of the 2D phononic crystal shielded membrane used throughout the work presented in this thesis. The membrane itself is the white square in the middle also seen in the top right inset. It is 60 nm thin SiN membrane supported by a local defect of Si in a larger phononic crystal structure etched in the supporting 500 µm thick Si. The structure of this periodic pattern is shown in the top left inset. The modulation of this structure can be viewed as periodic high and low mass regions which give rise to a phononic bandgap. **Right:** Dispersion relation of an infinite phononic crystal structure (geometry corresponding to the left figures top left inset), showing a phononic bandgap (shaded grey area), where no vibrational modes (blue lines) are sustained. The band diagram traces the elastic wave-vector through the high symmetry points of a two-dimensional square lattice known as Γ, X and M. The bandgap is wide and designed such that multiple mechanical modes of the membrane can lie within it. The structure is simulated using finite element modeling in COMSOL. Figure reproduced with permission from the Tsaturyan (2016).

Hybridization with silicon defect

The membrane is held by a local Si support, which unfortunately introduces a defect in the periodic lattice. This defect consists of both the SiN membrane and the Si defect. The modes of the Si defect can, thus, hybridize with the vibrational modes of the SiN membrane, which reduces the Q of the membrane mode. It further acts as a driving force for the membrane mode leading to added decoherence. We see these undesirable defect modes often, but of course choose only to work where the hybrization is small.

A very clear example of this effect can be seen in fig. 3.9 which shows an optical spectrum of transduced membrane motion. The spectral heights are proportional to membrane motion weighted by a transduction factor given, in part, by the mass of the mode. Without needing to know the specifics of the membrane or defect mode we can make the following qualitative observations. As the defect and membrane modes are brought away from each other in frequency), the membrane mode regains a high Q (seen as the large peak emerging to the right). This may be viewed as the hybrization being weakened and the two returning (once not nearly degenerate) to being distinct modes.

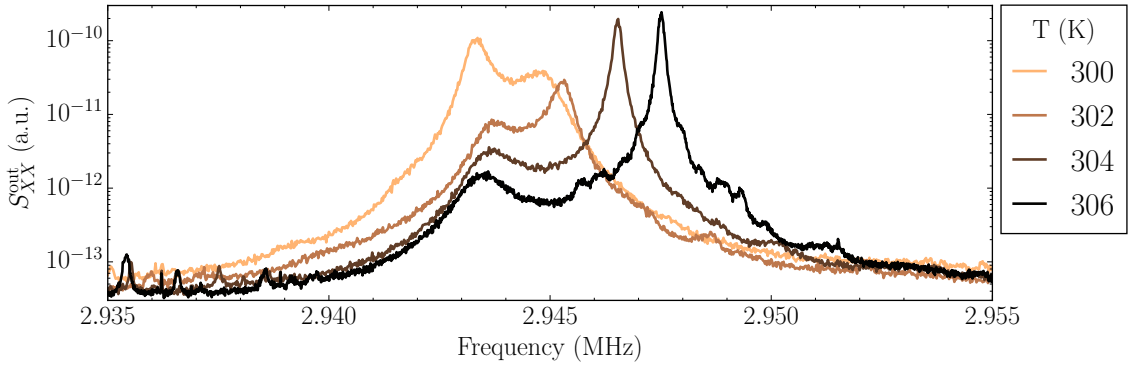

Figure 3.9: **Defect frame hybrization** Hybridization of a vibrational mode of the Silicon defect (left peak) and a mode of the Silicon Nitride membrane (right peak). As the temperature is tuned the slight shift in membrane frequency changes the coupling between the modes and hence the membrane Q.

This tuning is done in practice by changing the temperature T of the whole structure. Since the membrane modes are dominated by a large in-plane stress, and the Si defect is completely unaffected by this, they can be tuned apart by changing the stress. This is accomplished by changing the temperature which introduces a differential expansion of SiN compared to Si, changing the stress in the SiN pushing the membrane modes significantly in frequency.

This issue of hybridization, along with the larger (for low order modes) edge contribution to the dissipation dilution of eq. (3.67), has been countered by the latest innovation Tsaturyan et al. (2017).

Fabrication

The detailed fabrication process for the 2D membranes with a bandgap in the supporting silicon is described in Tsaturyan et al. (2014). In short, a standard double-side polished silicon wafer (500 µm thick) is covered by a thin layer of silicon nitride via low-pressure chemical vapor deposition. The wafer is subsequently coated with a photosensitive polymer (a photoresist) and the desired patterns (i.e. the square membrane and the phononic structure) are first transfered to the photoresist using a photolithographic mask via illumination with UV light, and subsequently into the silicon nitride, using reactive ion etching.

We define the membranes using a wet chemical etch (potassium hydroxide – KOH), stopping the etch $\sim$ 10 µm short of releasing the membranes, while the phononic crystal structure is etched into the wafer using deep reactive ion etching. Finally, the membranes are fully released at the very end of the process, with a short KOH etch, and cleaned using a hot piranha solution (which removes the potassium residues from the KOH etch).

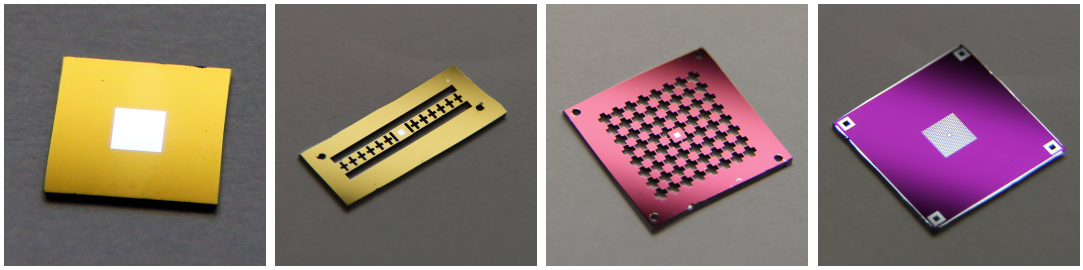

Figure 3.10: **Membrane generations.** A chronological (left to right) selection of SiN membrane generations used in the labs of Eugene Polzik and Albert Schliesser. Going from left to right we have: A membrane purchased from Norcada Inc. (white) held be a rigid Si structure (yellow). A membrane (white) held by a 1D phononic crystal structure in Si (yellow). A membrane (white) held by a 2D phononic crystal structure in Si (pink). A SiN membrane (center white), perforated with a 2D phononic crystal structure, where the localized defect modes constitute the vibrational modes of relevance. This whole structure is held by a Si frame (purple). All devices have comparable overall sizes and images are not to scale. The membranes shown have useful modes at $\sim 1\,\mathrm{MHz}$ frequencies.

Membrane generations

To conclude this chapter, it is interesting to consider the many generations of membranes, each improving upon the last, that have accompanied my PhD. A selection are shown in fig. 3.10 and are meant to highlight the significant progress made on the fabrication and characterization front in as it pertains to highly stressed SiN membranes.

The 1D phononic structures in Silicon improved upon the standard (often bought from Norcada Inc.) membranes in that they have a bandgap making them less susceptible to clamping loss. They were superceded by the 2D version as the bridge of the 1D structure was too floppy for our early day experiments. These are what have been used for the work presented in this thesis and enabled us to enter the quantum regime. Unfortunately these structures have hybridization with the Silicon defect supporting it. As it also turns out the "hard clamping" of the membrane at the edges by the Silicon defect limited the Q. The latest development described in Tsaturyan et al. (2017) addresses both these issues. The hybridization with the Silicon defect is now gone and the "soft clamping" approach has boosted the Q factors by more than an order of magnitude for the same resonance frequencies and membrane thickness.

Chapter 4

Optomechanics

So far we have introduced the basics of cavities in chapter 2 and mechanical oscillators in chapter 3. These two harmonic oscillators can be coupled via radiation pressure, and provides a desirable increased sensitivity to mechanical motion. We will first describe this fundamental concept in section 4.1.1 and then move on to describe some important results. These involve the most important effects for this work, namely dynamical back-action, described in section 4.1.4, and the quantum back-action resulting a sensitive measurement from the interaction, described in section 4.1.5. This latter effect is the effect limiting the sensing of the oscillator motion in our motivational example of section 1.1 and is of utmost concern.

In section 4.2, we discuss how we physically realize a system displaying this optomechanical interaction as well as how to map the behavior of our system onto the canonical system discussed in section 4.1. Then we describe and show an example of the practically useful technique of optomechanically induced transparency in section 4.3. We will then describe, and show, the strongest yet observed (to my knowledge) ponderomotive squeezing in section 4.4. These results show that we can measure the mechanical motion so sensitively that the quantum back-action of the light influence the motion significantly and serves as a demonstration that to further increase motional sensitivity we need the famous negative mass oscillator described in section 1.1.

Lastly, in section 4.5, we discuss some practical concerns relating to our implementation of cavity optomechanics.

4.1 Canonical cavity optomechanical system

4.1.1 Basics

The canonical optomechanical system can be understood from fig. 4.1, where the basic logic goes as follows. A cavity mirror is allowed to move. This motion alters the cavity resonance frequency, and thus energy of the cavity mode. Thus, a coupling between the cavity mode and the mechanical mode is born.

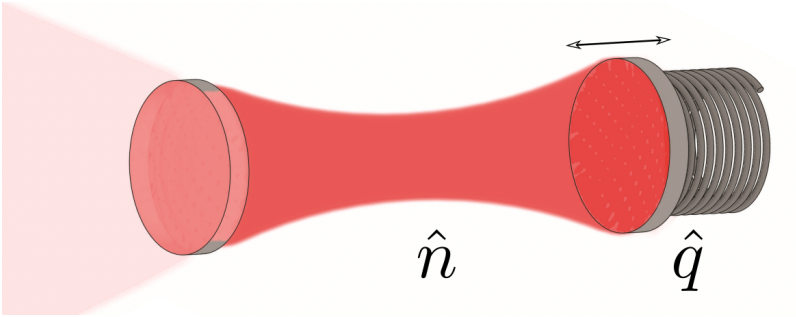

Figure 4.1: **Canonical optomechanical system.** The canonical optomechanical system is an optically driven cavity, populated by $\hat{n}$ photons, consisting of two mirrors where one is mechanically compliant (indicated by being held on a spring, right) and the other is fixed. Motion of the mirror, $\hat{q}$, changes the cavity resonance frequency, thus, affecting the light mode inside. Conversely the light mode inside the cavity can exert a radiation pressure on the mechanically compliant mirror.

The interaction can be seen from the Hamiltonian describing the energy of a cavity field, of frequency ω_c, as

$$\hat{\mathcal{H}} = \hbar\omega_c(\hat{n} + 1/2) \tag{4.1}$$

where $\hat{n} = \hat{a}^\dagger\hat{a}$ is the cavity photon number operator.

If we allow the cavity resonance frequency to depend on the mirror position $q(t)$, i.e. $\omega_c = \omega_c(q)$ and Taylor expand for small excursions around the equilibrium position $q = 0$,

$$\hat{\mathcal{H}} = \hbar\left(\omega_c(0) + \frac{\mathrm{d}\omega_c}{\mathrm{d}q}\bigg|_{q=0} q\right)(\hat{n} + 1/2), \tag{4.2}$$

The cavity resonance shift per displacement is given by[1] $G = \mathrm{d}\omega_c/\,\mathrm{d}q$. In the case of the canonical "end mirror" coupling of fig. 4.1 this parameter is given by $G = \omega_c/L$, where L is the cavity length[2]. For a cavity of $\sim 1\,\mathrm{mm}$ long with a resonance at $1\,\mu\mathrm{m}$ this coupling is $G/2\pi = 300\,\mathrm{MHz/nm}$, which is a near useless number unless it is referenced to the natural excursion lengths of the mirror, i.e. its zero point motion.

Referencing G to the zero point position fluctuations x_{zpf} defined in eq. (3.28) comes about naturally when we quantize the mirror displacement variable $q \to \hat{q}$. We then write our interaction Hamiltonian in terms of the dimensionless mechanical position operator of eq. (3.29) as[3]

$$\hat{\mathcal{H}}_{\mathrm{int}} = \sqrt{2}\hbar g_0 \hat{Q}\hat{n}, \tag{4.3}$$

$$g_0 \equiv G x_{\mathrm{zpf}}. \tag{4.4}$$

[1] sometimes called the frequency pull parameter

[2] The sign of G is a choice of coordinate system. Here we have a positive displacement of the mirror resulting in a shorter cavity and with a higher frequency.

[3] the $\sqrt{2}$ is due to our chosen definition of $\hat{Q}$, see eq. (3.29).

This Hamiltonian describes the coupling of the mirror position with the intracavity photon number mediated by the radiation pressure force. The interaction is easily motivated in hindsight. Radiation pressure of the cavity light field can affect the motion of the end mirror. Likewise, the motion of the end mirror affects the resonance frequency of the cavity thereby affecting the cavity field.

We can work out the force on the mirror by

$$\hat{F} = -\frac{\mathrm{d}\hat{\mathcal{H}}_{\mathrm{int}}}{\mathrm{d}\hat{Q}} = -\sqrt{2}\hbar g_0 \hat{n}. \tag{4.5}$$

which adds an additional forcing term (on top of the thermal Langevin force) to eq. (3.32). The effect of the interaction Hamiltonian will also modify the cavity mode evolution equation of eq. (2.65). Considering a single input optical mode $\hat{s}_{\mathrm{in}}$ (with vacuum δv_{vac} leaking in through the remaining optical channels) and a single mechanical mode Ω_m, we can write the quantum Langevin equations as,

$$\dot{\hat{a}} = \left(i\left(\Delta - \sqrt{2}g_0\hat{Q}\right) - \frac{\kappa}{2}\right)\hat{a} + \sqrt{\eta\kappa}\,\hat{s}_{\mathrm{in}} + \sqrt{(1-\eta)\kappa}\,\delta v_{\mathrm{vac}}, \tag{4.6}$$

$$\dot{\hat{P}} = -\Omega_m^2\hat{Q} + \gamma_m\hat{P} + \sqrt{2\gamma_m}\,\hat{F}^{\mathrm{th,in}} - \sqrt{2}\,g_0\hat{n} \tag{4.7}$$

To see what to expect from this coupling of light and mechanics let us consider, classically, what happens to the cavity mode under sinusoidal mechanical motion of $Q = Q_0\cos(\Omega_m t)$. We then find that

$$a\,(t) \propto a(0)e^{i\bar{\Delta}t - \frac{\kappa t}{2}}e^{-i\beta\sin(\Omega_m t)} \tag{4.8}$$

$$\propto \sum_{n=-\infty}^{\infty} J_n(\beta)e^{in\Omega_m t}, \quad \beta = \frac{\sqrt{2}gq_0}{\Omega_m}. \tag{4.9}$$

where we used the Jacobi–Anger expansion of eq. (E.2.9) to express $\hat{a}(t)$ in terms of Bessel functions J of the first kind and of order $n \in \mathbb{Z}$. Thus, we expect to see the cavity field being comprised of a constant component (oscillating at the cavity frequency of course) and harmonics of the mechanical motion at Ω_m. Through this modulation we see sidebands being generated at $\pm n\Omega_m$. The strength of these sidebands is set by the modulation depth β, essentially quantifying how large cavity frequency excursions are compared to the mechanical frequency. Of most practical relevance for us is the regime of small modulations depths, where only the first order sidebands ($n = 1$) need be considered[4].

Treating this problem a little more generally, as done by Kippenberg and Vahala (2007), one can find the first order correction to the intracavity amplitude to be

[4]For small modulation depths, $\beta \ll 1$, each Bessel function can be expanded to first order giving $J_n(\beta) \propto \beta^n$. Thus, each sideband will be β times smaller in amplitude than the previous.

given by

$$a^{(1)} = \frac{\sqrt{2}\, g_0 Q_0}{2} a^{(0)} \left(\underbrace{\frac{e^{-i\Omega_m t}}{i(\Delta + \Omega_m) - \kappa/2}}_{\text{Anti-Stokes}} + \underbrace{\frac{e^{i\Omega_m t}}{i(\Delta - \Omega_m) - \kappa/2}}_{\text{Stokes}} \right) \tag{4.10}$$

where $a^{(0)}$ is the unperturbed field (zeroth order) given by the cavity Lorentzian and in the input drive. From above it is clear that the sidebands will, in general, not be equally weighted. Their rate of generation is a function of the cavity Lorentzian evaluated at the sideband frequencies $\pm\Omega_m$ and is enhanced by the optomechanical coupling. These two scattering rates represent Raman scattering processes, which will shortly be described further in section 4.1.3. They are known as Stokes and Anti-stokes processes and signify whether optical energy is being depleted or increased, respectively.

For a more detailed derivation of eq. (4.10) see Schliesser et al. (2008, Supplementary). This asymmetry of the perturbed cavity field, as well as its in and out of phase quadrature components (sin and cos), will play a significant role in the dynamics of the mechanical motion $\hat{Q}$. Before we explore this lets make a highly useful and relevant approximation, namely that of mean fields.

4.1.2 Mean fields

Just as in eq. (2.67), we will take the case where the cavity field has a large mean coherent amplitude $\bar{a}$ and quantum fluctuations given by $\delta\hat{a}$ on top as a result of the input field $\hat{s}_{\text{in}}$ being similarly composed. This mean field clearly gives rise to a mean displacement $\bar{Q}$, which, of course, will also have quantum fluctuations $\delta\hat{Q}$ on top. Additionally, we will assume that the mechanical motion is in equilibrium with a zero mean momentum, $\bar{P} = 0$ and that the thermal Langevin force is ergodic, namely $\bar{F}_L = 0$. The mean fields are given by

$$\hat{a} = \bar{a} + \delta\hat{a}, \tag{4.11a}$$

$$\hat{Q} = \bar{Q} + \delta\hat{Q}, \tag{4.11b}$$

$$\hat{s}_{\text{in}} = \bar{s}_{\text{in}} + \delta\hat{s}_{\text{in}}, \tag{4.11c}$$

which, if applied to eq. (4.7) in the steady state, give

$$\bar{a} = \frac{\sqrt{\eta\kappa}}{i\left(\Delta - \sqrt{2}\, g_0 \bar{Q}\right) - \kappa/2}, \tag{4.12}$$

$$\bar{Q} = -\frac{\sqrt{2}\, g_0 \bar{n}}{\Omega_m}. \tag{4.13}$$

Since $\bar{n} = |\bar{a}|^2$ in general, we have a cubic in $\bar{n}$ solution[5] for the intracavity mean field (if $g_0 \neq 0$), where the intracavity field may have multiple solutions

[5] $\bar{n}\left(\Omega_m^2\left(\Delta^2 + 4\Delta\Omega_m g_0^2 \bar{n} + (\kappa/2)^2\right) + 4g_0^4 \bar{n}^2\right) = \Omega_m^2 \eta\kappa|\bar{s}|^2$

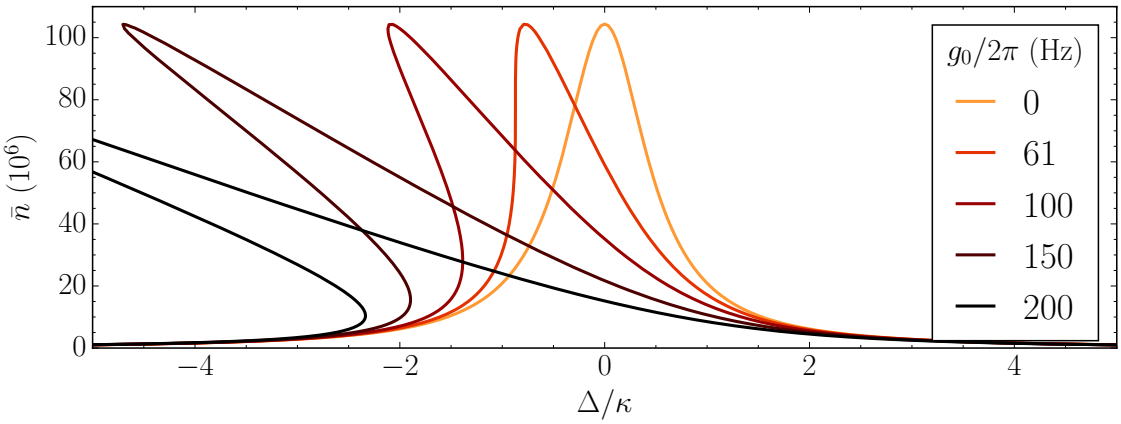

Figure 4.2: **Membrane bistability.** As the single photon coupling rate g_0 is ramped up the membrane is displaced more by the static radiation pressure force. Eventually this diplacement becomes so large as to displace the cavity resonance frequency enough from its original (no coupling) point that a bistability arises, here at $g_0/2\pi = 61\,\mathrm{Hz}$. Shown are the solutions to the intracavity power as a function of detuning in a single sided cavity ($\eta = 1$) of linewidth $\kappa/2\pi = 1\,\mathrm{MHz}$. The cavity is driven with a $40\,\mu\mathrm{W}$ input power corresponding to an on resonance intracavity mean photon number of $\bar{n} = 110 \times 10^6$. The optomechanical coupling g_0 is varied showing the clear onset of this bistability.

for a given detuning. The effect of this interplay is shown in fig. 4.2 and is a result of the intracavity power changing the effective cavity detuning by forcing a mechanical displacement. We can define this effective detuning from eq. (4.12) as $\bar{\Delta} = \Delta - \sqrt{2}g_0\bar{Q}$, which returns the cavity field to the familiar form of eq. (2.76).

The onset of the bistability occurs when the slope of the intracavity field folds back over and was first observed in an optical Fabry-Pérot cavity by Dorsel et al. (1983). This happens when the slope of eq. (4.12) exceeds that of eq. (4.13), which will happen first where the effective cavity Lorentzian is the steepest, i.e.

$$\underbrace{\frac{\partial\bar{n}}{\partial\bar{Q}}\bigg|_{\bar{\Delta}=\frac{-\sqrt{3}\kappa}{6}}}_{\substack{\text{slope of eq. (4.12)}\\ \text{squared}}} \geq \underbrace{\frac{\partial\bar{n}}{\partial\bar{Q}}}_{\substack{\text{slope of}\\ \text{eq. (4.13)}}}. \tag{4.14}$$

This onset occurs at a particular intracavity photon number, $\bar{n}_{\mathrm{onset}}$, and limits the interaction strength available before this effect becomes present to,

$$\frac{g_0^2\bar{n}_{\mathrm{onset}}}{\kappa} \geq \frac{2\sqrt{3}}{9}\Omega_m, \tag{4.15}$$

In practice, a mechanical structure will have multiple modes that are coupled to the optical field, all with different frequencies, which all contribute to the onset of this stability. However, since $g_0^2 \propto x_{\mathrm{zpf}}^2 \propto (m_{\mathrm{eff}}\Omega_m)^{-1} \propto \Omega_m$ the onset on this bistability is roughly affected by modes of any frequency equally.

Notice that once beyond the bistability onset, the range of accessible effective cavity detunings is reduced. In this case of end mirror coupling, imagine tuning the input field frequency, the red detuned regime $\bar{\Delta} < 0$ anywhere near resonance is

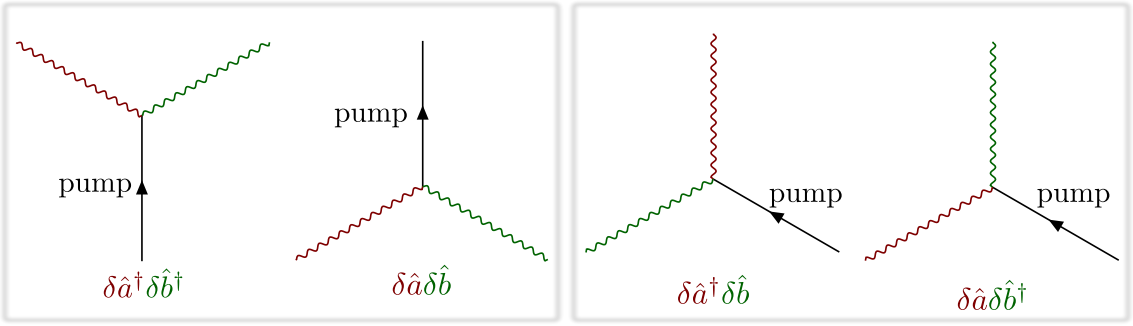

Figure 4.3: **Optomechanical scattering picture interactions.** Feynman diagrams of the two optomechanical scattering processes described by the Hamiltonian of eq. (4.16). **Left:** The processes of $\delta\hat{a}^\dagger\delta\hat{b}^\dagger$ and $\delta\hat{a}\delta\hat{b}$ are known as the two mode squeezing or parametric down conversion interactions. These interactions clearly correlates mechanical motion with the optical field. **Right:** The processes of $\delta\hat{a}^\dagger\delta\hat{b}$ and $\delta\hat{a}\delta\hat{b}^\dagger$ are known as the beamsplitter or state swap interactions. They describe Stokes Raman scattering (former) and anti-Stokes Raman scattering (latter) scattering.

simply off limits. On the other hand, near most of the blue detuned regime $\bar{\Delta} > 0$ is accessible. This is a consequence of the sign g_0, which is positive for[6] our end mirror coupling. If we construct a system where the sign of g_0 is negative then we can have the red detuned regime be the highly accessible one. We will see in section 4.2.4 that an optomechanical setup with the membrane in the middle of a cavity will manifest coupling rates of both signs.

4.1.3 Fluctuations

Having linearized the optical and mechanical fields, the interaction Hamiltonian is

$$\hat{\mathcal{H}}_{\rm int} = \sqrt{2}\hbar g_0(\delta\hat{a} + \delta\hat{a}^\dagger)(\delta\hat{b} + \delta\hat{b}^\dagger) \tag{4.16}$$

$$\propto \underbrace{\delta\hat{a}\delta\hat{b} + \delta\hat{a}^\dagger\delta\hat{b}^\dagger}_{e^{\pm i(\bar{\Delta}-\Omega_m)t}} + \underbrace{\delta\hat{a}\delta\hat{b}^\dagger + \delta\hat{a}^\dagger\delta\hat{b}}_{e^{\pm i(\bar{\Delta}+\Omega_m)t}} \tag{4.17}$$

from which we can identify two unique terms (and their Hermitian conjugates) namely $\delta\hat{a}\delta\hat{b}$ and $\delta\hat{a}\delta\hat{b}^\dagger$. The weighting of these terms,which depends on the cavity detuning $\bar{\Delta}$ relative to the mechanical frequency Ω_m as well as the cavity linewidth κ, give rise to three distinct regimes. The iteractions can be view as scattering events as shown in fig. 4.3.

For so called blue sideband operation where $\bar{\Delta} \approx \Omega_m$ we see from eq. (4.16) that some terms evolve quickly in time with $\pm 2\Omega_m t$, whereas others have a slowly varying envelope. If the quick evolution is much faster than the cavity response time, i.e. if $2\Omega_m \gg \kappa$, then we can employ the rotating wave approximation and neglect these terms. Thus, the dominant terms with be the ones slowly varying in time, namely $\delta\hat{a}\delta\hat{b} + \text{h.c.}$ These terms annihilate (create) a cavity sideband photon whilst

[6] in our definition of eq. (4.4)

annihilating (creating) a mechanical phonon. This process (unsurprisingly) leads to correlations between the mechanical and optical modes given to rise to effects such as two-mode squeezing and entanglement. This process is also known as the Stokes Raman process.

For red sideband operation of $\bar{\Delta} \approx -\Omega_m$ we have near resonant mechanical and optical modes. Using the same logic as above, the dominant terms will be $\delta\hat{a}\delta\hat{b}^\dagger + \text{h.c}$, which describe the annihilation (creation) of a cavity sideband photon whilst creating (annihilating) a mechanical phonon. This process leads to swapping of mechanical and optical excitations. Therefore, this regime is known as the state-swap or beam-splitter regime.

The misbalance of these two subprocesses $\delta\hat{a}\delta\hat{b}^\dagger$ and $\delta\hat{a}^\dagger\delta\hat{b}$ can lead to a net addition or removal of mechanical phonons at the expense of optical photons (or vice versa). In the optical case one can think of phonons being converted into photons which are then lost from the cavity. This is effeciently done in the highly resolved sideband regime, where the cavity effectively favours one process over the other, and so you do not have the competing reverse process. This will be discussed in section 4.1.4.

Finally, the balance of these two processes is realized when $\bar{\Delta} = 0$ and realizes the so called quantum non-demolition interaction. This is because the linearized interaction Hamiltonian looks like

$$\hat{\mathcal{H}}_{\text{int}} = \sqrt{2}\hbar g \delta\hat{X}\delta\hat{Q}, \tag{4.18}$$

and the coupling is between the mechanical and optical amplitude quadratures only. In this case the mechanical position (and optical amplitude) quadrature commutes with the interaction Hamiltonian and can thus be measured without measurement influence. The measurement will however impact the position quadrature at later times via the harmonic motion mixing position and momentum.

To gain further insight into the system dynamics with this interaction Hamiltonian we now look at the first order fluctuating terms of the quantum Heisenberg-Langevin equations of eq. (4.7) under the assumption of the large mean fields as given by eq. (4.11). The quantum Heisenberg-Langevin equations read

$$\delta\dot{\hat{a}} = \left(i\bar{\Delta} - \frac{\kappa}{2}\right)\delta\hat{a} - i\sqrt{2}\,g_0|\bar{a}|e^{i\theta}\delta\hat{Q} + \sqrt{\kappa}\,\delta\hat{s}_{\text{in}}, \tag{4.19}$$

$$\delta\dot{\hat{P}} = -\Omega_m\delta\hat{Q} - \gamma_m\delta\hat{P} + \sqrt{2\gamma_m}\,\hat{F}^{\text{th,in}} - \sqrt{2}\,g_0|\bar{a}|\left(e^{-i\theta}\delta\hat{a} + e^{i\theta}\delta\hat{a}^\dagger\right) \tag{4.20}$$

$$\delta\dot{\hat{Q}} = \Omega_m\delta\hat{P} \tag{4.21}$$

where θ is the phase of the mean intracavity field, which, relative to the input field, is given by eq. (2.82)[7]. These equations are known as the linearized quantum Langevin equations and are the foundational equations on which this work is built.

[7] where the detuning is given by $\bar{\Delta}$, not just Δ.

The input fluctuations $\delta\hat{s}_{\text{in}}$ will generally come from different baths. The most common example used here is one where one port is driven by some field of interest, whilst the other contains just vacuum. In that case we would write simply,

$$\sqrt{\kappa}\,\delta\hat{s}_{\text{in}} \to \sqrt{\eta\kappa}\,\delta\hat{s}_{\text{in}} + \sqrt{(1-\eta)\kappa}\,\delta v_{\text{vac}}. \tag{4.22}$$

One can, in general, spot whether all the ports are being collectively treated or whether they are broken up into component sub-ports by the appearance of the coupling efficiency η for some port.

From eq. (4.21) we see that the coupling between the optical and mechanical modes is boosted by $|\bar{a}|$, allowing us to define a linearized coupling rate

$$g \equiv g_0|\bar{a}| = g_0\sqrt{\bar{n}}. \tag{4.23}$$

This underscores that the linear coupling rate can be enhanced by a large mean intracavity field, thus, making the bistability onset of eq. (4.15) of practical relevance.

Furthermore, the mechanical motion is coupled to a quadrature of the intracavity field, which in the case of $\theta = 0$ is the expected familiar amplitude quadrature. The intracavity field quadratures are given by

$$\delta\dot{\hat{X}} = -\frac{\kappa}{2}\delta\hat{X} - \bar{\Delta}\delta\hat{Y} + 2g\sin\theta\delta\hat{Q} + \sqrt{\kappa}\,\delta\hat{X}^{\text{in}}, \tag{4.24}$$

$$\delta\dot{\hat{Y}} = -\frac{\kappa}{2}\delta\hat{Y} + \bar{\Delta}\delta\hat{X} - 2g\cos\theta\delta\hat{Q} + \sqrt{\kappa}\,\delta\hat{Y}_{\text{in}}, \tag{4.25}$$

where we have written a single collective input quadrature as shorthand for the general case of multiple drives.

In the CW regime, the Fourier domain is more appropriate. Here the equations of motion for the relevant quadratures are given by[8],

$$\begin{pmatrix} i\Omega + \kappa/2 & \bar{\Delta} & 2g\sin\theta \\ -\bar{\Delta} & i\Omega + \kappa/2 & -2g\cos\theta \\ 2g\cos\theta & 2g\sin\theta & \chi^{-1}(\Omega) \end{pmatrix} \begin{pmatrix} \delta\hat{X} \\ \delta\hat{Y} \\ \delta\hat{Q} \end{pmatrix} = \begin{pmatrix} \sqrt{\kappa}\,\delta\hat{X}^{\text{in}} \\ \sqrt{\kappa}\,\delta\hat{Y}^{\text{in}} \\ \sqrt{2\gamma_m}\,\hat{F}_L \end{pmatrix} \tag{4.26}$$

where we have used the susceptibility χ defined in eq. (3.35) with a unit mass since we are working with dimensionless operators[9]. It is also clear that the mechanical motion is generally coupled to both intracavity light quadratures. The mixing given by the field phase θ, and the relation to the input light quadratures gives governed by $\bar{\Delta}$.

To investigate this interplay a bit further let us choose the input field phase such that the intracavity field is real, i.e. $\theta = 0$. We can then solve for the mechanical

[8] An additional prefactor of 2 in the coupling terms present here compared to Møller et al. (2017) is due to a $\sqrt{2}$ difference in both the definition of g_0 and the light quadratures $\delta\hat{X}$, $\delta\hat{Y}$.

[9] Note this definition is different from the one used in Møller et al. (2017) by a Ω_m^{-1}.

degree of freedom and from eq. (4.26) we find,

$$\underbrace{\left(\chi^{-1}+\chi_{\rm dba}^{-1}\right)}_{\chi_{\rm eff}^{-1}}\delta\hat{Q}=\underbrace{\sqrt{2\gamma_m}\,\hat{F}_{\rm th}^{\rm in}}_{\rm TN}+\underbrace{\hat{F}_{\rm BA}^{\rm in}}_{QBA}, \tag{4.27}$$

$$\hat{F}_{\rm BA}^{\rm in}=\frac{g}{\kappa/2}\Big\{i\left[L(\Omega)-L^*(-\Omega)\right]\sqrt{\kappa}\,\delta\hat{X}^{\rm in}- \tag{4.28}$$

$$\left[L(\Omega)+L^*(-\Omega)\right]\sqrt{\kappa}\,\delta\hat{Y}^{\rm in}\Big\}, \tag{4.29}$$

Thus, the mechanical motion is, in general, driven by thermal noise (TN) and both input light noise from both quadratures (QBA). These light quadratures act as a force, just like the Langevin force. The force in addition to the thermal noise is known as the quantum back-action and the fluctuations of this force drive motion. The balance of these two forces is a very relevant experimental turning point and is discussed in section 4.1.5.

It is also clear from eq. (4.29) that the mechanical susceptibility is modified to some effective susceptibility $\chi_{\rm eff}^{-1}=\chi^{-1}+\chi_{\rm dba}^{-1}$. The additional term is known as the dynamical back-action (dba) term and is given by,

$$\chi_{\rm dba}^{-1}=\frac{2g^2}{\kappa/2}\left(\frac{\kappa/2}{(\bar{\Delta}-\Omega)+i\kappa/2}+\frac{\kappa/2}{(\bar{\Delta}+\Omega)-i\kappa/2}\right) \tag{4.30}$$

$$=\frac{2g^2}{\kappa/2}\left[L(\Omega)+L^*(-\Omega)\right], \tag{4.31}$$

where we have used eq. (3.38) to define the the complex cavity Lorentzian as

$$L(\Omega)\equiv\frac{\kappa/2}{(\bar{\Delta}-\Omega)+i\kappa/2}. \tag{4.32}$$

This modified susceptibility tells us how the cavity treats fluctuations at sideband frequencies of $\pm\Omega$ and may indeed dominate the bare mechanical susceptibility χ. In that case the mechanical susceptibility can be molded by tuning cavity parameters.

4.1.4 Dynamical back-action

By decomposing the added dynamical back-action susceptibility $\chi_{\rm dba}^{-1}$ into its real and imaginary components the modified susceptibility can be framed in terms of an effective mechanical frequency $\Omega_{\rm eff}$ and damping rate $\gamma_{\rm eff}$.

$$\Omega_m\chi_{\rm eff}^{-1}=\underbrace{\left(\Omega_m^2+{\rm Re}(\chi_{\rm dba}^{-1})\right)}_{\Omega_{\rm eff}^2}-\Omega^2+i\Omega\underbrace{\left(\gamma_m+\frac{1}{\Omega}{\rm Im}(\chi_{\rm dba}^{-1})\right)}_{\gamma_{\rm eff}}. \tag{4.33}$$

The frequency change $\delta\Omega_m$ and added optical damping $\gamma_{\rm opt}$ can be defined through a natural extension of the bare susceptibility as follows,

$$\Omega_m\chi_{\rm eff}^{-1}\equiv\Omega_m^2+2\Omega\delta\Omega_m-\Omega^2+i\Omega\left(\gamma_m+\gamma_{\rm opt}\right). \tag{4.34}$$

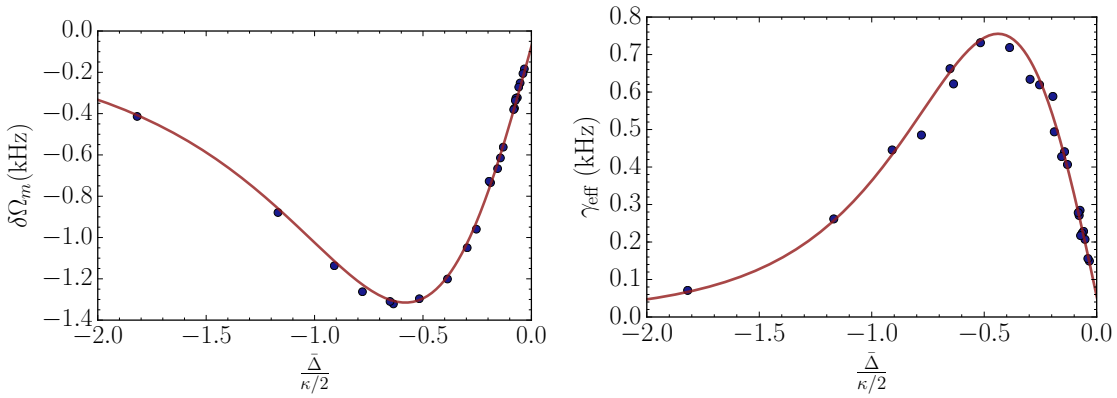

Figure 4.4: **Example of dynamical back-action.** Optical spring and damping measured on a mechanical (2,1) mode of frequency $\Omega_m/2\pi = 1.37\,\text{MHz}$ in a near single sided cavity of $\kappa/2\pi = 15\,\text{MHz}$. The system was probed with a fixed $10\,\mu\text{W}$ input power, and a coupling rate of $g_0/2\pi = 110\,\text{Hz}$. Here the coupling rate $g = g(\bar{\Delta})$ since $\bar{n} = \bar{n}(\bar{\Delta})$ due to the fixed input power.

These can be interpreted as an additional sideband frequency dependent optical damping channel and spring. They can be expressed in terms of the cavity parameters from as

$$\begin{aligned}\delta\Omega_m(\Omega) &= g^2\frac{\Omega_m}{\Omega}\left[\frac{\bar{\Delta}+\Omega}{(\kappa/2)^2+(\bar{\Delta}+\Omega)^2}+\frac{\bar{\Delta}-\Omega}{(\kappa/2)^2+(\bar{\Delta}-\Omega)^2}\right], \\ &= \frac{g^2}{(\kappa/2)^2}\frac{\Omega_m}{\Omega}\left[(\bar{\Delta}+\Omega)\left|L(\Omega)\right|^2+(\bar{\Delta}-\Omega)\left|L(-\Omega)\right|^2\right],\end{aligned} \tag{4.35}$$

$$\begin{aligned}\gamma_{\text{opt}}(\Omega) &= \frac{2g^2\Omega_m}{\Omega}\left[\frac{\kappa/2}{(\bar{\Delta}+\Omega)^2+(\kappa/2)^2}-\frac{\kappa/2}{(\bar{\Delta}-\Omega)^2+(\kappa/2)^2}\right], \\ &= \frac{2g^2}{\kappa/2}\frac{\Omega_m}{\Omega}\left[\left|L(\Omega)\right|^2-\left|L(-\Omega)\right|^2\right],\end{aligned} \tag{4.36}$$

where we have re-expressed each in terms of the cavity power Lorentzian $|L|^2$ evaluated at the upper and lower sideband. This is a particularly useful parameterization when considering the low coupling regime of $g \ll \kappa/2$ relevant to this work, but is valid even in the strong coupling regime $g > \kappa/2$.

In the relevant low coupling regime these corrections to the susceptibility can often be evaluated at the mechanical frequency $\Omega = \Omega_m$ since the mechanical linewidth γ_{eff} will be small compared to the cavity linewidth κ. In this case we simply have

$$\delta\Omega_m \approx \frac{g^2}{(\kappa/2)^2}\left[(\bar{\Delta}+\Omega)\left|L(\Omega)\right|^2+(\bar{\Delta}-\Omega)\left|L(-\Omega)\right|^2\right] \tag{4.37}$$

$$\gamma_{\text{opt}} \approx \frac{2g^2}{\kappa/2}\left[\left|L(\Omega)\right|^2-\left|L(-\Omega)\right|^2\right]. \tag{4.38}$$

These dynamical back-action effects are shown in fig. 4.5 for a few representative choices of $\Omega_m/(\kappa/2)$. Notice how the dynamical back-action cooling always has same functional dependence, essentially just asymmetry in the cavity Lorentzian response

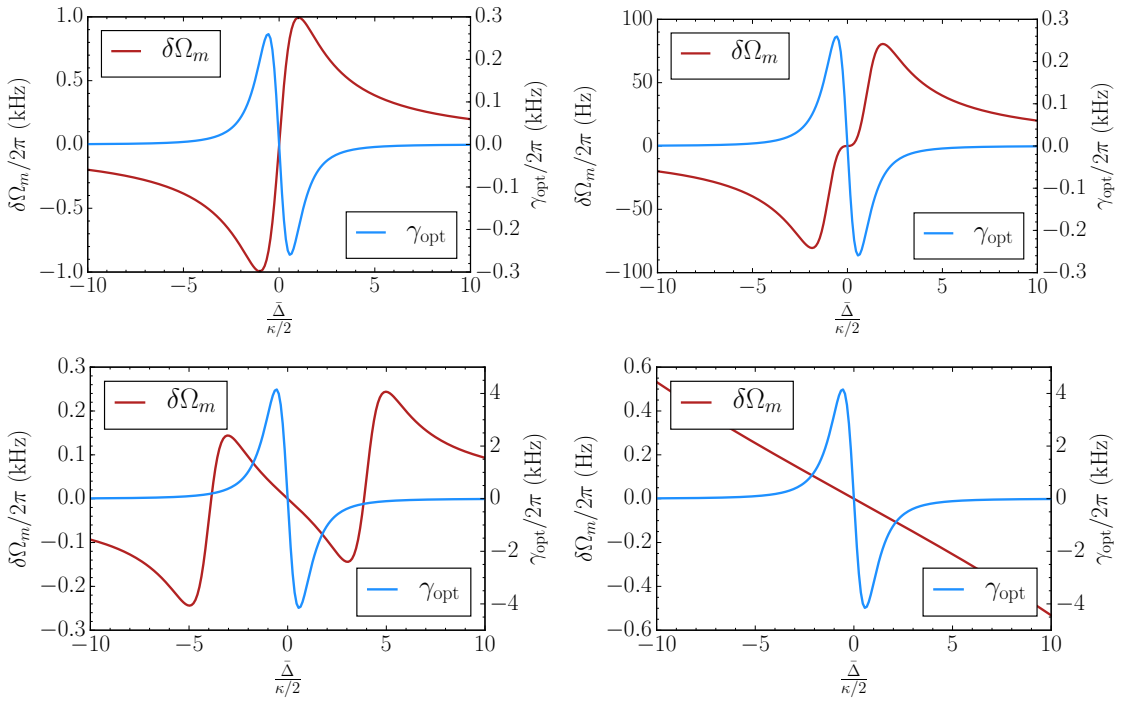

Figure 4.5: **Dynamical back-action in different regimes**. First unresolved sideband regime with (**top left**) $\frac{\Omega_m}{\kappa/2} = 1/10$ and $g/2\pi = 100\,\text{kHz}$, then (**top right**) $\frac{\Omega_m}{\kappa/2} = 1$ and $g/2\pi = 10\,\text{kHz}$, then (**bottom left**) $\frac{\Omega_m}{\kappa/2} = 4$ and $g/2\pi = 10\,\text{kHz}$, finally (**bottom right**) $\frac{\Omega_m}{\kappa/2} = 10$ and $g/2\pi = 1\,\text{kHz}$. Mode frequency $\Omega_m = 1\,\text{MHz}$.

at the sideband frequencies. The frequency shift however is more complex. Now let us look in a bit more detail at the cooling part of the dynamical back-action associated with the added optical broadening.

Dynamical Back-action cooling

The sign of the optical damping described in eq. (4.38) will always depend on the sign of the detuning $\bar{\Delta}$. For $\bar{\Delta} < 0$ we have a positive additional optical broadening of the mechanical motion, whilst for positive detuning $\bar{\Delta} > 0$ the added broadening is negative. If the added broadening is negative and exceeds the intrinsic broadening you have an instability as the mechanical motion will grow exponentially. This is not a regime which one can easily stay in continuously, and thus we will mostly focus on red detuning.

The amount of added broadening depends on the difference between the cavity Lorentzians evaluated at $\pm\Omega_m$, see eq. (4.36). This difference is maximized in the so called resolved sideband regime, where $\Omega_m \gg \kappa/2$. In case you are favouring the anti-Stokes process which removes mechanical energy by swapping phonons for photons.

At a detuning of $\bar{\Delta} = \pm\Omega_m$ this assymetry is maximized and the ratio of the upper $(+\Omega)$ vs lower $(-\Omega)$ sideband weights is given by $\left(\frac{2\Omega}{\kappa/2}\right)^2$, which can in principle be as large as desired. This is important for certain experiments in which cooling to

the mechanical ground state is desirable, since the remaining Stokes scattering will inevitably lead to heating. In this resolved sideband regime it is easy to implement either a pure beam-splitter or squeezer Hamiltonian described in section 4.1.3, since the relevant scattering terms can be efficiently selected by cavity detuning.

The complementary regime is known as the unresolved sideband regime, where $\Omega_m \ll \kappa/2$ and the cavity mode follows the changing mechanical boundary condition adiabatically. For this reason, it is easy in this regime to realize a quantum non-demolition type interaction, as described in section 4.1.3. This is further compounded by the small sideband asymmetry that can be realized. These are in turn what limits the achievable sideband cooling.

In the absence of light the only dissipation channel for mechanical energy was the mechanical bath. The damping was, therefore, also originally solely associated with a coupling to the thermal bath through the Langevin force. Now by optical coupling we have, in effect, coupled the motion to the light bath. This can be seen from eq. (4.29), where it is clear that the light modes now present an additional force, which drives the motion. This has also however, opened a dissipation channel. Let's examine the effect of this additional damping as it pertains to the temperature of the mechanical oscillator.

Mechanical mode temperature

First, consider the mechanical motion without any light. The variance of the motion $\mathrm{Var}(\hat{q}) = \langle \hat{q}^2(t) \rangle$ will be a classical measure of the mode temperature, which is in thermal equilibrium with the bath T_{bath}. In traditional dimensionfull units we have by equipartition[10]

$$\frac{1}{2} m \Omega_m^2 \langle q^2(t) \rangle = \frac{1}{4} k_{\mathrm{B}} T_{\mathrm{bath}}, \tag{4.39a}$$

$$\therefore \mathrm{Var}(q) = \langle q^2(t) \rangle = \frac{k_{\mathrm{B}} T_{\mathrm{bath}}}{2 m \Omega_m^2} = x_{\mathrm{zpf}}^2 \frac{k_B T}{\hbar \Omega}. \tag{4.39b}$$

Now in the Fourier domain we have our dimensionless motion operator given by

$$\delta\hat{Q}(\Omega) = \chi(\Omega) \sqrt{2\gamma_m}\, \hat{F}^{\mathrm{th,in}}(\Omega), \tag{4.40a}$$

$$S_{QQ}(\Omega) = |\chi(\Omega)|^2\, 2\gamma_m S_{FF}(\Omega). \tag{4.40b}$$

where we have written the power spectral density of motion[11] as S_{QQ}. It is driven by the power spectral density of the thermal force S_{FF} given by the correlation function eq. (3.34).

[10] With a 1D oscillator the energy is $\frac{1}{2} k_B T$ which is shared equally between the potential and kinetic contributions.

[11] The subscripts here refer are a bit of notational convenience. They indeed refer to $\delta\hat{Q}$ and not $\hat{Q}$.

Converting to dimensionfull units using our definition $\hat{q} \equiv \sqrt{2}\, x_{\mathrm{zpf}} \hat{Q}$ we see that the motional variance calculated in the Fourier domain is

$$\begin{aligned} \mathrm{Var}(\hat{q}) = 2x_{\mathrm{zpf}}^2 \mathrm{Var}(\hat{Q}) &= 2x_{\mathrm{zpf}}^2 \int_{-\infty}^{\infty} S_{QQ} \frac{\mathrm{d}\Omega}{2\pi} \\ &= x_{\mathrm{zpf}}^2 \left(2\bar{n}_{\mathrm{bath}} + 1\right) \end{aligned} \tag{4.41}$$

where we have used the result of eq. (3.39) and the motional power spectral density of eq. (4.40b).

By invocation of Parsevals theorem (eq. (E.2.10)) the results of eqs. (4.39) and (4.41) should be equivalent. Thus, we have

$$\bar{n}_{\mathrm{bath}} + 1/2 \approx \bar{n}_{\mathrm{bath}} = \frac{k_{\mathrm{B}} T_{\mathrm{bath}}}{\hbar \Omega_m}, \tag{4.42}$$

which is only valid in the approximation made since our treatment of eq. (4.39) followed a rather classical argument.

Now consider what happens when the optical mode is part of the game. Denoting motion driving terms to do with the light quadratures as simply "light" we have,

$$\delta\hat{Q} = \chi_{\mathrm{eff}} \left(\sqrt{2\gamma_m}\, \hat{F}^{\mathrm{th,in}} + \text{light quads} \right), \tag{4.43}$$

$$\mathrm{Var}(\hat{Q}) = \int_{-\infty}^{\infty} S_{QQ} \frac{\mathrm{d}\Omega}{2\pi} = \int_{-\infty}^{\infty} |\chi_{\mathrm{eff}}|^2 \left(2\gamma_m S_{FF} + \text{light}\right) \frac{\mathrm{d}\Omega}{2\pi}, \tag{4.44}$$

$$= \mathrm{Var}(\hat{Q})_{\mathrm{TN}} + \mathrm{Var}(Q)_{\mathrm{Light}}. \tag{4.45}$$

which means that the contribution to the variance due to the thermal noise (TN) is given by,

$$\mathrm{Var}(\hat{Q})_{\mathrm{TN}} = \frac{\gamma_m}{\gamma_{\mathrm{eff}}} \left(\bar{n}_{\mathrm{bath}} + 1/2\right). \tag{4.46}$$

This thermal noise variance is clearly reduced by the increased damping from the light field, with the suppression given by the cooling factor $\gamma_m/\gamma_{\mathrm{eff}}$. In dimensionfull units this thermal noise contribution to the total variance is given by

$$\mathrm{Var}(\hat{q})_{\mathrm{TN}} = x_{zpf}^2 \frac{\gamma_m}{\gamma_{\mathrm{eff}}} \left(2\bar{n}_{\mathrm{bath}} + 1\right) \approx x_{zpf}^2 \frac{\gamma_m}{\gamma_{\mathrm{eff}}} 2\bar{n}_{\mathrm{bath}} = x_{zpf}^2 2\bar{n}_{\mathrm{M}}^{\mathrm{th}}. \tag{4.47}$$

The approximation is valid for large bath occupations, which is always the case for our devices where we typically have $\bar{n}_{\mathrm{bath}} \simeq 10^5$ at cryogenic temperatures of $\sim 10\,\mathrm{K}$. The thermal bath is optically cooled to an effectively lower occupancy given by $\bar{n}_{\mathrm{M}}^{\mathrm{th}}$.

The total variance will, of course, also have a contribution from the light. In effect the mechanical oscillator now sees a modified bath of effective temperature T_{eff} having two contributions. The steady state temperature given by a weighted sum of its components, namely

$$T_{\mathrm{eff}} = \frac{\gamma_m T_{\mathrm{bath}} + \gamma_{\mathrm{opt}} T_{\mathrm{opt}}}{\gamma_{\mathrm{eff}}}. \tag{4.48}$$

By analogy with eq. (4.42) we can recast this in terms of the thermal bath occupancy $\bar{n}_{\text{bath}}$ and one associated solely with the light force $\bar{n}_{\text{min}}$, namely

$$\bar{n}_{\text{eff}} + 1/2 = \frac{\gamma_m(\bar{n}_{\text{bath}} + 1/2) + \gamma_{\text{opt}}(\bar{n}_{\text{min}} + 1/2)}{\gamma_{\text{eff}}}. \tag{4.49}$$

where we notice that in the case of a high cooling power $\gamma_{\text{eff}} \approx \gamma_{\text{opt}} \gg \gamma_m$ we severely dilute the thermal contribution and are dominated by light noise. Furthermore, the relevant vacuum contribution (1/2) is also associated predominantly with the light noise. Regardless of $\bar{n}_{\text{bath}}$ or $\bar{n}_{\text{min}}$ there will always be the vacuum noise (some linear combination of the two baths) driving the systems ground state motion. The minimum effective occupancy is given by n_{min} and is typically referred to as the quantum back-action limit of sideband cooling. Reaching this limit was recently demonstrated Peterson et al. (2016b) for in a very similar setup as the one used here.

This minimal occupancy $\bar{n}_{\text{min}}$ that is added by the coupling with light is given by Marquardt et al. (2007),

$$\bar{n}_{\text{min}} = \frac{|L(-\Omega_m)|^2}{|L(\Omega_m)|^2 - |L(-\Omega_m)|^2} \tag{4.50}$$

$$= -\frac{(\kappa/2)^2 + \left(\bar{\Delta} + \Omega_m\right)^2}{4\bar{\Delta}\Omega_m} \tag{4.51}$$

and is plotted in fig. 4.6 for various cavity parameters. Clearly there are two ways one may seek to minimize this parameter, namely by changing either your mechanical frequency or the cavity detuning. These two choices are seen as the two branches in fig. 4.6. They converge in the resolved sideband regime where there is only one sensible choice, and diverge in the unresolved sideband regime where once again there is only one sensible choice. Between these regimes there are two equivalent choices owing to the symmetry between changing the mechanical frequency and altering the detuning.

Experimentally, typically the free parameter is the cavity detuning whose optimum is given by,

$$\bar{\Delta}_{\text{opt},\bar{n}_{\text{min}}} = -\sqrt{\Omega_m^2 + (\kappa/2)^2} \approx \begin{cases} -\Omega_m, & \text{for } \Omega_m \gg \kappa/2, \\ -\kappa/2, & \text{for } \Omega_m \ll \kappa/2, \end{cases} r \tag{4.52}$$

which can be easily understood by considering the sideband picture.

In the resolved sideband regime the best SB asymmetry you can achieve is when the anti-Stokes SB is on resonance with the cavity Lorentzian. In the unresolved sideband regime the best asymmetry you can get is when you are detuned by exactly half the cavity linewidth. This optimal detuning is shown in fig. 4.7 and gives an optimal minimum occupancy given by

$$\bar{n}_{\text{min}} = \frac{1}{2}\left(\sqrt{1 + \left(\frac{\kappa/2}{\Omega_m}\right)^2} - 1\right) \approx \begin{cases} \left(\frac{\kappa/2}{2\Omega_m}\right)^2 < 1, & \text{for } \Omega_m \gg \kappa/2, \\ \left(\frac{\kappa/2}{2\Omega_m}\right) > 1, & \text{for } \Omega_m \ll \kappa/2. \end{cases} \tag{4.53}$$

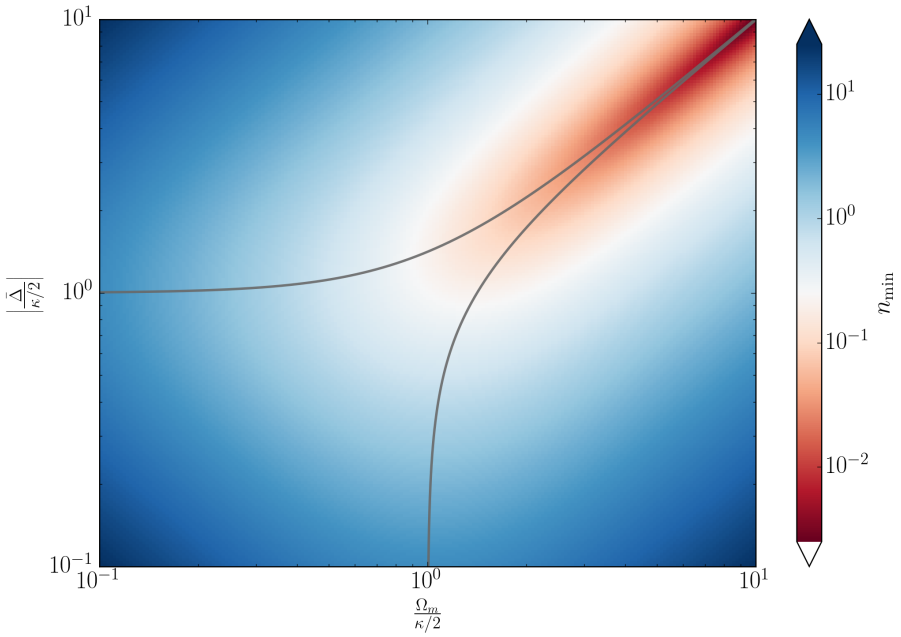

Figure 4.6: **2D plot of $\bar{n}_{\min}$** as described in eq. (4.51) for a varying detuning and mechanical frequency. Solid lines show contour of $\bar{n}_{\min}$ according to eq. (4.53) as is also shown in fig. 4.7. This represents the optimal choice of detuning for a given mechanical frequency, as is often the experimentally relevant case. The remaining branch represents the converse choice, which is equivalent to eq. (4.52), where $\bar{\Delta}$ and Ω_m simply switch roles.

Thus, it is clear that if one desires to add little light noise to the mechanical oscillator, a high degree of SB resolution is required.

The other half of the effective occupancy is the diluted thermal noise contribution. Here the important parameter is the amount of added optical broadening, which is maximized for a detuning of

$$\bar{\Delta}^2_{\text{opt},\gamma_{\text{opt}}} = \frac{\Omega_m^2}{3} - \frac{\kappa^2}{12} + \frac{2}{3}\sqrt{\Omega_m^4 + \Omega_m^2\left(\frac{\kappa}{2}\right)^2 + \left(\frac{\kappa}{2}\right)^4} = \begin{cases} \Omega_m^2, & \text{for } \Omega_m \gg \kappa/2 \\ \kappa^2/12, & \text{for } \Omega_m \ll \kappa/2 \end{cases} \tag{4.54}$$

which, just like eq. (4.52), can be reasoned within the sideband picture. From eq. (4.38) this quantity is maximized when the difference in the scattering rates is the highest. In the unresolved sideband regime this happens exactly when the sidebands are symmetric with respect the highest slope point of the cavity. In the unresolved sideband regime the optimum is the same as for $\bar{n}_{\min}$ for the same reason. Due to their similar asymptotic with $\bar{n}_{\min}$ this optimal detuning is shown side by side in fig. 4.7.

The optical broadening for this choice of optimal red detuning is (to lowest order) given by

$$\gamma_{\text{opt}} = \begin{cases} \frac{16g^2}{\kappa}\left(\frac{\Omega}{\kappa/2}\right)^2, & \text{for } \Omega_m \gg \kappa/2, \\ \frac{3\sqrt{3}g^2}{\kappa}\frac{\Omega}{\kappa/2}, & \text{for } \Omega_m \ll \kappa/2. \end{cases} \tag{4.55}$$

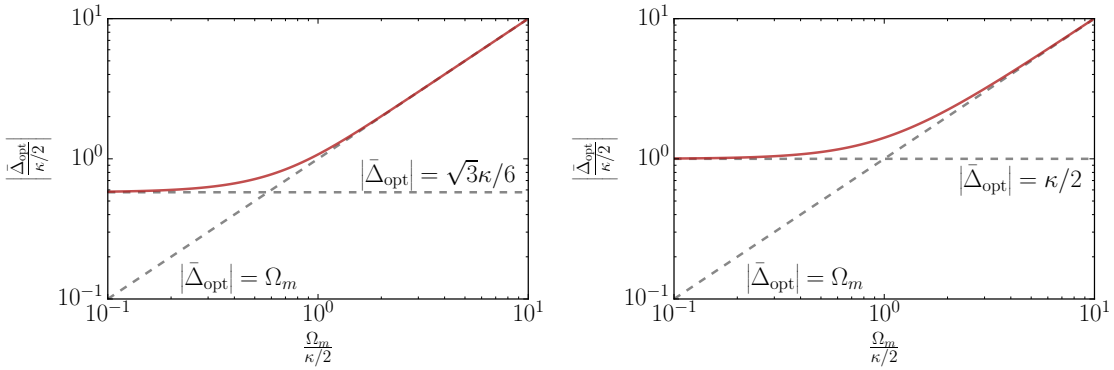

Figure 4.7: **Left:** Optimal detuning for added optical broadening according to eq. (4.54). **Right:** Optimal detuning for minimal $\bar{n}_{\rm min}$ according to eq. (4.52).

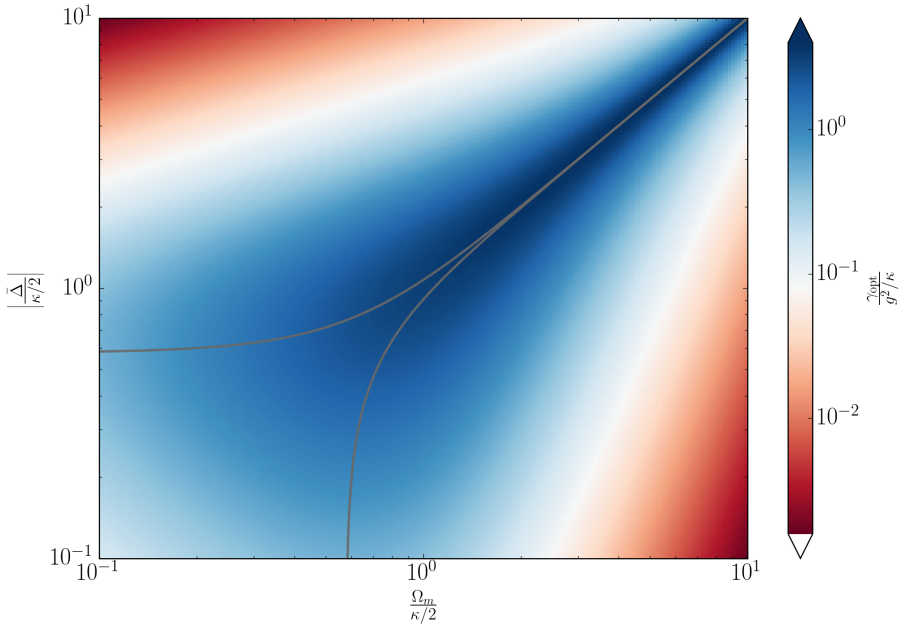

Figure 4.8: **Optical broadening, $\gamma_{\rm opt}$,** for choices of cavity parameters, see eq. (4.38). The two branches (grey lines) of maximum $\gamma_{\rm opt}$ are apparent and converge in the resolved sideband regime. In the unresolved sideband regime the two branches represent an optimal detuning for a given mechanical frequency as described in eq. (4.54), or vice versa, which is equivalent to $\bar{\Delta}$ and Ω_m switching roles.

and the optical broadening is shown in fig. 4.8. Notice how this has the same qualitative behavior as fig. 4.6 as they both relate to sideband asymmetry.

If we look back at eq. (4.49) we see that the minimum effective occupancy that can be reached is given by a trade-off between the dilution of the thermal bath and an increased effect of the light bath. Assuming that significant optical cooling is present, i.e. $\gamma_{\rm opt} \gg \gamma_m$, a balance is struck when the decoherence rates associated with the two baths are equal, i.e. when

$$\gamma_m \bar{n}_{\rm bath} = \gamma_{\rm opt} \bar{n}_{\rm min} = \begin{cases} \frac{4g^2}{\kappa}, & \text{for } \Omega_m \gg \kappa/2, \\ \frac{3\sqrt{3}g^2}{2\kappa}, & \text{for } \Omega_m \ll \kappa/2. \end{cases} \tag{4.56}$$

where we have chosen the optimal conditions for both regimes for simplicity. At

this balance the effective occupancy is given by $\bar{n}_{\text{eff}} \approx 2\bar{n}_{\text{min}}$. Thus, by optical sideband cooling you can only cool into the ground state if you have enough sideband resolution to begin with. That is, unless change the input assumption of vacuum states. Probing with pre-squeezed light source constitutes such a change, and was recently done by Clark et al. (2017).

Mechanical quantum cooperativity

This balance also indicates the point at which the thermal and optical baths are of comparable importance for the dynamics of the mechanical motion. Reinspecting eq. (4.56) we may define a useful figure of merit which allows us to judge whether we may approach the quantum regime, namely the quantum cooperativity,

$$C_q \equiv \frac{4g^2}{\kappa\gamma_m(\bar{n}_{\text{bath}} + 1/2)} \tag{4.57}$$

where we have added vacuum to the mechanical decoherence rate and assumed the optical bath to be in the quantum ground state[12]. These are excellent assumptions for most optical optomechanics experiments and certainly true in our case. The balance struck in eq. (4.56) happens when $C_q \sim 1$ and as we shall see this parameter is relevant whenever light noise is being contrasted with thermal noise.

Let us look further at the effect light has on the motion of the mechanics and vice versa.

4.1.5 Quantum back-action

Quantum cooperativity

Looking back at eq. (4.29) we see that the motional degree of fredoom has contributions from both the thermal reservoir and the back-action of the optical field. Writing this in terms of power spectral densities we have[13]

$$\bar{S}_{\text{QQ}} = |\chi_{\text{eff}}|^2 \left(\bar{S}_{\text{FF}}^{\text{TN}} + \bar{S}_{\text{FF}}^{\text{BA}}\right), \tag{4.58}$$

$$\bar{S}_{\text{FF}}^{\text{TN}} = 2\gamma_m(\bar{n}_{\text{bath}} + 1/2) \tag{4.59}$$

$$\begin{aligned}\bar{S}_{\text{FF}}^{\text{BA}} &= \frac{4g^2}{\kappa}\left(\frac{(\kappa/2)^2}{\left(\bar{\Delta}+\Omega\right)^2 + (\kappa/2)^2} + \frac{(\kappa/2)^2}{\left(\bar{\Delta}-\Omega\right)^2 + (\kappa/2)^2}\right) \\ &= \frac{4g^2}{\kappa}\left(|L(\Omega)|^2 + |L(-\Omega)|^2\right)\end{aligned} \tag{4.60}$$

[12] Note this is not $\bar{n}_{\text{min}}$, but rather the mean thermal excitations of the light field.

[13] In calculating $\langle \hat{F}_{\text{FF}}^{\text{BA}}(\Omega)\hat{F}_{\text{FF}}^{\text{BA}}(-\Omega)\rangle$ the following relation is useful, $u(\Omega)u^*(\Omega) + v(\Omega)v^*(\Omega) = \frac{1}{2}\left(|L(\Omega)|^2 + |L(-\Omega)|^2\right)$, where u and v are combinations of the complex Lorentzian $L(\Omega)$ as defined in eq. (4.111).

where we see that the back-action contribution is weighted by the cavity Lorentzians $L(\Omega)$ evaluated at the sideband frequency of interest. This sideband frequency is typically near the mechanical frequency as the mechanical susceptibility is strongly peaked there (for a high Q). We have used the correlation functions for the input fields given by eq. (2.73) and assumed them to be shot noise limited, i.e. $S^{\text{in}}_{XX} = S^{\text{in}}_{YY} = 1/2$.

If we consider the relative importance of the thermal and quantum back-action (QBA) forces we find that

$$\frac{\text{QBA}}{\text{TN}} = \frac{\bar{S}^{\text{BA}}_{\text{FF}}}{\bar{S}^{\text{TN}}_{\text{FF}}} = C_q \frac{1}{2}\left(|L(\Omega)|^2 + |L(-\Omega)|^2\right) \tag{4.61}$$

where C_q is the quantum cooperativity as defined in eq. (4.57). As suspected, when this quantity is near unity the quantum back-action and thermal noise play a comparable part. In the resolved and unresolved sideband regimes (RSB and uRSB) the contributions are given by

$$\frac{\bar{S}^{\text{BA}}_{\text{FF}}}{\bar{S}^{\text{TN}}_{\text{FF}}} = \begin{cases} C_q, & \text{for uRSB regime } \Omega_m, \left|\bar{\Delta}\right| \ll \kappa/2, \\ C_q \frac{1}{2}\left(1 + \left(\frac{\kappa/2}{2\Omega_m}\right)^2\right), & \text{for RSB regime } \Omega_m \gg \kappa/2, \left|\bar{\Delta}\right| = -\Omega_m. \end{cases} \tag{4.62}$$

It is clear that in the unresolved sideband regime a $C_q = 1$ implies equal contributions to the driving of the mechanical motion. In the absence of significant quadrature rotations this ratio of the contributions translates into the observed variance of the mechanical motion as read-out in the optical phase quadrature.

The quantum cooperativity can also be thought of in terms of a "measurement", Γ_{meas}, and thermal decoherence, $\gamma^{\text{th}}_{\text{dec}}$, rate. Using the eqs. (3.43) and (4.57) we can write

$$C_q = \frac{\Gamma_{\text{meas}}}{\gamma^{\text{th}}_{\text{dec}}}, \Gamma_{\text{meas}} = \frac{4g^2}{\kappa}. \tag{4.63}$$

In this sense the quantum cooperativity quantifies the interaction strength as compared to the decoherence rate. As we shall see now, in a simple case, the measurement rate is related directly to the rate of mechanical motion readout.

Readout

Suppose we observe the phase quadrature output of port 1 of the cavity. Using the input-output relations of eq. (2.80) we have

$$\delta\hat{Y}^{\text{out},1} = \delta\hat{Y}^{\text{in},1} - \sqrt{\eta_1 \kappa}\,\delta\hat{Y} \tag{4.64}$$

where the intracavity field will, in general, contain contributions from external amplitude and phase quadratures, as well as transduced fluctuations of the mechanical

motion. Let us, for simplicity, consider the case of zero detuning, $\bar{\Delta} = 0$, and choose the intracavity mean field to be real. In this case we find that

$$S_{\mathrm{YY}}^{\mathrm{out},1} = \left|1 - \frac{\eta_1\kappa}{i\Omega + \kappa/2}\right|^2 S_{\mathrm{YY}}^{\mathrm{in},1} + \left|\frac{\sqrt{\eta_1(1-\eta_1)}\,\kappa}{i\Omega + \kappa/2}\right|^2 S_{\mathrm{YY}}^{\mathrm{in},2} + \left|\frac{\sqrt{\eta\kappa}}{i\Omega + \kappa/2}\right|^2 4g^2 S_{\mathrm{QQ}} \quad (4.65)$$

$$= S_{\mathrm{YY}}^{\mathrm{in}} + \eta_1\Gamma_{\mathrm{eff}} S_{\mathrm{QQ}}, \quad (4.66)$$

where all the input light noise contributions can be collectively written as $S_{\mathrm{YY}}^{\mathrm{in}}$. Note that if both input fields are in the vacuum state then this is just shot noise, since the prefactors in eq. (4.66) sum to unity.

From eq. (4.66) it is clear that the transduced mechanical fluctuations need to be read out with sufficient strength to overcome this noise floor $S_{\mathrm{YY}}^{\mathrm{in}}$ set by the fluctuations of the input fields. This transduction strength is given by the effective readout rate given by

$$\Gamma_{\mathrm{eff}} = 4\Gamma_{\mathrm{meas}}|L(\Omega, \bar{\Delta} = 0)|^2 = \frac{16g^2}{\kappa}|L(\Omega, \bar{\Delta} = 0)|^2 = \Gamma_M|L(\Omega, \bar{\Delta} = 0)|^2. \quad (4.67)$$

This rate is related to the measurement rate defined in eq. (4.63). We further define one last useful rate, namely the on resonance mechanical readout rate given by

$$\Gamma_m = \frac{16g^2}{\kappa}. \quad (4.68)$$

This is the readout rate, on cavity resonance, in the unresolved sideband regime where $\Gamma_{\mathrm{eff}} = \Gamma_m$.

Notice the Lorentzian penalty factor given simply by the reduced gain of the cavity seen by the mechanical sidebands. In general, for a detuned cavity the penalty is more of a weighted average as in eq. (4.60), and can actually be quite substantial for even moderate detunings.

The aforementioned noise floor can be related to an equivalent transduced mechanical motion that would produce the observed variance. This is known as the imprecision noise floor and sets the level of motion sensitivity. From eq. (4.66) we find that it is given by

$$S_{\mathrm{QQ}}^{\mathrm{imp}} = \frac{1}{\eta\Gamma_{\mathrm{eff}}} S_{\mathrm{YY}}^{\mathrm{in}}. \quad (4.69)$$

Seemingly, there is no limit to the achievable measurement sensitivity. We will read out the mechanical motion S_{QQ} together with the imprecision (imp) noise floor $S_{\mathrm{QQ}}^{\mathrm{imp}}$ as

$$S_{\mathrm{YY}}^{\mathrm{out},1} = \eta\Gamma_{\mathrm{eff}} \underbrace{\left(S_{\mathrm{QQ}}^{\mathrm{imp}} + S_{\mathrm{QQ}}\right)}_{S_{\mathrm{QQ}}^{\mathrm{tot}}}. \quad (4.70)$$

However, in general the mechanical motion will have contributions from thermal noise and the back-action noise as described in eq. (4.58) and will be given by

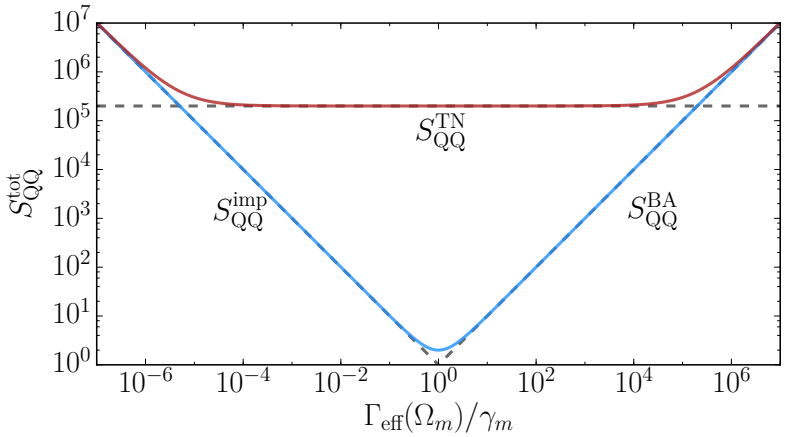

Figure 4.9: **Standard quantum limit.** Apparent mechanical displacement $S^{\mathrm{tot}}_{\mathrm{QQ}}$ inferred from measurement, see eq. (4.70), for $\gamma_m = 1$, $\eta = 1$. Two cases are shown, one with no thermal noise contribution (blue curve) and one with $\bar{n}_{\mathrm{bath}} = 10^5$ (red curve). The latter is the typical order of magnitude reached in the experiments presented here. Also shown and annotated are the (dashed grey) contributions from the imprecision noise floor $S^{\mathrm{imp}}_{\mathrm{QQ}}$, the quantum back-action noise $S^{\mathrm{BA}}_{\mathrm{QQ}}$, and the thermal noise $S^{\mathrm{TN}}_{\mathrm{QQ}}$.

$S_{\mathrm{QQ}} = S^{\mathrm{TN}}_{\mathrm{QQ}} + S^{\mathrm{BA}}_{\mathrm{QQ}}$. Neglecting for the moment the thermal noise contribution we have only the quantum back-action from the input light fields which drive the mechanical motion.

This produces a back-action (BA) force on the oscillator is given by

$$\hat{F}_{\mathrm{BA}} = -2g\delta\hat{X} \tag{4.71}$$

$$S^{\mathrm{BA}}_{\mathrm{FF}} = \Gamma_{\mathrm{eff}} S^{\mathrm{in}}_{\mathrm{XX}}, \tag{4.72}$$

where we have also written the input optical driving quadrature terms $\delta\hat{X}^{\mathrm{in,i}}$ comprising $\delta\hat{X}^{\mathrm{in}}$ collectively as $S^{\mathrm{in}}_{\mathrm{XX}}$. The read-out rate Γ_{eff} also turns out to be the write-in rate of optical fluctuations on the mechanics. Thus, clearly the imprecision noise floor scales inversely with the back-action. Indeed,

$$S^{\mathrm{imp}}_{\mathrm{QQ}} S^{\mathrm{BA}}_{\mathrm{FF}} = \frac{1}{\eta} S^{\mathrm{in}}_{\mathrm{XX}} S^{\mathrm{in}}_{\mathrm{YY}} \geq S^{\mathrm{in}}_{\mathrm{XX}} S^{\mathrm{in}}_{\mathrm{YY}}, \tag{4.73}$$

where we see a Heisenberg uncertainty principle apply to the sensing of the mechanical displacement. If the quadratures are shot noise limited, then, putting $\hbar$ back in, we have the canonical relation $S^{\mathrm{in}}_{\mathrm{XX}} S^{\mathrm{in}}_{\mathrm{YY}} \geq (1/2)^2$. In what follows we will assume that they are both shot noise limited, and thus equal to $1/2$.

The quantum back-action associated with the readout of mechanical motion invariably disturbs it, writing in optical fluctuations, thus limiting the achievable sensitivity. The total apparent motion is then

$$S^{\mathrm{tot}}_{\mathrm{QQ}} = S^{\mathrm{imp}}_{\mathrm{QQ}} + S^{\mathrm{BA}}_{\mathrm{QQ}} + S^{\mathrm{TN}}_{\mathrm{QQ}}, \tag{4.74}$$

$$S^{\mathrm{BA}}_{\mathrm{QQ}} = |\chi|^2 S^{\mathrm{BA}}_{\mathrm{FF}}, \tag{4.75}$$

$$S^{\mathrm{TN}}_{\mathrm{QQ}} = |\chi|^2 S^{\mathrm{TN}}_{\mathrm{FF}}. \tag{4.76}$$

These terms are shown in fig. 4.9 evaluated at the mechanical resonance frequency as the effective readout rate is increased.

Consider the transduced mechanical motion in the absence of thermal noise as would be observed in a power spectral density of the detected optical phase quadrature $\bar{S}_{\mathrm{YY}}^{\mathrm{out},1}$. The peak of the motion due to quantum back-action (BA) in units of the imprecision shot noise floor (SN) is given by

$$\frac{\mathrm{BA}}{\mathrm{SN}} = \frac{S_{\mathrm{QQ}}^{\mathrm{BA}}(\Omega_m)}{S_{\mathrm{QQ}}^{\mathrm{imp}}} = \eta \left(\frac{\Gamma_{\mathrm{eff}}(\Omega_m)}{\gamma_m} \right)^2 . \tag{4.77}$$

When the ratio is unity, the competing terms of imprecision and quantum back-action balance. In this case the transduced spectral density associated with the mechanical motion driven by the light noise has an equal contribution to the apparent motion of shot noise floor, this is the standard quantum limit.

In practice the presence of thermal noise typically dominates the imprecision noise floor at mechanical resonance. The point at which the BA force begins to dominate the thermal noise (see fig. 4.9) happens when $C_q \sim 1$ as described in section 4.1.5. It is much harder to reach as the readout rate needs to be larger by the thermal bath occupancy.

The regime relevant for this work is the case where the mechanics is significantly broadened by dynamical back-action as compared to its intrinsic broadening. Since both $\gamma_{\mathrm{opt}} \propto g^2 \propto \bar{n}$ and $\Gamma_m \propto g^2 \propto \bar{n}$ the height of the back-action contribution in the power spectral density, as described by eq. (4.77), is independent of the intracavity power $\propto \bar{n}$. Thus this quantity, if desired, can only be tuned by changing the cavity detuning or by cavity linewidth κ, the former being a more experimentally convenient knob.

Changing the cavity detuning changes the the optical broadening and, in conjuction with the input optical power, is a way to fine tune the readout rate required for a particular optical broadening. This is important for the experiments of chapter 6. To achieve a larger (smaller) BA/SN, whilst maintaining the maximum optical broadening, the sideband resolution $\Omega_m/(\kappa/2)$ must be made smaller (larger). This is easily understood from eq. (4.38) where a larger sideband resolution means that a smaller readout rate is required for a given amount of optical broadening.

Efficiencies

Let us look again at eq. (4.66) from the perspective of particular quantum fields. Let us first consider only the fluctuations not related to the mechanics. We see that the detected output quadrature from the cavity really has two contributions. One from the light reflected off the port which you are detecting (say port 1) and the other from the remaining port (say port 2). If these are both SN limited quadratures then the total detected quadrature is also SN limited.

However, a fraction of the quadrature reflected off the cavity is lost and the fluctuations replaced by those of the other port. This limits the detection efficiency

of the input quadrature, and in the highly overcoupled regime this is equivalent to a power loss of η^4, as mentioned in eq. (2.79).

Similarily, we can consider the output fluctuations associated with the mechanical fluctuations, in particular the QBA contribution. If the fields from both ports are degenerate and have $\bar{\Delta} = 0$, then this contribution is given by

$$S_{\mathrm{YY}}^{\mathrm{out,1,BA}} \propto \eta\kappa S_{\mathrm{QQ}}^{\mathrm{BA}} \propto S_{\mathrm{XX}}^{\mathrm{in}} \tag{4.78}$$

$$= \eta\kappa \left(\eta\kappa S_{\mathrm{XX}}^{\mathrm{in,1}} + (1-\eta)\kappa S_{\mathrm{XX}}^{\mathrm{in,2}}\right). \tag{4.79}$$

This means that the QBA contribution to the output spectrum deriving from the input amplitude quadrature fluctuations of port 1 is diminished by an equivalent power loss of η^2. The contribution to the back-action is, however, given linearly proportional to η.

From this general analysis it is clear that the overcoupling of the cavity is of primary concern for a quantum limited readout of the input fluctuations, as this scales with η^4. Of secondary concern is the detection of the mechanical QBA, which scales as η^2. Finally, the mechanical motion is driven by the input quadrature of interest by a fractional amount η.

Cavity mode matching

In practice the input field incident on our optomechanical system is not in a spatial mode with perfect overlap with the driven cavity mode of interest. The degree of spatial mismatch, is characterized by the overlap integral of eq. (B.5.39) and known as the cavity mode matching η_{mm}. The modes of our plano-concave cavity are hermite-Gaussian modes described by eq. (D.3.31), which have a Gaussian profile and a spatial distribution given by a Hermite polynomial. The Gaussian nature of these modes means that we can couple a Gaussian beam very efficiently to them, in principle reaching a mode matching efficiency of $\eta_{mm} = 1$.

In practice however our input fields are never perfectly Gaussian, typically distorted by various optics, and so our input field only has a less than unity overlap with the cavity mode. This can be viewed as a source of incoupling loss to the cavity, as is shown and explained further in appendix B.5.3.

Importantly, in such a real life case, the efficiency η just discussed in section 4.1.5 is not only comprised of the cavity overcoupling, which we may write as $\eta_c = \kappa_1/\kappa$. The cavity mode matching η_{mm} also impacts this such that $\eta = \eta_c\eta_{mm}$.

This impact of mode matching depends crucially on the type of measurement being done. The efficiency is clearly of huge importance if the quantum fluctuations of the input field are important, particularly so if the cavity is probed in reflection as just discussed in section 4.1.5. This will limit the hybrid experiments discussed later in section 6.4. The mode matching is on the other hand completely irrelevant for the purely optomechanical results of section 4.4.2.

4.2 Membrane-in-the-middle

4.2.1 Introduction

Before diving into the specifics of our system it is instructive to view a few canonical system. There are many groups who work with such end mirror coupling optomechanical systems. Limiting the scope to those implementing micromechanical resonators as the mechanical degree of freedom we have a more manageable subset. To name a few groups who have pursued systems like this we have the following.

In the group of Markus Aspelmeyer, a double clamped SiN beam with a deposited micromirror was used to demonstrate strong coupling between the mechanical motion and the intracavity field in Gröblacher et al. (2009a). Furthermore they demonstrated strong optical sideband cooling down to an occupancy of ~ 30 phonons, see Gröblacher et al. (2009b). A similar system was introduced a few years later by Dirk Bouwmeester and colleagues in Kleckner et al. (2011). They realized a SiN trampoline resonator with a micromirror forming part of a high a finesse optomechanical cavity. More recently they have demonstrated an improved mechanical quality factor by realizing nested trampoline structures, see Weaver et al. (2016). They simultaneously improved the cavity finesse by a factor of 4.5.

In an attempt to "integrate" the mirror into the mechanical resonator the group of John Lawal introduced SiN membrane resonators with a high-contrast grating etched into the membranes. In this system they demonstrated an achievable cavity finesse of ~ 3000, see Kemiktarak et al. (2012). Similar pursuits, with photonic crystal perforation in SiN instead of a high-contrast grating, include those of Jack Harris in collaboration with Chee Wei Wong (Bui et al. (2012)), Jack Sankey (Bernard et al. (2016)), Simon Gröblacher (Norte et al. (2016)), and Pierre-François Cohadon (Chen et al. (2017)).

A different approach was taken by Michele Bonaldi, where mechanical resonators in Si with a deposited mirror were realized demonstrating cavity finesses of $\sim 65 \times 10^3$. These structures in contrast to the aforementioned groups had much larger effective masses ($\sim 100\,\mu g$), see Serra et al. (2012, 2013).

Finally, the group of Antoine Heidmann has similarly high effective masses ($70\,\mu g$) in a quartz micropillar resonator with a micromirror at the end, see Neuhaus et al. (2013); Kuhn et al. (2014).

In practice, the mechanical motion we are interested in is not the canonical cavity end mirror on a spring. Instead we have opted to place a SiN membrane, as described in section 3.10, in the middle of a plano-concave Fabry-Pérot cavity, such as described in section 2.3. This optomechanical system is illustrated in the left panel of fig. 4.10. The coupling between the mechanical motion of the membrane and the optical field is dispersive and will be described further shortly.

This arrangement is chosen as it has numerous practical advantages. Let us name a few, some of which are not necessarily exclusive to this type of setup. First the high mechanical quality factors of the SiN membranes combined with their very

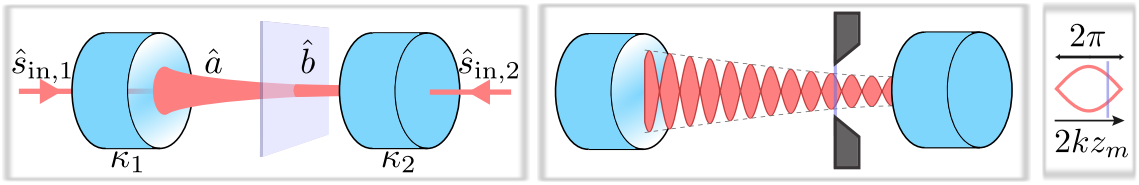

Figure 4.10: **Membrane in the middle illustration and $2kz_m$.** A membrane in placed inside a Fabry-Pérot cavity shown by the two cylindrical (blue) mirrors. **Left:** Relation to the canonical optomechanical setup. Input modes $\hat{s}_{\mathrm{in,j}}$ couple through mirror ports j generating an intracavity field $\hat{a}$. The field describing the common mode excitations of the membrane (translucent square) is described by field operator $\hat{b}$. **Middle:** View of cavity again with the standing wave of the intracavity field shown. The dashed lines shown the transverse Gaussian profile. The membrane (blue line) is held by a Silicon structure (dark grey). It samples the intracavity field at a particular point in the standing wave, which has a half-wavelength periodicity. **Right:** The location z_m of the membrane (blue line) with respect to this half wavelength, also known as "bubble" (red), affects the cavity dynamics and is quantified through the field phase $2kz_m$ which is periodic every 2π.

low optical loss, see Zwickl et al. (2008); Wilson et al. (2009), invites their addition to an optical cavity. Optical cavities with very high finesses are readily available and well understood. The decoupled mechanical and optical properties allow for both to be optimized and tailored independently. Furthermore, decoupling the mechanical element from the end mirror allows for smaller masses since the onus for a high cavity finesse no longer rests with the mechanical element.

Placing a membrane in the cavity as shown in fig. 4.10 means that the cavity field probes the mechanical motion at a particular point, as is seen in the left panel. This is typically arranged to coincide with the spatial displacement maxima of a chosen mechanical mode. In the middle panel of fig. 4.10 the standing wave nature of the intracavity field is shown. The membrane position with respect to this periodic field is quantified through the phase $2kz_m$ where k is the cavity fields wavevector and z_m the location of the membrane inside the cavity with respect to mirror 2. This relative placement alters the cavity dynamics as we will shortly see.

So long as the cavity is long compared to the wavelength, the optomechanical dynamics are unchanged under translation, maintaining the same relative position with respect to the standing wave, of course. That is, locally, adjacent standing wave "bubbles" are equivalent. Thus we cast the membrane position in terms of a large scale position z_m and further by a $2kz_m$ phase $\mod 2\pi$, since the exact location is unimportant. This $2kz_m$ bubble is shown in the right panel of fig. 4.10.

In practice, our membrane-in-the-middle setup consists of three primary elements; the two end mirrors and the membrane. However we are only interested in the motion of the membrane. As we saw in the previous section the motion of the end mirrors will unfortunately (in this case) also be transduced by the cavity. So we need to be careful to differentiate between the fluctuations associated with the cavity, and those of the membrane. These unwanted mirror modes are discussed in section 4.5.7.

4.2.2 Experimental realization

More specifically, the optomechanical system is based on the near-monolithic cryogenic membrane-in-the-middle system described in detail in Nielsen (2016); Nielsen et al. (2016). The system built here consists of a membrane device (SiN membrane with a larger Si chip surrounding it) pressed towards a plano mirror together with a Si spacer. This is achieved by sandwiching these elements between a rigid larger copper structure compressing an O-ring placed beneath the mirror. This spring holds the sandwich in place and all these elements are shown in fig. 4.11. The Si spacer has a square groove big enough to not clamp the Si phononic crystal structure of the membrane device. It also has a small square hole large enough to allow the cavity mode through and small enough to be in contact with the plano mirror everywhere along the edge.

Above this stack floats a plano-concave mirror glued[1] to a piezo-electric transducer, which itself is glued to a copper support. Since this mirror is decoupled from the remaining stack the piezo-mirror combination can tune the cavity resonance frequency. The ring piezo is 3 mm long and provides enough travel at cryogenic temperatures of $\sim 4\,\mathrm{K}$ to move a cavity free spectral range. This is essential as we wish the cavity to be on resonance with a probe at 852.3490 nm for the experiments of chapter 6. Furthermore, the piezo-electric transducer is used to compensate low frequency excursions of the cavity resonance frequency with respect to the probe. This is further explained where applicable.

The Fabry-Pérot cavity formed is 1.3 mm long with a finesse $F = 4500$ ($\kappa = 2\pi \times 25\,\mathrm{MHz}$) and is mounted in a continuous flow cryostat[2] in order to achieve a high vacuum as well as low operating temperatures of $\sim 4.4\,\mathrm{K}$. The power transmissions of the mirrors are 20 ppm (plano) and 1400 ppm (concave) thus, giving a largely one-sided cavity with $\eta_1 = 97\,\%$ in the absence of any other losses besides the transmissions and losses of the mirrors[3]. This one-sidedness is of practical importance for the detecting quantum fluctuations in section 4.4 and more importantly in chapter 6. The cavity mirrors are further anti-reflection coated on the back.

The cavity assembly itself is placed in a liquid helium flow cryostat capable of operating at 4 K. The assembly is housed in a larger copper structure which is anchored to a cold finger of the cryostat. A radiation shield protects the assembly from the 300 K radiation load of the environment. The vacuum chamber has windows for optical access which are anti-reflection coated on both sides. Such a cryostat provides vacuum at a level of 1×10^{-6} mbar and can be evacuated, heated, or cooled in a very short period of time (< 30 min).

The membrane is placed 500 µm from the 20 ppm mirror. This distance is set

[1] Stycast 2850FT

[2] Janis ST-100.

[3] While the 20 ppm mirror has negligible losses compared to transmission, the 1400 ppm mirror is suspected to have losses amounting to ~ 20 ppm.

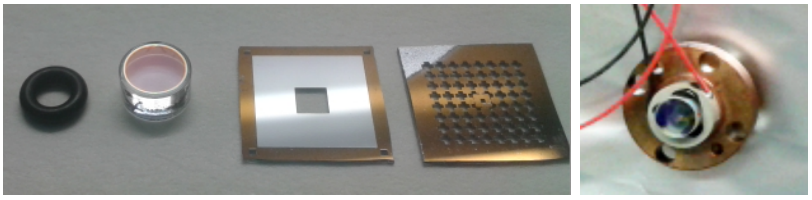

Figure 4.11: **Basic MIM assembly components.** From left to right we have: A standard O-ring. Then a high finesse mirror of 20 ppm transmission and negligible loss coated on top of a 7.7 mm diameter 4 mm thick BK7 substrate. Then a 500 µm Si spacer. Then an example of a membrane device as described in fig. 3.8. Lastly (looking from top to bottom) a high finesse mirror of 1400 ppm transmission coated on top of a plano-concave 6.35 mm diameter 3 mm thick fused substrate. This substrate is then glued (plano side) to a 3 mm thick ring piezo-electric transducer, which is itself glued to a copper support structure. The wires seen allow for electrical control of the transducer.

by the thickness of the underlying Si spacer. The actual mechanical oscillator is the highly stressed, 60 nm thick SiN membrane supported by the Si. This device can be seen as the last element in fig. 4.11 and in greater detail in fig. 3.8.

We will predominantly be concerned with the (1,2) drum mode of the membrane with a frequency $\Omega_M = 2\pi \times 1.28$ MHz at cryogenic temperatures. This mode is used as it is the lowest frequency mode to lie within the bandgap, see fig. 3.8, and has a high quality factor of $Q = 13 \times 10^6$ as measured by ringdowns ($\gamma_{M0} = 2\pi \times 0.1\,\mathrm{Hz}$), see section 3.5.3 and specifically fig. 3.4. The frequency of the mode is chosen such that it does not coincide with unwanted empty cavity mirror modes as described in section 4.5.7.

An $\sim 8\,\%$ side length difference of the membrane breaks the degeneracy of the (1,2) and (2,1) modes significantly, with the desirable (1,2) mode being $\sim$ 60kHz lower in frequency than its sibling. This membrane is placed in a cavity and aligned such that the cavity TEM_{00} mode has a good spatial overlap with the (1,2) mode and a poor overlap with the (2,1) mode. This further separates the modes as the optical spring effect described in section 4.1.4 pushes the (1,2) mode even further away, while having only a marginal impact on the (2,1) mode.

Since the dielectric membrane reflects light, its central placement forms two sub-cavities. It turns out that one can map the behavior of this membrane-in-the-middle setup directly to the canonical OM system described in the previous section. This is done by defining effective parameters such as κ and g.

4.2.3 Motivational effects

First, let us motivate the effect of such a dielectric thin film placed inside MIMposs-calingbasicthe cavity. Note that since the membranes employed are typically never thicker than $\sim 70\,\mathrm{nm} < \lambda/10$ they add very little to the optical path length of a cavity $\sim 1000\ \lambda$ long. In principle the membrane constitutes an etalon with the first resonance occurring when the thickness is $nd = \lambda/2$, which is about 200 nm for SiN. Since we are still far below this and the etalon has a very low finesse we

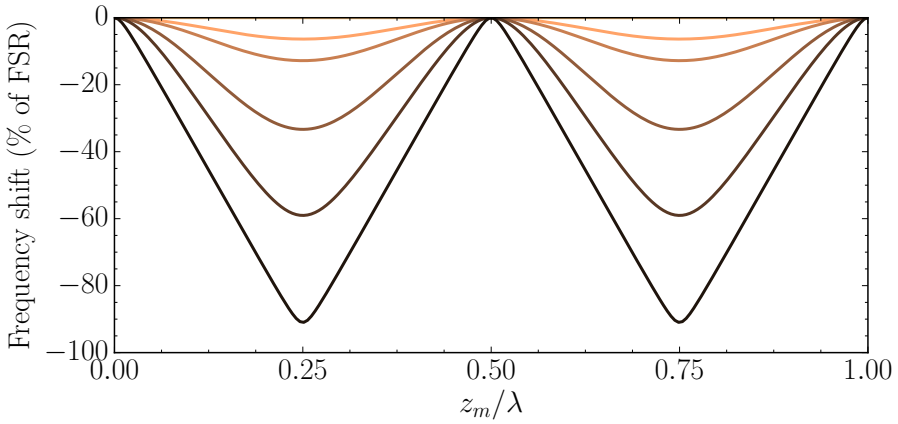

Figure 4.12: **Cavity frequency shift for membrane in the middle** Membrane is placed in the center of a long cavity with a varying absolute amplitude reflectivity $r_m = (0,\ .1,\ .2,\ .5,\ .8,\ .99)$ (lightest to darkest). The frequency shift is relative to the maximum cavity frequency.

can simply treat the membrane as an infinitely thin dielectric film segmenting the cavity into two sub-cavities. The complex reflection and transmission coefficients of the membrane are still calculated with their finite width, however, and are given by,

$$r_m = \frac{(n^2-1)\sin(knd)}{2in\cos(knd) + (n^2+1)\sin(knd)}, \tag{4.80a}$$

$$t_m = \frac{2n}{2in\cos(knd) + (n^2+1)\sin(knd)}. \tag{4.80b}$$

The two sub-cavities are defined by the position of the membrane and their dynamics, it turns out, depend strongly on where the membrane is placed. This can be reasoned by realizing that the membrane acts as a boundary condition one side of each sub-cavity. Supposing the membrane position in the cavity can be tuned, then the boundary conditions of the sub-cavities change, and thus we should expect to an overall change in the cavity as a whole. We should, therefore, also expect that the fluctuations of the membrane change the resonance frequency of the cavity, i.e. that a coupling exists.

In what follows we will pay close attention to the work and formalism of Jayich et al. (2008); Wilson (2012). The cavity resonance frequency can be found by requiring that the transmitted field phase is a multiple of π with respect to the input. Suppose we place a lossless membrane in the center of a long symmetric cavity ($z_m = L/2$). In that case, the cavity resonance frequency $\omega_{c,n}$ as a function of the fine position Δz_m (where $z_m = L/2 + \Delta z_m$), with respect to the center of the cavity, can be shown to be

$$\frac{\omega_{c,n}}{\mathrm{FSR}} = 2\left(\arg(r_m) + \arccos(|r_m|\cos(2k\Delta z_m))\right) + n\frac{\omega_{c,0}}{\mathrm{FSR}}, \tag{4.81}$$

where FSR is the bare cavity free spectral range and $n\omega_{c,0}$ takes into account that we are considering a high harmonic of the cavity $n \gg 1$. Whilst the first term

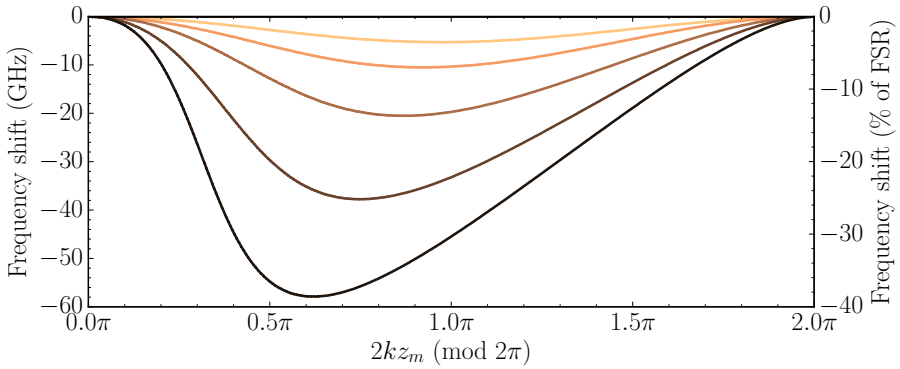

Figure 4.13: **Cavity frequency shifts in $2kz_m$.** Membrane off cavity center at $z_m = 345\,\mu\text{m}$ and a cavity length of $L = 1\,\text{mm}$. The membrane reflectivity is varied by changing the thickness from $h = (5,\ 10,\ 20,\ 40,\ 80)$ nm (lightest to darkest), which changes the absolute amplitude relfectivity $r_m = (0.06,\ 0.11,\ 0.21,\ 0.39,\ 0.57)$ (lightest to darkest). In total the wavelength is tuned from 852 nm to 856 nm.

represents a constant frequency offset, the second shows a clear modulation of the cavity eigenfrequency. The size of this modulation is given by the membrane amplitude reflectivity $|r_m|$ whilst the periodicity is given by the phase $2kz_m$. The cavity frequency shift, removing the constant frequency offset, as the membrane position is varied is seen in fig. 4.12.

The coupling rate ($\propto \partial\omega_c/\partial z_m$) is clearly modulated with the location of the membrane in the "2kz" phase of $2kz_m$. We can think of this $2kz_m$ phase as the position of the membrane with respect to the optical standing wave. If the cavity is long (with respect to λ) the dynamics are periodic in this quantity as long as we only are locally translating the membrane one standing wave period over. Some quantities are period not just on the local scale, but also on the global placement of the membrane within the cavity.

Talking about this periodicity in terms of the $2kz_m$ is very handy since one may not always be able to tune the membrane position directly. Indeed this is the case for the work presented here. In that case one has to change the wavevector in order to address different places in $2kz_m$. This is done in two main ways.

Firstly, in the case where one cannot adjust even the length of a subcavity, one can still cycle through this $2kz_m$ picture by jumping multiple FSRs. After $\sim L/z_m$ FSRs the membrane returns to original location in $2kz_m$. Thus, if L/z_m is very close an integer you will not sample very many locations in $2kz_m$ by this method. Cycling through $2kz_m$ in this way sets the number of FSRs you need to go before you roughly return to where you started. This method allows you to discreetly sample the $2kz_m$ phase of fig. 4.13, which can actually be sufficient. This method was described in more detail Nielsen (2016) and used to great effect in Nielsen et al. (2016).

Secondly, as is relevant to the main work presented here, the length of one subcavity (subcavity bounded by mirror 1) can be changed. If the wavelength is tuned and the cavity kept on resonance by adjusting the tunable subcavity length, the effective $2kz_m$ phase can be changed. The amount of wavelength change required

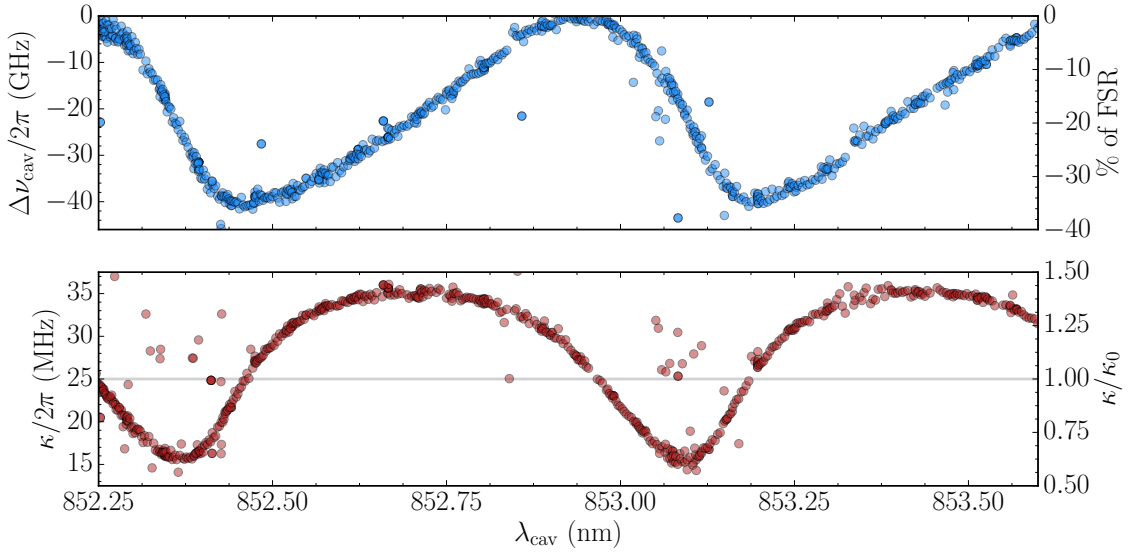

Figure 4.14: **Cavity linewidth and resonance frequency shift in $2kz_m$.** Here the laser frequency is tuned, whilst keeping the cavity on resonance by tuning of the cavity length. The membrane is placed at $z_m = 500\,\mu\mathrm{m}$ from the flat mirror. This wavelength map can be folder into $2kz_m$, but is left as is to show the periodicity and practical realization of such a measurement. **Top:** Change in cavity resonance frequency as the wavelength is tuned referenced to the case where no membrane is present. **Bottom:** Cavity linewidth as the wavelength is tuned. The grey line at 25 MHz indicates the empty cavity linewidth.

to tune through a $2kz_m$ bubble in this case is

$$\Delta\lambda = \frac{\lambda}{2}\left(\frac{\lambda}{z_m}\right), \tag{4.82}$$

where it is clear that a $2kz_m$ bubble can be tuned an FSR ($= \lambda/2$) by the accumulated shift by $2z_m/\lambda$ bubbles each having their size increase $\Delta\lambda$. This is also intuitively obvious; just as a small mirror displacement results in a large accumulated phase shift far away (after many λ), so too does a small wavelength change at the source produce a large accumulated phase shift far away. Tuning through $2kz_m$ in this fashion results in frequency shifts much like that of fig. 4.12. These frequency shifts can be seen in fig. 4.13 for various membrane reflections.

In practice a $2kz_m$ map can be seen in fig. 4.14 where the cavity resonance frequency shift is clearly seen in the top panel. As the probing laser wavelength is tuned, the cavity length is appropriately adjusted so as to stay on resonance with a wavelength λ_{cav} equal to that of the laser. From here we could convert the clearly period dependence into the $2kz_m$ phase by multiplication of $k = 2\pi/\lambda_{\mathrm{cav}}$ with the membrane position $\mod 2\pi$. This would result in a figure like that offig. 4.13.

The cavity frequency shifts are calculated by how far the cavity must be tuned by the piezo-electric transducer in order to be on resonance. The cavity linewidth is measured by scanning the cavity resonance across a probe with known frequency modulation sidebands. These sidebands are generated by an electro-optic modulator a provide an absolute frequency reference. A fit of the cavity Lorentzian then yields

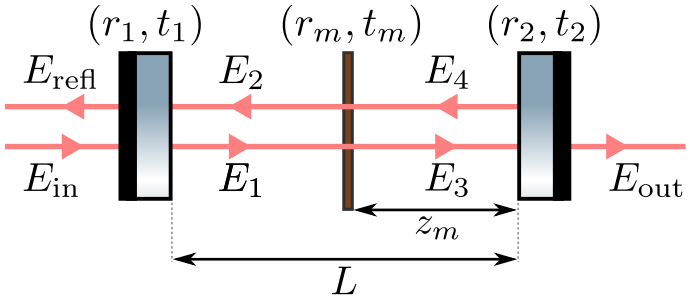

Figure 4.15: **Membrane-in-the-middle transfer matrix fields.** The input E_{in} and reflected E_{refl} fields are seen on the left. In the middle of the L long Fabry-Pérot cavity formed by the two mirrors with amplitude reflection and transmission coefficients (r_i, t_i), $i \in \{1, 2\}$ sits the membrane with amplitude reflection and transmission coefficients (r_m, t_m). The membrane is taken to be a distance z_m away from the back mirror. The counter propagating fields inside the subcavities are $E_1, 2$ and $E_3, 4$. The transmitted field is given by E_{trans}.

the linewidth.

To understand why the cavity linewidth, shown in the lower panel of fig. 4.14, is modulated, we need to treat the membrane-in-the-middle system a bit more formally. In doing so we will find that other canonical optomechanical properties are also modulated.

4.2.4 Theoretical model

The approach to a system like this can be generally treated using the transfer matrix model approach, as is done in Wilson (2012). For a more formal example implementing multiple elements see Genes and Dantan (2017). Our system, however, is simple enough that we can simply write down the relations between the intracavity fields, as is done in Jayich et al. (2008), whose convention we will follow. Using the simple cavity described in section 2.3 as a reference we can write down the following intracavity fields as illustrated in fig. 4.15,

$$E_{\text{refl}} = r_1 E_{\text{in}} + i t_1 E_2 e^{ik(L-z_m)}, \tag{4.83}$$
$$E_1 = i t_1 E_{\text{in}} + r_m E_2 e^{ik(L-z_m)}, \tag{4.84}$$
$$E_2 = i t_m E_4 e^{ikz_m} + r_m E_1 e^{ik(L-z_m)}, \tag{4.85}$$
$$E_3 = i t_m E_1 e^{ik(L-z_m)} + r_m E_4 e^{ikz_m}, \tag{4.86}$$
$$E_4 = r_2 E_3 e^{ikz_m}, \tag{4.87}$$
$$E_{\text{trans}} = i t_2 E_3 e^{ikz_m}. \tag{4.88}$$

We are, of course, most interested in the coupling between the membrane motion and the cavity fields. The net DC force on the membrane depends on the radiation pressure forces experienced, and provides a clear way to determine the coupling. If $\bar{n}_1$ photons are populating subcavity 1 then the radiation pressure force will be given by the rate of change of the momentum transfer, which happens on a timescale

given by the subcavity roundtrip time τ_1. The momentum transfer of each photon is $2\hbar k$ and the net radiation pressure force on the membrane is, making a similar definition for subcavity 2, then given by,

$$F = F_1 - F_2 = 2\hbar k \left(\frac{\bar{n}_1}{\tau_1} - \frac{\bar{n}_2}{\tau_2} \right), \tag{4.89}$$

$$\tau_1 = \frac{2(L - z_m)}{c}, \tau_2 = \frac{2z_m}{c}. \tag{4.90}$$

The net force simply depends on the power difference of the two subcavities. We can contrast this to the force on the canonical end-mirror coupled mechanical oscillator of eq. (4.5), which was

$$\hat{F} = -\frac{\partial \hat{\mathcal{H}}_{\text{int}}}{\partial \hat{q}} = -\hbar g_0 \hat{n} / x_{\text{zpf}}, \tag{4.91}$$

we can map our dynamics onto this by defining the coupling rate as[4]

$$g_0^{\text{MIM}} \equiv \frac{2k x_{\text{zpf}}}{n_1 + n_2} \left(\frac{n_1}{\tau_1} - \frac{n_2}{\tau_2} \right). \tag{4.92}$$

Although we motivated this mapping through a classical consideration of the mean photon subcavity populations, it naturally extends to the quantum case as originally done for the canonical case. The intracavity photon numbers are related to the cavity fields via

$$n_1 = \left(|E_1|^2 + |E_2|^2 \right) \tau_1, \tag{4.93}$$

$$n_2 = \left(|E_3|^2 + |E_4|^2 \right) \tau_2. \tag{4.94}$$

As the membrane modulates $2kz_m$ the photon populations n_1 and n_2 change. This is shown in fig. 4.16 for various membrane reflectivities. In the very relevant (and currently hard to avoid) limit where the cavity mirrors are much more reflective than the membrane this $2kz_m$ modulation only depends on the membrane transmission and reflectance as can easily be checked from eq. (4.88). Both subcavity fields are modulated in a non-trivial manner in the case of reasonable membrane reflectivity. However, the subcavity furthest away from the driving port experiences the largest absolute modulation as a function of $2kz_m$.

4.2.5 Effects on canonical optomechanical parameters

From fig. 4.16 we can also see that a significant differential subcavity photon population can be achieved for particular $2kz_m$ positions. Thus, we should expect the

[4]Note that there is an additional negative sign difference between eq. (4.89) and eq. (4.91) has been included due to the opposite directions taken to be positive displacement. Thus, eq. (4.92) can be directly mapped to the canonical system coupling.

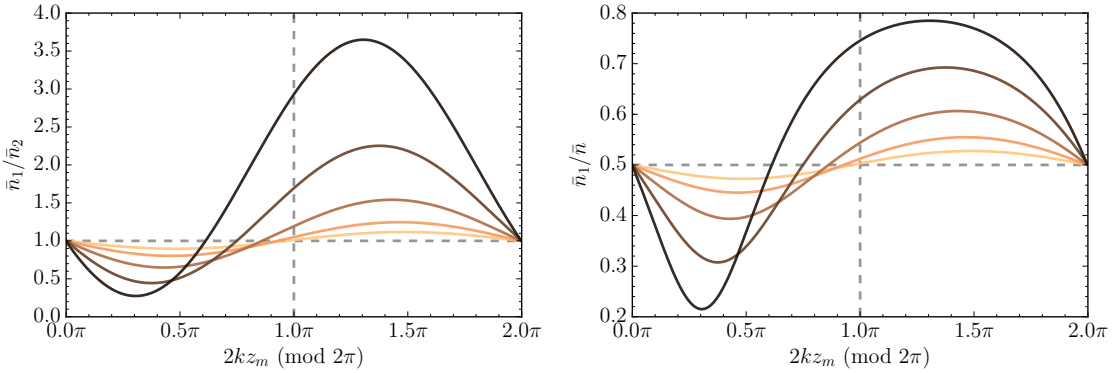

Figure 4.16: **Intracavity fields dependence on membrane thickness**. A SiN membrane is positioned at $z_m = 500\,\mu\text{m}$ in a $L = 1\,\text{mm}$ one-sided cavity. The thickness is varied from $h = (5, 10, 20, 40, 80)$ nm (lightest to darkest) which also changes the absolute amplitude reflectivity $r_m = (0.06,\ 0.11,\ 0.21,\ 0.39,\ 0.57)$ (lightest to darkest) The total cavity length is probed at 852 nm the cavity length adjusted by $\ll L$ to keep the cavity on resonance.

coupling g_0 to be modulated also, and with the subcavity roundtrip times we can directly calculate the dependence. This modulation clearly depends on the reflectivity of membrane, where higher couplings can be achieved with higher membrane reflectivities. This is partly shown in fig. 4.17, where the thickness is varied as this is typically the experimental parameter that may be toggled. This, however, has the added effect that a thicker membrane has a higher mass, and thus a lower g_0. However, even with this, the effect is clearly of a larger coupling for larger reflectivities is the dominant effect.

The disparity of the subcavity powers also modulates other important overall cavity parameters. One that immediately jumps to mind is of the cavity loss rate. Imagine a one-sided cavity[5] with subcavity populations modulated as in fig. 4.16. When the subcavity adjacent to the lossy port has a larger population the overall cavity loss rate will be higher, because a larger fraction of the total cavity photons are being lost per unit time. Conversely, in the situation where most cavity photons populate the subcavity adjacent to the perfect mirror, the cavity will lose fewer overall photons per unit time, as compared to the bare cavity. Thus, the addition of the membrane can enhance (or reduce) the cavity finesse/bandwidth. This effect can be seen in fig. 4.17 where the membrane reflectivity is varied by changing the membrane thickness.

The roundtrip time of the particular subcavity is also important for this overall linewidth modulation. A trade-off exists as the total number of photons in a subcavity, and its roundtrip time, depends on the global position of the membrane (always chosing the point of maximum modulation in $2kz_m$). For the one-sided cavity the point of no finesse/linewidth modulation lies very close to the near perfect

[5]In a one-sided cavity we can think of one port (termed the "lossy" port) as having some finite transmission, whereas the other port is perfectly reflecting.

mirror. Moving the membrane across the cavity this effect is shown in fig. 4.18. For a symmetric cavity, this point of no modulation lies right in the middle of the cavity, since the subcavity roundtrip times are then equal (and again the photon populations care not for the absolute location of the membrane).

This reduced or enhanced linewidth/finesse is really due to a smaller or greater number of photons leaving from a given port. Thus, the coupling effeciency of a given port can also be thought of as modulated. Considering again the one-sided cavity, in the enhanced linewidth $2kz_m$ region (where more photons populate the subcavity with the lossy port) a greater fraction of the total cavity photons leave through the lossy port. Thus, the overcoupling is higher and one should expect a higher overall reflected power. Likewise, in the other port the transmitted light should be reduced by this fractional increase. This can be seen in fig. 4.17 for the transmitted light. The reflected light sees the same modulation, with $(1-R)/(1-R_0)$ being modulated exactly as shown for T/T_0 in the case of no additional cavity losses. Here R, T are the power reflection and transmission and the subscript 0 indicate that of the bare cavity.

Unfortunately, it is not possible to simultaneously achieve a large degree of overcoupling while simultaneously having a reduced cavity linewidth (increased finesse) as would often be desirable. However, this effect allows the overcoupling of a particular membrane-in-the-middle cavity to be tuned by choice of the membrane reflectivity. In a similar vein, one can also tune the size of the cavity linewidth modulation by choosing where to place the membrane. When doing this one often needs to consider both the relevant parameters g_0^2/κ and κ as such a choice often involves a desire for a particular readout rate and/or sideband resolution. These parameters are also shown in figs. 4.17 and 4.18. The collection of all these optomechanical parameters in $2kz_m$ is colloquially known as a column of wisdom. Once a setup has been characterized, the measurement of one of these parameter, most often the cavity linewidth κ, is enough to infer the others.

4.3 Optomechanically induced transparency

4.3.1 Theoretical treatment

An optomechanical system like ours can display a feature analogous to atomic electromagnetically induced transparency (EIT). In an atomic medium where a probing field resonant with a transition would normally be absorbed, adding a strong pump field can, under the right circumstances, open up a transparency window for the weaker probe to leak through. This is typically done in a three level system where the pump drives a transition between a level the probe addresses and one it does not. This scheme can lead to a destructive interference effect between the transition probability amplitudes of the levels. This effect on Strontium atoms was first reported in Boller et al. (1991) and is concomitant with a severely distorted dispersion

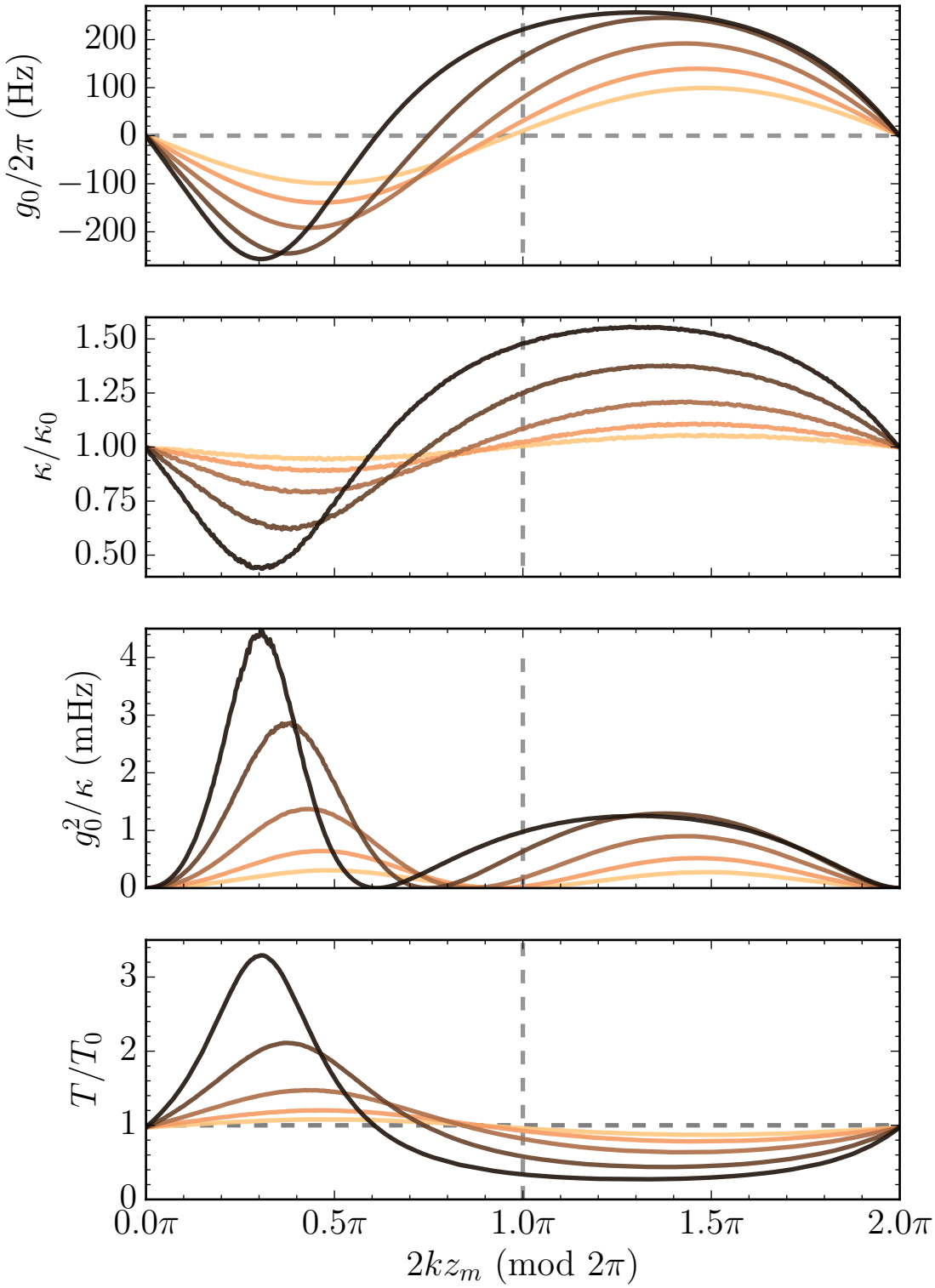

Figure 4.17: **Periodic $2kz_m$ modulation of optomechanical parameters with membrane thickness.** The membrane thickness is scaled from $h = (5, 10, 20, 40, 80)$nm (lightest to darkest) for a membrane placed at $z_m = 500\,\mu$m in a $L = 1$ mm long cavity.

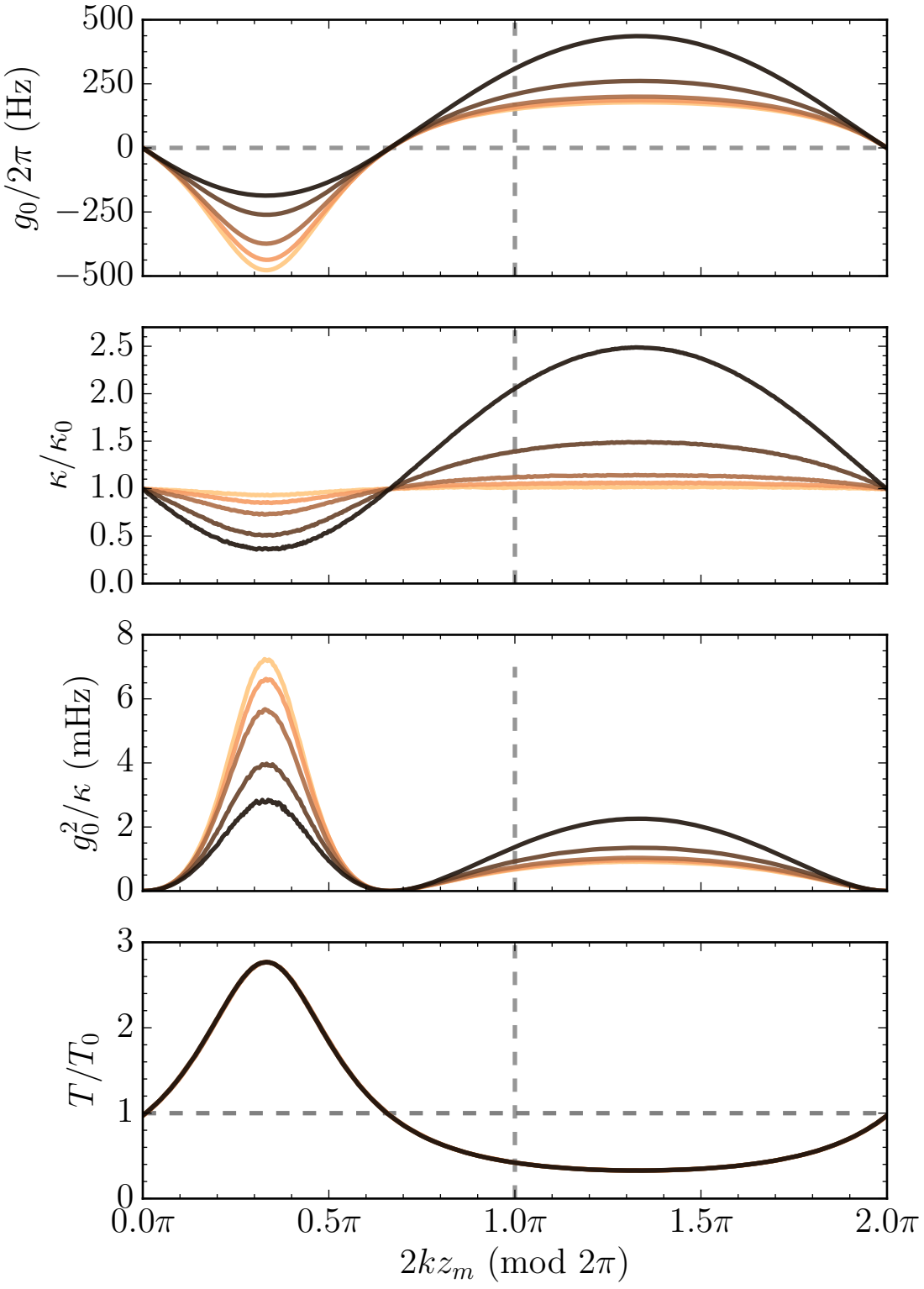

Figure 4.18: **Periodic $2kz_m$ modulation of optomechanical parameters with global membrane position** The global position of the membrane is tuned $z_m = (50, 100, 200, 500, 900)$ (lightest to darkest). The cavity length is fixed at $L = 1\,\mathrm{mm}$ and the membrane thickness is taken to be $h = 60\,\mathrm{nm}$.

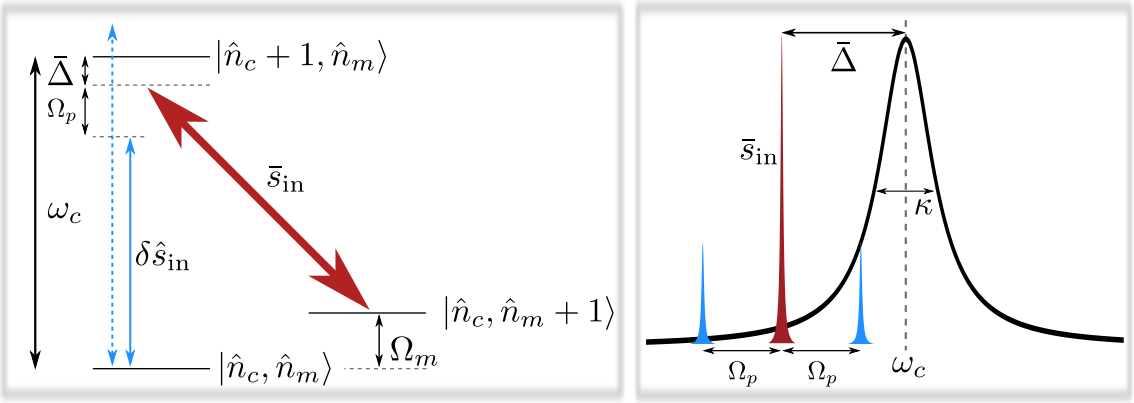

Figure 4.19: **Simplified OMIT.** Pump field $\bar{s}_{\rm in}$ (red) is detuned from cavity resonance frequency ω_c by a detuning given by $\bar{\Delta}$. The probe field $\delta s_{\rm in}$ (blue) has two contributions in the frequency modulation case as indicated by the additional dashed field. These detuned from the pump by the sideband modulation frequency $\pm\Omega_p$. **Left:** Optomechanical state picture. The cavity has photon number operator $\hat{n}_c$ and the membrane a phonon number operator is $\hat{n}_m$. Note similarity to atomic EIT in e.g. a Λ scheme. **Right:** Probe and sidebands in relation to the cavity Lorentzian (black) with linewidth κ.

relation. This leads to a severe reduction in the group velocity of the probing field, as shown in Kasapi et al. (1995), and thus this effect can be used for storage.

In an optomechanical system this three-level system dynamics can also be realized as was demonstrated by Weis et al. (2010). The effect is used in this work not for slowing light, but as a handy characterization tool to determine optomechanical parameters. Let us see how induce this effect[1].

As our input, let us take a large coherent field as our pump and a small probe. Using our previous notation we can write the input as $s_{\rm in} = \bar{s}_{\rm in} + \delta s_{\rm in}$. In practice the probe field is made by an electro-optic modulator, which phase modulates the light at an experimentally tunable frequency $\Omega_{\rm p}$. The input field, thus, attains sidebands at $\pm\Omega_{\rm p}$, which in the case of a small modulation depth β is can be written as

$$s_{\rm in}e^{i\omega t} = s_{\rm in}e^{i(\omega_L t+\beta\sin(\Omega_{\rm p}t))} \tag{4.95}$$

$$= s_{\rm in}e^{i\omega_L t}\left[1+\frac{\beta}{2}\left(e^{i\Omega_{\rm p}t}-e^{-i\Omega_{\rm p}t}\right)\right] = \bar{s}_{\rm in}+\delta s_{\rm in}, \tag{4.96}$$

$$\delta s_{\rm in} = \bar{s}_{\rm in}\frac{\beta}{2}\left(e^{i\Omega_{\rm p}t}-e^{-i\Omega_{\rm p}t}\right) \tag{4.97}$$

Where we have identified our small probe field $\delta s_{\rm in}$, which is purely imaginary ($\delta s_{\rm in} = \delta s_{\rm in}^\dagger$)[2] if we take our input field to be a large real field ($\bar{s}_{\rm in} = \bar{s}_{\rm in}^\dagger$). Sending these fields to the cavity we realize the level scheme illustrated in fig. 4.19, which is reminiscent of a traditional Λ scheme for atomic EIT.

In the most simple detection scheme possible we simply seek to detect the amplitude quadrature $\delta\hat{X}^{\rm out}$ coming from the cavity. As we are applying the probe field

[1] We take a similar approach to Nielsen (2016).

[2] $\delta s_{\rm in}(t) = i\beta\sin(\Omega t) = -\delta s_{\rm in}^\dagger(t)$

at a known frequency we can simply demodulate this quadrature at $\Omega = \Omega_{\rm p}$. As this probe field is very large, and we are only interested in the steady state dynamics of the system, we will neglect quantum effects as well as the mechanical thermal reservoir. Looking in transmission, the detected quadrature is related to the intracavity quadrature δX by

$$\delta X^{\rm out} = \sqrt{\eta_{\rm out}\kappa}\,\delta X, \tag{4.98}$$

where the $\eta_{\rm out}$ is the cavity output coupling efficiency. For simplicity let us take the mean intracavity field $\bar{a}$ to be real. Thus, we write the rotation of the cavity on the input field as an effective phase on the input, i.e.

$$\bar{s}_{\rm in} = \frac{i\bar{\Delta} - \kappa/2}{\sqrt{\bar{\Delta}^2 + (\kappa/2)^2}}\bar{a}, \tag{4.99}$$

$$\delta s_{\rm in} \to \frac{i\bar{\Delta} - \kappa/2}{\sqrt{\bar{\Delta}^2 + (\kappa/2)^2}}\delta s_{\rm in}. \tag{4.100}$$

We can then use the equations of eq. (4.26) to write down the mechanical motion and the intracavity field as,

$$\delta Q(\Omega) = -\chi_m(\Omega)\sqrt{2}\,g\delta X(\Omega), \tag{4.101}$$

$$\delta a(\Omega) = \frac{iL(-\Omega)}{\kappa/2}\left(\sqrt{\eta_{\rm in}\kappa}\,\frac{i\bar{\Delta} - \kappa/2}{\sqrt{\bar{\Delta}^2 + (\kappa/2)^2}}\delta s_{\rm in}(\Omega) - i\sqrt{2}\,g\chi(\Omega)\delta Q(\Omega)\right). \tag{4.102}$$

We can now find the intracavity amplitude quadrature $\delta X(\Omega) = \left(\delta a(\Omega) + \delta a^\dagger(-\Omega)\right)/\sqrt{2}$ to be given by,

$$\delta X(\Omega) = C(\Omega)\delta s_{\rm in}(\Omega) + M(\Omega)\delta X(\Omega), \tag{4.103}$$

$$C(\Omega) = \frac{\sqrt{\eta_{\rm in}\kappa}}{\sqrt{\bar{\Delta}^2 + (\kappa/2)^2}}\frac{(\bar{\Delta} - i\kappa/2)L^*(\Omega) - (\bar{\Delta} + i\kappa/2)L(-\Omega)}{\kappa/2}, \tag{4.104}$$

$$M(\Omega) = \frac{2g^2}{\kappa/2}\chi_m(\Omega)\left(L(-\Omega) + L^*(\Omega)\right), \tag{4.105}$$

where we have used $\delta s_{\rm in}(\Omega) = -\delta s_{\rm in}^\dagger(-\Omega)$ as stated previously. From this result we realize that the intracavity field has two contributions. The first is a cavity conversion of the input phase modulation into amplitude fluctuations, which we will write as $C(\Omega)$. The second is the transduced driven mechanical motion, which in the case of the detuned cavity mixes the phase quadrature response into amplitude fluctuations. We write this mechanical contribution as $M(\Omega)$ and notice that its contribution is only substantial when the coupling rate is large and when $\Omega_{\rm p} \approx \Omega_m$ since the response is filtered by the mechanical susceptibility. Using this result and the input–output equation of eq. (4.98) the detected quadrature is given by,

$$\delta X^{\rm out}(\Omega) = \sqrt{(1-\eta)\kappa}\,\frac{C(\Omega)}{1 + M(\Omega)}\bar{s}_{\rm in}\frac{\beta}{2}\left(\delta(\Omega + \Omega_{\rm p}) + \delta(\Omega - \Omega_{\rm p})\right). \tag{4.106}$$

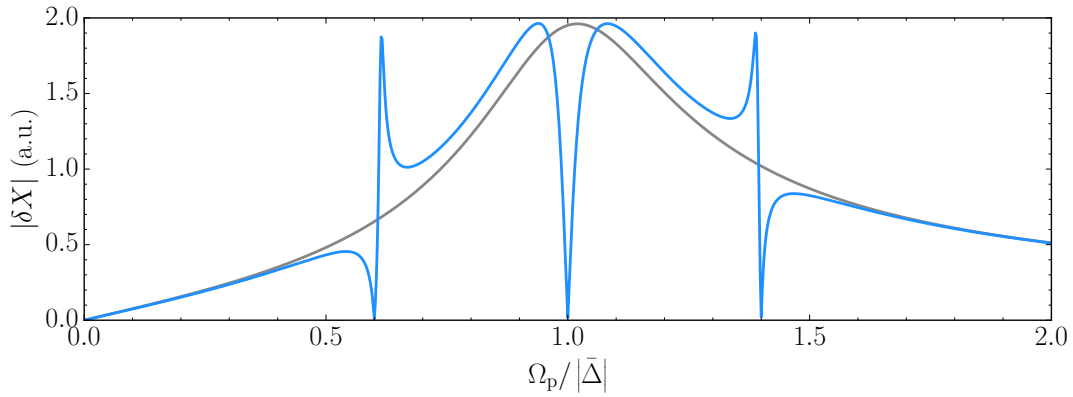

Figure 4.20: Theoretical OMIT response. Grey line is only $|C(\Omega)|$ whereas blue includes the mechanical response $M(\Omega)$. A mechanical susceptibility is chosen to contain only 3 modes with frequencies $\Omega_m = (\bar{\Delta} - \kappa, \sqrt{\bar{\Delta}^2 + (\kappa/2)^2}, \bar{\Delta} + \kappa)$. The detuning was set to be $\bar{\Delta} = -5(\kappa/2)$ and $g^2/\kappa = .03$.

We can think of this scheme as probing the mechanical response of the optomechanical cavity to an input phase modulation. Demodulating the detected quadrature at $\Omega = \Omega_p$ and looking at the amplitude of the signal (treating both sidebands equally) we see the transparency window, initially advertized, in fig. 4.20. The overall cavity transduction of the probe is shown in grey and the full response in blue. Where there is a mechanical mode the probe field is not transduced into δX^{out} and thus the cavity appears transparent to the phase modulation field.

The mechanical susceptibility used in fig. 4.20 includes 3 modes for illustrative effect. Including these modes (or more) requires only a minor modification to eq. (4.102) to extend the susceptibility to be the sum of many susceptibilities and the coupling constants to be written individually.

The cavity response is maximum where $\Omega_p = \sqrt{\bar{\Delta}^2 + (\kappa/2)^2}$, and the OMIT feature of a mechanical mode here is symmetric (see fig. 4.20) in frequency since the probe is on cavity resonance, and thus the sidebands are weighted equally. A mode with a frequency above or below this point has unequally weighted sidebands, and thus a distorted and dispersive response. This phase difference has a sign difference above and below resonance as is clearly seen.

The detected signal strength can, in practice, be boosted to the required signal-to-noise by a simple increase of modulation β (so long as it remains small). Furthermore this method acts as a nice way to coherently probe the mechanical response of a potential mode. Indeed it can also be used to check whether something is mechanical pliable or an artifact of detection. For very narrow mechanical modes with a high mass this is, however, difficult in practice.

4.3.2 Measurement

In a monolithic, symmetric, 1.7 mm long cavity like the one described in Nielsen et al. (2016) the optomechanical system is cryogenically operated and probed in

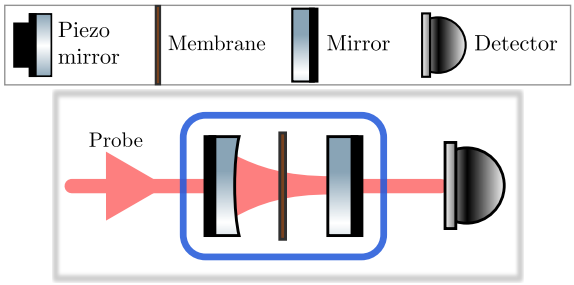

Figure 4.21: **OMIT optical setup.** A probe with frequency modulation sidebands is sent through the optomechanical cavity and detected in transmission on a diode. The cryostat (blue square) surrounds the optomechanical system.

transmission by a strong probe with frequency modulation sidebands generated by an electro-optic modulator. A simplified optical setup of the experiment is shown in fig. 4.21.

In practice a bias tee splits the detected photocurrent fluctuations. The high frequency branch ($> 100\,\mathrm{kHz}$) is directed to demodulation and signal processing. The low frequency branch forms part of a feedback loop stabilizes the laser to the cavity on long time scales compared to the dynamics of the mechanics[3]. The transmission Lorentzian of the cavity is used as the error signal. A good reference for understanding such feedback, which are of huge practical importance, but not thoroughly discussed in this work, can be found in Bechhoefer (2005).

The output transmitted light from the cavity is detected and the resulting photocurrent demodulated at the sideband frequency. As this frequency is swept we obtain the OMIT response of the optomechanical system as seen in fig. 4.22.

The cavity mirrors each have a 20 ppm transmission in contrast to those described in section 4.2.2. This provided a significantly higher finesse and the achieved linewidth was $\kappa/2\pi = 1.4\,\mathrm{MHz}$. The membrane has a large number of modes within a few cavity linewidths[4]. Thus, the OMIT response seen in[5] fig. 4.22 looks a bit more messy. Nonetheless, the same underlying dynamics are at play. Typically the overall cavity dynamics described by $C(\Omega)$ is the dominating feature, and can always be made so by reducing the intracavity field amplitude.

We can use the fit of the overall cavity response to fit both cavity linewidth and detuning. Fits of the individual modes can be used to extract the coupling strength g for that mode. To get g_0 from the fitted g the intracavity power needs to be known, which can in practice be calculated if the input power and coupling efficiencies are measured, or, if the output coupling efficiency and ultimate detection efficiency are measured.

In this particular experiment, shown in fig. 4.22, the (3, 3) membrane mode with a frequency of 2.2 MHz is significantly optically broadened to $\gamma_{\mathrm{opt}}/2\pi = 70\,\mathrm{kHz}$. In

[3]Feedback bandwidth of $\sim 10\,\mathrm{kHz}$.
[4]This is typical for us as we have so far not ventured deep into the unresolved sideband regime
[5]This is a particularly extreme case of large dynamical back-action.

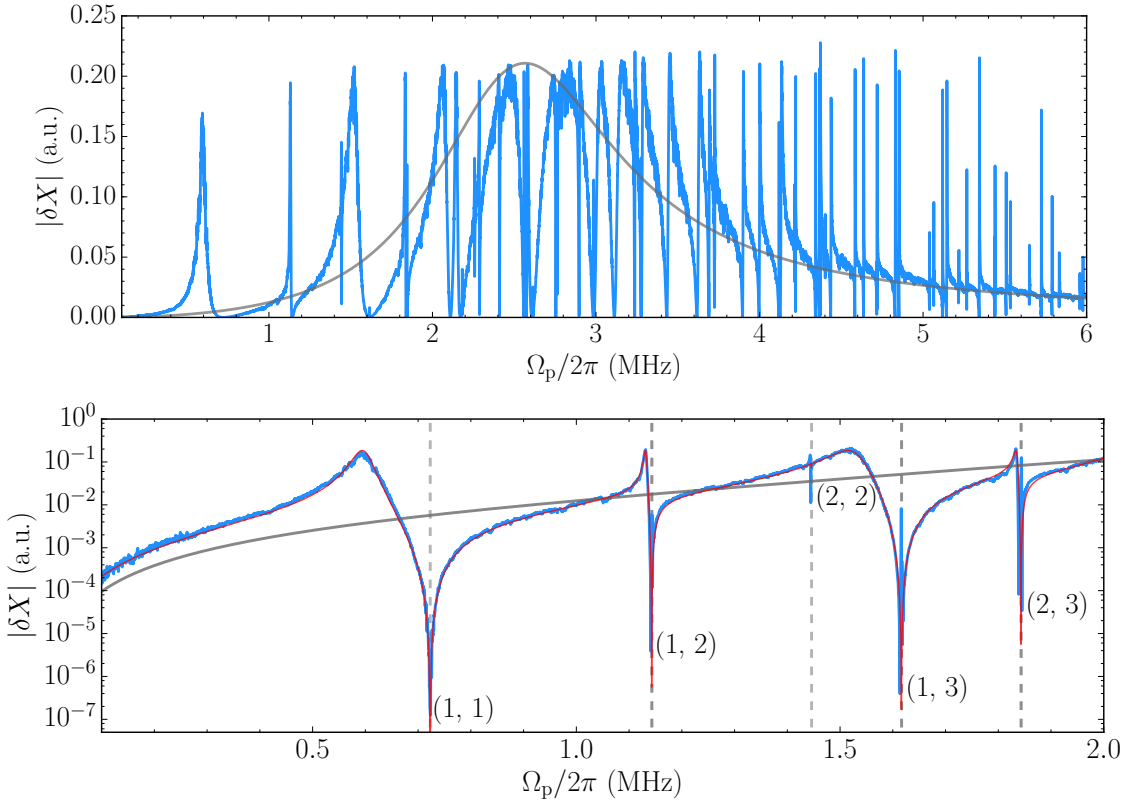

Figure 4.22: **Practical OMIT response.** In the absence of a membrane (or with zero optomechanical coupling) we have the grey line. This is the bare cavity response and clearly shows the cavity linewidth $\kappa/2\pi = 1.4\,\text{MHz}$ and is roughly centered on the cavity detuning $\bar{\Delta}/2\pi = -2.5\,\text{MHz}$. The OMIT response of the membrane in this case is significant due to a large coupling and the mechanical modes are significantly broadened. **Top:** Linear scale OMIT response in a wide bandwidth. **Bottom:** Logarithmic scale with zoom of the first few modes with the theoretical OMIT response included (red line). The dips are very deep, and thus the transparency in this window is very high.

the absence of other decoherence mechanisms (unfortunately likely not the case) this cooling would effectively bring it into the quantum ground state, with an effective occupancy of about 0.4 phonons, as it has a measured quality factor of $Q = 7.8\times10^6$. A conservative estimate of the bath temperature of $\sim 10\,\text{K}$ was used as the cryostat was operated at $4\,\text{K}$.

This OMIT technique is typically used as a way to measure optomechanical parameters in conjuction with other methods. This allows for characterization and is often a useful consistency check. It also allows for diagnostics in conditions of bad signal-to-noise as the large coherent response to the classical probe is demodulated in a narrow bandwidth.

4.4 Ponderomotive squeezing

4.4.1 Theoretical treatment

The mechanical oscillator, as we discussed in section 4.1.5, is driven by the fluctuations of the input light fields. In practice, seeing this radiation pressure induced back-action effect on the mechanical motion is challenging as it has to first overcome an often very large thermal noise component. This has only recently been demonstrated in Purdy et al. (2013a) who use a very similar optomechanical setup. It has also been demonstrated for a mechanical resonator coupled to the radiation pressure of microwaves Teufel et al. (2016) as well as the collective mechanical degree of freedom of a cold atomic gas ensemble in a cavity Murch et al. (2008).

This light induced quantum back-action force on the mechanical motion can be viewed as a heating term. Equally, however, it correlates the mechanical motion with the fluctuations of the light. We can probe this correlation by way of what is known as ponderomotive sqeezing, which we can think of in the following way.

Traditionally in the QND case of $\bar{\Delta} = 0$ only the ampltide quadrature $\delta\hat{X}$ drives the resonator and the response is imprinted as additional fluctuations in the phase quadrature $\delta\hat{Y}$. When this QBA driving force is appreciable significant correlations between the two light quadratures arise, since $\delta\hat{Y} \propto \delta\hat{X}$. Thus, if we mix these quadratures, as can be done by a detuned cavity ($\bar{\Delta} \neq 0$), interference should manifest. Observing this interference presents a straightforward way to demonstrate that the QBA on the mechanical resonator and shows that the light noise is a relevant factor in the dynamics. It can also lead to sub-poissonian statistics of the light field at particular Fourier frequencies and is, thus, also – in principle – of interest from an improved imprecision point of view.

This effect was recently demonstrated for the motional degrees of freedom of the aforementioned cold atomic ensemble in a cavity Brooks et al. (2012b). This was followed shortly thereafter for solid state optomechanical implentations by Safavi-Naeini et al. (2013) and then Purdy et al. (2013b) in a very similar setup as our own. Each time the observed squeezing was increased. Our entrance into this quantum optomechanics regime follows this trend. We recently demonstrated this ponderomotive squeezing in Nielsen et al. (2016), where the effect is quite substantial (for optomechanical standards). So, let's see how this all comes about, where we will follow the approach of Nielsen et al. (2016). More on the background of our work towards this achievement is detailed in Nielsen (2016).

Like in section 4.3 we will take the mean intracavity field as a real quantity and seek to find the output amplitude quadrature, as this is typically where this effect is detected. The logic is easily extended to detection in an arbitrary quadrature phase. In the detuned cavity case the intracavity amplitude quadrature has contributions from both input quadratures as well as some mechanical response. Once again using

the QLE of eq. (4.26) It can be written as we find

$$\delta\hat{X}(\Omega) = \Big\{ i\left[L(\Omega) - L^*(-\Omega)\right]\sqrt{\kappa}\,\delta\hat{X}^{\text{in}} - \left[L(\Omega) + L^*(-\Omega)\right]\sqrt{\kappa}\,\delta\hat{Y}^{\text{in}} \Big\} - \tag{4.107}$$

$$\frac{g}{\kappa/2}\left[L(\Omega) + L^*(-\Omega)\right]\delta\hat{Q}. \tag{4.108}$$

We know from eq. (4.29) that the mechanical position $\delta\hat{Q}$ is also driven by a light term identical to that contained in the curly brackets of eq. (4.108) above. This we can anticipate that the power spectral density will contain correlations related to the mechanical susceptibility. Using the input output equations of eq. (2.80), for the moment assuming a perfectly one-sided cavity, we find the symmetrized output power spectral density (relative to shot noise) of,

$$\frac{\bar{S}^{\text{out}}_{\text{XX}}}{\text{SN}} = 1 + 8\Gamma_{\text{meas}}\,\text{Re}\left(\chi_{\text{eff}}(\Omega)u(2u^2+2v^2-v)\right) + 16\Gamma^2_{\text{meas}}\left|\chi_{\text{eff}}\right|^2\left|u(u+v)\right|^2 + \tag{4.109}$$

$$8\Gamma_{\text{meas}}\left|\chi_{\text{eff}}\right|^2|u|\,2\gamma_m(n_{\text{bath}}+1/2). \tag{4.110}$$

where we have summarized the typically complicated cavity response factors in two parameters u and v. These parameters are not the real and imaginary components of the complex Lorentzian, but rather useful expressions defined as

$$u(\Omega) \equiv -\frac{1}{2}\left[L(\Omega) + L^*(-\Omega)\right], \tag{4.111a}$$

$$v(\Omega) \equiv \frac{i}{2}\left[L(\Omega) - L^*(-\Omega)\right]. \tag{4.111b}$$

In the unresolved sideband regime where $|\bar{\Delta}|, \Omega \ll \kappa/2$ the cavity response terms significantly simplify and allow us to approximate eq. (4.110) to

$$\frac{\bar{S}^{\text{out}}_{\text{XX}}}{\text{SN}} = 1 - \underbrace{8\left(\frac{\bar{\Delta}}{\kappa/2}\right)\Gamma_{\text{meas}}\,\text{Re}(\chi_{\text{eff}})}_{\text{correlations}} + \underbrace{16\left(\frac{\bar{\Delta}}{\kappa/2}\right)^2\Gamma_{\text{meas}}\left|\chi_{\text{eff}}\right|^2\left(\Gamma_{\text{meas}} + \gamma^{\text{th}}_{\text{dec}}\right)}_{\text{transduced motion}} \tag{4.112}$$

The first term is the shot noise term and the last represents the fraction of the transduced mechanical motion appearing in the amplitude quadrature. This is a small fraction of the total response, which is predominantly mapped into the phase quadrature. Notice how this contribution grows for larger cavity detunings, and thus quadrature rotations. This rotation term necessary as the mixing provides us with the middle term, which derives from the correlations between the amplitude and phase quadratures. This correlation term has the characteristic dispersive shape of the effective mechanical response $\text{Re}(\chi_{\text{eff}})$ which can be negative.

One can heuristically think of the correlations as originating from the mechanical response to say $\delta\hat{X}$, which is given by χ_{eff}, being then projected back onto $\delta\hat{X}$. Thus, the interference will follow the phase response of the mechanical resonator.

Below (mechanical) resonance the response is in phase and the interference is then constructive, whereas above (mechanical) resonance, the response is out of phase, and thus the interference can be destructive.

Operating the cavity in transmission (driving it through the high reflector), will produce correlations with this characteristic response of $\mathrm{Re}(\chi_{\mathrm{eff}})$. In Nielsen et al. (2016) we present a realization of an optomechanical setup with a multitude of mechanical modes all responsible for ponderomotive squeezing. Strong squeezing (by optomechanical standards) of $-2.4\,\mathrm{dB}$ is reported, which correcting for detection efficiencies would be $-3.6\,\mathrm{dB}$.

A finite detection efficiency, η, simply replaces the correlations present with uncorrelated shot noise. This loss, be it from out-coupling efficiency or detection losses, reduce the measured (meas) squeezing by

$$\frac{\bar{S}_{\mathrm{XX}}^{\mathrm{meas}}}{\mathrm{SN}} \gtrsim \eta \frac{\bar{S}_{\mathrm{XX}}^{\mathrm{out}}}{\mathrm{SN}} + (1-\eta). \tag{4.113}$$

Beyond the purely technical imperfection of detection efficiency, which in Nielsen et al. (2016) and in the work presented here, can easily be drastically improved,[1] the squeezing is limited by the ever finite thermal noise component whose fraction to the driving force of the mechanics is given by $\sim C_q$. This thermal noise limiting sets a bound given by

$$\frac{\bar{S}_{\mathrm{XX}}^{\mathrm{out}}}{\mathrm{SN}} \gtrsim 1 - \frac{\Gamma_{\mathrm{meas}}}{\Gamma_{\mathrm{meas}} + \gamma_{\mathrm{dec}}^{\mathrm{th}}} \tag{4.114}$$

$$= 1 - \frac{C_q}{C_q + 1} \approx \frac{1}{C_q}, \ \forall C_q \gg 1. \tag{4.115}$$

4.4.2 Measurements in transmission

To measure squeezing in the amplitude quadrature as just discussed we first send a probe through the cavity as shown in the left panel of fig. 4.23. The output transmitted light is then collected by a single diode in direct detection, as described in appendix B.1. This single diode is half of a differential detector where the other diode is dark for these measurements and those that follow in section 4.4.3. This complication, along with the assortment of waveplates and polarizing beam splitters (PBS) are a result of this setup being a subset of a larger setup shown in fig. 6.2 needed for the experiments discussed in chapter 6. These unnecessary optics give rise to a rather low detection efficiency, which, as we will see, limits the detected amount of squeezing. The measurements discussed here and in section 4.4.3 were measurements done as a test as to whether our optomechanical system was indeed quantum limited. Thus, the detection chain was not optimized for high efficiency, as it was built for the experiments described in chapter 6.

[1] The limiting losses are optical in both cases and could be eliminated by a simply implementing higher quality optical components and striping the detection path to the bare minimum.

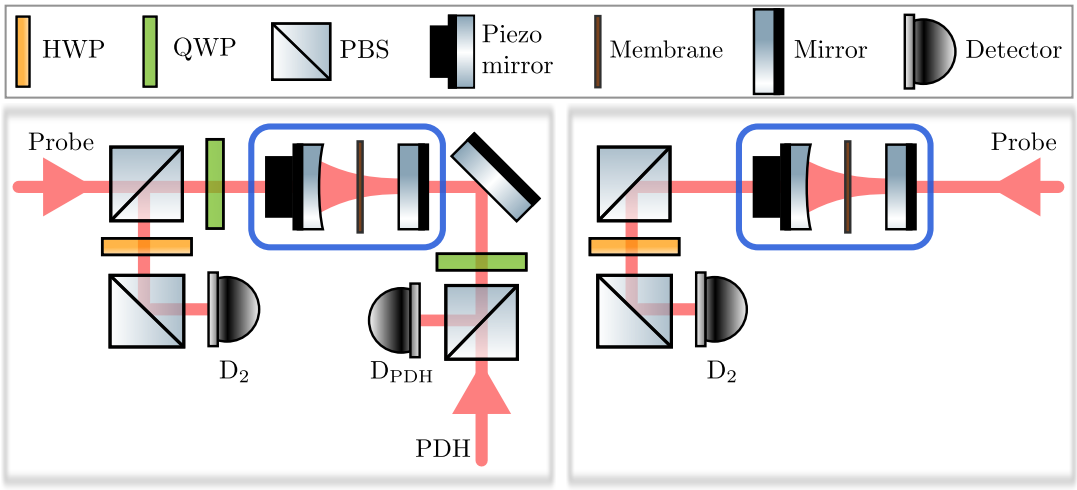

Figure 4.23: **Squeezing optical setup.** The optomechanical setup used for the measurements in transmission (**left**) and reflection (**right**) the results of which are shown in figs. 4.24 and 4.25 respectively. A legend is shown (**top**) and the optomechanical system is enclosed in a cryostat (blue square).

The power spectral density of the detected photocurrent fluctuations is then calculated. This is shown in fig. 4.24, where the detected amplitude quadrature for a cavity probed in transmission, is normalized to shot noise (of an source with equivalent power) as measured through a similar setup as that used in Nielsen et al. (2016). The details of our setup is described in more detail in section 4.2.2. In the figure two mechanical modes are shown. The lower frequency one is the (1,2), with bare $\Omega_m^{(1,2)} = 2\pi \times 1.28\,\mathrm{MHz}$, and the higher frequency one the (2,1) $\Omega_m^{(2,1)} = 2\pi \times 1.34\,\mathrm{MHz}$. Both have high quality factors with $Q = 13 \times 10^6$. They are split by a slight asymmetry in the membrane side lengths and are also asymmetrically coupled to by an intentional choice of cavity mode overlap with the spatial profile of these membrane modes.

The sharp noise peaks at the edges of the top panel of fig. 4.24 are likely empty cavity mirror noise peaks as discussed in section 4.5.7. These peaks are seen with an increasing signal to noise ratio as the imprecision is increased concomitant with the larger cooperativity. The sharp peaks seen immediately to the red of the (1,2) mode is interest as different. These appear to additionally grow in proportion to the mechanical motion. They are likely hybrid modes driven to larger amplitude as the mechanical mode is pushed into them by dynamical back-action. Such hybrid modes are discussed in section 3.10.

While these system imperfections complicate the broadband picture, the overall dynamics are largely unaffected. This is clear from the excellent agreement between the optomechanical theoretical fit and the measurements shown in the bottom left panel of fig. 4.24.

The one-sided cavity described in section 4.2.2 is operated at the $2kz_m$ point where the linewidth is $\kappa = 2\pi \times 15\,\mathrm{MHz}$, see fig. 4.14. It is driven through the high reflector (overcoupled) port and the amplitude quadrature detected is seen through

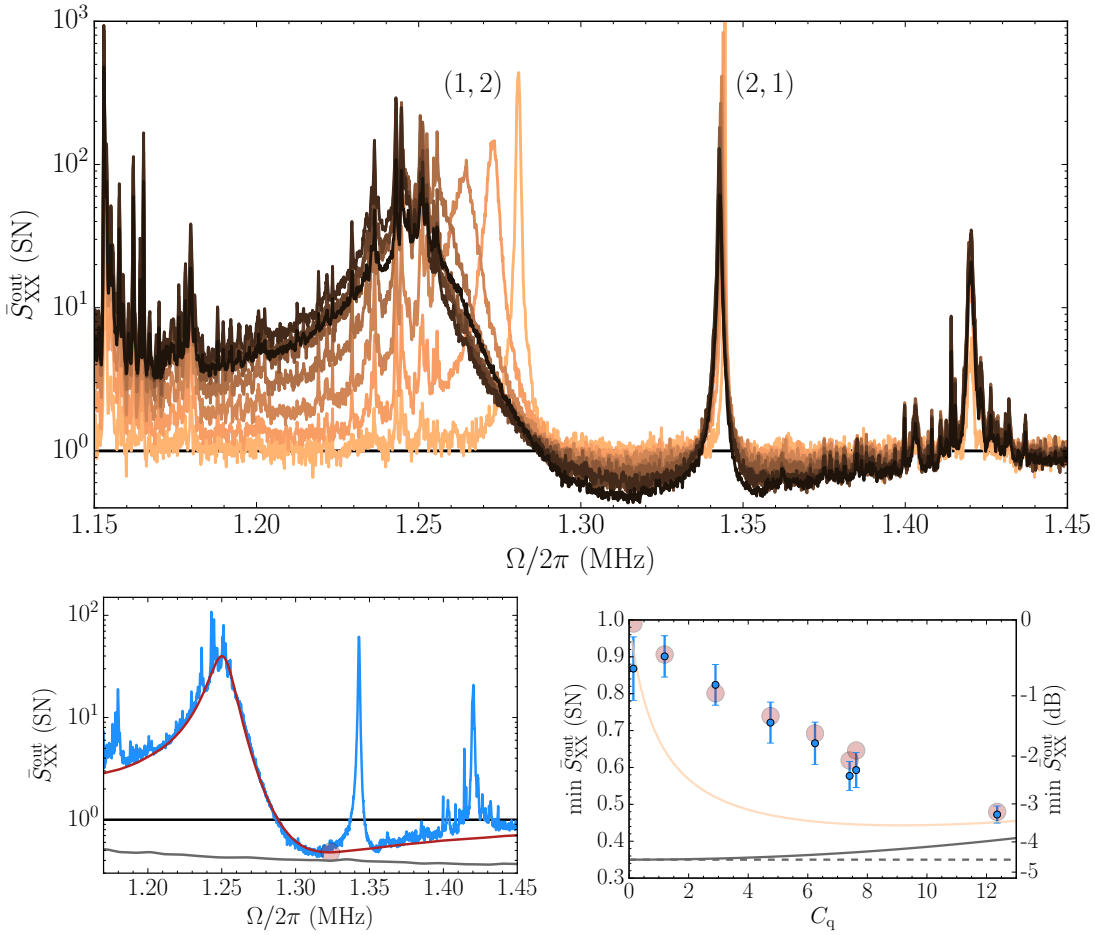

Figure 4.24: **Squeezing in transmission for (1,2) mode.** Cavity $\kappa/2\pi = 15.2\,\mathrm{MHz}$ and the detuning varies steadily from $\bar{\Delta}/2\pi = -5.5\,\mathrm{MHz} \to -1.5\,\mathrm{MHz}$ as C_q is increased. **Top:** Measured PSDs relative to SN. The broad feature is the (1,2) mode and the narrow adjacent feature is the (2,1) mode. **Bottom left:** Squeezing trace of $C_q = 12.4$. The discrepancy at higher frequency is due to the tail of the (2,2) mode and the sharp mirror modes. The maximum squeezing is of $(-3.3 \pm 0.2)\,\mathrm{dB}$ ($(53 \pm 2)\,\%$ below SN) for a $C_q = 12.4$. Correcting for detection and additional classical amplitude noise gives $-8.6\,\mathrm{dB}$ (86 % below SN). The red line is a fit from the dynamics of the QLE. The red dot is the point of minimum predicted squeezing from the model. The grey line is the noise floor set by the classical AM noise and finite detection efficiency. **Bottom right:** Measured squeezing, blue dots, corresponding to the minimum value of the trace low passed with a Hanning window of 40 adjacent frequency bins. The error corresponds to the standard deviation of the noise in a region of 30 adjacent frequency bins. This corresponds to a range of 3 kHz. The detected squeezing does not come close to the yellow bound described in eq. (4.116) for the low cooperativity traces as the detuning was far from optimal. Red transparent dots are the minimum squeezing as fitted by the model. See bottom left figure.

the overcoupled port with an efficiency of $\eta_{\text{out}} = 95.5\,\%$. Upon exiting the cavity light is converted into a photo-electron with an efficiency of 65 %.

The cooperativity is scaled by increasing the probe power thus increasing the intracavity field. The residual light not reflected by the final PBS before the balanced detector D2, see fig. 4.23, is directed onto an avalanche photodiode (not shown) and the variation of the transmitted power with the cavity Lorentzian used as an error signal. The cavity frequency is stabilized to the laser frequency on long time scales compared to the dynamics of the mechanics[2] by feedback on the cavity piezo. The lock point was set by hand and thus when the power increased the detuning changed.

As the quantum cooperativity grows we see the effects of dynamical back-action, namely an increased mechanical damping due to the increased optical broadening, as well as a frequency shift. This is clear for both the mechanical modes, although by far dominant for the highly coupled (1,2) mode of interest. If we look at a particular trace, bottom right panel of fig. 4.24, we can clearly see significant squeezing over a wide bandwidth. The (2,1) mode lies almost in the middle of this range, which is, of course, not ideal. It is, however, quite narrow compared to the squeezing feature, and its effect is minimal. The squeezing is well predicated by the QLE equations as shown by the fit, which assumes only a single mechanical (1,2) mode. At higher frequencies the agreement is worse as there are additional mirror modes littering the landscape and the tail of the inescapably highly coupled (2,2) mode. In grey we plot the de-facto squeezing floor $(1-\eta) + \bar{S}_{\text{XX}}^{\text{in,AM}}/\text{SN}$ given by the finite total detection efficiency η and additional classical amplitude noise from the laser $\bar{S}_{\text{XX}}^{\text{in,AM}}$.

Classical laser amplitude noise scales $\propto P_{\text{in}}^2$, whereas the cooperativity and the shot noise scale $\propto P_{\text{in}}$. Thus, at some finite power the classical amplitude noise of the laser will begin to dominate or at least significantly contribute to the noise of the input field $\delta\hat{X}^{\text{in}}$. This additional noise contribution is of $\bar{S}_{\text{XX}}^{\text{in,AM}}(\Omega)$ is shown in section 4.5.1 and falls off for higher frequencies.

Despite these serious limitations to the amount of squeezing attainable, a remarkable $(-3.3 \pm 0.2)\,\text{dB}$ ($(53 \pm 2)\,\%$ below SN) of sub-shot noise squeezing is measured for a $C_q = 12.4$. If one were to correct for the detection efficiency this would increase to $-8.6\,\text{dB}$ (86 % below SN). This measured squeezing is the mean over a 3 kHz bandwidth and the error simply the given by the standard deviation. Thus, the actual peak squeezing may be a bit higher, but over a smaller bandwidth.

The squeezing for the varied C_q is shown in bottom right of fig. 4.24 along with the grey line displacing the aforementioned practical limit. Additionally shown in yellow is the combined bound of eq. (4.115) and eq. (4.113) plus the amplitude noise of the probe, i.e.

$$\frac{\bar{S}_{\text{XX}}^{\text{out}}}{\text{SN}} \gtrsim \eta\left(1 - \frac{C_q}{C_q+1}\right) + (1-\eta) + \frac{\bar{S}_{\text{XX}}^{\text{in,AM}}}{\text{SN}}. \tag{4.116}$$

[2] Feedback bandwidth of $\sim 1\,\text{kHz}$.

Clearly this bound is not reached for the initially small cooperativities, but is reached as the detuning is brought closer to resonance for a larger cooperativity.

4.4.3 Measurements in reflection

Squeezing can also be observed probing in reflection, although often with higher losses due to finite cavity modematching, see section 4.1.5. The logic to solving the QLE is exactly the same. In this case the response gets an additional π phase shift from the interference with the input field, and thus the detected amplitude fluctuations have the form of $-\mathrm{Re}(\chi_{\mathrm{eff}})$.

For the measurements displayed in fig. 4.25, which we shall shortly discuss, we operate a wide cavity side of $2kz_m$ where we have a $\kappa = 2\pi \times 33\,\mathrm{MHz}$, see fig. 4.14. We keep the cavity at a fixed detuning of $\bar{\Delta} = -2\pi \times 8\,\mathrm{MHz}$, and probe in reflection by the scheme illustrated in the right panel of fig. 4.23.

Cavity stabilization

The stabilization of the cavity used in this setup is worth discussing in a little more detail as it is also used for the measurements described in chapter 6. The cavity is locked by the use of an auxiliary low power beam (labelled PDH), originating from the same laser. The intracavity fields from the probe and PDH (locking) beams are in orthogonal polarizations ensured by use of quarter waveplates on either side of the cavity. On the side of the probe field, the waveplate is adjusted such that the probe is reflected off the input PBS upon returning from the cavity. This allows the field from the cavity originating from the probe and having interacted with the optomechanical cavity to be stripped from the input and directly detected on the D_2 detector as just in section 4.4.2.

The waveplate on the PDH locking beam side of the cavity is adjusted such that the fraction of this field transmitted through the cavity is also transmitted from the PBS on the probe side, thus not being detected. The reflected fraction of the PDH field is picked off by a PBS, just as the probe was on the other side of the cavity, and detected on detector D_{PDH}.

The locking beam is referred to as "PDH" since it contains two frequency modulation sidebands at 12 MHz. These sidebands beat with the carrier and the differential phase shift these experience in reflection off the cavity is used to generate an error signal. This is done by mixing the detected photocurrent with a tone at the sideband frequency and low passing the output. This is known as the Pound-Drever-Hall (PDH) technique and is further described in Black (2001). The error signal derived is used to stabilize the cavity to the laser by feedback on the cavity piezo with a feedback bandwidth of $\sim 1\,\mathrm{kHz}$.

The PDH beam is blue shifted from the probe by use of an acousto-optic modulator. If the cavity is stabilized so as to be on resonance with the PDH beam, then the probe will address the cavity red detuned by their frequency difference. This is

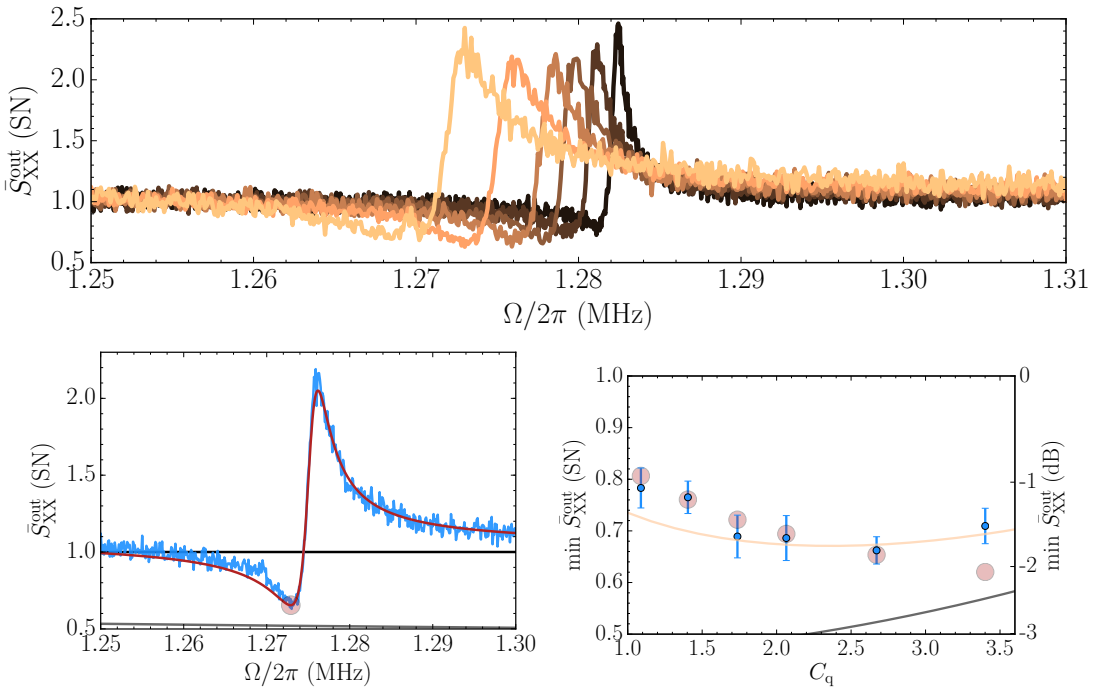

Figure 4.25: **Squeezing in reflection for (1,2) mode.** Cavity $\kappa/2\pi = 33\,\text{MHz}$ and a fixed detuning of $\bar{\Delta}/2\pi = -8\,\text{MHz}$ as C_q is increased. **Top:** Measured PSDs relative to SN. **Bottom left:** Squeezing trace of $C_q = 2.7$. The discrepancy near maximum squeezing is due to a mirror mode. The maximum squeezing is of $(-1.8 \pm 0.2)\,\text{dB}$ ($(34 \pm 3)\,\%$ below SN) for a $C_q = 2.7$. Correcting for detection and additional classical amplitude noise gives $-4.4\,\text{dB}$ (64 % below SN). The red line is a fit from the dynamics of the QLE. The red dot is the point of minimum predicted squeezing from the model. The grey line is the noise floor set by the classical AM noise and finite detection efficiency. **Bottom right:** Measured squeezing, blue dots, corresponding to the minimum value of the trace low passed with a Hanning window of 10 adjacent frequency bins. The error corresponds the standard deviation of the noise in a region of 15 adjacent frequency bins. This corresponds to a range of 1.5 kHz. The detected squeezing is quite close to the yellow bound described in eq. (4.116) as the cavity was not too far detuned. Red transparent dots are the mininum squeezing as fitted by the model. See bottom left figure.

used to controllably set and change the cavity detuning Δ with respect to the probe field.

This PDH beam couples to the cavity through the undercoupled port 2 with a low power. The contribution this field has to the intracavity power is always kept to $< 1\,\%$ of the probe. This locking beam thus has a negligible impact on the intracavity dynamics and, due to polarization filtering, the final detection.

Measurements

A series of measurements where the probe input power is varied is shown in fig. 4.25, where the observed squeezing is quite large. It does reach the same level as that shown in fig. 4.24 since the cavity now has twice as big linewidth without a much

different single photon coupling rate. This is seen in fig. 4.17 where the relevant g_0^2/κ interaction strength is smaller on the wide cavity side of $2kz_m$. Thus, the input power required to reach the same C_q is higher. This means that the amplitude noise begins to be limiting that much faster. All the curves shown in fig. 4.25 have the same meaning as is fig. 4.24.

In all of these traces the thermal noise contribution was assumed to be that of a bath with a constant temperature of 7 K as is constistent with what was measured in section 4.5.5. It is plausible that the membrane temperature would increase with an increased intracavity power, but this has unfortunately not yet been studied in detail.

4.5 Practical considerations

Of practical importance for design and operation are the basic optomechanical parameters of g, κ, $\gamma_{\mathrm{dec}}^{\mathrm{th}}$ and Ω_m, as well as tangential system properties which affect these. These are all important as they impact the light-matter interaction of interest. Also important are the underdesired modes of the cavity mirrors themselves as well as the classical noise properties of the interacting light fields.

Here we will discuss these parameters and practical considerations and techniques that are relevant for our particular implementation of a membrane-in-the-middle system.

4.5.1 Classical laser noise

In reality laser systems typically do not produce perfect vacuum states at their outputs. This means that the fluctuations in the optical quadratures that drive the mechanics are not shot noise by default. The laser we use for our probe of the optomechanical (and hybrid) system is a Ti:sapphire laser system from Msquared. We are concerned with any frequency (phase) noise or amplitude noise as they will both constitute a classical drive of the mechanics. The amplitude noise directly through an increased S_{XX}^{in} and the latter through increased S_{YY}^{in} which, in a detuned cavity, is converted into amplitude fluctuations which drive the mechanics.

Our cavity is not phase sensitive enough to convert any laser phase noise into appreciable amplitude noise at the frequencies of the mechanics. The amplitude noise on the other hand is a concern and our laser system has ample of it at a few 100 kHz. This noise is caused by the relaxation oscillations of the intracavity field of the laser. As this intracavity field is perturbed from steady state, by say noise of the pump, it oscillates as it returns to equilibrium. Both the oscillation frequency and damping rate depend on the intracavity power and are are seen experimentally in fig. 4.26.

First note that the classical amplitude noise scales quadratically with power whereas the optical shot noise scales linearly. Thus, the absolute optical probe

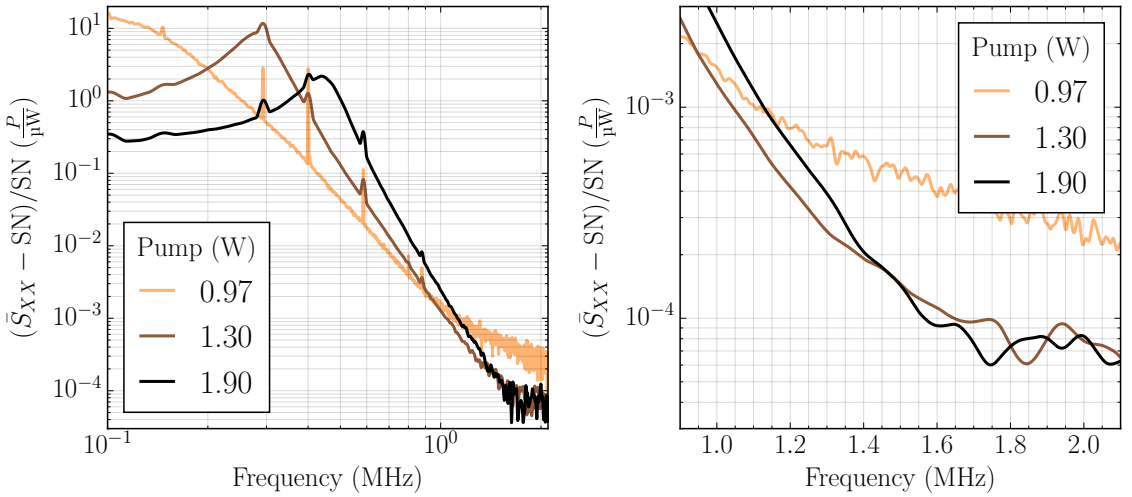

Figure 4.26: **Amplitude noise of Ti:Sapph probe laser.** A power spectral density of the Ti:Sapph probe lasers amplitude noise. The shown is the classical contribution added on top of optical shot noise relative to a particular optical power and for a given power pumping the laser (legends). This pump power is directly related to the intracavity laser power. **Left:** log-log scale. **Right:** Zoom of noise in the region 900 kHz to 2.1 MHz. **Both:** the abrupt change of scaling at higher frequencies is due to measurement noise rather than a changing noise response.

power used is important. Consider the case of the laser cavity pumped by with a power of 1.9 W resulting in some laser intracavity power. For the continuous wave light emanating from the laser this results in an added classical amplitude noise equivalent to 1.0 unit of shot noise at a Fourier frequency of 1.0 MHz with a probe power of 400 µW. Thus, at this frequency the amplitude quadrature noise will be 1 unit of shot noise plus 1 unit of classical noise. This noise falls off fast and already at 1.3 MHz, where our membrane mode sits, there is already ≈ 6 times less amplitude noise. This added noise drives the mechanics and limits quantum behavior such as the ponderomotive squeezing discussed in section 4.4.

4.5.2 Coupling rate

The linearized coupling rate $g = g_0\sqrt{\bar{n}}$ can be tuned by the optical or mechanical properties. The single photon coupling rate g_0 depends on the $2kz_m$ modulation discussed in section 4.2.4 and tuning to an optimal point can be done by changing the probing wavelength or the membrane position with respect to the flat mirror.

The spatial position of the membrane with respect to the cavity mode is also important as the cavity mode samples the displacement of the membrane. Probing at an anti-node is therefore desirable and is in practice aligned such that this is the case. This is done by imaging the plane of the membrane and moving the concave mirror so as to localize the cavity mode as the desired location. This, along with the penalty associated with a mismatch, is described in Nielsen (2016). This mismatch is often made worse by more extended, higher order, cavity modes. Thus working

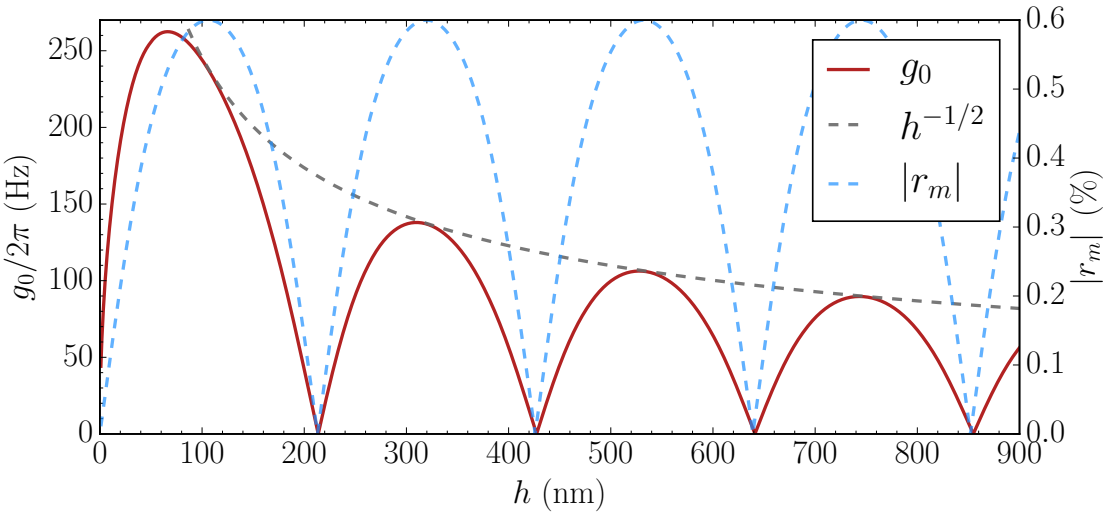

Figure 4.27: **Single photon coupling rate with membrane thickness.** As the membrane thickness is varied, the absolute value of the membrane amplitude reflectivity is shown in blue, while the single photon coupling rate is shown in red. The envelope of the coupling rate decays due to the $h^{-1/2}$ scaling of the zero point fluctuations due to the mass dependence on thickness. This assumes a 1.3 MHz mode on a 500 × 500 µm wide SiN membrane probed at 852 nm.

with the TEM_{00} mode is desirable and also what is done throughout this work.

The coupling also depends on mechanical parameters such as the reflectivity, as well as the zero point motion. The membrane reflectivity is periodic in the thickness h whereas the zero point motion falls of as $\propto h^{-1/2}$. This is shown in fig. 4.27 where the optimum g_0 lies at $h = 65\,\mathrm{nm}$ (the highest reflectivity is at $h = \lambda/8 = 106.5\,\mathrm{nm}$).

Clearly if the amplitude reflectivity was larger for thinner membranes a higher coupling could be achieved. Using a much shorter wavelength of light is not an option as the SiN membranes have larger absorption at shorter wavelengths. This would limit the cavity finesse. One could also envision coating the membrane with a more reflective layer. This, however, also introduce absorption as the coating material is unlikely to be as transparent as SiN and would impact the mechanical quality factor Q.

One can also imagine making a photonic pattern on the membrane in an effort to boost the reflectivity. This photonic pattern would cover the region on the membrane where light probes the mechanics. High reflectivities, of $\sim 99.95\,\%$, have been realized with such an approach has been realized by Chen et al. (2017). In practice however, fabrication imperfections result in losses still too high for practical application in our experiments discussed in this work. The losses limit the degree of cavity overcoupling and by extension the achievable cavity linewidth finesse.

4.5.3 Cavity length

The cavity length L impacts both $g_0 \propto 1/L$, $\kappa \propto 1/L$ and for a fixed input power the intracavity photon number $\bar{n} \propto L$. Suppose we keep a fixed relative detuning from

cavity resonance and fix the relative location of the membrane within the cavity. The quantity $g_0^2\bar{n}/\kappa$ is then independent of the cavity length, which means that the bistability onset described in eq. (4.15) is unchanged, and determined by Ω_m. This is a handy feature since it means that if other experimental parameters are otherwise fixed, then making the cavity longer can offer an increased or decreased sideband resolution. If a shorter or longer cavity is desired this can be done until some disadvantageous effect does too much harm.

For shorter cavities the membrane will also be closer to a surface. This will increase squeezing film damping which eventually will limit the membrane Q, see section 3.9. A very short cavity will also lead to an ever smaller cavity waist, see appendix D.3. This will lead to an increase in background noise associated with the cavity mirrors. Many of these loss noise mechanisms scale non-linearly with the cavity waist, see section 4.5.7.

For longer cavities one has to watch out for the cavity mode mostly. If it gets too large at the membrane you can have a reduced $g0$ due to a poor mode overlap[1]. A bigger waist can also lead to beam clipping or diffraction at the edges of the membrane which would increase cavity losses. For a very long cavity the beam spot on the mirrors may also be of concern. In the plano-concave cavity the beam spot on the plano mirror will be small and the aforementioned concern of mirror noise should be considered. Also, the beam spot on the curved mirror may become very large in this regime. This can lead to increased cavity losses as HR cavity mirrors are typically not clear of defects over the entire surface. Having a clear aperature is more likely for smaller areas. To see how the cavity waists scale in the short or long cavity limits, see appendix D.3.

4.5.4 Quality factor

Improving Q is an ongoing challenge for all groups striving to work in the regime of quantum optomechanics. The limitations for the currently used SiN membranes are discussed in sections 3.7 and 3.9. The new generation of membranes Tsaturyan et al. (2017) have the Q not only scaling $\propto h^{-1}$ but also $\propto \Omega_m^{-2}$ (Higher Q for larger membranes). Thus, the trade-off needed to be balance is between whether one wishes the higher coherence times at the expence of lower coupling rates and/or SB resolution.

Let us first consider the case of scaling the membrane size, and thus the frequency. Assuming a 2D membrane with a characteristic size L, then the quantum cooperativity will scale as $C_q \propto L \propto \Omega_m^{-1}$ with the new patterned membranes. Thus, operating with lower frequency membranes is advantageous from the point of view of the quantum cooperativity, all else being equal.

[1]Essentially sampling not just at an anti–node of displacement, but some broader region with smaller or even opposite displacement.

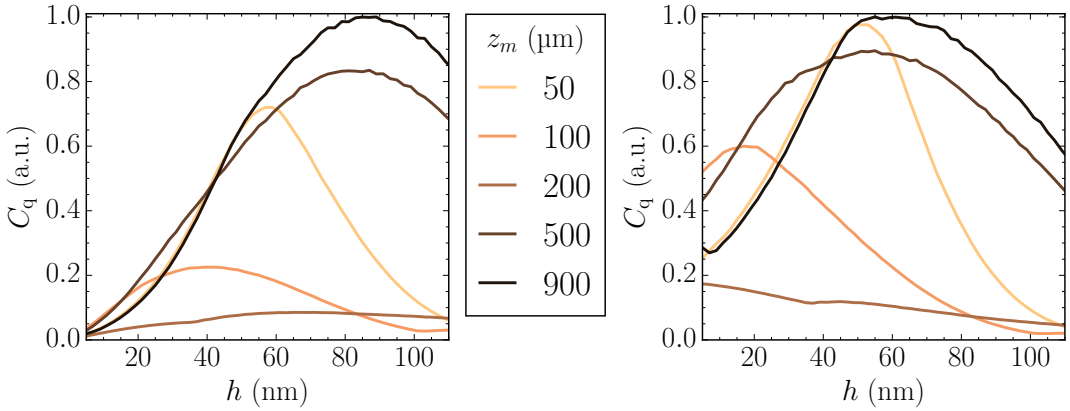

Figure 4.28: ***C_q* for scaling with membrane thickness.** Maximum achievable quantum cooperativity in $2kz_m$ for various global membrane positions z_m in a 1 mm long one-sided cavity probed on resonance with a fixed input power. The mirrors have transmissions of 20 ppm and SI1400ppm and there is no added loss. Legend is common and the cavity linewidth is numerically calculated with the model described in eq. (4.88). **Left:** For the membranes used in this work the cooperativity scales according to $C_q \propto (g^2/\kappa)$, i.e. the mechanical damping does not scale with thickness. This is due to surface effects as explained in Villanueva and Schmid (2014). **Right:** Future patterned membranes, see Tsaturyan et al. (2017), have a thickness dependent damping scaling as $Q \propto h^{-1}$. Thus the cooperativity scales as $C_q \propto (g^2/\kappa)/h$.

For the thickness scaling the quantum cooperativity scaling is slightly more tricky as it will depend on the non-trivial modulation of the cavity linewidth κ and the period nature of the membrane reflectivity r_m, how they interact together, and the placement of the membrane within the larger cavity, z_m. By considering these effects, for a fixed input power on cavity resonance ($\bar{n} \propto 1/\kappa$), we can see from fig. 4.28 that there are two decent strategies, both for the new generation of membranes and for the old.

Either one positions the membrane such that there is little $2kz_m$ modulation of κ and a high $g0$, which in this overcoupled case means very close to the high reflector. Here the choice of membrane thickness (due to r_m) is quite limited. Alternatively one can position the membrane at the point of large κ modulation in which can the scaling of C_q with thickness is much broader and indeed optimized for thicknesses of maximum reflectivity.

Of course, the quantum cooperativity is not always the sole quantity of interest. In practice, for the new membrane for instance, one may also wish to trade off a higher C_q for a thinner membrane. An example of such a case would be if the absolute dynamical broadening required was restricted by another spectral feature or experimental timescale.

Making the membrane modes of interest higher Q may result in other modes which are not of interest also being higher Q. This may present a problem if they additionally have a low mass (due to a thinner membrane) and a large displacement. If not addressed, these high Q modes may have very large displacements making

locking difficult, can produce harmonics at undesirable frequencies and if they have too large amplitudes may even mix with the modes of interest. One can imagine a large amplitude mode whose displacement causes a stress modulation which couples to the mode of interest.

Additionally, making membranes thinner increases the thermal impedance and sets a higher steady state temperature in the case of a thermal load from the probing beam. This is expected to be an issue for the new membranes were the membranes are not only thin but very extended compared to the previous generation.

4.5.5 Bath temperature

Reducing the temperature of the thermal bath, all else being equal, is always favourable for the experiments of this work. This simply reduces the thermal occupancy driving the membrane, and thus the thermal decoherence rate.

Liquid helium flow cryostat

In practice, the membranes are cooled to liquid helium temperatures in a continuous flow cryostat. Liquid helium from a refillable dewar is brought through the cryostat coldfinger, to which our optomechanical assembly is attached, before being let out through an exhaust. The speed of the flow has previously proved to be a limitation to the achievable temperature, Nielsen (2016), since higher flow comes with additionally induced vibrations. This is a product of both cryostat design and operation, as well the specific design of the optomechanical setup.

A pressure differential between the dewar and the outside world is necessary for flow. For the experiments reported in this work the cryostat used was operated in so called "push mode". This means that instead of relying on a pump to create a low pressure at the cryostat exhaust ("pull mode"), an over-pressure is created inside the dewar leaving the cryostat exhaust at atmospheric pressure. This removes the need for a noisy pump and provides a smoother flow. It also allows the dewars to be easily left overnight in a low flow configuration. This ensures that the operating point in $2kz_m$ remains constant from day to day over the duration of an experimental run (typically about 8 days).

Drift from cryogenic cycles

In practice the optomechanical system is seen to drift between cryogenic cycles in such a way that the distance between the membrane and the flat mirror changes. This shifts the $2kz_m$ map and we can thus in practice move this map to suit an absolute wavelength of choice by deliberately going through temperature cycles. This is done by successively heating and cooling the cavity by roughly 100 K. The resulting drift is always observed to be in the same direction thus allowing for fine

control[2] over the membrane position in the cavity and thus the $2kz_m$ map.

While for purely optomechanical experiments, like that of section 4.4, the precise operating wavelength is of little importance. Once a $2kz_m$ map has been measured, such as fig. 4.14, the desirable point in $2kz_m$ can be chosen at will by choice of wavelength. In this case the $2kz_m$ drift associated with temperature cycles is a minor inconvenience. However, the point in $2kz_m$ a particular absolute wavelength samples is important in chapter 6. In that case a static $2kz_m$ map is undesirable.

Thermalization

Although the liquid helium used can bring the cryostat cold finger to 4.4 K, the thermal bath which the mechanical oscillator sees does not reach this in practice. It has not yet been studied thoroughly but the achievable temperature is presumably limited by residual heating either by absorbed or scattered probe light, or a hot immediate environment due black body radiation heating from the cryostat surround materials which the membrane is in contact with, such as the flat mirror.

We can infer the mechanical bath temperature by noting that a spectrum of $\bar{S}_{XX} \propto \bar{S}_{QQ} \propto T_{\text{bath}}$. Probing and locking the optomechanical system in transmission just as described in section 4.3.2, and by appropriately calibrating a detected spectrum of $\bar{S}_{XX}$, we infer the mechanical bath temperature as the cryostat temperature is varied. The details of this method are described in Nielsen (2016) and make use of a standard technique in which the the observed motional variance is calibrated to a known frequency modulation as described in Gorodetksy et al. (2010).

At each set cryostat temperature the mechanical Q is measured and a $2kz_m$ map is made. Adjusting the wavelength if necessary the same narrow linewidth point of $2kz_m$ is used. The optomechanical system is then probed at various detunings where the optical broadening always dominates the intrinsic linewidth. An example of such a series is seen in the left panel of fig. 4.29.

At each detuning an optical broadening is fitted and, an from a spectral integral, a variance proportional to the mechanical mode temperature calculated. The interaction strengths are kept weak so that there is negligible back-action heating from the probe, i.e. $C_q \ll 1$. Using the fitted optical broadening to correct for the cooling done by dynamical back-action we can compare the measured mode variances at the different cryostat temperatures, averaging each over many detunings. This is done for three modes of the membrane used throughout this work and the resultant inferred bath temperature seen for each is shown in the right panel of fig. 4.29. All modes are assumed to be thermalized at 28 K and begin to deviate from the cryostat temperature at about 12 K eventually thermalizing to (8.5 ± 1.0) K when the cryostat is operated at the base temperature of 4.4 K.

An increase in the cryostat radiation shield surface area (leaving a small hole for the probe input and output fields) was observed to have a small (if any) impact on

[2] Although a quite laborious task!

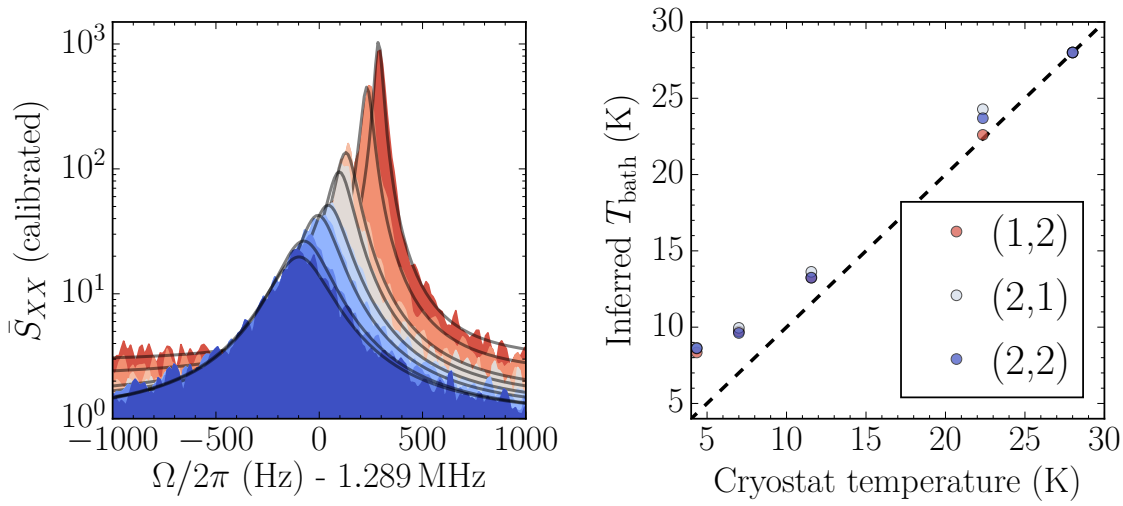

Figure 4.29: **Membrane thermalization as a function of cryostat temperature.** The inferred temperature of the mechanical thermal bath is found for various cryostat operating temperatures. At each set temperature, calibrated spectra from a detuning series are used to inferred the membrane bath temperature up to a proportionality constant. **Left:** Example of a detuning series for the (1,2) mode at 4.4 K cryostat temperature. From near cavity resonance we increase the red detuning, and subsequent sideband cooling, is coloured from red to blue. **Right:** Referencing all measurements of inferred bath temperature to those at 28 K shows a linear dependence with respect to the cryostat temperature at high temperatures and deviation at lower temperatures. This is particular true for the (1,2) mode, which features the cleanest measurements at all temperatures.

the achieved thermalization. In subsequent assemblies used for results of section 4.4 and chapter 6 the bath temperature for the (1,2) mode was found to be closer to (7.0 ± 0.5) K when operating at a cryostat temperature of 4.4 K. This was inferred from the observed ponderomotive squeezing seen in section 4.4, as well as fig. 6.11, knowing the remaining relevant system parameters from independent measurements. These thermalizations are consistent with those observed in the aforementioned scaling of the cryostat temperature. This suggests that our optomechanical system can be significantly improved if the source of this added heating can be removed (all else being equal).

Similar thermalization was observed in the closely related system used for the results discussed in section 4.3. This is further discussed in Nielsen (2016). Not thermalizing to the cryostat temperature is a limitation experienced by many experiment groups, particularly as the temperature is further decreased as in a dilution refrigerator. Examples of such insufficient thermalization for SiN membranes have been reported in both optical and microwave systems, see Fischer et al. (2016) and Yuan et al. (2015), respectively.

4.5.6 Membrane loss

Any tilt between the membrane and cavity mode leads to added loss. In practice this is avoided by aligning the membrane to the flat mirror of the cavity. This is done by the supporting Silicon structure either being in direct contact or indirect through a spacer akin to the full membrane device, but without the actual membrane itself. Our setup features no degree of freedom which may toggle this tilt. Thus acheiving a low tilt loss in practice necessitates multiple assemblies as well as very clean mirrors and membrane devices.

The membranes have very low absorption and we have been able to reach finesses of 150 k implying a total absorption bounded at the ppm level as our mirrors have known transmissions of 20 ppm. The membranes used in this work are bounded by an opaque Silicon support structure. This may clip the probing cavity mode leads to loss. In practice this is a negligible effect as may be seen in appendix D.2.2.

Any added loss from the membrane complicates the $2kz_m$ picture as it needs to be accounted for in the transfer matrix model described in section 4.2.4. The effects are interesting but undesirable for our purpose. Thus they are not studied as we routinely realize setups with negligible added loss.

4.5.7 Mirror Noise

A multitude of mechanisms give rise to loss and thus fluctuations of the cavity mirrors. The most relevant are discussed and described in DeSalvo (2012). Here we will only briefly address the currently dominant source of added noise in our optomechanical system, namely substrate Brownian noise.

Substrate Brownian noise

Mirrors themselves have eigenmodes, which cause a displacement and modulate the cavity frequency just like the membrane. These modes behave with the canonical end-mirror coupling of optomechanics, but have a very high mass which makes the coupling to them quite weak. This also means that they are not affected by dynamical back-action, and thus are not significantly cooled by a detuned cavity field. Thus, despite their low coupling, the relatively large thermal occupancy (especially at room temperature) means that they still modulate the cavity significantly on the scale of the mechanical zero-point motion. This is the imprecision level of interest and excursions on this order will introduce additional decoherence, mediated by the light field, of the mechanical oscillator.

We do not see the bare eigenmodes of the substrate mirrors unfortunately. The mirrors hybridize with our support structure, see section 4.2.2, significantly increasing the density of modes and rendering an effectively narrow spectral region of practical interest. This region can be clearly seen in fig. 4.30.

We have made many assemblies with different springs. With stiff copper springs featuring a low contact area to the mirror we measure higher mirror Qs reaching

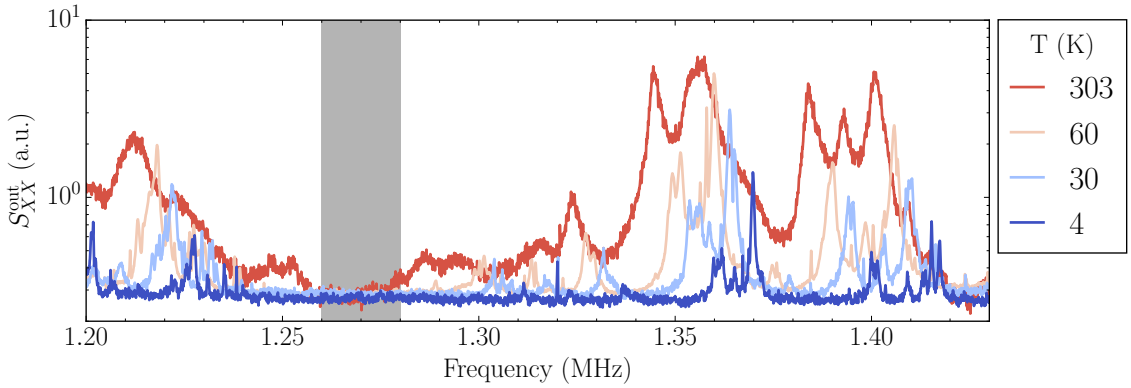

Figure 4.30: **Empty noise as a function of temperature.** The peaks seen are modes of the mirror and possible hybridized with the entire support structure. Modes are low Q at RT, but get better at cryogenic temperatures reaching as high as ~ 2000. Traces are normalized to a known frequency modulation tone, and thus can be compared on an absolute scale. The shaded region indicates a region of 10 kHz around 1.27 MHz. This is a $\sim 2\gamma_M$ region around the mechanics for the experiments of section 6.4.

as high as $Q \sim 10^4$. O-rings, however, proved the most stable under the cryogenic flow conditions experienced in our present hybrid setup. These O-rings have a relatively large contact area when compressed and are soft thus still providing a large impedance mismatch between it and the mirror. These O-rings have quite low quality factors, but still allow the mirror modes to have $Q \sim 10^3$ at cryogenic temperatures.

In our assembly one mirror is not in contact with a spring but is instead glued to a piezo-electric transducer, reducing its Q considerably. There is also significant hybridization between piezo and mirror. Efforts are ongoing to design an assembly that creates a large acoustic impedance mismatch between the piezo and mirror. This will reduce hybridization and produce a less dense mode spectrum.

Having the membrane spacer clamp the mirror also produces significant hybridization of the mirror modes with the larger Silicon chip. Engineering a solution to this requires adding a new degree of freedom to adjust the tilt of the membrane with respect to the flat mirror, or designing the decoupling such that the tilt alignment is preserved (and is stable upon cryogenic cooling).

Direct approach

Predicting the empty cavity mode spectrum is difficult as due to the hybridization between the elements of the structure. An approach to this end is known as the direct application of the fluctuation dissipation theory as described by Levin (1998).

In practice we can model our structure in a finite element model. We wish to see the noise a cavity mode sees on the surface of a mirror. Thus we apply a force with a spatial profile of the cavity mode. The force is modulated and the frequency f swept. The power admitted into the system is dissipated, W_{diss}, and by the fluctuation dissipation theorem this is related to the scale of the fluctuations

seen by the probe by

$$S_{xx}(f) = \frac{2k_B T W_{\text{diss}}}{\pi^2 f^2}. \tag{4.117}$$

This Brownian noise depends on the temperature T of the structure as well as the loss angle (Q^{-1}) indirectly through the magnitude of the dissipated power.

FEM simulations[3] of our structures are use and predict the qualitative features of our complicated setup. However, the important details of exactly where hybrid modes appear is still not understood and requires more work and experimental realizations to pin down.

[3]We use COMSOL. In particular the outward mechanical energy feature of the solid mechanics module.

Chapter 5

Atomic spins

For the quantum back-action evasion protocol described in chapter 6 we desire a negative mass harmonic oscillator. In this chapter we will show that such a system can be realized by appropriately preparing an ensemble of cesium-133 atoms.

This particular isotope is (still) used to define the second and is very well studied, in particular here in Eugene Polzik's labs. It is an alkali with only a single electron in the outer most shell, making its (comparatively) simple dynamics particularly well suited for quantum optics experiments.

They are also commercially available, and locally present, laser sources to address relevant transitions. These light sources will serve both to create the required spin oscillator from the ensemble of atoms, and to subsequently read out its motion.

We will first describe the basic structure of cesium and then consider the effect of an externally applied magnetic field. We will introduce a basic model useful in deriving the light-matter interaction. After including a magnetic field to this interaction we will see under which conditions we can create the required effective negative mass harmonic oscillator.

Then, a more general interaction Hamiltonian will be discussed, shedding light on a few important interactions not captured by the basic model originally introduced. Then various experimental realities, and sources of loss for the effective harmonic oscillator will be discussed. Before we dive into all this, let us first briefly introduce our physical platform in more detail.

5.1 Spin ensemble

We make use of a large ensemble of $N \sim 10^9$ atoms confined in a vapour cell like the one shown in fig. 5.1. Such cells are made locally by Mikhail Balabas[1]. Each atom k have their own spin vector $\boldsymbol{j}_k$, which we align to an externally applied magnetic field around which they collectively precess.

[1] Associate Professor at Saint-Petersburg State University.

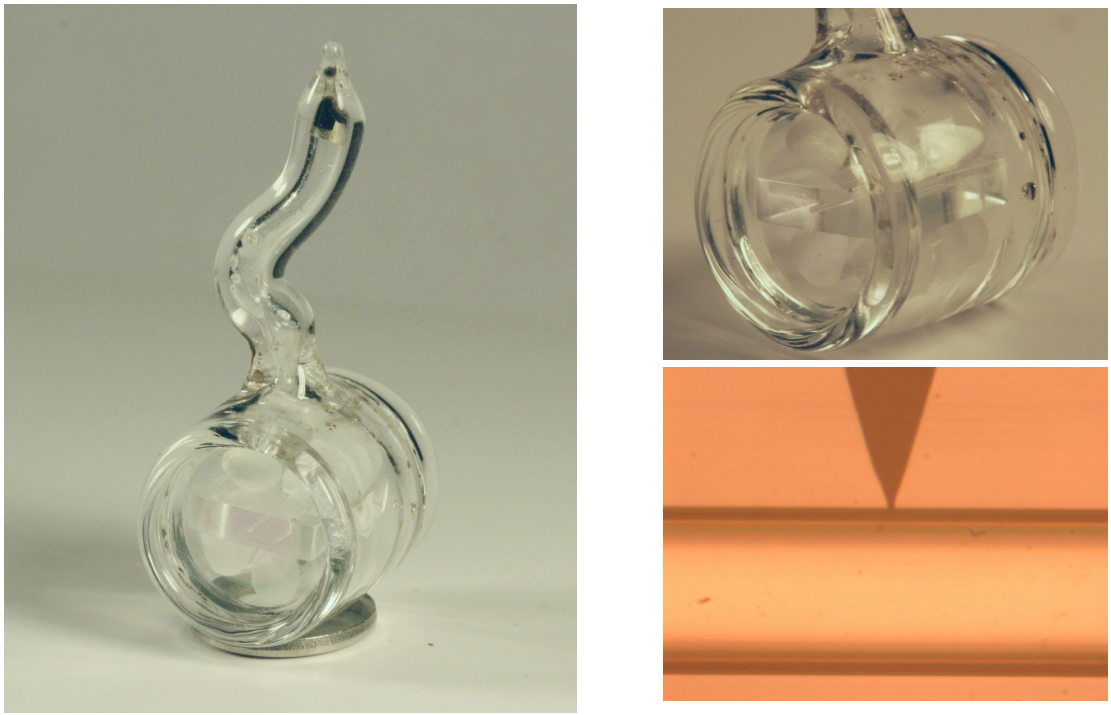

Figure 5.1: **Atomic vapour cell.** Glass cell used to encapsulate a cesium vapour. **Left:** Full view of the vapour cell standing on large washer. The curvy stem houses a liquid (black) drop of cesium at the top. This is the source of the vapour which fills the inside of the glass cell. In the main (large cylindrical) chamber sits a microchip. This is the small rectangular box in the middle. **Top right:** This microchip is more easily seen in this zoom. Right in the middle of the chip is a square 300µm × 300µm × 10mm channel leading straight through the chip to the other side. The entrances to this microchannel are sealed by the glass windows of the big cylindrical cell. Thus, the atoms have no way of entering (or leaving) the channel but through a small hole leading through the chip into the channel. **Bottom right:** This hole is seen in profile here. At the bottom is the channel and at the top is a hole tapering down to a small opening of about 30 µm. This hole provides a connection between the cesium droplette and the microchannel.

Since the atoms are sensitive to magnetic fields we seek to shield them from extraneous sources not under our control. This is done by housing the vapour cell in a cylindrically symmetric four layer magnetic shielding, protecting the spins from ambient magnetic fields and external RF sources. An inner system of coils produces a homogeneous bias field, B_x, in the x direction. This is used to control the precession frequency known as the Larmor frequency. This setup is shown in fig. 5.2.

Adding up the individual spins from N_a atoms we can motivate a collective total ensemble spin as

$$\boldsymbol{J} = \sum_{k=1}^{N_a} \boldsymbol{j}_k. \tag{5.1}$$

It turns out that the dynamics of a single spin, which will be described in section 5.5, largely translates to that of the ensemble. Thus, we use the notation of upper case J. There are however a few corrections, and a more full treatment is given in Julsgaard

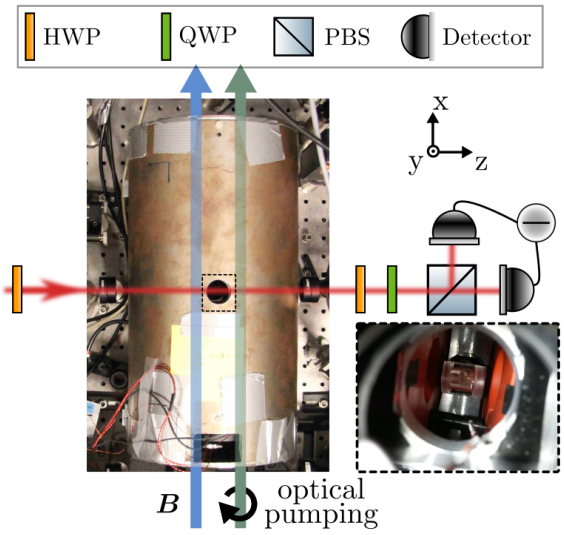

Figure 5.2: **Atomic experimental layout.** A linearly polarized (along x) field propagates along z through the cell seen through the hole indicated by the black dashed square. This cell is the one in fig. 5.1 but viewed from above. It is placed within a cylindrical magnetic shield (the major object in the image). The polarization quadratures of the output light are detected using balanced polarimetry, as described in appendix B.3, by the detector shown to the right. The cell is optically pumped (green arrow) along the x direction, as described in section 5.10.6, and is subject to a constant magnetic field $\boldsymbol{B}$ (blue arrow) along the x direction. Both these fields prepare the atoms in the cell as an effective harmonic oscillator.

(2003). For example, we will not optically probe the entire microchannel of the cell, nor will the strength of the probe be of equal intensity everywhere. We thus define an effective ensemble spin as

$$\hat{J}_i(t) = \int_0^L \hat{j}_i(z,t)\rho(z)A(z)\,\mathrm{d}z,\ \ i \in \{x,y,z\}\,, \tag{5.2}$$

where the $\hat{J}_i$ are the collective spin spatial components. We have assumed that we probe along the z direction and that since we have so many atoms we can treat their number density $\rho(z)$ throughout the channel (of length L) as a smooth function. The volume sampled is determined by the optical probing cross-sectional area $A(z)$.

This optical field is a free space Gaussian mode, as described in appendix D.1, with a focus at the center of the channel. Such a probe will clearly not address all atoms equally. However, in practice we will consider dynamics on a time scale long compared to the thermal transit time within this volume. This averages the interaction with each atom allowing us to treat them all equally, and is further discussed in section 5.11.2. The atomic motion may be readout through the polarization quadratures of this optical probe field and detected as shown in fig. 5.2.

Notice that if all the individual spins align this means that our total spin, from eq. (5.1), is boosted $\propto N_a$. As we will see in eq. (5.38) it turns out that this boosts our effective atom-light interaction strength, which is partly why a great number of atoms addressed collectively is of such high interest!

Probing this ensemble collectively we may further realize an oscillator with an effective negative mass, as shown in section 5.10.1, a crucial asset in the back-action evasion scheme detailed in chapter 6. Let us now develop a more detailed description of the cesium ensemble.

5.2 Basic cesium structure

The element cesium was first discovered via its emission spectrum, which features two strong blue lines giving the element its name[1]. In the near-infrared there are two vastly brighter (although not visible) lines in the near-infrared at 894.6 nm and 852.3 nm. These are the so-called D1 and D2 lines. This work makes use of both of these and to see what transitions these correspond to we must take a more detailed look at the atomic structure.

We focus on neutral Cesium-133[2] where the single outer most electron occupies the $6^2S_{1/2}$ ground state. This notation summarizes the following basic properties of the atomic state. First, the principal quantum number (here $n = 6$), secondly the exponent refers to the spin multiplicity (here 2), thirdly the orbital angular momentum quantum number L is written as a letter (a historical shorthand with $S \Leftrightarrow (L = 0)$, $P \Leftrightarrow (L = 1)$, etc.), and finally the total angular momentum quantum number of the electron J is written as the subscript (here $J = 1/2$).

Two components, namely the electron intrinsic spin $\boldsymbol{S}$ and the orbital angular momentum $\boldsymbol{L}$, comprise the total angular momentum $\boldsymbol{J} = \boldsymbol{L} + \boldsymbol{S}$. Their interaction, with strength β_{LS}, is characterized by the spin-orbit Hamiltonian

$$\hat{\mathcal{H}}_{\text{spin-orbit}} = \beta_{LS} \boldsymbol{S} \cdot \boldsymbol{L} \tag{5.3}$$

and gives rise to an energy level splitting known as fine-structure. This interaction is not present (to first order) for the ground state $6^2S_{1/2}$ since $L = 0$. However, the next orbital of 6^2P, having $L = 1$, is split into $6^2P_{1/2}$ and $6^2P_{3/2}$.

In general, the allowed total angular momentum can be calculated from the selection rules eq. (5.4) below.

$$|L - S| \leq J \leq |L + S| \tag{5.4a}$$
$$|J - I| \leq F \leq |J + I| \tag{5.4b}$$
$$-F \leq m_F \leq F \tag{5.4c}$$

The quantum numbers governing the selection rules of eqs. (5.4b) and (5.4c) will be discussed shortly. From eq. (5.4a) we expect to see distinct transitions from $6^2S_{1/2} \leftrightarrow 6P_{1/2}$ and $6^2S_{1/2} \leftrightarrow 6^2P_{3/2}$, which indeed we do: these are the aforementioned D1 and D2 lines.

[1] deriving from *sky blue* in Latin.

[2] By far the most abundant ($\simeq 100\,\%$) and only stable isotope.

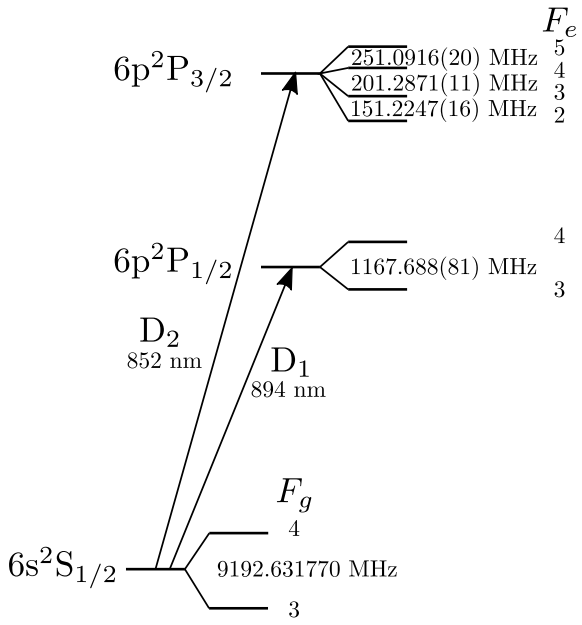

Figure 5.3: **Hyperfine structure of Cs-133.** The D1 and D2 lines describe the transition from the ground state $6^2S_{1/2}$ to the excited states $6^2P_{1/2}$ and $6^2P_{3/2}$ respectively. These states are further split due to the hyperfine interaction of eq. (5.5).

The fine-structure is not the only coupling relevant for the atomic energy levels, although it is the largest. The nuclear spin $\boldsymbol{I}$ interaction with the total angular momentum of the electron provides another correction known as the hyperfine splitting (HFS). This interaction has one main term relevant for us. This term arises due to the nuclear magnetic dipole moments interaction with the electronic spin $\boldsymbol{J}$. The strength of these interactions is characterized by A_{HFS}. The Hamiltonian for this interaction is given by Arimondo et al. (1977) as

$$\hat{\mathcal{H}}_{\text{HFS}} = A_{HFS}\boldsymbol{I}\cdot\boldsymbol{J} + \text{higher order terms} \tag{5.5}$$

where the immediate higher order terms are the electric quadradupole moment and the magnetic octupole moment, in order of importance. These are only relevant for states with $J \neq 1/2$. These are the excited manifolds of the alkalis, of secondary importance to us, and are thus omitted in our simple treatment here.

The ground state $6^2S_{1/2}$ splits into a doublet, denoted by quantum numbers $F = 3$ and $F = 4$. This is, in fact, true for all alkali ground states which have $F = I \pm 1/2$. This means that the total energy splitting of the ground state manifold is given by

$$\Delta E_{\text{HFS}} = A_{\text{HFS}}(I + 1/2), \tag{5.6}$$

which is valid for all alkalis. For Cs-133 with nuclear spin $I = 7/2$ this splitting amounts to 9.2 GHz[3]. This splitting is much smaller than the fine-structure and

[3]For the $6^2S_{1/2}$ manifold $A_{\text{HFS}} \approx 2.3\,\text{GHz}$

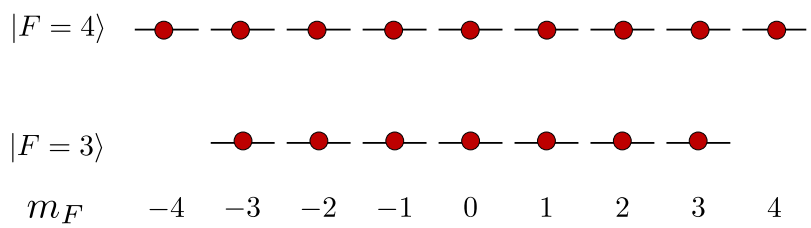

Figure 5.4: **Zeeman structure of Zeeman sublevels of $6^2S_{1/2}$.** The $2F+1$ degenerate magnetic sub-levels in each hyperfine level F are labeled by their magnetic quantum number m_F. The red dots represent individual atoms in the case where we consider an ensemble. The uniform distribution of the atomic population throughout this manifold is known as an unpolarized atomic spin state as described further in section 5.10. These degenerate levels may be split by a magnetic field as described in section 5.3.

depends on the total atomic angular momentum $\boldsymbol{F} = \boldsymbol{I} + \boldsymbol{J}$ which, in general, takes values given by the selection rules of eq. (5.4b).

The excited states of $6^2P_{1/2}$ and $6^2P_{3/2}$ are also split as shown in fig. 5.3. The additional energy (from the fine structure) of a particular hyperfine level is given by

$$E_{\mathrm{HFS}} = A_{\mathrm{HFS}} \frac{F(F+1) - I(I+1) - J(J+1)}{2} + \text{higher order terms}, \tag{5.7}$$

where the exact details of the higher order terms can be found in Steck (2010).

To get a sense of scale we notice that the spin-orbit interaction splits the $6^2P_{1/2}$ and $6^2P_{3/2}$ excited states by 16.5 THz, whilst the hyperfine manifold of the ground state $6^2S_{1/2}$ is split by only 9.2 GHz. An overview of this fundamental structure is seen in fig. 5.3. Exact splittings and relevant constants can be found in Steck (2010)

Additionally, there are $2F+1$ degenerate magnetic sub-levels in each hyperfine level F. These are shown for the $6^2S_{1/2}$ ground state in fig. 5.4. These so-called Zeeman sub-levels can be split due by an external magnetic field. That such fields would affect the structure is clear from the aforementioned interaction with the magnetic dipole moment.

5.3 Zeeman splitting

In the case of an externally applied uniform magnetic field $\boldsymbol{B}$ an additional contribution to the hyperfine Hamiltonian of eq. (5.5) must be added. This contribution is given by Foot (2005) as

$$H_B = \boldsymbol{\mu}_{\mathrm{atom}} \cdot \boldsymbol{B} \tag{5.8}$$

$$\boldsymbol{\mu}_{atom} = \frac{\mu_B}{\hbar}(g_J \boldsymbol{J} + g_I \boldsymbol{I}) \cdot \boldsymbol{B}. \tag{5.9}$$

where the magnetic moment of the whole atom $\boldsymbol{\mu}_{\mathrm{atom}}$ has contributions from the electronic and nuclear magnetic moments. Their strengths are given by the Landé g factors g_J and g_I in units of the Bohr magneton μ_B. As with fine and hyperfine structure the dominant contribution to this interaction is the electronic moment.

The Landé factors also absorb various (and ever smaller) modifications and complications not addressed here[1].

The effect of this additional magnetic field is, in general, not trivially solved. Let us consider the typical case where the magnetic field – of strength B – is aligned along the atomic quantization axis. The projection of the total angular momentum along this axis is here given by the magnetic quantum number m_F. In this work we utilize small B-fields, and thus the splitting caused by this interaction will be small compared to the total hyperfine splitting (ΔE_{HFS}) and – fortunately – an exact solution is known, see Breit and Rabi (1931); Steck (2010). This solution applies to the $S_{1/2}$ ground states of all the alkalis and predicts the additional energy of a particular state $|I, F, m_F\rangle$ above the fine structure to be

$$E_{I,F,m_F} = \frac{\Delta E_{HFS}}{2(2I+1)} + g_I \mu_B m_F B \pm \frac{\Delta E_{HFS}}{2}(1 + \frac{2m_F x}{2I+1} + x^2)^{1/2}, \tag{5.10}$$

$$x = \frac{(g_J - g_I)\mu_B B}{\Delta E_{HFS}}. \tag{5.11}$$

The $\pm$ depends on which hyperfine level $F = I \pm 1/2$ is being considered.

5.4 Larmor frequency

Expanding eq. (5.10) to first order[1] in B we find the m_F levels degeneracy broken. The splitting between adjacent m_F levels, to first order, is known as the Larmor frequency and is given by

$$\Omega_L \equiv (E^{(1)}_{m_F+1} - E^{(1)}_{m_F})/\hbar = (g_F \mu_B B)/\hbar, \tag{5.12}$$

$$g_F = g_I \pm \frac{g_J - g_I}{2I+1} \approx \pm \frac{g_J}{2I+1}. \tag{5.13}$$

We have defined the hyperfine Landé factor g_F and note that its sign changes depending on whether we are in $F = 3$ or $F = 4$. We will always be interested in the $F = 4$ manifold. Evaluating eq. (5.12) gives a convenient scale for the Larmor frequency given an applied magnetic field strength, namely 0.35 MHz/G.

Larmor frequencies typically used in this work are ~ 1 MHz requiring ~ 3 G. This is quite a weak magnetic field, though still only about 10 times that of the Earths. This also means we are rather sensitive to magnetic fields as they alter the Larmor frequency. Having a firm control over the external magnetic fields interacting with our Cesium ensemble is, therefore, of critical importance, and is addressed by magnetic shielding as mentioned in section 5.1. If instead you care about the transition from $|m_F = 0, F = 3\rangle$ to $|m_F = 0, F = 4\rangle$, on which the second is defined, then you are only susceptible to external magnetic fields to second order.

[1] e.g. structure of the nucleus and atomic diamagnetism which contributes to g_I, and the sixth-order magnetic moment of the electron which contributes to g_S Levine and Wright (1971).

[1] In our regime of interest $x \ll 1$.

The second order contribution to adjacent m_F level splittings is known as the *Quadratic Zeeman Effect*. From eq. (5.16b) we can see this contribution scales with m_F^2. The amount of quadratic Zeeman splitting is approximately given by

$$(E^{(2)}_{m_F+1} - E^{(2)}_{m_F})/\hbar \approx \mp(2m_F + 1)\frac{\Omega_L^2}{\Delta E_{HFS}/\hbar}, \tag{5.14}$$

where the sign convention is as in eq. (5.10), namely dependent on the choice of hyperfine level $F = I \pm 1/2$.

This splitting leads to transitions, e.g. $E_{2\to3}$ and$E_{3\to4}$, having Larmor frequencies that differ by

$$\Delta\Omega_L^{\mathrm{QZS}} = \frac{2\Omega_L^2}{\Delta E_{HFS}/\hbar}. \tag{5.15}$$

These transitions can be easily driven and measured as shown in the example of fig. 5.13. Here the quadratic Zeeman splitting of eq. (5.15) is also shown as the Larmor frequency is tuned.

The difference in Larmor frequencies, eq. (5.15), correspond to about 26.6 Hz/G^2 which means that we should expect Larmor frequency differences of ~ 210 Hz for our transitions with Larmor frequencies of ~ 1 MHz. This is an inconvenience as it adds anharmonicity to the effective harmonic oscillator we wish to create, see section 5.10, and is further discussed in section 5.11.1. Likewise it is also a handy tool as it allows for population differences of neighboring states to be probed, see section 5.10.8.

The first and second order corrections to the energy are given by

$$E^{(1)}_{I,F,m_F}/\hbar = m_F\Omega_L, \tag{5.16a}$$

$$E^{(2)}_{I,F,m_F}/\hbar = \pm\frac{m_F^2\Omega_L^2}{\Delta E_{HFS}/\hbar}\left[(I+1/2)^2 - m_F^2\right]. \tag{5.16b}$$

5.5 Spin half toy model

Suppose we prepare our atoms in an extreme magnetic Zeeman level (i.e. $m_F = \pm 4$) as shown in the left panel of fig. 5.11. Suppose also that we probe the D2 line from the $|F = 4\rangle$ to $|F' = 4\rangle$, see fig. 5.3, very far detuned from the entire $6^2P_{3/2}$ manifold. We may then approximate the atom-light dynamics by considering only the last two magnetic Zeeman levels. This is justified since excitations, and thus population redistribution, is suppressed. These two ground states constitute an effective spin-1/2 system. We now follow Julsgaard (2003, Erratum) in deriving the basic spin-light interaction by use of two excited states whose dynamics are eliminated. These can be thought of as states of the excited state manifold in the real atomic structure. They are necessary to our description as we are ultimately interested in the effect of the atomic operators on an optical probe field set to this transition.

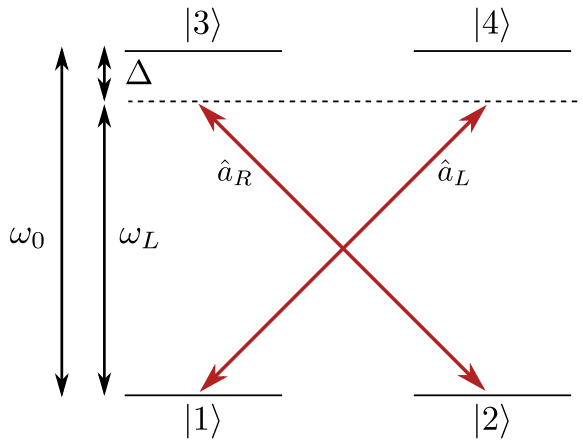

Figure 5.5: **Spin 1/2 toy model.** In this two ground states $|1\rangle$ and $|2\rangle$ are coupled by far off-resonant fields $\hat{a}_{L,R}$ to two excited states $|3\rangle$ and $|4\rangle$ who dynamics are eliminated. This leaves the dynamics of the ground states who together constitute a spin 1/2 system.

In fig. 5.5 we see this (4 level) so called spin-1/2 toy model represented diagrammatically. The ground states of $|1\rangle$ and $|2\rangle$ can be thought of as the $|F = 4, m_F = \pm 3\rangle$ and $|F = 4, m_F = \pm 4\rangle$ levels, for example. The excited states of $|3\rangle$ and $|4\rangle$ can be thought of as corresponding $|F' = 4\rangle$ levels in the $P_{3/2}$ manifold. If we choose our quantization axis to be along the probe direction, then the transitions $|1\rangle \to |2\rangle$ and $|3\rangle \to |4\rangle$ are dipole forbidden, making the system dynamics particularly simple to calculate. The remaining transitions are coupled by right and left hand circularly polarized light fields $\hat{a}_R$ and $\hat{a}_L$ respectively.

Furthermore, we make the simplifying assumption that the transitions $|1\rangle\langle 4|$ and $|2\rangle\langle 3|$ have equal Clebsch-Gordan coefficients[1]. In any real world atom this may not be the case, but can be accounted for subsequently. Omitting the each operators time dependence (t) we can write the full system Hamiltonian as

$$\hat{\mathcal{H}} = \hat{\mathcal{H}}_{\text{light}} + \hat{\mathcal{H}}_{\text{atoms}} + \hat{\mathcal{H}}_{\text{int}}, \tag{5.17a}$$

$$\hat{\mathcal{H}}_{\text{light}} = \hbar\omega_L \left[\left(\hat{a}_R^\dagger \hat{a}_R + 1/2\right) + \left(\hat{a}_L^\dagger \hat{a}_L + 1/2\right)\right], \tag{5.17b}$$

$$\hat{\mathcal{H}}_{\text{atoms}} = \hbar\omega_0 \left(|3\rangle\langle 3| + |4\rangle\langle 4|\right), \tag{5.17c}$$

$$\hat{\mathcal{H}}_{\text{int}} = -\hbar g \left(\hat{a}_R^\dagger |1\rangle\langle 4| + \hat{a}_R |4\rangle\langle 1| + \hat{a}_L^\dagger |2\rangle\langle 3| + \hat{a}_L |3\rangle\langle 2|\right). \tag{5.17d}$$

where g is a light-matter coupling rate. Henceforth, we will use the notational shorthand $\hat{\sigma}_{ij} \equiv |i\rangle\langle j|$ for the atomic operators.

All these light and atomic operates in the Hamiltonian above evolve very fast on timescales of $e^{i\omega_0 t}$ and $e^{i\omega_L t}$. Transforming into a rotating frame, see appendix E.1[2], oscillating at the light frequency ω_L we can look at the slow dynamics, which are of

[1] These coefficients are determine the relative strength of decay channel as are related to the wavefunction overlap between the final and initial states.

[2] Using $\hat{A} = \hbar\omega_L \left(\hat{a}_R^\dagger(t)\hat{a}_R(t) + \hat{a}_L^\dagger(t)\hat{a}_L(t) + \hat{\sigma}_{33}(t) + \hat{\sigma}_{44}(t)\right)$.

importance to us. Neglecting constant terms we have

$$\hat{\mathcal{H}} = \hbar\Delta\left(\hat{\sigma}_{33} + \hat{\sigma}_{44}\right) + \hbar g\left(\hat{a}_R^\dagger \hat{\sigma}_{14} + \hat{a}_L^\dagger \hat{\sigma}_{23} + \text{h.c.}\right), \tag{5.18}$$

where the operators are now in the rotating frame. We are most interested in the dynamics of the operators describing the populations and coherences of the ground states. We can work these out by considering their evolution according to the Hamiltonian of eq. (5.18) and find that

$$\dot{\hat{\sigma}}_{11} = \frac{i}{\hbar}\left[\hat{\mathcal{H}}, \hat{\sigma}_{11}\right] = -ig\left(\hat{a}_R^\dagger \hat{\sigma}_{14} - \hat{\sigma}_{41}\hat{a}_R\right), \tag{5.19a}$$

$$\dot{\hat{\sigma}}_{22} = -ig\left(\hat{a}_L^\dagger \hat{\sigma}_{23} - \hat{\sigma}_{32}\hat{a}_L\right), \tag{5.19b}$$

$$\dot{\hat{\sigma}}_{12} = -ig\left(\hat{a}_L^\dagger \hat{\sigma}_{13} - \hat{\sigma}_{42}\hat{a}_R\right), \tag{5.19c}$$

$$\dot{\hat{\sigma}}_{21} = \dot{\hat{\sigma}}_{12}^\dagger. \tag{5.19d}$$

Our large detuning means that we can effectively neglect any excited state populations, i.e. $\hat{\sigma}_{44} = \hat{\sigma}_{33} = 0$. Additionally, adiabatically eliminating the excited state transitions by setting $\dot{\hat{\sigma}}_{14} = \dot{\hat{\sigma}}_{41} = 0$ we ultimately find that the resultant dynamics are the result of an effective Hamiltonian of the form

$$\hat{\mathcal{H}}_{\text{eff}} = -\frac{\hbar g^2}{\Delta}\left(\hat{a}_R^\dagger \hat{a}_R \hat{\sigma}_{11} + \hat{a}_L^\dagger \hat{a}_L \hat{\sigma}_{22}\right). \tag{5.20}$$

From this simple Hamiltonian we can see that having a large RHCP ($\hat{n}_R = \hat{a}_R^\dagger \hat{a}_R$) or LHCP ($\hat{n}_L = \hat{a}_L^\dagger \hat{a}_L$) light component shifts the energies of the ground states. This is known as a Stark shift and the vacuum fluctuations of these light modes can be considered the source of the quantum back-action force ultimately limiting the measurements of important atomic spin quadratures, which are described next.

5.6 Atomic spin operators

Consider a generic system of spin F with ground levels labeled by their Zeeman number m probed along the quantization axis taken to be z. It is natural to define

the following spin operators[1],

$$\hat{J}_0 = \sum_{m=-F}^{F} |m| \hat{\sigma}_{mm}, \tag{5.21a}$$

$$\hat{J}_z = \sum_{m=-F}^{F} m \hat{\sigma}_{mm}, \tag{5.21b}$$

$$\hat{J}_+ = \sum_{m=-F}^{F} C(F,m) \hat{\sigma}_{m+1,m}, \tag{5.21c}$$

$$\hat{J}_- = \hat{J}_+^\dagger, \tag{5.21d}$$

$$C(F,m) = \sqrt{F(F+1) - m(m+1)}. \tag{5.21e}$$

The weight $C(F,m)$ depends on the total spin F and that of each sublevel m. Here $\hat{J}_z$ simply counts the energy in the spin system along the quantization axis, whereas the $\hat{J}_\pm$ are ladder operators.

Just as was the case when considering the optical and mechanical fields, it will prove useful to define quadrature operators as the real and imaginary components of these atomic ladder operators. They turn out to describe the spin components of the quantization axis and are given by,

$$\hat{J}_x = \frac{1}{2}\left(J_+ + J_-\right), \tag{5.22a}$$

$$\hat{J}_y = \frac{i}{2}\left(J_+ - J_-\right). \tag{5.22b}$$

These spin operators obey the angular momentum relations of

$$\left[\hat{J}_j, \hat{J}_k\right] = i\epsilon_{jkl}\hat{J}_l, \;\; j,k,l \in \{x,y,z\}, \tag{5.23a}$$

$$\hat{J}_0\left(\hat{J}_0 + 1\right) = \hat{J}_x^2 + \hat{J}_y^2 + \hat{J}_z^2, \tag{5.23b}$$

$$\left[\hat{J}_k, \hat{J}_0\right] = 0, \;\; k \in \{x,y,z\}. \tag{5.23c}$$

For our simple spin 1/2 effective two level system (having now eliminated the dynamics of the excited manifold) we have, $F = 1/2$ and thus $m_F = \pm 1/2$. Therefore,

[1]Not to be confused with an individual atoms total electron angular momentum also denoted $\boldsymbol{J}$ in sections 5.2 and 5.3. The use of the same symbol is commonplace in the field and is employed here to be consistent with relevant literature and commonplace nomenclature.

eq. (5.21) can be simplified as

$$\hat{J}_0 = \frac{1}{2}\left(\hat{\sigma}_{22} + \hat{\sigma}_{11}\right), \tag{5.24a}$$

$$\hat{J}_z = \frac{1}{2}\left(\hat{\sigma}_{22} - \hat{\sigma}_{11}\right), \tag{5.24b}$$

$$\hat{J}_+ = \hat{\sigma}_{12}, \tag{5.24c}$$

$$\hat{J}_- = \hat{\sigma}_{21}, \tag{5.24d}$$

$$\hat{J}_x = \frac{1}{2}\left(\hat{\sigma}_{12} + \hat{\sigma}_{21}\right), \tag{5.24e}$$

$$\hat{J}_y = \frac{i}{2}\left(\hat{\sigma}_{12} - \hat{\sigma}_{21}\right). \tag{5.24f}$$

We can invert this relationship and find that we can express the atomic state operators as

$$\hat{\sigma}_{11} = \hat{J}_0 - \hat{J}_z, \tag{5.25a}$$

$$\hat{\sigma}_{22} = \hat{J}_0 + \hat{J}_z, \tag{5.25b}$$

$$\hat{\sigma}_{12} = \hat{J}_x - i\hat{J}_y, \tag{5.25c}$$

$$\hat{\sigma}_{21} = \hat{J}_x + i\hat{J}_y. \tag{5.25d}$$

Thus, we can re-write our Hamiltonian of eq. (5.20) in terms of these atomic spin quadrature operators. We now have,

$$\hat{\mathcal{H}}_{\text{eff}} = \frac{2\hbar g^2}{\Delta}\left(\hat{J}_0\hat{S}_0 - \hat{J}_z\hat{S}_z\right), \tag{5.26}$$

where we have expressed the light operators in terms of the Stokes operators described in eq. (2.23d).

5.7 External magnetic field

We now wish to add an external magnetic field, and in keeping with the notation commonplace in this group we will let this direction be x. The optical probe will be orthogonal to this along z and these can be seen in fig. 5.2. This change of basis does not change the interaction Hamiltonian, which now reads

$$\hat{\mathcal{H}}_{\text{eff}} = \frac{2\hbar g^2}{\Delta}\left(\hat{J}_0\hat{S}_0 - \hat{J}_z\hat{S}_z\right) + \hbar\Omega_L\hat{J}_x, \tag{5.27}$$

where we have used the magnetic field in terms of the effective Larmor frequency ($\Omega_L \propto B_x$) it produces according to eq. (5.12).

Choosing this quantization axis we have effectively cyclically permuted the atomic

spin operators, which now read

$$\hat{J}_x = \sum_{m=-F}^{F} m\hat{\sigma}_{mm}, \tag{5.28a}$$

$$\hat{J}_y = \frac{1}{2}\left(J_+ + J_-\right), \tag{5.28b}$$

$$\hat{J}_z = \frac{i}{2}\left(J_+ - J_-\right). \tag{5.28c}$$

where J_+ and J_- are defined as before, but the atomic state operators $\hat{\sigma}_{jk}$ are in the basis of a quantization axis along x. A summary of the relation between probe direction, Stokes operators and the interaction Hamiltonian is summarized in section 5.9.

Let us consider the dynamics of the spins according to eq. (5.27). For the quadrature operators we have[1],

$$\dot{\hat{J}}_x = -g\hat{S}_z\hat{J}_y, \tag{5.29a}$$

$$\dot{\hat{J}}_y = +g\hat{S}_z\hat{J}_x - \Omega_L\hat{J}_z, \tag{5.29b}$$

$$\dot{\hat{J}}_z = \qquad\quad + \Omega_L\hat{J}_y, \tag{5.29c}$$

$$\dot{\hat{J}}_0 = 0, \tag{5.29d}$$

from which we observe the following well known facts about spin oscillators. The term related to the magnetic field represent a precession at the Larmor frequency of the orthogonal spin components $\hat{J}_y$ and $\hat{J}_z$ around the spin eigenvector $\hat{J}_x$ along the quantization axis.

The term related to $\hat{S}_z$, denoting the light angular momentum content along the probe direction z, causes the spin operators to evolve similarly. We can think of this as another effective magnetic field causing the spins to precess around $\hat{J}_z$.

This interaction of the spins and light also impacts the dynamics of the light operators orthogonal to $\hat{S}_z$, the linear polarization components of $\hat{S}_x$ and $\hat{S}_y$. Using the input-output equations for the Stokes components described in eq. (2.29), the output light operators are

$$\hat{S}_x^{\text{out}} = \hat{S}_x^{\text{in}} - g\hat{S}_y\hat{J}_z, \tag{5.30a}$$

$$\hat{S}_y^{\text{out}} = \hat{S}_y^{\text{in}} + g\hat{S}_x\hat{J}_z, \tag{5.30b}$$

$$\hat{S}_z^{\text{out}} = 0, \tag{5.30c}$$

$$\hat{S}_0^{\text{out}} = 0. \tag{5.30d}$$

This rotation of the output $\hat{S}_x$ and $\hat{S}_y$ polarization quadratures due to the interaction with the atoms is the effect known as Faraday rotation. This rotation of the linearly polarized light components and can be quite substantial for ensembles of atomic spins and the effect is quantified in section 5.11.3.

[1]The term in eq. (5.29c) is deliberately offset for ease of comparison with eq. (5.29b).

5.8 General Hamiltonian

A more general approach than that of our simple model described in section 5.5 would have given a Hamiltonian containing higher order interaction terms. Such a detailed derivation can be found in Julsgaard (2003) and yields an Hamiltonian containing contributions up to second order given by

$$\begin{aligned}\hat{\mathcal{H}}_{\text{int}} = -\frac{\hbar c \gamma_{\text{sp}}}{8A\Delta}\frac{\lambda^2}{2\pi}\int_0^L \Big\{ & 2a_0\hat{S}_0 + a_1\hat{S}_z\hat{j}_z \\ & + 2a_2\left[\hat{S}_0\hat{j}_z^2 - \hat{S}_x\left(\hat{j}_x^2 - \hat{j}_y^2\right) - \hat{S}_y\left(\hat{j}_x\hat{j}_y + \hat{j}_y\hat{j}_x\right)\right]\Big\}\rho(z)A\,\mathrm{d}z.\end{aligned} \tag{5.31}$$

where the atomic system is probed along the z direction over a cross-sectional area A taken here to be constant. The spontaneous emission rate of the excited state manifold is given by γ_{sp} which for cesium is 5.32 MHz.

The successively higher order light-matter interaction terms are weighted by a_i factors which are shown as a function of probe detuning in fig. 5.6. These factors, see Julsgaard (2003), are given by

$$a_0 = \frac{1}{4}\left(8 + \frac{7}{1+\Delta_{45}/\Delta} + \frac{1}{1+\Delta_{35}/\Delta}\right) \to 4, \tag{5.32a}$$

$$a_1 = \frac{1}{120}\left(176 - \frac{21}{1+\Delta_{45}/\Delta} - \frac{35}{1+\Delta_{35}/\Delta}\right) \to 1, \tag{5.32b}$$

$$a_2 = \frac{1}{240}\left(16 - \frac{21}{1+\Delta_{45}/\Delta} + \frac{5}{1+\Delta_{35}/\Delta}\right) \to 0, \tag{5.32c}$$

where the detunings Δ_{35} and Δ_{45} are the absolute detunings of $F' = 3, 4$ to $F = 5'$ respectively. Two effects associated the higher order interaction terms are discussed in sections 5.10.9 and 5.10.10.

The Hamiltonian eq. (5.27) derived from the simple model does however capture the relevant physics. This is confirmed by neglecting the higher order terms of the general case in eq. (5.31). This gives the effective light-matter interaction Hamiltonian of our spin system is given by

$$\hat{\mathcal{H}}_{\text{eff}} \approx -\beta\left(\hat{S}_0\hat{J}_0 - \hat{S}_z\hat{J}_z\right), \tag{5.33}$$

where the light quadratures of that of the probe field, aligned along z and far detuned by Δ. In the limit of a large detuning compared to the Doppler broadening we have an effective coupling rate of

$$\beta = \frac{\gamma_{\text{sp}}}{8A\Delta}\frac{\lambda^2}{2\pi}a_1(\Delta) \approx \frac{\gamma_{\text{sp}}}{8A\Delta}\frac{\lambda^2}{2\pi} \tag{5.34}$$

where $a_1(\Delta) \approx 1$ is an excellent approximation as seen in fig. 5.6.

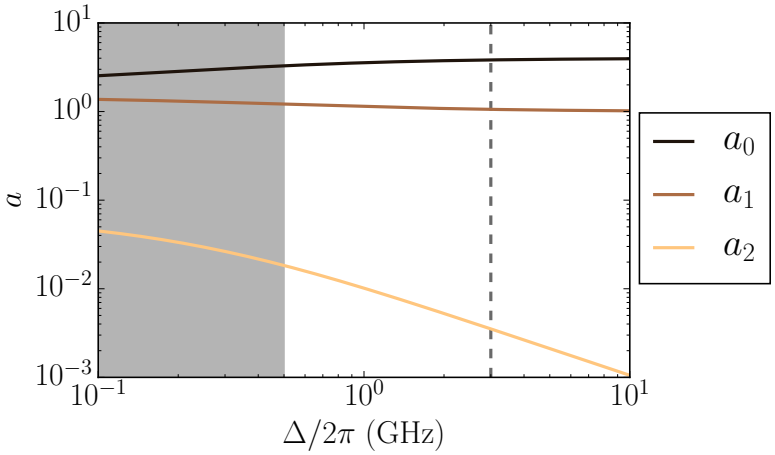

Figure 5.6: **Atomic coupling strength paramters.** Atomic coupling strength parameters a as a function of probe detuning Δ according to eq. (5.32). Blue detuning is considered negative, and thus what is plotted goes to roughly 3GHz blue detuned. The shaded region indicates the region corresponding to the 400 MHz full width (i.e. two half widths) of the Doppler broadening profile, see section 5.11.4, that is practically far from useful due to high absorption. Similarly bounded from above we cannot detuned too far as we start to probe $F = 3 \to F'$. The dashed line indicates our typically experimental detuning.

5.9 Quantization axis, probe direction and interaction Hamiltonian

Throughout this chapter we discuss different quantization axes and probing directions. In particular, when multiple fields are concerned, potentially in different directions, it may be difficult to orient oneself with respect to the spin and optical quadratures. To help prevent a confused state of affairs we review a few facts.

First off, the interaction Hamiltonian will always be

$$\hat{\mathcal{H}}_{\text{int}} \propto (\boldsymbol{S} + \boldsymbol{B}) \cdot \boldsymbol{J}, \tag{5.35}$$

where $\boldsymbol{B}$ is the externally applied magnetic field which may point in any direction. In our discussions (although it need not be), if present, this will *always* coincide with the quantization axis. The Stokes vector $\boldsymbol{S}$ points in the direction of light propagation which for us will commonly be along z for the probe and along x for other optical fields such as those discussed in section 5.10.6.

Taking the quantization direction to be along x means that eq. (5.35) will only have a $B_x \hat{J}_x$ term. Here $\hat{J}_x$ is the spin operator that has the ground states of the spin oscillator as eigenstates, namely eq. (5.21b). Had we chosen to quantize along z the previous states would have been identical, but we would change all $x \to y$.

Similarly, if we choose to probe along z then we will have a term $\hat{S}_z \hat{J}_z$. Here $\hat{S}_z = (\hat{n}_R - \hat{n}_L)/2$ is the Stokes operator for differences in circularly polarized light. Notice also that this interaction term is independent of our choice of quantization

axis and will always be $\hat{S}_z\hat{J}_z$. Our interpretation of $\hat{J}_z$ will, in a different basis, however, be different.

Probing in a different direction, say x, would give $\hat{S}_x\hat{J}_x$, where now we define $\hat{S}_x = (\hat{n}_R - \hat{n}_L)/2$. Thus, just as our quantization axis defines the spin operator, so too does the probe direction define the Stokes operators. We will always take the Stokes component in the direction of propagation to be the one quantifying the amount of circularly polarized light. Thus, saying S_z light needs to be qualified by a statement about the probing direction. In case this is omitted, it should be noted that throughout this work the probing direction is going to be along z.

5.10 Effective harmonic oscillator

From the spin precession described by eq. (5.29) the route to an effective oscillator is clear. The two atomic spin quadratures $\hat{J}_y$ and $\hat{J}_z$ should become canonically conjugate variables like with the mechanics and behave like eq. (3.32). The way to realize this is described next.

5.10.1 Holstein-Primakoff approximation

Using optical pumping, described in section 5.10.6, we can achieve a large, effective macroscopic, spin with $\hat{J}_x \approx J_x$ along the applied bias magnetic field by pumping atoms into an extreme m_F state.

The degree to which the spin of the ensemble is maximized/minimized is described by,

$$P \equiv \frac{1}{F}\sum_{m=-F}^{F} m\langle\hat{\sigma}_{m,m}\rangle \tag{5.36}$$

where the $|P|$ is referred to as the spin polarization[1]. In the limit of large optical pumping the spin polarization can approach unity.

Suppose we prepare an ensemble with a spin polarization $|P| \sim 1$. We can then make what is known as the Holstein-Primakoff approximation and create effective normalized spin (S) operators. We can then write these as

$$\hat{Q}_S \equiv \frac{\hat{J}_z}{\sqrt{|J_x|}}, \tag{5.37a}$$

$$\hat{P}_S \equiv -\operatorname{sgn}(J_x)\frac{\hat{J}_y}{\sqrt{|J_x|}}. \tag{5.37b}$$

Since $\left[\hat{J}_y, \hat{J}_z\right] \approx iJ_x$ the quadratures $\hat{Q}_S$ and $\hat{P}_S$ behave as canonical variables with $\left[\hat{Q}_S, \hat{P}_S\right] = i$. This approximation is typically very good as we commonly have

[1] This is also known as the spin orientation.

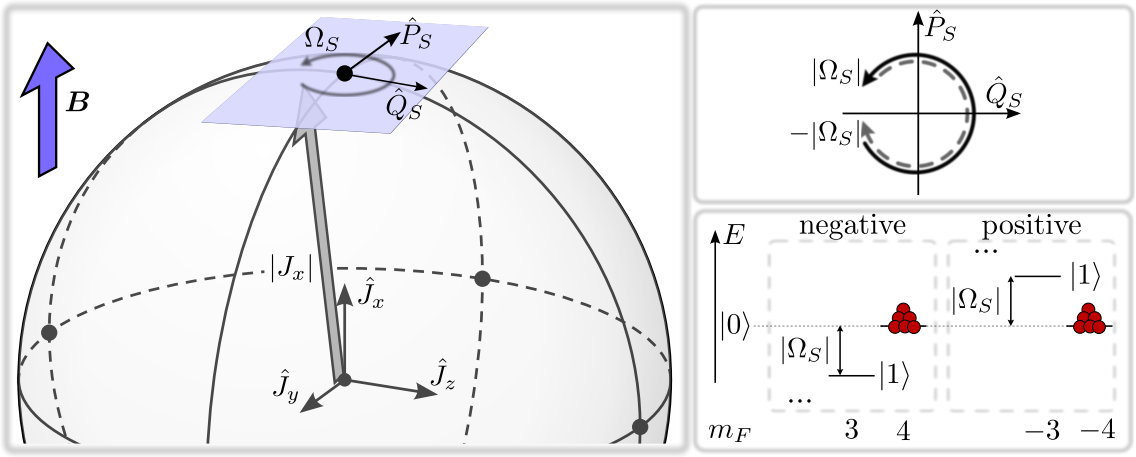

Figure 5.7: **Holstein-Primakoff approximation** Visualization of the physical basis for the Holstein-Primakoff approximation. **Left:** The total spin vector (grey) seen on sphere described by the spin vectors $\hat{J}_x, \hat{J}_y$ and $\hat{J}_z$. Precession around magnetic field $\boldsymbol{B}$ (blue arrow) is small compared to the macroscopic spin vector magnitude $|J_x|$ and corresponds to simple harmonic motion in a plane (translucent blue) of effective spin operators $\hat{Q}_S$ and $\hat{P}_S$ with a frequency Ω_S. **Right top:** The aforementioned simple harmonic motion in the cases of positive and negative spin mass resulting from the macroscopic spin orientation. **Right bottom:** States of the effective harmonic oscillator on an energy scale E. In the negative mass case (**left subpanel**) atoms are prepared in the highest energy magnetic sublevel $m_F = 4$. In the positive mass case (**right subpanel**) atoms are prepared in the lowest energy magnetic sublevel $m_F = -4$. The ground and first excited states of these effective oscillators are shown as $|0\rangle$ and $|1\rangle$. Part of this figure is a modified version of Geek3 (2014).

$|J_x| \sim N \sim 10^9 \gg 1$. In this limit the spin ensemble behaves like a traditional harmonic oscillator when $\mathrm{sgn}(J_x)$ is positive. The sign of the macroscopic spin vector is $\mathrm{sgn}(J_x)$.

This approximation can be viewed as in-plane precession of $\hat{J}_y$ and $\hat{J}_z$ on the surface of a larger sphere (of radius $|J_0|$) defined by the spin components, just like the Poincaré sphere of the Stokes polarization components. This is shown in the left panel of fig. 5.7, where our total spin vector is predominantly the large spin component along x. It has a magnitude essentially equal to $|J_x|$ and precesses around the applied magnetic field at the Larmor frequency.

The case shown in the left panel of fig. 5.7 is for an ensemble prepared in the maximum m_F state, with a spin aligned along the magnetic field. The evolution in our effective coordinate system $(\hat{Q}_S, \hat{P}_S)$ runs counter clockwise as is shown in the top right panel of fig. 5.7. Such counter clockwise phase space rotation is the behavior of a harmonic oscillator as if had a negative frequency, or equivalently a negative mass.

If instead we had prepared the ensemble in the minimum m_F state the sign of the macroscopic spin would be negative. The spin precession in the $(\hat{Q}_S, \hat{P}_S)$ phase space would evolve in a clockwise manner like in a traditional positive mass harmonic

oscillator.

The atomic population in the magnetic sublevels for the cases of effective positive and negative mass harmonic oscillators are shown in the bottom right panel of fig. 5.7. In the positive mass case, right dashed subpanel, spins populate the lowest energy state $m_F = -4$. Excitations in this harmonic oscillator result in higher energy, thus positive mass and the traditional counter clockwise phase space rotation. In the negative mass case however, left dashed subpanel, the spins populate the highest energy state and excitations of this harmonic oscillator corresponds to a de-excitation of the inverted spin population. Making the ground state $|0\rangle$ the highest energy state requires input energy (as does the positive mass oscillator) from the optical pumping, but does not constitute an unstable oscillator.

5.10.2 Effective Hamiltonian and equations of motion

A similar approximation of the optical Stokes quadratures was described in section 2.2.3 where, for a strong linearly polarized input field along x, propagating along z, we had $\hat{S}_x \to S_x$. The resulting effective polarization amplitude and phase quadratures $\hat{X}$, $\hat{Y}$ are described by eq. (2.31).

These approximations for the spin and Stokes operators mean that we can re-write the Hamiltonian of eq. (5.27)[2] and the equations of motion eqs. (5.29) and (5.30) now read (setting $\hbar = 1$),

$$\hat{\mathcal{H}}_{\text{eff}} \approx \sqrt{\Gamma_S}\,\hat{Q}_S\hat{X} + \frac{\Omega_S}{2}\left(\hat{Q}_S^2 + \hat{P}_S^2\right), \tag{5.38}$$

$$\Gamma_S \equiv \beta^2\,|S_x|\,|J_x| \approx \frac{\alpha^2}{2}\beta^2\,|J_x|\,, \tag{5.39}$$

$$\Omega_S \equiv -\operatorname{sgn}(J_x)\Omega_L. \tag{5.40}$$

We have recast the Larmor frequency in terms of the spin frequency Ω_S for two reasons. First, keeping the subscript of L could be misleading as it is not associated with the light field. Secondly, absorbing the sign of J_x into Ω_S lets us differentiate the two possible regimes of operations for the spin ensemble. Finally, there are mean field interactions with the linearly polarized input field that give rise to Stark shifts effectively changing the Larmor frequency, see section 5.10.10.

We have also collected the effective light matter interaction strength into the term Γ_S. This is the readout rate for the spin motion and sets the scale for the rate at which the motion couples to the light degrees of freedom, just like for optomechanics. It depends on the large mean field $|S_x|$, which, since we probe with a field linearly polarized along x, is just equal to half the optical photon flux α^2. Thus the readout rate, like in the optomechanical system can be linearly tuned by increasing the probe power. Likewise the readout rate is also dependent on the mean spin $|J_x|$, which is proportional to the number of atoms and the degree of spin polarization.

[2]Using the relation of eq. (5.23b).

The spin motion is, just like mechanics, not immune to loss. In practice the motion is that of a damped harmonic oscillator with a damping rate γ_S. This damping introduces the "thermal" Langevin spin noise driving force written as $\hat{F}_S$. We will assume it has a correlation function of

$$\langle \hat{F}_S(t)\hat{F}_S(t')\rangle = \delta(t-t')\left(\bar{n}_S + 1/2\right), \tag{5.41}$$

describing a Markovian bath of mean occupancy $\bar{n}_S$. While this reservoir lacks a clear link to any particular physical bath, it will be a measure of how much added noise the spin system sees.

We can thus write down the Heisenberg-Langevin equations of motion for the effective light and spin operators under the effective Hamiltonian given by eq. (5.38). These are

$$\hat{X}^{\text{out}} = \hat{X}^{\text{in}}, \qquad (\text{old } \hat{S}_z) \tag{5.42a}$$

$$\hat{Y}^{\text{out}} = \hat{Y}^{\text{in}} - \sqrt{\Gamma_S}\,\hat{Q}_S, \qquad (\text{old } \hat{S}_y) \tag{5.42b}$$

$$\dot{\hat{Q}}_S = \Omega_S \hat{P}_S, \qquad (\text{old } \hat{J}_z) \tag{5.42c}$$

$$\dot{\hat{P}}_S = -\sqrt{\Gamma_S}\,\hat{X}^{\text{in}} - \Omega_S \hat{Q}_S - \gamma_S \hat{P}_S + \sqrt{2\gamma_S}\,\hat{F}_S. \qquad (\text{old } \hat{J}_y) \tag{5.42d}$$

where $\Omega_S = \pm\Omega_L$ implies positive and negative mass respectively. As was shown in the upper right panel of fig. 5.7 this difference is tantamount to a reversed phase space evolution. The spins oscillator, by contruction, has a susceptibility, just like that of mechanics in eq. (3.35), given by

$$\chi(\Omega) = \frac{\Omega_S}{\Omega_S^2 - \Omega^2 + i\Omega\gamma_S}. \tag{5.43}$$

The resource to flip the sign of this susceptibility by choice of positive or negative mass is the key to the quantum back-action evasion in chapter 6.

Now that we have an effective harmonic oscillator, we can use the exact same language developed for the mechanical oscillator. Of primary interest are the readout, damping and decoherence rates, and of course the quantum cooperativity. To fully discuss these we must first address a physical difference between the spin and mechanical systems. For atomic spins it turns out that the nature of the interaction not only adds decoherence, the quantum back-action of the probe light just as seen in the optomechanical case, but also invariably dampens the spin oscillator, somewhat unlike the optomechanical system.

The total damping rate γ_S of the spins is thus usefully decomposed into two contributions. The damping induced by the probe, γ_{probe}, and all other extraneous sources, which we will write, in analogy with the mechanics, as the "intrinsic" damping $\gamma_{S,0}$. Thus we have

$$\gamma_S = \gamma_{S,0} + \gamma_{\text{probe}}. \tag{5.44}$$

The sources of intrinsic damping are discussed in section 5.11.5 and the probe induced broadening is discussed next.

5.10.3 Probe induced spontaneous emission broadening

The spin-light interaction described by the our simple toy model of section 5.5 is really a coherent interaction mediated by coupling to the excited state manifold. Due to the ever finite detuning, as this interaction strength is increased, so too are excitations to the excited state manifold. Subsequent incoherent decay through spontaneous emission is an effective source of damping, and is known as the probe induced spontaneous emission, or power broadening.

To more fully capture the essence of this dynamic it is thankfully not necessary to treat the general case 16 Zeeman sublevels (7 in $F = 3$ and 9 in $F = 4$) and the complicated set of excited state manifolds. We may instead continue to use our spin 1/2 toy model, but will treat it as an open quantum system with spontaneous emission as a dissipation channel. This is done in appendix F, where we utilize the wonderfully applicable effective operator formalism described in Reiter and Sørensen (2012).

We make use of this Schrödinger picture master equation approach since it has the benefit of being scalable and of explanatory utility. Due to our in practice finite spin polarization, endeavors to describe more magnetic sublevels, as done in Vasilyev et al. (2012), and understand their coupled dynamics, are relevant for future experiments. The formalism further allows for effective parameters to be calculated which can be used in the Heisenberg-Langevin approach preferred throughout this work.

In the relevant case of spontaneous emission such an effective parameter for the damping, γ_{eff} is given by eq. (F.2.12). Solving the dynamics shows that the probe, with large mean photon flux α^2, gives rise to an enhanced damping of the atomic spin quadratures, see eq. (F.3.18). This probe induced power broadening is given by

$$\gamma_{\text{probe}} = \gamma_{\text{eff}} \frac{\alpha^2}{2} \approx \frac{\gamma g^2}{\Delta^2} \frac{\alpha^2}{2}, \tag{5.45}$$

where the approximation is for the experimentally relevant case of large probe detunings Δ. The functional dependence of the broadening can be understood as follows. The damping is related to absorption and subsequent spontaneous emission from the excited state manifold. The absorption scales as $1/\Delta^2$ and rate scales with the light-matter coupling rate g and the photon flux α^2. Similarly, an effective coherent coupling rate, g_{eff}, can be found, see eq. (F.2.10), which is related to the readout rate as $\Gamma_S \propto g_{\text{eff}}^2$.

5.10.4 Spin quantum cooperativity

To read out the spin motion well requires a large readout rate. The larger the readout rate, the larger the probe induced broadening. Consider the typically relevant regime where the probe induced broadening dominates the other sources of damping, i.e.

$\gamma_S \approx \gamma_{\text{probe}}$. Here the ratio of the readout rate to the total broadening is given by

$$\frac{\Gamma_S}{\gamma_S} \approx g^2 |J_x| \propto \frac{|J_x|}{A}. \tag{5.46}$$

Thus the amount of readout rate available per unit of induced power broadening is given, essentially, by the atomic density [3]. It does not depend on the detuning, as long as we stay far detuned, nor on the optical power as the readout rate and broadening both scale linearly with power.

We can think of the power broadening as a decoherence due to probe field, which, just as for mechanics, is also the source of the quantum back-action. This back-action is from the optical driving term from the light quadrature $\hat{X}^{\text{in}}$ in eq. (5.42). It is thus natural to want the spin ensemble decoherence (and thus broadening) to be dominated by the probing light field as this will give a large quantum cooperativity. In practice, we seldom broaden to more than 10 kHz, but always try to dominate the intrinsic losses. In fact, in the experiments detailed in section 6.3 we broaden to $\simeq 8$ kHz, and in section 6.4 to about $4-5$ kHz. In both cases the intrinsic damping was about 1 kHz.

From eq. (5.42) we can compare the quantum back-action (QBA) drive to that of the thermal noise (TN) and work out the contributions to the variance of $\hat{Q}_S$, just as with mechanics in section 4.1.5. This allows us to define the quantum cooperativity for the spin ensemble as

$$C_q^S \equiv \frac{\text{QBA}}{\text{TN}} = \frac{\Gamma_S/4}{\gamma_S(\bar{n}_S + 1/2)}. \tag{5.47}$$

This is in practice an experimentally measured quantity since the atomic mean occupancy $\bar{n}_S$ is not easily measurable or readily available from theoretical considerations. Rather it is a product of experimental conditions and sets the baseline decoherence achieved for a particular readout rate.

From eq. (5.46) it is clear that the quantum cooperativity of section 4.1.5 does not scale with optical probing power once once the power broadening is dominant. This is routinely observed for our spin ensemble. In practice, before saturating, the quantum cooperativity increases as the optical probing power is increased. Since the optical power also determines the readout rate, the amount of power broadening is a typically a trade-off with the tolerable readout rate. In chapter 6, where we put the spin system to use, the absolute value of readout rate must be contrasted with that of the optomechanical system.

Experimentally, the way to increase the atomic cooperativity is to put the atoms inside a cavity, or by having more atoms, specifically a higher density. In this work we take the latter approach. This is done by heating the vapour cell and thereby

[3] Recall that $|J_x|$ is related to the number of atoms seen by the probe of cross-sectional area A according to eq. (5.31).

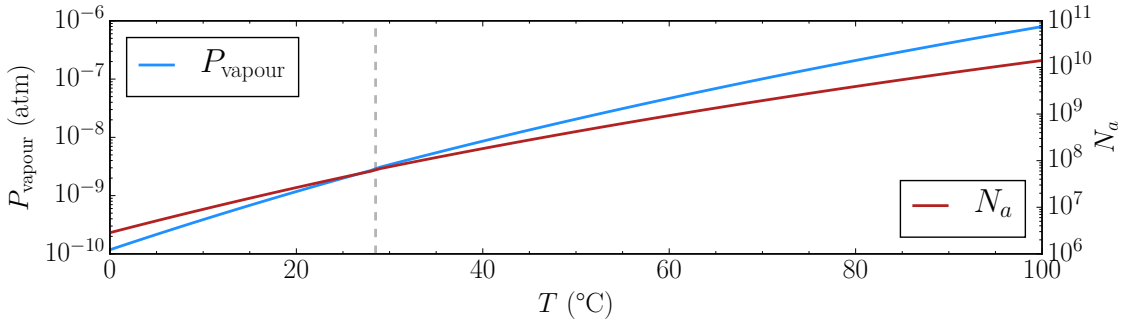

Figure 5.8: **Cesium vapour pressure** Shown is cesium vapour pressure (blue) as function of ambient temperature. Also shown is the number of atoms (red) contained within a $300 \times 300\,\mu\text{m}$ square channel of 10 mm length. Grey dashed line indicates phase transition of cesium from solid to liquid at $T = 28.5\,°\text{C}$.

increasing the vapour pressure. The dependence of the atom number on the vapour pressure is described in section 5.10.5. The amount of atoms contributing to $|J_x|$ would also help. This is akin to saying that the degree of ensemble spin polarization is important. Thus optical pumping is desirable, this is described in section 5.10.6.

Having a low spin polarization also effectively adds more noise through the Langevin drive $\hat{F}_S$ in eq. (5.42). The amount of extra noise compared to the case of perfect polarization is described in section 5.10.7.

5.10.5 Vapour pressure

Atoms in the gaseous phase are seeded by a reservoir of Cs in the stem of the vapour cell which is shown in fig. 5.1. These gaseous atoms form our spin oscillator and, as we just saw, the more the merrier.

The vapour pressure of Cs is highly temperature dependent and undergoes a phase change from solid to liquid at 28.5 °C. In the two regimes the vapour pressure has the same functional dependence given by B. Alcock et al. (1984) as

$$P_{\text{vapour}} = 10^{A - B/T}, \tag{5.48}$$

$$(A, B) = \begin{cases} (4.711, 3999)\,, & \text{for } T < 28.5\,°\text{C}, \\ (4.165, 3830)\,, & \text{for } T > 28.5\,°\text{C}, \end{cases} \tag{5.49}$$

where the pressure is in atm and the temperature in K. Through the phase change the vapour pressure rises slightly. However, the overall uncertainty in the model parameters is likely larger than this rise and the absolute values should be taken with a specified $\sim 5\,\%$ error. In practice this small error is of little matter to us, and we care mostly about large increase in number density, n, with temperature.

The atoms are typically confined in a volume V, which using the ideal gas law, yields an absolute number N_a of Cs atoms simply given by

$$N_a = nV = \frac{P_{\text{vapour}} V}{k_B T}. \tag{5.50}$$

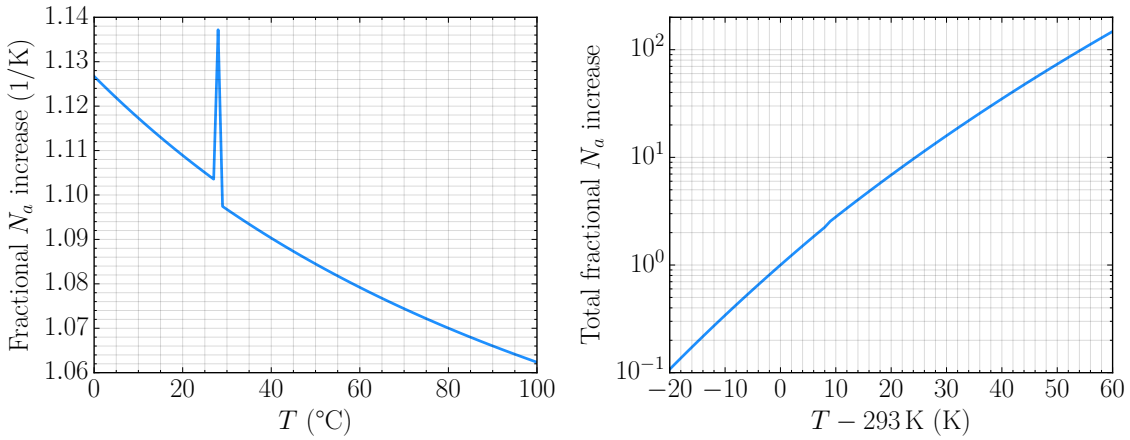

Figure 5.9: **Increase in number of atoms with temperature. Left:** Fractional increase in encased number of atoms per degree. The spike happens at the phase transition of $T = 28.5\,°\mathrm{C}$. Clearly the per degree fractional increase falls off quite fast with a 1 °C change at 60 °C being roughly 30 % lower than that at 20 °C. **Right:** Total fractional increase in number of atoms as referenced to room temperature of 20 deg where cells are typically initially characterized.

N_a is typically on the order of $10^8 - 10^9$ for the experiments discussed in this work, but of course depends critically on temperature. The vapour pressure and atomic number versus temperature are shown in fig. 5.8.

The fractional increase in the number of atoms, which is typically of experimental interest, is shown in fig. 5.9. Incredibly, one can increase the number of atoms by roughly a factor of 34 by increasing the temperature by 40 °C from 20 °C (room temperature) to a balmy, but easily feasible, 60 °C.

5.10.6 Optical pumping

If left to their own devices, the large ensemble of atoms would thermally populate the Zeeman states within each hyperfine level of $F = 3$ and $F = 4$ as shown in fig. 5.4. In this case we would on average find a net zero spin,

$$\langle \boldsymbol{J} \rangle_{\text{space}} \approx \mathbf{0}, \tag{5.51}$$

as the individual atoms would have a randomly oriented spin direction in space. The fraction of atoms in the extreme m_F state is known as the spin polarization and is typically desirable as it provides a larger mean spin and lower noise.

In practice, we use auxiliary fields to prepare the atoms in (or near to) a particular state of extreme m_F in the $F = 4$ ground state manifold, an example is shown in fig. 5.10. This produces a large mean ensemble spin $\langle \boldsymbol{J} \rangle \neq 0$. To do this, we use two separate, co-propagating optical fields oriented along the quantization axis (x), i.e. orthogonal to our probe but parallel with our bias magnetic field. These two fields are known as the pump and repump, as their main jobs are simple.

The repump brings atoms into the $F = 4$ ground state manifold, while the pump brings all atoms towards the extreme $m_F = \pm 4$ state. These fields are shown in the

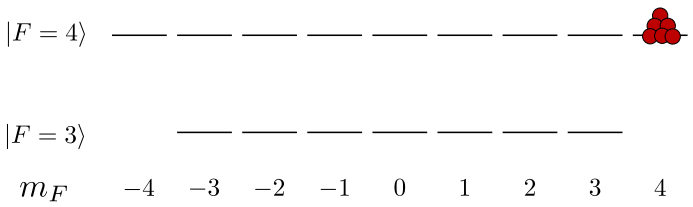

Figure 5.10: **Spin polarization in the Zeeman sublevels of $6^2S_{1/2}$.** An example of a highly spin polarized ensemble. All atoms (red dots) occupy an extreme Zeeman sublevel, in this case the $m_F = 4$, in the $F = 4$ hyperfine manifold.

right panel of fig. 5.11 with respect to the atomic energy structure. For the work in this thesis the pump, repump and probe are on continuously in the experiments discussed in section 6.3 whilst the pump is turned off in section 6.4. Let us discuss these now in a bit more detail.

Pump

The pump beam is a right hand circularly polarized field[4] (σ_+) set to the D1 line at 894.6 nm and is tuned on resonance with the $F = 4 \rightarrow F' = 4$ transition. This beam co–propagates with the repump field and drives atoms to the excited state with $\Delta m_F = +1$. From there any subsequent decay back to $F = 4$ will be with a Δm_F set by Clebsch-Gordan coefficients. This process cannot reduce the overall, m_F and thus a steady state is reached where the atomic population has a higher average m_F. This principle is illustrated in the left panel of fig. 5.11.

Since the pump addresses states in the $6^2P_{1/2}$, $F = 4$ manifold it adds broadening proportional to the intensity and thus the pumping rate. Notice that although the $|4, 4\rangle$ is a dark state of the probe, the coherence of interest are between the $|4, 4\rangle$ and $|4, 3\rangle$, the latter of which the pump addresses, and thus unfortunately adds decoherence to.

Pumping $F = 4 \rightarrow F' = 3$ renders both $|4, 3\rangle$ and $|4, 4\rangle$ dark states. Since this cannot bring atoms to the maximum m_F state of $|4, 4\rangle$, this scheme appears not worth considering. This is true in pulsed probe experiments[5] where you wish to pump to your ensemble to $|4, 4\rangle$, turn off the pump and then probe. In this case you do not care about the reduced coherence between $|4, 3\rangle$ and $|4, 4\rangle$ arising from the pump as it is turned off during the probing of the spin ensemble. However, in the continuous probing regime this counter intuitive pumping approach is worth considering as it increases the overall polarization without influencing the coherence between $|4, 3\rangle$ and $|4, 4\rangle$.

[4] A field with right hand circularly polarized light propagting along the quantization axis is known as σ_+ polarized.

[5] Not implemented anywhere in this thesis.

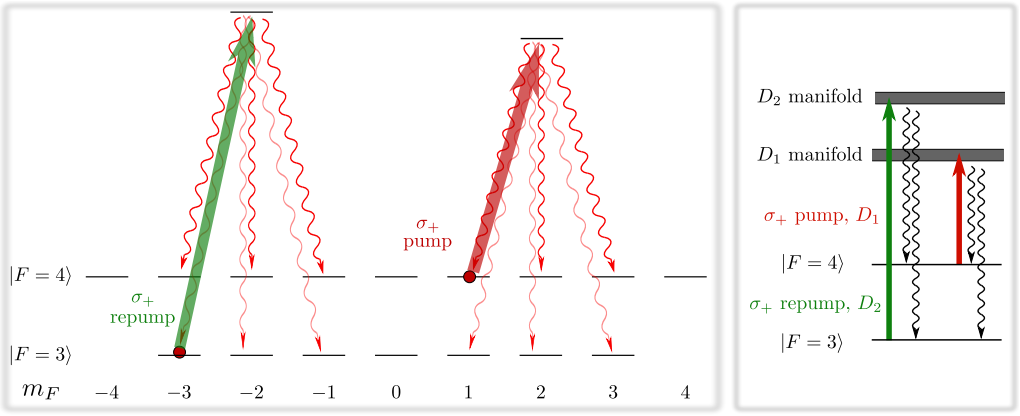

Figure 5.11: **Optical pumping of the Zeeman sublevels in $6^2S_{1/2}$.** Effects of the pump and repump are shown through an example and an overview. **Left:** The σ_+ repump field excites atoms from $F = 3$ bringing atoms ultimately into $F = 4$. It does so yielding a increased overall m_F. The pump field moves atoms to higher m_F by within $F = 4$. **Right:** Overview of optical pumping on the D1 and D2 lines.

Repump

The repump beam operates broadly on $F = 3 \rightarrow F' = 2$ transition of the D2 line at $\sim 852.3\,\text{nm}$, see right panel of fig. 5.11. This is transition is driven in order to bring atoms from the unprobed $F = 3$ ground state hyperfine manifold into $F = 4$. This is achieved since the repump field drives atoms populating $F = 3$ into the $6^2P_{3/2}$ excited states from which they decay to either $F = 3$ or $F = 4$ according to the Clebsch-Gordan coefficients and selection rules. Provided enough optical power is used the repumping will eventually dominate other decay channels and all atoms will populate the $F = 4$ ground state manifold. See fig. 5.11 for an illustration of this.

Additionally, since we use a right hand circularly polarized repump, the atoms ending in the $F = 4$ manifold will be asymmetrically distributed tending towards higher m_F. It is for this reason that we set our repump to near the $F = 3 \rightarrow F' = 2$ transition. This may seem like a paradoxical choice since we cannot decay from $F' = 2 \rightarrow F = 4$ as desired. However, due to the doppler broadening and finite detuning, the other F' excited states which can decay to $F = 4$ are also driven. This choice thus increases the average gained m_F for atoms going from $F = 3 \rightarrow F = 4$ since atoms most often decay back to $F = 3$, before that low probability event of ending up in $F = 4$. We are essentially using the repump as a "pump" for the $F = 3$ manifold, as well as a "repump" for the $F = 4$ manifold. This provides us with a more favourable spin polarization.

5.10.7 Added noise from finite spin polarization

In our case of continuous optical pumping and probing a trade-off exists between benefits of optical pumping and the noise added by these fields. Having a high pump field means a high pumping rate and a larger polarization, but is concomitant with

an increased decoherence due to increased spontaneous emission and absorption.

In the experiments of section 6.3 the optimal scenario was found to be lots of repump (which adds little broadening) and little pump. However, in section 6.4 the pump was completely removed.

A high degree of spin polarization reduces the effective noise seen by the atomic spin quadratures, i.e. it reduces the bath occupation $\bar{n}_S$ seen in eq. (5.41). This can be seen by considering, say, the decay term of the $\hat{J}_y$ quadrature given by eq. (5.29b). Writing a quantum Heisenberg-Langevin equation for this quadrature by adding a noise term $\hat{F}_{Jy}$ with a coupling given by the quadrature damping rate γ_S, we have

$$\dot{\hat{J}}_y = g\hat{S}_z\hat{J}_x - \Omega_L\hat{J}_z - \frac{\gamma_S}{2}\hat{J}_y + \sqrt{\gamma_S}\hat{F}_{Jy}. \tag{5.52}$$

The noise the quadratures see, given by the correlations of the driving Langevin noise terms, can be shown to be

$$\langle F_{Jy}(t)F_{Jy}(t-t')\rangle = \frac{N_a}{2Z}\sum_{m=-F}^{F} e^{m\beta}\left[F(F+1)-m^2\right] \tag{5.53}$$

$$= \begin{cases} F, & \text{for } |P|\to 1, \\ 2F(F+1)/3, & \text{for } |P|\to 0, \end{cases} = \begin{cases} 4, & \text{for } F=4, \\ 40/3, & \text{for } F=4, \end{cases} \tag{5.54}$$

$$Z = \sum_{m=-F}^{F} e^{m\beta}, \tag{5.55}$$

where $\beta = \log[(1+|P|)/(1-|P|)]$ and Z is the partition function. This is further described in Vasilakis et al. (2011), and the the underlying assumption is that for a given spin polarization $|P|$ the ensemble distribution in m_F levels is such that entropy is maximized.

From eq. (5.54) it is clear that a completely unpolarized ensemble sees $10/3 \simeq 3.3$ times more noise than a perfect polarized ensemble. For a particular polarization $|P|$ the noise added compared to the perfectly polarized case of $|P| = 1$ is shown in fig. 5.12. Experimentally in chapter 6 we typically achieved $\sim 60\,\%$ spin polarization, and thus add an additional $50\,\%$ of noise, which is quite substantial. Increasing polarization, and thereby reducing this extra noise is thus highly desirable and is being investigated. Recent measurements have shown that larger spin polarizations can be achieved with a new batch of cell coatings although the exact mechanism is not yet understood.

5.10.8 Magneto-optical resonance (MORS)

A powerful tool used predominantly for purposes of spin characterization is the technique of magneto-optical resonance (MORS). The basic idea is to coherently drive the atomic spins to a very large precession amplitude and probe the now classically enhanced spin dynamics optically. This is done in practice by modulating

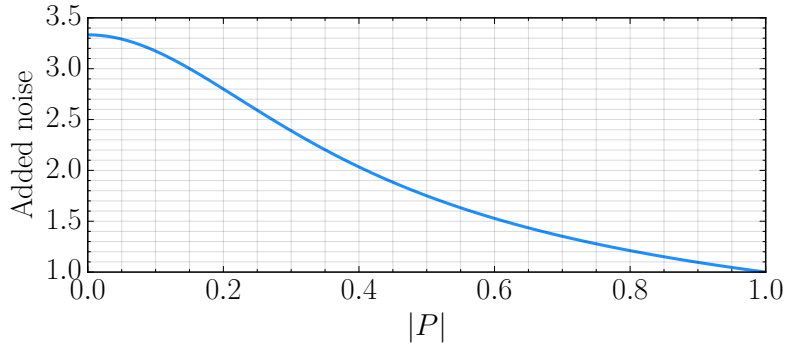

Figure 5.12: **Spin quadrature added noise for finite spin polarization** Noise added to atomic spin quadratures relative to the case of perfect spin polarization for an atomic ensemble in the $F = 4$ manifold.

a magnetic field at an angular frequency Ω_{mod} perpendicular to the quantization axis x, where we have a large constant (DC) magnetic field.

Adding this modulated magnetic field (also known as RF drive) to the Hamiltonian gives a extra contribution of $B_y \hat{J}_y$, where $B_y = |B_{\text{RF}}| \sin(\Omega_{\text{mod}} t)$. The effect is immediately seen from the evolution of the precessing spin components, which now read

$$\dot{\hat{J}}_z = -\Omega_L \hat{J}_y + |B_{\text{RF}}| \sin(\Omega_{\text{mod}} t) J_x - \frac{\gamma_S}{2} \hat{J}_z + \sqrt{2\gamma_S}\, \hat{F}_{Jz}, \tag{5.56}$$

$$\dot{\hat{J}}_z = \Omega_L \hat{J}_y - \frac{\gamma_S}{2} \hat{J}_z + \sqrt{2\gamma_S}\, \hat{F}_{Jy}. \tag{5.57}$$

The RF drive acts as a driving force at Ω_{mod} boosted by the large mean spin J_x. This force drives the spin oscillations to amplitudes governed by the susceptibility. Thus, if we sweep the modulation tone and demodulate the detected light quadrature $\hat{S}_y^{\text{out}} \propto \hat{J}_y$ we can directly see the atomic response. The motion is readout in this optical polarization quadrature as can be seen from eq. (5.42). How these polarization quadrature are measured in practice is explained in appendix B.3.

As an example, the quadratic Zeeman splitting is easily observed with a high signal to noise using MORS. In fig. 5.13 we show an example MORS data set and a model fit assuming all the Zeeman sublevels have an equal linewidth. This model is the same as the one detailed in Julsgaard (2003). Also shown in the figure is the quadratic Zeeman splitting as a function of Larmor frequency together fit showing an excellent agreement with the quadratic dependence expected from eq. (5.15).

5.10.9 Tensor rotation

Non-linear interactions terms with the second–order prefactor a_2 in the general Hamiltonian eq. (5.31) distorts the simple Faraday rotation by mixing the $\hat{S}_y$ and $\hat{S}_z$ components in an effect akin to birefringence. The mechanism mediating the tensor effect is associated with a two photon scattering process and depends crucially on the finite excited state populations. It is thus efficiently suppressed compared to

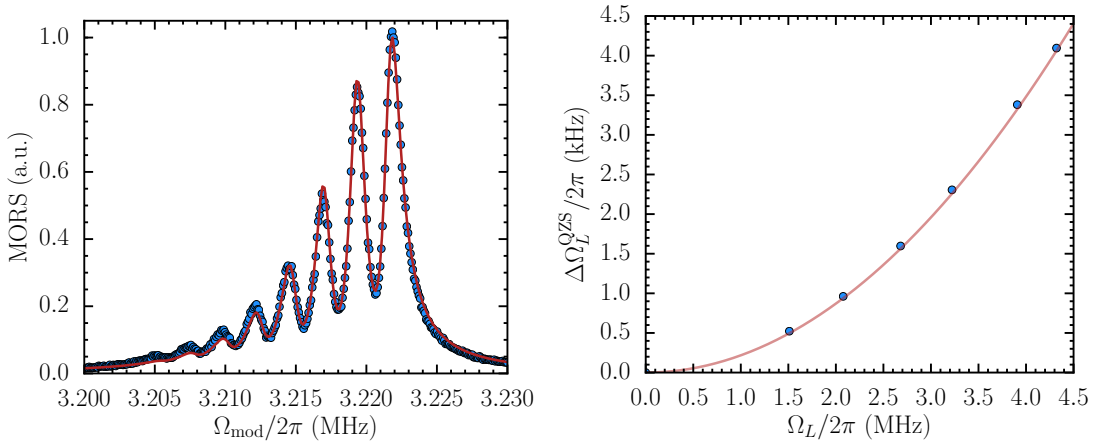

Figure 5.13: **Quadratic Zeeman splitting measured by MORS.** Shown in an example of a MORS (**left**) signal as a function of demodulation frequency Ω_{mod}. The blue points are the measurement and the red line is a model fit. To the **right** we show the quadratic Zeeman splitting (blue points) as derived from MORS data at various Larmor frequencies. The red curve is not a fit but the quadratice prediction according to eq. (5.15).

the other processes by a large probing detuning, which in practice is how they are rendered negligible.

Although the tensor effect may be small, the effect on the measured $\hat{S}_z$ quadrature can still be quite significant compared to quantum noise (shot noise) of $\hat{S}_z$. This is because for a large interaction strength the $\hat{S}_y$ quadrature has a very large contribution from the atomic precession. This contribution is on the order of 100s of times that of shot noise in $\hat{S}_y$ for the experiments of chapter 6. Thus, even a small tensor effect on the order of a percent may lead to a contribution appreciable compared to the shot noise in $\hat{S}_z$.

The size of this contribution in $\hat{S}_z$ is, in practice, the most important effect. This is because we require the shot noise in $\hat{S}_z$ after the interaction with the spin ensemble to be the same as that coming in. This is important for the hybrid quantum back-action evasion scheme detailed in chapter 6 since the $\hat{S}_z$ quadrature output from the spin ensemble ultimately interacts with (and drives) the mechanical system. Experimentally, this is addressed by increasing the atomic detuning until a_2/a_1 is sufficiently small.

5.10.10 Stark shifts

The higher order interaction term proportional to a_2 in eq. (5.31) also gives rise to a light induced Stark shift. This term arises from Zeeman energy levels shifts associated with coupling to the probe's electric field and depends on the angle θ_{pol} between the direction of the linearly polarized probe field and the direction of macroscopic spin. The effect is probe power dependent and can be shown, e.g. in Julsgaard (2003), to be of the form

$$\Delta\Omega_L^{\mathrm{Stark,\ probe}} \propto \alpha\,(1 + 3\cos(2\theta_{\mathrm{pol}})) \tag{5.58}$$

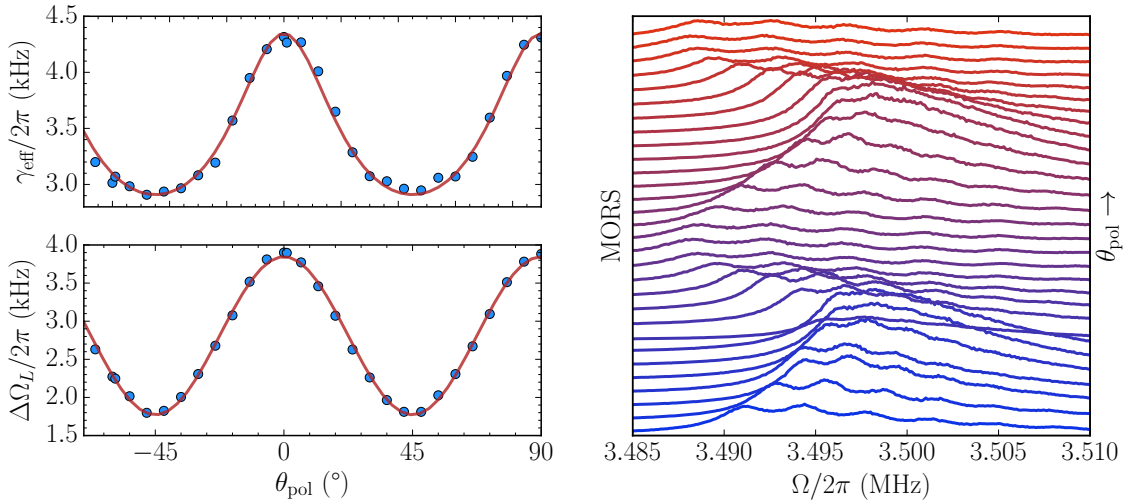

Figure 5.14: **Stark shifts and broadenings for a variable input polarization θ_{pol}. Left top**: Broadenings of the Zeeman sublevels levels fitted from MORS in blue. Guess for functional dependence in red. See text for details. **Left bottom**: Total Zeeman splitting $\Delta\Omega_L = \Delta\Omega_L^{\text{Stark, probe}} + \Delta\Omega_L^{\text{QSZ}}$, see eq. (5.58) for the Stark shift $\Delta\Omega_L^{\text{Stark, probe}}$ and eq. (5.15) for the quadratic Zeeman shift $\Delta\Omega_L^{\text{QSZ}}$. **Right:** Raw MORS signals for each polarization as a function of demodulation frequency Ω_{mod}. Signals for various polarizations are offset for clarity. Increasing polarization angle θ_{pol} is blue towards red.

where the constant α depends linearly the probe power and inversely on the detuning.

Using magneto-optical resonance signals (MORS) technique described in section 5.10.8 we can measure this effect as a function of input polarization angle. This is shown in fig. 5.14 along with the oscillator broadening. The functional dependence of this broadening is not fully understood and is guesses here, only out of curiosity, to have the form $\gamma_{\text{eff}} = A + (B + C/\Delta\Omega_L^{\text{Stark, probe}})^{-1}$, where A, B and C are fit constants.

5.11 Practical considerations

5.11.1 Anharmonicity and finite polarization

A reasonable concern is the anharmonicity caused by the quadratic Zeeman splitting described in section 5.4. For the experiments of chapter 6 we cannot just reduce Larmor frequency as it needs to roughly match the mechanical oscillator. For the experiments this was near 1.3 MHz and so the quadratic Zeeman splitting was 370 Hz, a non-negligible amount.

The Stark shift, as described in section 5.10.10, from the probe helps in this regard. We adjust the probe input polarization such that the quadratic Zeeman splitting is compensated as much as possible. This also corresponds to a reduced probe power broadening which allows more power to be used (if the wish is to keep the broadening constant). The probe induced broadening also helps with the

anharmonicity as the quadratric Zeeman splitting is washed out by the broadening.

Having a higher spin polarization also decreases the severity of the anharmonicity. In our experiments a spin polarization of $\sim 60\,\%$ was reached. Such a polarization is already enough for the the effective harmonic oscillator model to work well in practice, as witnessed by its utility and behavior in chapter 6. Compare the polarized oscillator case shown in the right panel of fig. 5.15 with the unpolarized case seen in left panel of fig. 5.13.

5.11.2 Motional averaging and broadband spin noise

So far we have not spoken as to the choice of dimensions, $300\mu m \times 300\mu m \times 10mm$, for the microchannel in which we confine and probe the atoms, which was shown in fig. 5.1. The narrow transverse size was chosen to have a short wall-to-wall transit of 1.4 µs, using eq. (5.66). This short timescale means that on the time scale of the mechanical decoherence, $\sim 14\,\mu s$[1], each atoms has transited the probe beam many times. This allows us to treat the entire ensemble of atoms as equally addressed and indistinguishable, and constitutes a motionally averaged interaction, as described in Hammerer et al. (2010); Borregaard et al. (2016).

Suppose now we readout the motionally averaged interaction of the spin oscillator. Detecting the output optical phase quadrature $\hat{Y}^{\text{out}}$ (polarization quadrature $\hat{S}_y$) from the spin system we observe the effective harmonic motion of the spin oscillator with a broadening of $\gamma_S = 2\pi \times 2.7\,\text{kHz}$ and resonance at the Larmor frequency of 1.343 MHz. This is as expected from the spin motion evolution and transduction according to eq. (5.42). This is the Lorentzian feature seen in the detected power spectral density shown in fig. 5.15.

Below this dominant contribution we see a small, and very broadband feature also centered at the Larmor frequency. The broadband response follows as the Larmor frequency is tuned and constitutes an undesirable increased imprecision noise floor. In this case the additional noise added is equivalent to 2 units of added shot noise.

The $\sim 1.2\,\text{MHz}$ spectral width of this feature suggests that the process responsible should occur on a very fast timescale of $\sim 1\,\mu s$, which is the rough timescale of an atom thermally crossing channel. From numerical simulations of the spin interaction in cell of our dimensions and probed in the same way, the transit time broadening caused by the thermal motion is found by Borregaard et al. (2016) to be 1.5 MHz, which is in reasonably good agreement.

The optical probe with a waist (radius) of 55 µm since the effect is related to a transient effect as the atoms fly through the beam one would expect this broadband effect to scale with the fraction of the confined atomic ensemble which is probed. This is indeed what is seen and is shown in Julsgaard (2003). This effect thus depends on the fraction of the cell that is optically probed. How this relates to the

[1] Using eq. (3.43) the mechanical decoherence rate is 11.5 kHz at a bath temperature of 7 K.

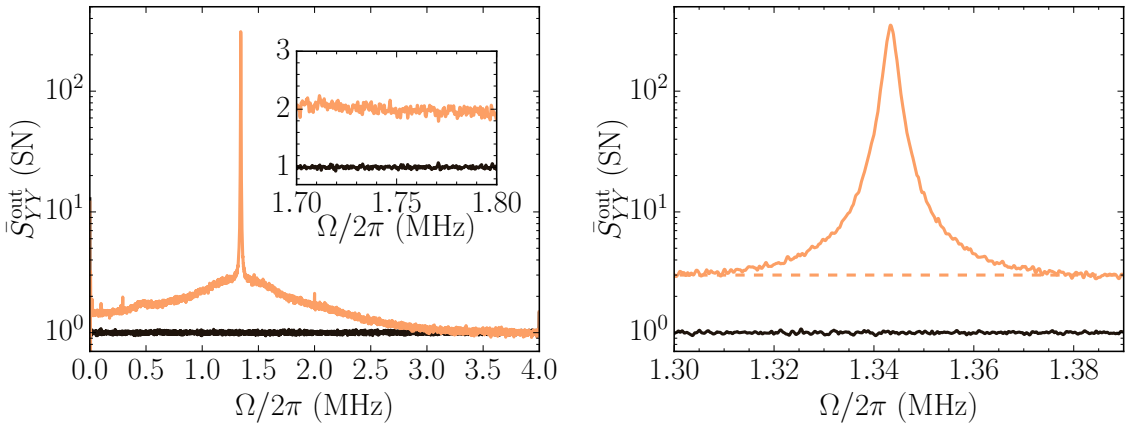

Figure 5.15: **Atomic broadband noise.** Measuring the $\hat{S}_y$ polarization quadrature we observe the spin motion readout in the optical phase quadrature. We show the power spectral density of this quadrature in the case of no atoms (black), which is simply shot noise, and with spin motion (yellow). **Left:** A broadband, 1.2 MHz at −3 dB, feature is seen with a peak at 3 units of optical shot noise. The spin effective oscillator response is the narrow feature. **Right:** A zoom of the effective oscillator spin response with the broadband pedestal contribution shown as the dashed yellow line. **Inset:** Zoom far from spin resonance.

optical probe is described in appendix D.2.3.

5.11.3 Faraday rotation

The Faraday rotation described by the $\hat{S}_z\hat{J}_z$ interaction term is responsible for the transduction of the atomic spin components into the light quadratures. The effect on input linear polarization components is such that the output contains a mix of the $\hat{S}_x$ and $\hat{S}_y$. This mixing on time scales near the Larmor frequency encodes information about the spin components. In steady state this mixing means the input polarization is rotated by an angle θ_F.

If we consider the mean classical components of the Stokes vectors we find them to be mixed by an angle of $2\theta_F$ at the output[2]. Using the rotation matrix $\boldsymbol{R}$ defined in eq. (2.84) we have

$$\begin{pmatrix} S_x^{\text{out}} \\ S_y^{\text{out}} \end{pmatrix} = \boldsymbol{R}(2\theta_F) \begin{pmatrix} S_x^{\text{in}} \\ S_y^{\text{in}} \end{pmatrix}. \tag{5.59}$$

The Faraday angle is given by

$$\theta_F = -\beta\langle \hat{J}_z \rangle \tag{5.60}$$

where $\hat{J}_z$ is the spin component along the probe direction. If we assume a perfect spin polarized spin ensemble, the mean spin component will be $4N_a$. Thus, if we

[2]From the definitions of the Stokes components this rotation of $2\theta_F$ corresponds to the axis of an linearly polarized input beam being rotated by θ_F.

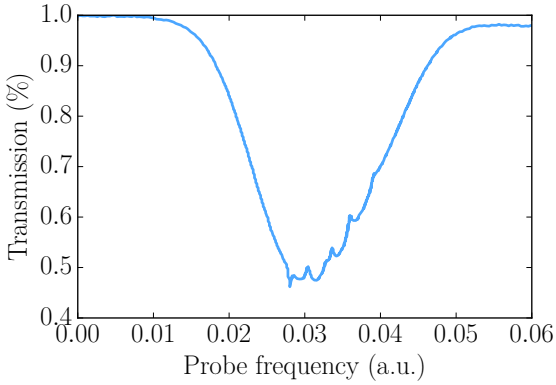

Figure 5.16: **Doppler broadening**. View of the 400 MHz wide atomic Doppler broadening (big dip) in the transmission of a probe through an atomic ensemble. This is measured through saturated absorption spectroscopy and the features seen are transitions from $F = 4 \rightarrow F'$ and crossover resonances, see Schmidt et al. (1994) for more details.

orient this spin along the probing direction we can get a very large ($\theta_F \gg 1$) rotation of the input polarization state. This can be used to calculate the interaction strength or number of atoms.

Since we orient our bias magnetic field along x, perpendicular to the probing direction of z, we can approximate $\langle \hat{J}_z \rangle \approx \sqrt{\langle \hat{J}_x \rangle} \approx \sqrt{4N_a}$, for the perfect polarized case. As a theoretical ballpark figure for our typically experimental conditions at 60 °C, $N_a \simeq 10^9$ and a detuning of $\Delta_S = 2\pi \times 3$ GHz the Faraday rotation is $< 0.01°$.

5.11.4 Doppler broadening

The atomic thermal motion in the microchannel mean that atoms moving along the probe direction see it Doppler shifted. Scanning the probe through the $F = 4 \rightarrow F'$ transition, with frequency F_{D2}, clearly shows this as seen in fig. 5.16. This is quite a large effect since the atoms are at about room temperature.

The Doppler broadening (FWHM) of the transitions is given by

$$\Delta f = \sqrt{\frac{8 k_B T \ln 2}{m_{\mathrm{Cs}}}} \frac{f_{\mathrm{D2}}}{c} \tag{5.61}$$

where m_{Cs} is the mass of a cesium atom and T the ensemble temperature. The scale of the Doppler broadening is roughly 400 MHz in our case and by far dominates the line broadenening of $\sim$ 5 MHz from spontaneous emission. In practice, we need to probe much further detuned than the doppler width to avoid absorption which we desire in order to neglect excited state populations. From a typical absorption profile of $\propto \frac{(\gamma_{\mathrm{doppler}}/2)}{(\gamma_{\mathrm{doppler}}/2)^2 + \Delta_S^2}$ it is clear that we need to be detuned by at least 2.8 GHz in order to have $< 0.5\,\%$ absorption relative to the on resonance case.

5.11.5 Sources of loss

In what follows we will describe a few relevant processes which lead to "intrinsic" damping of the effective spin oscillator described in section 5.10. The total dissipation rate relevant for the evolution of the spin oscillator, according the quantum Heisenberg-Langevin equations of eq. (5.42), is given by the sum of all relevant decay channels as written in eq. (5.44). Expanding the intrinsic loss $\gamma_{S,0}$ term into its component parts we find,

$$\gamma_{S,0} = \gamma_{\text{SE}} + \gamma_{\text{spin-flip}} + \gamma_{\partial B} + \gamma_{\text{pump}} + \gamma_{\text{repump}} + ... \tag{5.62}$$

The relevant loss mechanisms discussed here leading to this damping are the spin exchange (γ_{SE}) and spin-flips ($\gamma_{\text{spin-flip}}$). Also discussed are the effect magnetic field inhomogeneities ($\gamma_{\partial B}$) and finally the pump (γ_{pump}) and repump (γ_{repump}) induced spontaneous emission damping.

At the operating conditions of the work described in chapter 6 the excess noise sources comprised roughly 1 kHz of broadening. This was predominantly due to wall collisions since a measurement of $\gamma_{S,0}$ at very low Larmor frequencies (low magnetic field), very low probe power, and no pump or repump, gave a ~ 1 kHz broadening. This type of measurement is commonly referred to as the "T2 in the dark" of the cell. Further scaling of the magnetic field gradient showed that this was not the main culprit.

Spin-exchange collisions

The high atomic densities used mean atom-atom collisions may be a relevant factor. When atoms collide they may exchange electron spin whilst conserving the overall spin. This process is aptly named spin-exchange collisions and has the effect of depolarizing the ensemble and unsurprisingly scales with the collision rate. Since the number density $n(T)$ scales exponentially with temperature T, and the atoms have an increasing mean relative thermal velocity $\bar{v}_{\text{th}}(T)$ this collision rate increases substantially. This effect is diminished for higher spin polarized ensembles, since colliding atoms both in $|4,4\rangle$ leave indistinguishably. All other decoherence channels of course still apply in this case. More on this process, and the result below, can be found in Seltzer (2008).

The collision rate $\sigma n(T)\bar{v}_{\text{th}}(T)$ is related to the expected spin-exchange (SE) broadening γ_{SE} by

$$\gamma_{\text{SE}}/2\pi = \sigma n(T)\bar{v}_{\text{th}}(T)q_{\text{SE}}^{-1}, \tag{5.63}$$

$$q_{\text{SE}}^{-1} = \frac{2I(2I-1)}{3(2I+1)^2}, \tag{5.64}$$

$$\bar{v}_{\text{th}}(T) = \sqrt{\frac{8k_BT}{\pi M}} \tag{5.65}$$

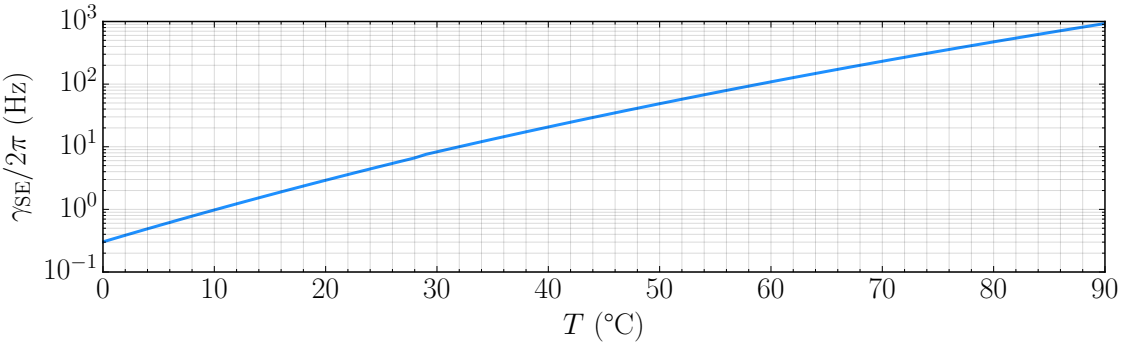

Figure 5.17: **Spin exchange broadening.** Added broadening due to spin exchange collisions according to eq. (5.63). Cesium atoms are confined to a rectangular channel that measures 10 mm in length and $300 \times 300\,\mu m$ in cross-section. A collisional cross-sectional area of $2.1\,nm^2$, as measured by Ressler et al. (1969), is assumed.

where M is the molar mass, σ the effective collisional cross-sectional area, and q_{SE}^{-1} a spin-exchange broadening factor related to the collision rate probability of effectively exchanging spins. This spin-exchange broadening is shown in fig. 5.17 as a function of temperature. Added broadenings of on the order of $100 - 200\,Hz$ is in practice seen at near 70 °C operating temperatures.

Atoms can, of course, also interact with other species of atoms in the cell. They may be deliberately added as a buffer gas or are simply a contaminant. These cases also lead to a larger decoherence, but are not discussed as they are not relevant in this work.

Wall collisions

Clearly when the atomic vapour is contained in the microchannel the atoms are constantly bouncing off the walls. This is true in general for a containing atomic vapours in a vessel, typically glass for optical purposes. This wall interaction introduces additional decoherence, painfully true for spin ensembles, thus, the walls are covered with an anti-relaxation coating. This coating preserves the spin polarization with a very high probability of an atom-wall collisions. The property was first discovered in 1958 by Robinson et al. (1958) and has since been extensively studied. See Seltzer et al. (2010) for an overview and the modern tools employed to further study the coatings.

These coatings see continuous improvements and those used in our experiments are made by Mikhail Balabas. Some are even able to withstand very high temperatures before compromising the spin coherence. This is clear from Seltzer and Romalis (2009), enabling a large vapour pressure, and thus a high number of atoms if desired.

In a thermal vapour of constant pressure, the average time between wall collisions in a cell of volume V and internal surface area S is given by

$$\tau_{wall} = \frac{4V}{\bar{v}_{th} S}, \tag{5.66}$$

which at room temperature means it takes an atom about 1.4 µs between each wall collision. In our realization of the vapour cell this collision rate is quite high as we confine the atoms within a square micro-channel measuring only 300 µm on the side and being 10 mm long.

While the probability of spin decoherence per wall collision may be low, many collisions occur per second in the small channel leading to a fairly high[3] spin decoherence rate. When an atom collides with the wall it will, in general, interact a lot with the surface causing the electron spin to flip which leads to decoherence. It turns out that a paraffin coating can severely reduce this spin-flip rate, and thus preserves the atomic spin over many atom-wall collisions. If the atoms can collide with the wall N times before a spin flip occurs then the contribution to the spin decoherence will be given by

$$\gamma_{\text{spin-flip}} \propto \frac{1}{N\tau_{\text{wall}}}. \tag{5.67}$$

This increased spin lifetime is crucial since we are interested in dynamics over many coherent evolutions (on time scale of $\gg 1/\Omega_L \sim 1\,\mu\text{s}$) of the spin oscillator. It is, thus, required that the atoms are able to endure multiple wall collisions without decohering. Furthermore, considering the ensemble on an extended time scale compared with the average wall collision rate means that we have some degree of thermal averaging. This means we address the atoms equally and indistinguishably allowing us to more accurately treat them as a single oscillator.

More severe atom-wall collisions where the nuclear spin also flips are also possible, though less frequent. These interactions do not preserve the total spin, and thus lead to a more severe form of depolarization.

Magnetic field inhomogeneity

The cell of fig. 5.1 is placed in a bias magnetic field which splits the Zeeman sublevels by the Larmor frequency. However, a spatially inhomogenous magnetic field means that as the atoms move around the cell they precess with differing Larmor frequencies. Suppose we have the bias field along a direction i where the cell length is L_i. In the relevant limit where the field gradient is small, the added decoherence from the inhomogeniety is roughly given by Julsgaard (2003)

$$\gamma_{\partial B} \approx \left(\frac{g_F \mu_B}{\hbar}\right)^2 \left(\frac{L_i^3}{\bar{v}_i}\right) \left(\frac{\partial B_i}{\partial x_i}\right) \tag{5.68}$$

where $\bar{v}_i$ is the mean speed along the i direction. The spatial inhomogeneity, and thus added decoherence, is largest along the axis of the microchannel as it is roughly 30 times longer than it is wide. For us this is a mostly negligible effect.

[3] Compared to larger cells which can have decoherence times on the timescale of minutes.

Similarly a bias field that is noisy on timescales comparable to the Larmor frequency will also add decoherence. In practice, this is straightforward to avoid by appropriate filtering of the current generating the field.

Optical pumping

Just as the probe induces spontaneous emission broadening, as discussed in section 5.10.3, so too do the optical pumping fields described in section 5.10.6. Most important is the pump field which addresses the same $F = 4$ manifold as our probe. Since the job of this field is to be absorbed, and thereby increase to over spin polarization, it is not far detuned as our probe. This allows for small optical powers to be used, but the associated increased spontaneous emission broadening from this field can still be very large. Thus in practice its use is a delicate trade-off pitting spin polarization, and by extension the readout rate, against added decoherence from the increased broadening.

Less important is the repump field as it addresses the $F = 3$ manifold. However, since the ground state hyperfine levels are split by 9.2 GHz it essentially acts as a far detuned probe. Since the optical power of the repump actually driving the atoms is low compared to the probe, its broadening of the $F = 4$ ground state manifold is in practice negligible.

Chapter 6

Hybrid system back-action evasion

We now, finally, turn to the part of the thesis motivated by our introductory example of section 1.1. In the example, we measured an oscillators motion with respect to some quantum reference frame with an effective negative mass. Here we realize such a measurement by observing the mechanical motion of the membrane discussed in chapter 3, by using optomechanics as discussed in chapter 4, in the reference frame of a negative mass atomic spin oscillator as just described in chapter 5.

The measurement is performed in a cascaded fashion as shown in fig. 6.1, where an optical field acts as the link between the two systems. The spin system is optically readout first and the output then appropriately filtered. This translates the optical language spoken by the spins to that spoken by the mechanics. The mechanical oscillators motion is then probed and detected with an improved sensitivity if the spin system is prepared in a negative mass configuration.

Before fully detailing exactly how this is all accomplished in practice, let us consider an idealized situation first in section 6.1. We will then discuss the experimental implementation in section 6.2 before presenting back-action evading measurements in the pulsed regime in section 6.3.

We then finally turn to the business of describing quantum back-action evading measurements section 6.4. Part of the work presented in this chapter, in particular parts of section 6.4, has been published in Møller et al. (2017).

6.1 Quantum non-demolition back-action evasion

In practice, losses abound and the light driving and reading out the atomic spins are only partly that which interacts with the mechanical oscillator. Here we will treat the lossless case first and only then include them. We will neglect any higher order tensor effects for the spin system, treating the interaction as purely quantum non-demolition (QND). Likewise for the optomechanical subsystem, we will consider the cavity to be on resonance ($\bar{\Delta} = 0$) along with a linearized QND interaction. The

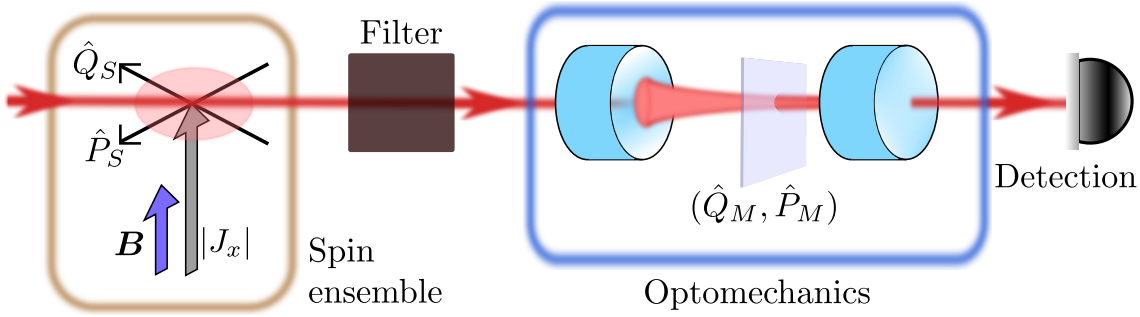

Figure 6.1: **Basic schematic of the cascaded hybrid subsystems.** The spin system (yellow box) is optically read out first and the output then appropriately filtered (dark box). This translates the optical language spoken by the spins to that spoken by the mechanics. The mechanical oscillators motion is then probed in the optomechanical system (blue box). The subsequent detection of its motion comes with an improved sensitivity if the spin system is prepared in a negative mass configuration. The output is drawn in cavity transmission to emphasize that the hybrid system has a cascaded read out scheme.

interaction Hamiltonian will, thus, be given by

$$\hat{\mathcal{H}}_{\mathrm{int},i} = \sqrt{\Gamma_i}\,\hat{Q}_i\hat{X}_i,\ \ i \in \{S, M\} \tag{6.1}$$

where Q_i is the canonical position quadrature of each subsystem and $\hat{X}_i$ is the light amplitude quadrature interacting with said subsystem.

We are interested in seeing the effect on the light from the cascaded interaction with the two subsystems. Let us consider the quadrature output from each system separately first. For both subsystems the input output relations are

$$\begin{aligned} \hat{X}_i^{\mathrm{out}}(t) &= \hat{X}_i^{\mathrm{in}}(t) \\ \hat{Y}_i^{\mathrm{out}}(t) &= \hat{Y}_i^{\mathrm{in}}(t) + \sqrt{\Gamma_i}\,\hat{Q}_i(t) \end{aligned} \tag{6.2}$$

where $i \in \{S, M\}$ for the spin and mechanical subsystems respectively. It is clear that each light amplitude quadrature $\hat{X}_i$ is a QND variable of the interaction Hamiltonian of eq. (6.1), which is reflected in the input-output equations.

6.1.1 Lossless case

Now, the spins couple to light polarization degrees of freedom whereas the mechanics couples to the amplitude and phase quadratures of light. Formally we map these under the same umbrella of $\hat{X}_i$, but in practice they are fundamentally different. However they can transformed into one another as described in section 6.2. In practice, we can ensure that the output of the spin system is fed as the input to the mechanical system according to

$$\hat{X}_M^{\mathrm{in}} = -\hat{X}_S^{\mathrm{out}}, \tag{6.3a}$$

$$\hat{Y}_M^{\mathrm{in}} = -\hat{Y}_S^{\mathrm{out}}. \tag{6.3b}$$

This is the action of the filter in fig. 6.1. The full input-output equations from before the spins to after the mechanics, i.e. the full hybrid input-output relations, will then be

$$\hat{X}^{\text{out}} = -\hat{X}^{\text{in}} \tag{6.4a}$$

$$\hat{Y}^{\text{out}} = -\hat{Y}^{\text{in}} - \left[\sqrt{\Gamma_M}\,\hat{Q}_M - \sqrt{\Gamma_S}\,\hat{Q}_S(t)\right]. \tag{6.4b}$$

If we take the readout rates to be the same $\Gamma_M = \Gamma_S = \Gamma$, and the oscillators to have the same frequency $\Omega_M = |\Omega_S| = \Omega$ then the output phase quadrature will contain the commuting EPR variables initially motivated in the generic oscillator case. Writing the time dependence of the operators out explicitly we see that

$$\begin{aligned}\hat{Y}^{\text{out}}(t) = -\hat{Y}^{\text{in}}(t) - \sqrt{\Gamma}\Big[&\left(\hat{Q}_M(0) - \hat{Q}_S(0)\right)\cos(\Omega t) + \\ &\left(\hat{P}_M(0) \mp \hat{P}_S(0)\right)\sin(\Omega t)\Big]\end{aligned} \tag{6.5}$$

where we have used the fact that for the spin oscillator, being considered "positive" or "negative" mass is tantamount to the direction of phase space rotation. Thus, we differentiate the two by the sign of the spin oscillator frequency $\pm\Omega_S$ ($\equiv$ positive / negative mass). This treatment is facilitated by our choice of dimensionless canonical operators. Notice that this input-output relation is just like eq. (1.2) and the sin and cos components commute in the case of negative mass ($\Omega_S = -\Omega$). Thus, they can both be simultaneously known unbounded by the Heisenberg uncertainty principle.

In the case of negative mass operation, it was previously stated that the back-action could be evaded. Further insight into how this is achieved is found by considering the thermal and light forces effect on the mechanical and spin oscillator. In the Fourier domain we have

$$\hat{Q}_M(\Omega) = \chi_M(\Omega)\left[\sqrt{\gamma_{M0}}\,\hat{F}_M(\Omega) + \sqrt{\Gamma_M}\,\hat{X}^{\text{in}}_M(\Omega)\right], \tag{6.6a}$$

$$\chi_M(\Omega) = \Omega_M/(\Omega_M^2 - \Omega^2 - i\Omega\gamma_{M0}), \tag{6.6b}$$

$$\hat{Q}_S(\Omega) = \chi_S(\Omega)\left[\sqrt{\gamma_S}\,\hat{F}_S(\Omega) + \sqrt{\Gamma_S}\,\hat{X}^{\text{in}}_S(\Omega)\right], \tag{6.7a}$$

$$\chi_S = \pm\Omega_S/(\Omega_S^2 - \Omega^2 - i\Omega\gamma_S). \tag{6.7b}$$

There could, of course, be additional forces, which add to the thermal and back-action drives. Both systems respond with their susceptibilities on the time scales given by their damping rates.

Using the above eqs. (6.6) and (6.7) together with eq. (6.4), the output phase quadrature of the full hybrid system is

$$\begin{aligned}\hat{Y}^{\text{out}}(\Omega) = &\underbrace{-\hat{Y}^{\text{in}}(\Omega)}_{\text{SN}} - \underbrace{\sqrt{\Gamma_M\gamma_M}\,\chi_M(\Omega)\hat{F}_M(\Omega) + \sqrt{\Gamma_S\gamma_S}\,\chi_S(\Omega) * \hat{F}_S(\Omega)}_{\text{TN}} \\ &+ \underbrace{\left[\Gamma_M\chi_M(\Omega) + \Gamma_S\chi_S(\Omega)\right]\hat{X}^{\text{in}}(\Omega)}_{\text{BA}}.\end{aligned} \tag{6.8}$$

It is clear that the thermal noise contributions cannot interfere as the driving thermal forces $\hat{F}_M$ and $\hat{F}_S$ draw from two uncorrelated reservoirs. However, the back-action contribution for both systems is driven by the fluctuations of the common light amplitude quadrature $\hat{X}^{\text{in}}$. Thus, by manipulation of the back-action term $\Gamma_M\chi_M(\Omega) + \Gamma_S\chi_S(\Omega)$ we can remove the back-action contribution at particular frequencies, or indeed, over a wider bandwidth. Indeed if we set $\Gamma_M = \Gamma_S$ and $\chi_S = -\chi_M$ the contribution can be completely removed from the output phase quadrature of light.

This is the essence of the back-action evasion discussed in the motivation example of section 1.1, and can be understood as follows. Although the individual systems still experience a stochastic quantum back-action force, and are thus kicked around in phase space, the light measures the relative motion, which is unaffected. This is due to the fact that both systems are perturbed by the *same* light noise but respond out of phase and with equal magnitude.

The above logic of the back-action cancellation works equally well in the time domain. In that case we have

$$\begin{aligned}\hat{Y}^{\text{out}}(t) = &\underbrace{-\hat{Y}^{\text{in}}(t)}_{\text{SN}} - \underbrace{\sqrt{\Gamma_M\gamma_M}\,\chi_M(t) * \hat{F}_M(t) + \sqrt{\Gamma_S\gamma_S}\,\chi_S(t) * \hat{F}_S(t)}_{\text{TN}} \\ &+ \underbrace{[\Gamma_M\chi_M(t) + \Gamma_S\chi_S(t)] * \hat{X}^{\text{in}}(t)}_{\text{BA}}\,.\end{aligned} \tag{6.9}$$

where the $*$ indicated the time convolution. In the time domain it is reasonable to speak of back-action cancellation on short and long time scales (relative to the subsystems), just as it makes sense in the Fourier domain to speak of evasion in a wide bandwidth or at a particular Fourier frequencies.

6.1.2 Equations of motion and input-output relations

The Heisenberg-Langevin equations for each oscillator $i \in \{S, M\}$ can be written as

$$\begin{aligned}\dot{\hat{Q}}_i &= \Omega_i\hat{P}_i \\ \dot{\hat{P}}_i &= -\Omega_i\hat{Q}_i - \gamma_i\hat{P}_i - \sqrt{2\gamma_i}\,\hat{F}^{\text{th,in}} - \sqrt{\Gamma_i}\,\hat{X}_i^{\text{in}},\end{aligned} \tag{6.10}$$

as can be read for both oscillators from eqs. (4.21) and (5.42). As described in section 5.10.1, positive or negative mass configuration of the spin oscillator is simply captured in the sign of the frequency Ω_S in the case of dimensionless motional quadrature operators. We write eq. (6.10) in compact matrix notation as

$$\dot{\boldsymbol{Q}}_i = \boldsymbol{M}_i\boldsymbol{Q}_i + \hat{\boldsymbol{F}}_i^{\text{in}}, \tag{6.11}$$

where we have defined

$$\boldsymbol{Q}_i \equiv \begin{pmatrix}\hat{Q}_i \\ \hat{P}_i\end{pmatrix},\ \boldsymbol{M}_i = \begin{pmatrix}0 & \Omega_i \\ -\Omega_i & -\gamma_i\end{pmatrix},\ \hat{\boldsymbol{F}}_i^{\text{in}} = -\sqrt{\gamma_i}\,\hat{\boldsymbol{F}}_i^{\text{th,in}} - \sqrt{\Gamma_i}\,\hat{\boldsymbol{F}}_i^{\text{L,in}}, \tag{6.12}$$

and the thermal and light force vectors given by

$$\hat{\boldsymbol{F}}_i^{\mathrm{th,in}} = \begin{pmatrix} 0 \\ \hat{F}_i^{\mathrm{th,in}} \end{pmatrix}, \quad \hat{\boldsymbol{F}}_i^{\mathrm{L,in}} = \begin{pmatrix} 0 \\ \hat{X}_i^{\mathrm{L,in}} \end{pmatrix}. \tag{6.13}$$

In the steady state spectral domain these output light quadratures from each system can by compactly written as

$$\hat{\boldsymbol{X}}_i^{\mathrm{out}}(\Omega) = \mathbb{H}_i(\Omega)\hat{\boldsymbol{X}}_i^{\mathrm{in}}(\Omega) + \sqrt{\Gamma_i\gamma_i}\,\chi_i(\Omega)\hat{\boldsymbol{F}}_i^{\mathrm{th,in}}(\Omega), \tag{6.14}$$

$$\mathbb{H}_i(\Omega) = \begin{pmatrix} 1 & 0 \\ \Gamma_i\chi_i(\Omega) & 1 \end{pmatrix}. \tag{6.15}$$

For visual clarity, when speaking of the individual subsystems, we will write $\mathbb{H}_S = \mathbb{S}$ and $\mathbb{H}_M = \mathbb{M}$.

6.1.3 Lossy case

We treat optical losses as an additional beam splitter as described in detail in appendix B.5.1, which introduces vacuum quadratures $\hat{\boldsymbol{X}}_j^{\intercal} = \left(\hat{X}_j^{\mathrm{vac}}, \hat{Y}_j^{\mathrm{vac}}\right)$. This field is uncorrelated with the other input fields and acts as a replacement for the lost fraction of the particular quadrature due to some loss channel j characterized by a power transmittivity η_j.

Let η_1 be the transmittivity between the spin and mechanical system. Using the mapping of the light quadratures described in eq. (6.4) with the aforementioned treatment of losses, the input light quadratures to the optomechanical system are

$$\hat{\boldsymbol{X}}_M^{\mathrm{in}} = -\sqrt{\eta_1}\,\hat{\boldsymbol{X}}_S^{\mathrm{out}} + \sqrt{1-\eta_1}\,\hat{\boldsymbol{X}}_1^{\mathrm{vac}}. \tag{6.16}$$

With the QND light-oscillator coupling, the oscillators are read out purely in the optical phase quadrature, leaving the amplitude quadrature unaltered except due to losses. Suppose that η_2 is the transmittivity between oscillator M and the detection system. If the input quadratures $\hat{\boldsymbol{X}}_S^{\mathrm{in}}$ contain just vacuum noise, then[1], taking losses into account we can modify the simple eq. (6.5) to give the hybrid full input-output equations of

$$\hat{\boldsymbol{X}}^{\mathrm{out}} = -\hat{\boldsymbol{X}}^{\mathrm{in}} + \left(1, 0\right)\sqrt{\eta_2}\left(\sqrt{\eta_1}\sqrt{\Gamma_S}\,\hat{\boldsymbol{Q}}_S - \sqrt{\Gamma_M}\,\hat{\boldsymbol{Q}}_M\right). \tag{6.17}$$

These equations will form the basis of the discussions in section 6.3.

[1]The input vacuum quadratures experience loss, and thus the output, say amplitude quadrature, would be $\hat{X}^{\mathrm{out}} = -\sqrt{\eta_1\eta_2}\,\hat{X}^{\mathrm{in}} + \sqrt{\eta_2(1-\eta_1)}\,\hat{X}_1^{\mathrm{vac}} + \sqrt{1-\eta_2}\,\hat{X}_2^{\mathrm{vac}}$. However, we can just as well write $\hat{X}^{\mathrm{out}} = -\hat{X}^{\mathrm{in}}$ since the resultant correlation function will be equivalent.

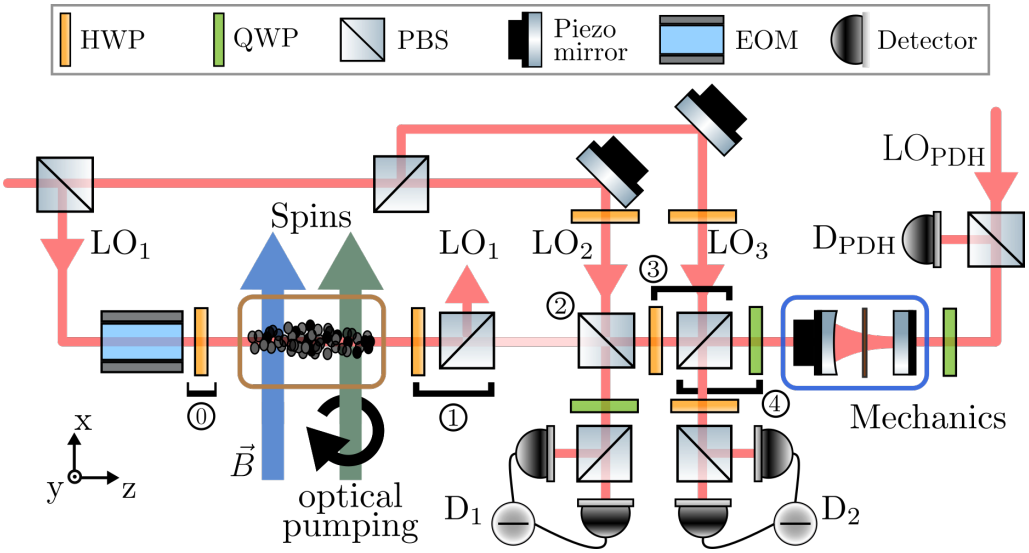

Figure 6.2: **Hybrid setup schematic** The atomic spin system (orange box, left) is subjected to a magnetic $\boldsymbol{B}$ field (blue arrow) and optical pumping (olive arrow) along the x direction. It is driven and probed by local oscillator 1 (LO_1), along the z direction, with linear polarization angle set by half-wave plate (0). The output is polarization filtered by section (1) and then phase filtered by the appropriate introduction of LO_2 in section (2). The conversion of polarization quadratures into phase and amplitude quadrature is done by a polarization projection in section (3). The optomechanical membrane-in-the-middle set-up (blue box, right), is probed in reflection by the injected LO_2. The reflected light is separated from the input by section (4) and homodyning this field with the high power LO_3 allows for the detection of the optical phase quadrature. The remaining cavity port is probed in reflection with by LO_{PDH} by the same method as (4). This field allows the optomechanical system to be stabilized on long time scales with respect to the probing field LO_2. **Legend:** HWP, half-wave plate; QWP, quarter-wave plate; PBS, polarizing beamsplitter; EOM, electro-optic modulator.

6.2 Experimental realization

In fig. 6.2 the hybrid experimental setup used for both pulsed and CW experiments is shown. On the left, in the orange box, we have the atomic spin ensemble, which was described in section 5.1, which realizes an effective harmonic oscillator as discussed in section 5.10. On the right, in the blue box, the optomechanical system consisting of a membrane in the middle of a high finesse cavity. This part of the experiment is described in section 4.2.

Beyond the two subsystems, the hybrid setup is characterized by polarization and phase filtering, shown as sections (1) and (2) in fig. 6.2 and further described in section 6.2.1. Also important is the optical link connecting both systems and the allowing the detection of their motion, shown in fig. 6.2 as the red optical path and section (4). This is further described in section 6.2.2.

The optomechanical cavity is probed in reflection. The cavity is locked in the same way as described in section 4.2.2 using a PDH signal derived from a low power, orthoganolly polarized, auxilary beam probing the cavity from the back

(undercoupled) port.

6.2.1 Polarization and phase filtering

Polarization filtering and phase rotations are necessary since the atomic spins respond to modulation out of phase, and in an orthogonal polarization, to the local oscillator probe LO_1, which is a linearly polarized field with a large classical S_x Stokes component. The orthogonal polarization components are $\hat{S}_y$ and $\hat{S}_z$ and form quadratures equivalent to amplitude and phase quadratures of the light, see section 2.2.3.

Subsequent polarization conversion is necessary since the mechanical oscillator ultimately responds only to modulation in phase with the LO (i.e. amplitude modulation) and necessarily in the same polarization mode. Since LO_1 was out of phase with the quadratures of $\hat{S}_y$ and $\hat{S}_z$ and in the orthogonal polarization, we wish to introduce a new LO, namely LO_2, replacing LO_1 with the following properties. LO_2 should be in an orthogonal linear polarization mode to LO_1 and $\pi/2$ phase shifted with respect to LO_1. This way the $\hat{S}_y$ and $\hat{S}_z$ quadratures are mapped into phase and amplitude modulation of the new carrier LO_2. To accomplish this, three filtering stages are required.

First, polarization filtering of LO_1 is done using a half-wave plate and polarizing beam splitter right after the microcell, see (1) in fig. 6.2. This filtering extinguishes the power of LO_1 better than $1{:}10^3$ from the optical path with little loss of the orthogonal polarization quadratures. The loss of these are given by the transmission of the PBS and which was typically $\sim 3\,\%$.

Secondly, the phase filtering, section (2) in fig. 6.2, consists of using a Mach-Zehnder interferometer, arms hosting LO_1 and LO_2 with output at PBS_2, is used. Observed interference on detector D_1 allows for the phase of the spin quadratures $\{\hat{X}_S^{\text{out}}, \hat{Y}_S^{\text{out}}\}$ to be set with respect to LO_2, and thus the input fields $\{\hat{X}_S^{\text{in}}, \hat{Y}_S^{\text{in}}\}$.

In practice this is accomplished by way of an electro-optic modulator in LO_1 prior to the atomic spins, driving by a coherent sinusoidal modulation at 10MHz. This produces sidebands in the $\hat{S}_z$ quadrature only, and with negligible added broadband noise in $\hat{S}_y$. This is ensured by tuning a DC bias voltage across the electro-optic modulator and by adjustment of its axis with respect to the optical polarization. It is set up to produce small modulations and as such a large AC voltage modulation, though still small with respect to the π voltage, is required for even modest modulation depths. The ratio of $\hat{S}_z$ modulation to $\hat{S}_y$ or $\hat{S}_x$ polarization modulation inadvertently introduced by the electro-optic modulator is typically $\gtrsim 10^5$ in power.

The coherent $\hat{S}_z$ drive at 10MHz is far from both oscillator responses. Both oscillators are typically set around 1.3 MHz and have linewidths of ~ 5 kHz. Only the broadband response of the atomic spins have a broad enough response to significantly affect (or be affected by) the $\hat{S}_z$ modulation. The high modulation frequency is chosen such that effect of the atoms on these sidebands, and vice versa, is negligible.

These modulation sidebands are in the same polarization mode as the quantum back-action driving the spin system as well as the response of the spin ensemble. This polarization is thus desired to be fully transmitting by the PBS in (2). In practice a half-wave plate allows for an adjustable fraction of this polarization to be picked off. Some finite sideband power is needed for the phase filtering lock, and thus typically $\sim 5\,\%$ is reflected towards detector D_1.

From the same PBS, most of LO_2 is reflected. A half-wave plate in the LO_2 arm allows some to be transmitting, which is modematched to the spatial mode of LO_1 with a visibility typically $> 95\,\%$. The demodulated balanced polarimetry measurement of $\hat{S}_z$ on detector D_1 produces a signal proportional to $\cos\delta\phi_{\mathrm{LO1,2}}$, where $\delta\phi_{\mathrm{LO_{1,2}}}$ is the phase difference between LO_1 and LO_2. This is used as an error signal in a feedback loop stabilizing their relative phase to be $\pi/2$ by actuating the piezoelectric transducer in the LO_2 arm. Adding an offset to the error signal allows for a stabilized relative phase $\neq \pi/2$. This enables rotations of the quadratures driving the subsequent optomechanical system to be controllably adjusted.

Now we have the quadratures $\{\hat{X}_S^{\mathrm{out}}, \hat{Y}_S^{\mathrm{out}}\}$, with the desired phase with respect to LO_2, at the output of the interferometer. However, they still occupy orthogonal polarization modes since LO_2 is reflected and the polarization quadratures transmitted through the output PBS. Thus, we turn to the the third, and final, step of the filtering. This can be seen as section (3) in fig. 6.2. A half-wave plate and a PBS projects a controllable (typically very small) fraction LO_2 into the polarization mode of the aforementioned polarization quadratures, which are transmitted in the absence of the have-wave plate. In practice the amount of projected LO_2 is $\lesssim 1\,\%$ resulting is little loss of the aforementioned optical quadratures $\{\hat{X}_S^{\mathrm{out}},\ \hat{Y}_S^{\mathrm{out}}\}$.

6.2.2 Optical link and detection

Suitable optics mode match and direct the optical output quadratures $\{\hat{X}_S^{\mathrm{out}}, \hat{Y}_S^{\mathrm{out}}\}$ from the spin system to the optomechanical cavity where they are considered the optical input quadratures $\{\hat{X}_M^{\mathrm{in}}, \hat{Y}_M^{\mathrm{in}}\}$. These quadratures are in a mode with the optical frequency of LO_1. The cavity resonance frequency is stabilized relative to this frequency using the Pound-Drever-Hall method, on long time scales, just as described in section 4.4.3.

The original output quadratures of the spin system are also in the spatial mode of LO_1, and thus this mode is matched to the optomechanical cavity. The degree of spatial overlap given by the modematching η_{mm} is typically in the range of $\simeq 90\,\%$. The mode matching is defined as the fraction of incident LO_1 power going into the TEM_{00} compared to all cavity modes and is discussed in appendix B.5.3.

In practice this is done by adjusting the waveplate in (1) allowing LO_1 through the setup. The optics directing the beam are then adjusted. Allowing this field through also allows for the total optical power transmission for the output optical spin quadrutures to be measured. This is typically in the $60 - 65\,\%$ range.

Detecting the full output of the hybrid system is done by isolating the reflection from the cavity as shown in section (4) shown in fig. 6.2. The amplitude and phase quadratures are measured on detector D_2 by direct and balanced homodyne detection, respectively, which are discussed in appendices B.1 and B.2. In the former case, all light was directed onto a single detector diode. In the latter case, the use of an additional local oscillator, LO_3, is needed as a phase reference.

LO_3 is split from LO_2 before the piezo-actuator in the interferometer arm shown in fig. 6.2 and when recombined on the polarizing beam splitter of section (4) constitutes another interferometer. This interferometer has balanced arm lengths (one arm goes to the cavity and back) and is low frequency stabilized by feedback on the peizo-electric transducer shown in the arm of LO_3.

For the experiments in section 6.3 the error signal derived from the 10 MHz, now amplitude modulation, sidebands also used to lock the phase filtering interferometer. Demodulating the homodyning current at this frequency gave an error signal whose minimum corresponded to minimal detected amplitude modulation, thus the optical phase quadrature. For the experiments in section 6.4, the error signal was simply the low frequency interference fringe of LO_2 and LO_3, which worked equally well.

6.2.3 Optical Losses

The relevant optical losses in the hybrid system are numerous, but of variable importance. We speak in terms of losses ϵ instead of efficiencies $\eta = 1-\epsilon$ since they are easier to compare. In order of importance, these losses can be broken down into two main parts. First, the loss between the spin and mechanical systems, and second, the detection losses. These will now be considered in the context of the quantum back-action evading measurements to be described in section 6.4.

The vapour cell used had a full transmission of 13 %, but only the loss going from inside the cell to outside is of importance from a quantum perspective. This corresponded to a roughly 7 % optical loss. From there (outside the cell) the transmission losses to the input of the optomechanical system were 33 %. Once there, there are the optical incoupling losses of the free space field to the intracavity field driving coupling to the mechanics. These losses derive from the cavity overcoupling and mode matching which where responsible for losses of 4 % and 11 %, respectively. In total these losses amount to roughly 55 % of the quantum vacuum driving spin system being replaced before driving the mechanics. This is a significant hindrance to our back-action evading protocol, but does not preclude it entirely as we will see in section 6.4.

Detection losses, from a quantum back-action evading measurement, is of little importance since it merely reduces the signal to noise ratio of the detected motion. The losses associated with exiting the cavity are as with the input, that is, the cavity overcoupling and mode matching are responsible for losses of 4 % and 11 % respectively. The optical loss from outside the optomechanical cavity to the detector

was 15 % and the typically achieved homodyne visibility of 89 % gave an extra 21 % loss. The glass encapsulated diodes of our homodyne detector have a quantum efficiency of about 90 %[1] and are thus responsible for a roughly 10 % loss. This makes for an overall loss in converting intracavity quantum fluctuations into photocurrent fluctuations of 61 %.

In the above loss budget calculation we used the fact that the power equivalent detection efficiency for a homodyning visibility of $\mathcal{V}$ is actually $\eta = \mathcal{V}^2$ as shown in appendix B.5.2. Thus, as we just saw, this visibility is of high importance in the case of homodyne detection.

Similarly important is the cavity mode matching η_{mm}, which is described in appendix B.5.3. First, in the transmittance of the fluctuations that drove the spin ensemble to get to the mechanical system. Then in the detection efficiency of the quantum fields from inside the cavity. Furthermore, the interference of the optical phase quadrature responses of the spin system and mechanical systems are further impacted by this. This is due to the spin noise being parsed through the cavity and interference in reflection from the cavity. The loss associated with this effect is the same as the cavity one-sidedness, which as we saw, also limited the efficiencies. The importance of cavity one-sidedness, as well as the effect mode matching has on it, was discussed in section 4.1.5.

While the optical transmission losses are a product of the experimentally chosen pieces of optic, the losses associated with η_{mm} and $\mathcal{V}$ are the result of spatial mode mismatch. The optical mode at the optomechanical cavity was distorted from transmission through the vapour cell as well as the plethora of optics linking the systems. This limited the achievable mode matching and visibilities across our setup.

6.2.4 Matching the systems

Clear from our discussions in section 6.1 we wish to have our auxiliary subsystem, the spin ensemble, in the negative mass configuration. It should have an equal and opposite susceptibility $|\chi_S| = -\chi_M$ and be probed with a readout rate equal to that of the mechanics, i.e. $\Gamma_S = \Gamma_M$. Furthermore, the two systems should see the same vacuum noise implying the need for a high efficiency optical link. Lastly, for the quantum back-action evasion scheme to even be relevant both systems must have $C_q \gtrsim 1$. With our fundamentally very different systems, see fig. 6.3, achieving these requirements, in practice, means balancing various trade-offs. Here we will simply discuss these in general. Let's start by discussing the two components defining the susceptibility, namely the resonance frequency and damping rate.

[1] These are typical values and have not been measured.

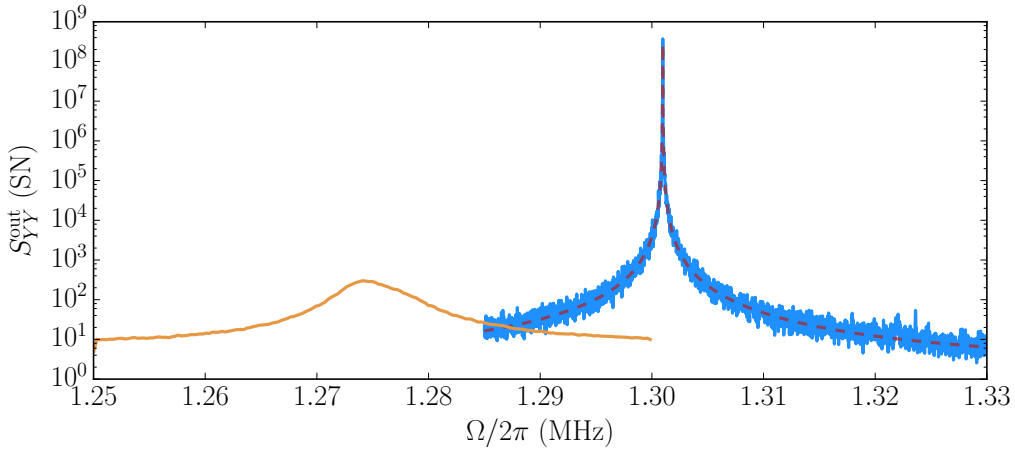

Figure 6.3: **Hybrid subsystems comparison.** Large susceptibility mismatch. Membrane probed near resonance. Mechanical mode is inadvertantly broadened by dynamical back-action to 7 Hz from the original intrinsic 0.1 Hz meaning that the undamped mechanical response would be an additional 70 times higher than shown. The dashed red line is a Lorentzian fit. The spin oscillator is broadened to ~ 4 kHz by the strong probe of LO_1 required for a high read-out rate and quantum cooperativity.

Resonance frequency

The resonance frequency of the spin oscillator can be changed at will by dialing the bias magnetic field. This is very easily accomplished experimentally, and is extensively used. The resonance is further shifted by the DC optical stark shift, but is typically a very small fractional change and depends on optical power, on which more important parameters depend. The DC stark shift helps reduce the quadratic zeeman splitting, see fig. 5.14, which improves the approximation of the spin system as a harmonic oscillator.

The mechanical frequency is tunable during the design stage. Once fabricated, however, our devices are not tunable[2] except by temperature changes. This change is, however, much too small for our samples to be useful, not to mention the fact that we wish to operate the device at the lowest bath temperature out of concerns for thermal decoherence. The mechanical resonance frequency, in the case of a detuned cavity, can also be tuned[3] by the optical spring effect of dynamical back-action described in section 4.1.4. This is not very useful, as the tuning range is much less than that of the atomic spins and furthermore linked to the readout rate. Thus, in practice the spin oscillator frequency is tuned to the desired frequency – often close to the mechanical frequency.

[2]One can imagine a bunch of ways to modify our assembly or device such that this is feasible. This has not been done and invariably has its own compromises related to Q, $\bar{n}_{\text{bath}}$, experimental complexity and space, etc.

[3]Due to our wide cavity linewidth compared to the mechanical frequency this always amounts to a small fractional amount.

Linewidths

Matching the damping rates is where the real difficulty lies. The intrinsic damping rates for both systems are very different, 4 orders of magnitude apart! The spin ensemble realized has a intrinsic damping of $\gamma_{S,0} = 2\pi \times 1\,\mathrm{kHz}$ and the membrane an intrinsic linewidth of $\gamma_{M,0} = 2\pi \times 0.1\,\mathrm{Hz}$. These rates derive from experimental and material imperfections and, in order to have a large quantum cooperativity, are desired to be as a low as possible. Conflict, thus, arises since it is not experimentally feasible to reduce the atomic linewidth, nor is it advantageous (although easily doable) to increase the mechanical intrinsic linewidth. In fact, concomitant with a large spin readout rate is an increased spin damping. Thus, in practice the spin oscillator is broadened to $\gamma_S \simeq 2\pi \times 5\,\mathrm{kHz}$ further exacerbating the mismatch. This mismatch is vividly seen in fig. 6.3 where the systems are probed with comparable readout rates.

To mitigate this mismatch we employ the additional optomechanical damping introduced via dynamical back-action arising from a red detuned optomechanical cavity. This damping serves two crucial roles. First, it allows for the mechanical damping rate to be matched to the spin linewidth. Secondly, it provides an enormous reduction in the thermal phonons driving the mechanical oscillator, cooling the mode by a factor of $> 10^4$. Whilst this does not (appreciably) affect the quantum cooperativity as the thermal decoherence rate remains unaltered, it does provide a more practical measurement environment by reducing the amplitude of the thermal state.

Using a detuned cavity means we no longer have a purely QND optomechanical interaction. Additionally, we now have a complicated optomechanical input-output relation due to the now present quadrature rotations. It turns out that in this regime back-action evasion is still possible, albeit with some additional complexity.

Readout rates

While sideband cooling with the probe can provide the desired mechanical broadening, the readout rate required depends on the cavity sideband resolution Ω_M/κ. If the mechanical readout rate Γ_M required to reach a desired broadening is so high that it exceeds the attainable spin readout rate Γ_S (increasing this would further increase the spin broadening), then perfect matching is not possible. This was the case for the experiments described in section 6.3 where the cavity linewidth was $\kappa = 2\pi \times 33\,\mathrm{MHz}$ and mechanical frequency $\Omega_M = 2\pi \times 1.3\,\mathrm{MHz}$.

In this case increasing the sideband resolution is a natural solution[4]. Following the experiments described in section 6.3 the optomechanical cavity was operated at $\kappa = 2\pi \times 15\,\mathrm{MHz}$ for exactly this reason. The results of this switch are discussed in

[4]In principle a cell with low intrinsic loss and a higher readout rate per unit broadening would also do the trick. However, if such a cell was available, it would, of course, already be in use!

section 6.4.

If we assume the optical broadening dominants the intrinsic mechanical broadening then the quantity Γ_M/γ_M describes the amount of broadening per unit readout rate since $\gamma_M \approx \gamma_{\text{opt}}$. This quantity is power independent and depends on optomechanical parameters g_0, κ, Ω_M and $\bar{\Delta}$. Only the cavity detuning, $\bar{\Delta}$, is tunable. Thus $\bar{\Delta}$, along with the LO_2 drive power allows us to match the mechanical readout rate *and* broadening to that of the spin ensemble[5].

For the spin ensemble, the readout rate may be increased by a larger probe field. This causes a linear probe induced broadening of the oscillator. The readout rate required for the atoms is in practice bounded from below by the requirement that the probe broadening dominates intrinsic broadening. This is equivalent to saying that we wish total decoherence to be dominated by the observed optical port. The readout rate achieved per unit of induced broadening is dependent upon experimental realities such as the number of atoms addressed and ensemble spin polarization.

Once the spin broadening is dominated by the probe induced broadening, the spin cooperativity saturates. The readout rate may still be increased arbitrarily, as long as we can neglect higher order interactions and Stark shifts. In practice however a specific broadening of the spin system is desired, thus limiting the readout rate from above.

This desired broadening is set by a restriction of the mechanical system. Since we wish to match the broadening of the mechanics to the spins, the latter cannot be too large as optomechanical mirror noise and hybridization become increasingly problematic for broader and broader mechanics. The setup thus select a narrow frequency band in which the mechanical mode must reside. Additionally, since mechanical broadening from dynamical back-action goes hand in hand with a frequency shift this further restricts the available broadening.

Spectral comparisons

By spectral comparison it is possible to gauge crucial system parameters. Observing the power spectral density of the optical phase quadrature output from the full hybrid system, or each system individually, we see the system response and the measurement noise floor. This is illustrated in fig. 6.4. From this spectrum we can identify a few important contributions and parameters.

First, the variance from the system can be broken up into two contributions. These derived from the thermal noise and quantum back-action forces acting on the system. The thermal contribution is illustrated as the shaded region whereas the back-action contribution is indicated by the hatched region.

[5]It is an interesting twist of fate that experimental realities force you to match the "target" system to the "auxiliary" system. Alas, such is the life of a pragmatic experimentalist.

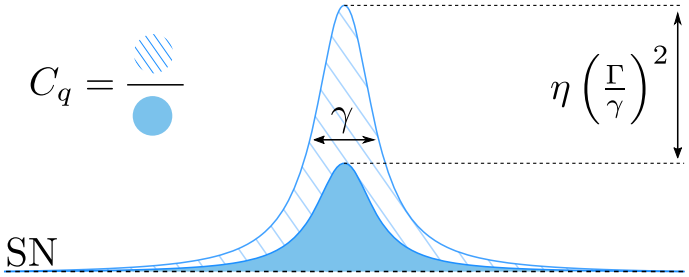

Figure 6.4: **Optical phase quadrature spectral overview** Oscillator response in optical phase quadrature. The noise floor is set by the optical short noise (SN). The shaded area is thermal noise contribution to the oscillator. The hatched blue region is the back-action contribution to the observed variance. The ratio of these two contributions to the variance is the quantum cooperativity C_q. The height of the oscillator response is associated with quantum back-action is in units of optical shot noise given by $\eta(\Gamma_i/\gamma_i)^2$. This is diminished by the detection efficiency η.

In principle there could be many more classical noise sources. For our purposes, so long as they are white, we simply absorb them into the thermal noise contribution. Classical laser noise such as amplitude noise is a very relevant such example. The ratio of these contributions is the quantum cooperativity for the spin system and directly proportional for the optomechanical system, see eq. (4.61).

Secondly, the quantum back-action system peak above shot noise is given by $(\Gamma_i/\gamma_i)^2$, $i \in \{S, M\}$. Suppose we now neglect the thermal noise contribution. Keeping both system linewidths the same and correcting for different detection efficiencies, the difference in spectral height is then a direct measure of the difference in readout rates. This is often a useful diagnostic tool in the hybrid system.

Finally, we consider the measurement noise floor in the optical phase quadrature. When the atomic ensemble is present, this is in practice not entirely shot noise. This is because the spin ensemble has additional broadband noise, see section 5.11.2. This noise is roughly white on the frequency scale of the system linewidths, and thus appears as an inflated noise floor.

Added white noise

For quantum back-action evasion to be observed (and indeed be useful), the quantum vacuum must be an important driver of the subsystem dynamics. We have seen that we are able to independently operate the spin and mechanical systems in a regime where the back-action is a major driving force. This is most clear from the observation of significant light noise squeezing achievable from both the mechanical system in section 4.4, and the spin system as we will see later in fig. 6.10.

However, the quantum back-action contribution to an oscillator's motion is, in practice, diminished in importance by thermal or other undesired classical noise sources. Thus it is often useful to intentionally inject additional classical light noise for purposes of diagnostics and characterization. We have already seen the use of this principle in the cases of a coherent excitation for both the mechanical and spin

system in the cases of OMIT in section 4.3 and MORS in section 5.10.8 respectively.

It is, thus perhaps not surprising that classically inflating the optical driving force responsible for the quantum back-action is diagnostically useful. This can be done by introducing additional white noise in the desired optical quadrature, which for our purposes is the optical amplitude quadrature $\hat{X}$. The resultant back-action noise on each system i is determined by the fluctuations of this light quadrature. The noise is characterized by the correlation function

$$\langle \hat{X}^{\mathrm{in},i}(t)\hat{X}^{\mathrm{in},i}(t')\rangle = \left(\bar{n}^{i}_{\mathrm{WN}} + 1/2\right)\delta(t'-t'), \tag{6.18}$$

where the vacuum contribution is the 1/2 and white additional classical noise is characterized by a mean field occupation of $\bar{n}_{\mathrm{WN}}$.

In the case of only vacuum noise ($\bar{n}^{i}_{\mathrm{WN}} = 0$) we refer to the resultant response as *quantum back-action*. Looking back at eqs. (6.6) and (6.7) however, if we boost the amplitude quadrature with additional classical noise $\bar{n}^{i}_{\mathrm{WN}}$ then we can introduce more back-action on the systems. This translates into a larger back-action variance in the optical quadrature as if the gain of the system was larger.

This provides a convenient way to probe the response of the systems as we can drown out thermal noise in favour of back-action. The back-action response has the added benefit that it is less susceptible to transmission losses between the systems, providing a convenient way to probe the expected back-action interference of the hybrid system. Losses between the systems reduce the classically added noise in the amplitude quadrature (as it does with the response in the phase quadrature). Unlike with vacuum, however, the lost classical noise is not replaced. Thus, the noise correlations that drove the spins will also drive the mechanics, regardless of the intra-system loss.

Finally, the added white noise is in the optical quadrature that drives the systems. Thus, the scaling of a systems variance with an increased light noise variance provides a metric by which to measure the systems quantum back-action contribution, and thus by extension the quantum cooperativity. This method is described in detail in appendix C, and is used to determine the quantum cooperativities relevant for the results of sections 6.3 and 6.4. An example of this scaling method is discussed in the following section.

Basic system characterization

The white noise scaling described above in section 6.2.4 is seen applied to both subsystems in fig. 6.5. From the top panels it is clear that both systems variances respond linearly to an increased amplitude quadrature variance ($\bar{n}_{\mathrm{WN}}$). This measurement was done for the full hybrid system with the atoms far detuned from the mechanical oscillator. Thus, we could drive both systems simultaneously under the conditions of the experiment, with the only difference being the spin system Larmor frequency. This is easily tuned back near the mechanical frequency and the

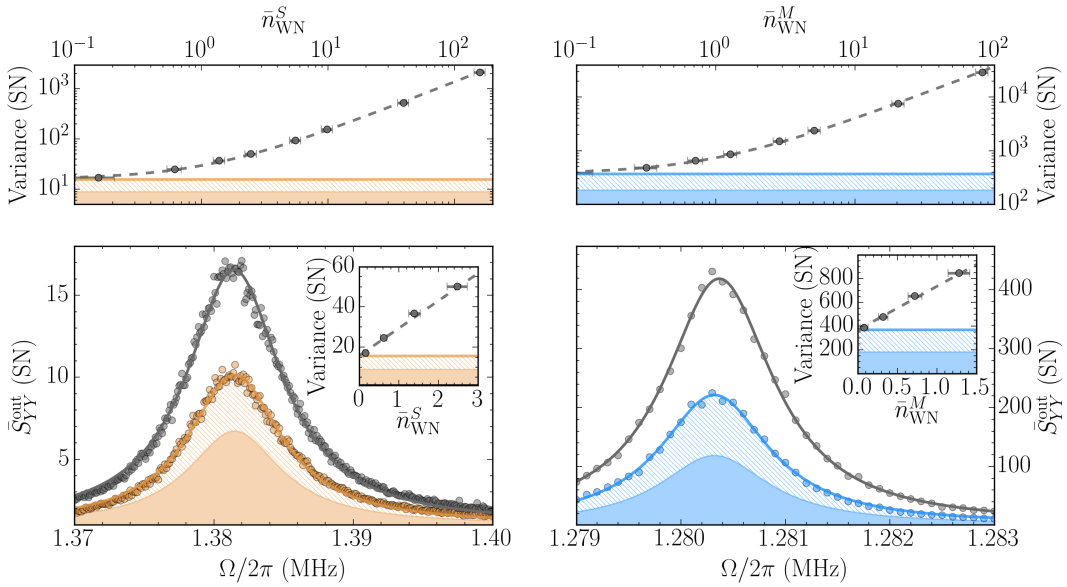

Figure 6.5: **Hybrid subsystems cooperativity for pulsed back-action evasion.** Spin system is far detuned from detuned from mechanics ($|\Omega_S| \neq \Omega_M$) to avoid interference. **Bottom left (right):** Power spectral densities of the full hybrid output optical phase quadrature (both bottom figures are from the same spectra) are normalized to the optical shot noise. Seen left (right) are the noise associated with the spin (mechanics). The grey data are for an added white noise drive of $\bar{n}^S_{\mathrm{WN}} = 1.4$ ($\bar{n}^M_{\mathrm{WN}} = 1.2$). Solid yellow (blue) lines gives fits to the spin (mechanical) system with no added modulation. The data for these are given by the dots of the same color. The shaded areas indicate the thermal contribution to the variance (not including shot noise). Likewise the hatched area is the contribution of the quantum back-action to the variance. Solid grey is a fit of the systems response to the added white noise. **Top left and right:** Shaded and hatched areas same as in bottom panel. The grey points are the integrated noise areas associated with each system as a function of added noise photon number $\bar{n}^i_{\mathrm{WN}}$. Dashed grey line is a linear fit. A zoom of these data are shown in the **insets** in the bottom panel.

back-action contribution to the spin system is unaffected by this small fractional resonance frequency change.

From the scaling to the additional white noise we can infer the fraction of the quantum back-action contribution to the thermal noise for both systems. These are 0.8 for the spin system ($C_q^S = 0.8$) and 1.0 for the mechanics ($C_q^M = 1.2$ correcting according to eq. (4.61) at the cavity detuning of $\bar{\Delta} = -2\kappa/9$). Their respective impacts are seen in the transduced motion of each observed in the optical phase quadrature power spectral densities shown in the lower panels of fig. 6.5.

The mechanical quantum cooperativity is consistent with that expected from the known experimental parameters of input power (200 µW), detuning, coupling rate, cavity linewidth and bath temperature. The expected readout rate from these independently measured parameters gives $\Gamma_M = 2\pi \times 13\,\mathrm{kHz} = 11\gamma_m$. A bath temperature of 7 K giving a thermal decoherence rate of $\gamma^{\mathrm{th}}_{\mathrm{dec}} = 2\pi \times 11\,\mathrm{kHz}$ can be inferred as it results in the measured quantum cooperativity.

The mechanical readout rate need not be constructed from quantities found from independent measurements as just described in section 6.2.4. The readout rate can also be estimated by noting that in lower right panel of fig. 6.5 the peak of the back-action contribution is 110 in units optical shot noise. With the broadening of $\gamma_m = 2\pi \times 1.2\,\mathrm{kHz}$ and detection efficiency for mechanical motion of $\eta_2 = 60\,\%$ this translates into a readout rate of $\Gamma_M = 2\pi \times 16\,\mathrm{kHz} = 13\gamma_m$, roughly consistent with that expected. This would imply a bath temperature of 8.5 K to yield the expected cooperativity.

Bath temperatures in this range are expected as discussed in section 4.5.5, and the discrepancies likely derive from uncertainties in various experimental parameters. Perhaps most of all the detection efficiency, which affects the expected amount of back-action as well as the inferred readout rates from considerations such as section 6.2.4. More careful measurements are made in cases where the back-action is of crucial importance as in section 6.4.

The readout rate for the much broader, $\gamma_S = 2\pi \times 8.4\,\mathrm{kHz}$, spin system can be similarly found from the lower left panel of fig. 6.5. The spin readout rate is found to be $\Gamma_S = 2\pi \times 30\,\mathrm{kHz}$. Here the peak of the back-action contribution is 3.5 in units optical shot noise and the detection efficiency is much $\eta_1\eta_2 = 30\,\%$.

In practice only rough knowledge of the absolute readout rates of the individual systems is required. Since they may be finely adjusted by the probing powers of LO_1 and LO_2 their desired value is usually set in reference to a measurement depending on the difference between the spin and optomechanical responses to some back-action force.

6.3 Pulsed back-action evasion

Let us consider a practical example of how we may measure and go about cancelling the aforementioned light induced back-action on the motion of the oscillators. We will consider that case where both oscillators are constantly monitored in a cascaded fashion as described in section 6.1, when suddenly an additional light force is added. This boosts the light noise which drives both subsystems and is kept on long enough for the subsystems to reach their steady state, after which the noise is switched off for a much longer period. This allows the systems to decay back to their initial steady state. As may be expected, the systems are driven to higher amplitudes at a rate proportional to their read-out rates Γ_S, Γ_M (coupling strength), which occur on a timescale determined by their damping rates γ_S, γ_M.

In section 6.3.2 we will consider the case of a coherent driving force being suddenly switched on. Then, in section 6.3.3, we will consider the case where the added force derives from additional white fluctuations. The former case will help us visualize the coherent response of the systems and the latter will aid us in understanding the response to noise. This latter case further provides us with a close analog, and stepping stone, to the case where the driving force is only the quantum vacuum of

the probing field. The quantum regime is probed in section 6.4.

For simplicity we will still consider the simple case of QND interaction for both subsystems $\{S, M\}$ (spins, mechanics) and that both systems are high Q, i.e. $\gamma_i \ll \Omega_i$ for $i \in \{S, M\}$. We will further assume that the filtering of the light quadratures output from the spin ensemble are appropriately converted into the light quadratures incident upon the optomechanical system according to eq. (6.3). The optomechanical cavity will also be treated as a purely one-sided system probed in reflection. Both of these constraints will be relaxed and considered in general in quantum regime ofsection 6.4.

Experimentally, adding a disturbance is tantamount to generating photons in a desired quadrature. We do this by modulating the electro-optic modulator placed prior to the spin ensemble. This modulation scatters photons from LO_1. This reduces its strength by a negligible amount as the modulation depths used will be incredibly small. Whether the added photons are coherent (spectrally narrow) or noisy (spectrally white) is chosen by the modulation voltage sent to the electro-optic modulator. The quadrature in which these are generated is set by orienting the axis of the electro-optic modulator appropriately and adjusting a DC voltage offset. All added photons described here are generated in the S_z polarization quadrature.

For the experiments described here in section 6.3, the near quantum limited spin and optomechanical system are those characterized in fig. 6.5. Furthermore, the spin system is tuned to be degenerate with the mechanical mode. Thus, unless otherwise stated, we will in the following sections assume $\Omega_M = |\Omega_S|$.

6.3.1 Response and readout

Suppose the force acting on oscillator i is described by $\hat{\boldsymbol{F}}_i(t')$ then the quadratures of motion $\hat{\boldsymbol{Q}}_i$ at some time t will be influenced by the accumulated action of the force. Solving eq. (6.11) we have

$$\hat{\boldsymbol{Q}}_i(t) = \int_{-\infty}^{t} \mathrm{d}t' e^{\boldsymbol{M}_i(t-t')} \hat{\boldsymbol{F}}_i(t'). \tag{6.19}$$

This motion is read out in the optical phase quadrature according to eq. (6.17). Furthermore, if we look back at eq. (6.5) we saw that the sin and cos components of $\hat{Y}^{\mathrm{out}}$ will contain the desired information about the mechanical state referenced to the atomic ensemble, namely $\hat{Q}_M(0) - \hat{Q}_S(0)$ and $\hat{P}_M(0) \mp \hat{P}_S(0)$. These sin and cos harmonic components for each oscillator also underlie eq. (6.19) as is clear from expanding $e^{\boldsymbol{M}_i(t-t')}$ as in eq. (G.1.4).

To access these components in practice we demodulate the optical output quadrature at a frequency Ω (typically $= \Omega_m$) by multiplying the detected photo-current by $q(\Omega, t) \in \{\cos(\Omega t), \sin(\Omega t)\}$ and integrating for a time T. The demodulated sin or cos components (denoted by subscript q) are given by

$$\hat{Y}^{\mathrm{out(in)}}_{(q)}(\Omega) \equiv \frac{2}{\sqrt{T}} \int_0^T \mathrm{d}t q(\Omega, t) \hat{Y}^{\mathrm{out(in)}}(t). \tag{6.20}$$

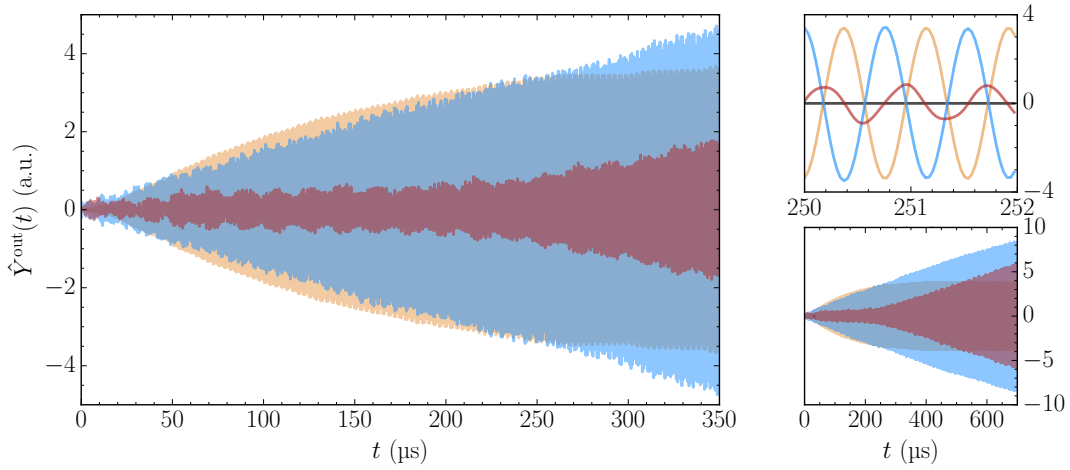

Figure 6.6: **Coherent back action dynamics and evasion**. Hybrid optical phase quadrature time trace has been bandpass filtered leaving only noise in a 50 kHz bandwidth around the demodulation frequency, equal to the mechanical resonance frequency. The systems are driven by a coherent optical amplitude quadrature tone at the mechanical frequency turned on at time $t = 0$. **Left:**. Time evolution of the back-action. The membrane (blue), the spin (yellow) and the joint (red) systems. **Top right:** Zoom in around 250 μs. The membrane and the spin back-action are out of phase resulting in just a small residual back-action of the joint system (red). **Bottom right:** Zoom out of time evolution. Notice the initial regime where both systems grow at roughly the same rate. Here the back-action is well and the hybrid response is growing slowly. Once the spin system reaches a steady state the amount of hybrid back-action begins to grow as the mechanical system outpaces the spin system.

These components are typically (as in our case) extracted by use of a lock-in amplifier. They are commonly referred to as the X and Y components of a signal, but will be referred to as the sine and cosine harmonic components here to avoid confusing with the optical quadratures $\hat{X}$ and $\hat{Y}$.

6.3.2 Pulsed coherent back-action

Suppose now that at $t = 0$ we switch on a coherent tone at $\Omega = \Omega_M = |\Omega_S|$. We generate this tone in the amplitude quadrature driving the spins such that $\langle \hat{X}^S_{L,\text{in}}(t) \rangle \propto \cos(\Omega t)$ and watch the systems respond according to eq. (6.19). This coherent time evolution response is seen in fig. 6.6 for the spins (configured in the negative mass setting), mechanics and joint hybrid system. Clearly evident are the features described previously. The individual systems grow at different rates and reach different steady state values. Furthermore, in the negative mass setting of the spin ensemble the joint response is significantly reduced. In fact, the joint response is smaller than both individual systems for many hundreds of periods. The positive mass, not shown for clarity, is larger than either individual system response.

Notice that the slopes of both systems are similar in the beginning and the back-action is canceled to a large extent. Eventually, however, the spin response begins to

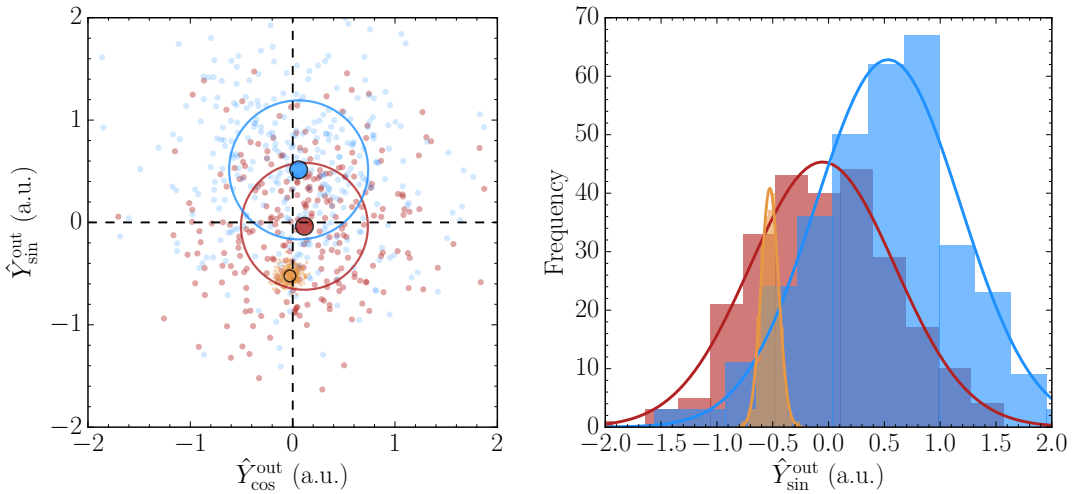

Figure 6.7: **Hybrid coherent back action in phase space**. Results of many realizations of pulsed coherent drive measurements, one of which is shown in fig. 6.6. The coherent drive consists of photon state with 2 photons $\text{s}^{-1}\,\text{Hz}^{-1}$ in the measurement bandwidth. The harmonic quadratures of the light quadrature $\hat{Y}^{\text{out}}$ taken at $T = 320\,\mu\text{s}$. **Left:** Phase space harmonic quadratures. Dots are individual realizations. Bold dots and circles display the mean and standard deviations of the cloud corresponding to the mechanical (blue), spin (yellow) and joint hybrid (red) systems. The variances for each are equal along all axes to within a few percent. The standard deviations are 0.68, 0.62, 0.07 for the aforementioned systems respectively. **Right:** Histrogram of slice through $\hat{Y}^{\text{out}}_{\text{sin}}$ where $\hat{Y}^{\text{out}}_{\text{cos}} = 0$. The mean coherent displacements are equal and opposite, $\langle \hat{Y}^{\text{out}}_{\text{sin}} \rangle_S = -.052$ and $\langle \hat{Y}^{\text{out}}_{\text{sin}} \rangle_M = 0.51$, whilst the hybrid response was cancels out pretty well, with $\langle \hat{Y}^{\text{out}}_{\text{sin}} \rangle_{\text{hybrid}} = -0.04$.

reach a steady state. As the mechanical response is slower, it continues to grow and thus the system responses begin to diverge. This is seen in the individual responses and appears as a very clear transition in the amount of hybrid back-action. At around 250 µs this begins to grow as the mechanics does.

Also, clear from the zoom in fig. 6.6 is that while the individual system responses are out of phase, the hybrid response does not perfectly cancel. While the conditions of the hybrid measurement are the same as for the mechanical response, they are different with respect to the measurement of the spin system individually.

The atoms are measured individually by detuning the cavity far from cavity resonance. This simply reflects the atomic response off the cavity towards the homodyne detection. The mechanical and hybrid measurements are done with the cavity locked. The mechanical system is probed individually by detuning the atomic oscillator frequency $|\Omega_S| \to \infty$. Thus, losses introduced from the cavity will reduce the response of the spins as compared to the mechanical. More importantly, the cavity is slightly detuned and the quadratures from the spin system will be rotated. Thus, the nice out of phase responses seen for the system individually are not exactly the relevant components for the hybrid system.

The response of the systems to this pulsed coherent tone can also usefully be visualized in phase space as seen in fig. 6.7. This is done by extracting the harmonic

components from a time trace such as in fig. 6.6 by demodulation as described by eq. (6.20). Many realizations of this measurement allows us to estimate the impact of the pulsed excitation. The out of phase nature of the two oscillators is clearly seen by their opposite displacement in phase space. The imperfect cancellation, as just discussed, is also seen by a displacement in $\langle \hat{Y}^{\text{out}}_{\text{cos}} \rangle_{\text{hybrid}} \neq 0$.

The main effect seen in fig. 6.7, however, is the cancellation of the $\langle \hat{Y}^{\text{out}}_{\text{sin}} \rangle$ quadrature component. Both systems are displaced by an absolute amount $\simeq 0.5$ and almost perfectly cancel yielding a hybrid displacement of $\simeq 0.0$. There is also a noticable $\simeq 20\,\%$ reduction in the variance ($\simeq 10\,\%$ standard deviation) of the hybrid system as compared to the membrane only case. However, in this case, the error on this quantity is too great to claim any noise cancellation. This feature of noise cancellation is, however, the feature of preeminent importance and we will discuss for the remainder of this chapter.

6.3.3 Pulsed white noise back-action

The added force is described by an additional classical back-action noise in the optical amplitude quadrature $\hat{X}^i_{\text{in}}$ responsible for driving each system $i \in \{S, M\}$. This force has a white spectral density and a mean occupancy given by $\bar{n}_i$, measured in photons per unit time per unit bandwidth[1]. The auto-correlation of this light quadrature is

$$\langle \hat{X}^i_{\text{in}}(t) \hat{X}^i_{\text{in}}(t') \rangle = \left(\bar{n}^i_{\text{WN}} s(t) + 1/2 \right) \delta(t - t'), \tag{6.21}$$

where for vacuum noise we have $\bar{n}^i_{\text{WN}} = 0$ leaving just the $1/2$ vacuum noise. This vacuum noise is referred to as the optical shot noise (SN) and provides a very useful reference point from which to measure $\bar{n}^i_{\text{WN}}$. The distinct regimes of pulsed and continuous wave (CW) operation are distinguished by the function

$$s(t) \equiv \begin{cases} 1 & \text{(CW)} \\ \Theta(t) & \text{(pulsed)} \end{cases} \tag{6.22}$$

where $\Theta(t)$ is the Heaviside step function ramping at $t = 0$.

We can, of course, just as well measure the quadrature components (sin and cos) for the systems individually as well as the cascaded joint measurement. Applying a pulsed white noise force for in the optical amplitude quadrature as just described, we see the individual systems displaced in phase space, see fig. 6.7. In time domain the responses are that previously shown in fig. 6.6. Notice both systems respond close to π out of phase, owing to the fact that the spin ensemble had been prepared in the negative mass configuration. The mechanical system is in a much higher occupancy thermal state, and thus has as a greater variance. Nonetheless, the systems have a

[1] Typically $\text{s}^{-1}\,\text{Hz}^{-1}$

comparable response to the white noise drive as the observed mean displacements are similar.

When the joint (hybrid) system is probed, the back-action on each system cancel, as intended. The result state has a reduced variance, and perhaps more noticeably, a comparably small displacement to the white noise drive. The reduced variance is the predominant feature of interest as it is the limiting factor in our estimation of the system quadrature. It will, thus, be discussed further in this chapter. To see more clearly how the back-action evolves, and in order to gain a useful language and intuition on how to think of its cancellation, we will now consider a rather idealized situation.

If we neglect transmission losses for simplicity ($\eta_1 = \eta_2 = 1$) such that $\bar{n}_{\mathrm{WN}}^M = \bar{n}_{\mathrm{WN}}^S \equiv \bar{n}_{\mathrm{WN}}$, we find from eqs. (6.21) and (G.2.11) the BA contribution,

$$\mathrm{Var}[\hat{Y}_{(q)}^{\mathrm{out}}(\Omega)]_{\mathrm{BA}} = \frac{4}{T}\int_{-\infty}^{T} \mathrm{d}t'(\bar{n}_{\mathrm{WN}} s(t') + 1/2 \cdot \left[\Gamma_S \mathbf{u}_{q,S}(\Omega, t') + \Gamma_M \mathbf{u}_{q,M}(\Omega, t')\right]_{1,2}^2 , \tag{6.23}$$

where $[\cdot]_{1,2}^2$ indicates the square of the (1,2) component of the matrix. The matrices $\boldsymbol{u}_{q,i}$, $i \in \{S, M\}$ parameterizes the filtering a harmonic component q (the sin and cos components) of an oscillator i's quadrature does of the driving force $\hat{\boldsymbol{F}}_i$. They are defined in eq. (G.1.3) and more fully detailed in appendix G.1.

Note that eq. (6.23) is the integral of a non-negative function, because contributions from different time steps $t \neq t'$ add incoherently. The physics of this is simply that back-action perturbations at times $t \neq t'$ are uncorrelated and hence no interference can occur between different time steps.

Thus, if the two oscillators do not respond equally (when including the weights Γ_i) and opposite at each individual time step t, there is no memory in the system that allows this imbalance to be counted at a later time t'. Hence to have perfect cancellation the integrand of eq. (6.23) must be zero for all $t' \in (-\infty, T]$. This is only possible if in this interval we have $\boldsymbol{u}_{q,M}(\Omega, t') = -\beta \mathbf{u}_{q,S}(\Omega, t')$ for some $\beta \in \mathbb{R}_+$(assuming we can choose the read-out rates Γ_i at will). Exact back-action cancellation cannot be achieved for $\gamma_M \neq \gamma_S$, except in the long-time limit $T \gg 1/\gamma_M, 1/\gamma_S$ as we will see below.

We will focus on the case of resonant demodulation $\Omega = \Omega_M = |\Omega_S|$ and for simplicity consider just the harmonic cosine quadrature component ($q = \cos$). By substituting eq. (G.1.9) into eq. (6.23) we have

$$\mathrm{Var}[\hat{Y}_{\cos}^{\mathrm{out}}(\Omega_M)]_{\mathrm{BA}} \approx \frac{2}{T}\int_{-\infty}^{T} \mathrm{d}t'(\bar{n}_{\mathrm{WN}} s(t') + 1/2) \cdot \left[\frac{\Gamma_S}{\gamma_S}\left(e^{\gamma_S \min\{t',0\}/2} - e^{-\gamma_S(T-t')/2}\right) \pm \frac{\Gamma_M}{\gamma_M}\left(e^{\gamma_M \min\{t',0\}/2} - e^{-\gamma_M(T-t')/2}\right)\right]^2 , \tag{6.24}$$

where in the last line we have replaced the rapidly varying factor $\sin^2(\Omega_M t')$ by its mean value, $1/2$, an excellent approximation in the high-Q limit for both systems when integrating for several oscillation periods (which we will always be doing).

Even though the integral eq. (6.24) is manageable analytically for any $T > 0$, we will explore two limiting cases to extract simple conditions for back-action cancellation:

i) Long integration time with respect to both decay times $T \gg 1/\gamma_S, 1/\gamma_M$.

ii) Short integration time with respect to both decay times $T \ll 1/\gamma_S, 1/\gamma_M$.

It should be noted that the pulsed results presented in section 6.3.4 occupy an intermediate regime, where $T \sim 1/\gamma_M$ while $T \gg 1/\gamma_S$. In this regime a simple parameter condition has not been found. Nonetheless, the above case are worth considering as they have explanatory utility.

Long-time limit

Looking at the variance in the long-time limit $T \gg 1/\gamma_S, 1/\gamma_M$, eq. (6.24) simplifies to

$$\mathrm{Var}[\hat{Y}^{\mathrm{out}}_{\cos}(\Omega_M)]_{\mathrm{BA}} \approx 2(\bar{n}_{\mathrm{WN}} + 1/2)\left[\frac{\Gamma_S}{\gamma_S} \pm \frac{\Gamma_M}{\gamma_M}\right]^2. \tag{6.25}$$

In this limit, back-action cancellation can be achieved in the positive-negative (mechanics-spin) mass configuration (minus sign in eq. (6.25)) by matching the gain factors of the two systems

$$\frac{\Gamma_S}{\gamma_S} = \frac{\Gamma_M}{\gamma_M}. \tag{6.26}$$

This can be understood as follows. A random kick applied to system i at time t' will only contribute significantly to the integration sub-interval $t \in [t', t' + 1/\gamma_i] \cap [0, T]$ due to the damping rate truncating the time interval of importance. Since the damping rates are in general different, the relevant time scales for noises are different. However, in the long-time limit $T \gg 1/\gamma_S, 1/\gamma_M$ we need only consider kicks occurring in the bulk of the integration interval, roughly speaking $t' \in [0, T - \max\{1/\gamma_S, 1/\gamma_M\}]$. These are kicks that are not truncated in mapping into the response.

Short-time limit (CW noise)

Turning now to the short-time limit, $T \ll 1/\gamma_S, 1/\gamma_M$, the dominant contribution in eq. (6.24) comes from the momentum kicks occurring prior to the start of integration and potential pulsing, $t' < 0$. In this regime their has not been enough time for the systems to respond and and their subsequent motion read out. This is clear from expanding eq. (6.24) in T, which to lowest order approximates to

$$\mathrm{Var}[\hat{Y}^{\mathrm{out}}_{\cos}(\Omega_M)]_{\mathrm{BA}} \approx (\bar{n}^{\mathrm{CW}}_{\mathrm{WN}} + 1/2)\frac{T}{2}\left[\frac{\Gamma_S^2}{\gamma_S} + \frac{\Gamma_M^2}{\gamma_M} \pm 4\frac{\Gamma_S\Gamma_M}{\gamma_S + \gamma_M}\right], \tag{6.27}$$

where we note that Γ_i^2/γ_i is proportional to the fractional area of the spectral response due to the back-action force. Thus, only in the case where CW noise has been added will there be a first order contribution. Once again the $\pm$ indicates the positive and negative mass configuration of the spin ensemble.

The interference in this regime depends crucially on the readout rates. Suppose the systems damping rates were matched, i.e. $\gamma_S = \gamma_M = \gamma$, then relevant term in eq. (6.27) simplifies as

$$\frac{\Gamma_S^2}{\gamma_S} + \frac{\Gamma_M^2}{\gamma_M} \pm 4\frac{\Gamma_S\Gamma_M}{\gamma_S + \gamma_M} = \frac{(\Gamma_S \pm \Gamma_M)^2}{\gamma}, \tag{6.28}$$

where the interference depends on the read-out rates Γ. In this configuration of matched oscillator susceptibilities, unsurprisingly the optimal choice is the same as in section 6.3.3.

6.3.4 Single noise quanta pulsed back-action evasion

Here we present evasion of the back-action resultant from the pulsed white noise of just a few added noise quanta. Just as described before we consider the effect of the noise for a finite duration $T = 150\,\mu s$, in this case shorter than the results shown in fig. 6.7. This measurement time is comparable to the membrane response time $1/\gamma_M = 1/(2\pi \times 1.2\,\text{kHz}) \simeq 130\,\mu s$, but significantly longer than the spin response time $1/\gamma_S = 1/(2\pi \times 8.4\,\text{kHz}) \simeq 20\,\mu s$.

From measurements of $\hat{Y}^{\text{out}}(t)$ we extract the two harmonic quadratures at $\Omega_M = |\omega_S|$ defined by eq. (6.20), which contain information about the desired commuting variables. In fig. 6.8 we see the phase space distributions of these harmonic components for the hybrid system with $\bar{n}_M^{\text{WN}} = 1.3 \pm 0.1$ added photons at the optomechanical system. Comparing the membrane alone with the hybrid system with the spins oriented in the negative and positive mass configurations we see the expected destructive and constructive interference. The results are normally distributed with isotropic standard deviations within a few percent.

The interference of the total back-action variance contribution, given by

$$\text{Var}[\hat{Y}^{\text{out}}(\Omega_M)]_{\text{BA}} = \text{Var}[\hat{Y}^{\text{out}}_{\text{cos}}(\Omega_M)]_{\text{BA}} + \text{Var}[\hat{Y}^{\text{out}}_{\text{sin}}(\Omega_M)]_{\text{BA}}, \tag{6.29}$$

is quite substantial as seen by comparing shaded circles at the top of fig. 6.8. These represent only the square root of variance. The added back-action variance of the hybrid system with negative spin mass is reduced by a factor of 3.6 compared to the membrane alone. Likewise the hybrid system with positive spin mass has an increased back-action variance by a factor of 2.8.

The order of magnitude contrast in back-action interference is diluted when considering the total system variance. The steady state quantum back-action and thermal noise from each systems comprising the undriven states. These are separately measured and are shown as the black circles in fig. 6.8. There are no statistically significant differences between the driven hybrid system configurations of positive and

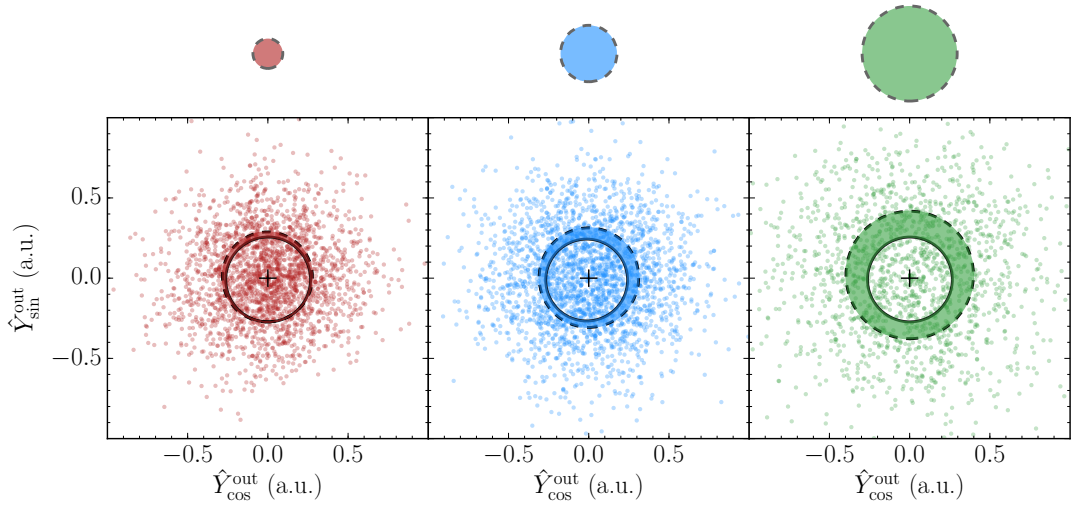

Figure 6.8: **Hybrid pulsed back-action quadrature variances.** Data for 1500 realizations (dots) for the harmonic quadratures of $\hat{Y}^{\text{out}}$ in the presence of 1.3 photons of added noise driving the mechanics. For each system the standard deviation is shown by a dashed black circle. The solid black circle shows the standard deviation of the system in the absence on any added noise. The difference between these dashed and solid lines is the back-action contribution associated with the added noise. The phase space area of this contribution is illustrated as the filled circles above each panel. These contributions are the square root of the contributions to the variance. The cross at the center marks the origin. **Left:** Joint measurement with the negative spin mass. **Center:** Measurement of mechanical oscillator only. **Right:** Joint measurement with the positive spin mass.

negative mass indicating negligible quantum back-action interference. These two cases are however different from the membrane only, as the thermal and quantum back-action noise from the spin system contribute to the overall variance. In these measurements, however, the contribution of the membrane variance was dominant, thus the small perceived difference in fig. 6.8.

Nonetheless, the overall effect of the interference is captured well by the basic QND model of eq. (G.2.11), which only takes the losses and thermal noises of the systems into account. It predicts the total variance of the hybrid system with negative spin mass to be in 20 % below that of the membrane alone in agreement with the results of fig. 6.8 where this is 20 %. In similarly good agreement is the expected ratio of the total variances of positive and negative mass hybrid systems. This is expected to be 2.0 and found to be 1.9.

The high contrast and significant cancellation of the back-action contributions to the hybrid positive and negative mass cases are shown in fig. 6.9 as the added white noise drive is increased. The variances are linear in this drive as expected from our initial characterization of each system in fig. 6.5.

The same basic model predicts large quantum back-action cancellation for our system parameters. They would however only result in a 5 % difference between the hybrid negative mass system and the membrane only. Observing differences on this scale was barely feasible within the experimental noise. Nonetheless, the

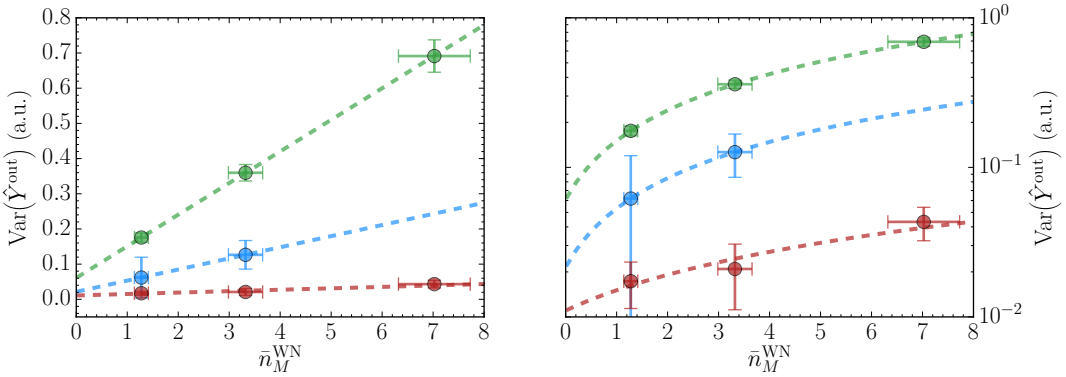

Figure 6.9: **Hybrid pulsed back-action quadrature variances.** Pulsed back-action (BA) variance as a function of added white noise photons $\bar{n}_{\mathrm{WN}}$ driving the mechanical oscillator. The variance of demodulated responses, in a duration of $T = 150\,\mu\mathrm{s}$, is considered for the hybrid system with both positive (green) and negative (red) spin mass, as well as the membrane only (blue).

absence of any hint of such interference was not fully understood at the time. It is now thought to have been due to a variety of underappreciation factors, such as optical losses, in particular cavity mode matching, and the long term stability of experimental parameters, in particular the polarization and phase filtering linking the optical quadratures addressing both systems.

6.4 Steady state back-action evasion

Following the experimental efforts culminating in the (single quanta) classical back-action evasion of section 6.3.4 we now shift our focus towards *quantum back-action* evasion. We will consider this evasion in the steady state regime where both oscillators are continuously monitored, just as in the pulsed case of section 6.3. Here however no added noise will be pulsed.

The hybrid system underwent a few changes and, while the structure of the experiment as described in section 6.2 remains unaffected, the following parameters are now significantly different. First, the operating optomechanical cavity linewidth was changed to $\kappa = 2\pi \times 15\,\mathrm{MHz}$. The change was motivated by a desire to further match the systems as described in section 6.2.4. In practice, this meant operating at the narrow cavity linewidth point in $2kz_m$ seen in fig. 4.14.

The spin ensemble was pushed to operate 65 °C from the previous 52 °C, thus significantly boosting the number of atoms. This raised the atomic cooperativity from $C_q^S = 0.8 \pm 0.1 \rightarrow 1.10 \pm 0.15$. This spin quantum cooperativity is inferred from the white scaling as described in appendix C. A mechanical quantum cooperativity of $C_q^M = 2.6 \pm 0.3$ is extracted from the observed ponderomotive squeezing seeing in the right panel of fig. 6.10. Knowing the detection efficiency and various optomechanical parameters the bath temperature $T_{\mathrm{bath}} = (7.0 \pm 0.5)\,\mathrm{K}$ is fitted thus yielding a quantum cooperativity.

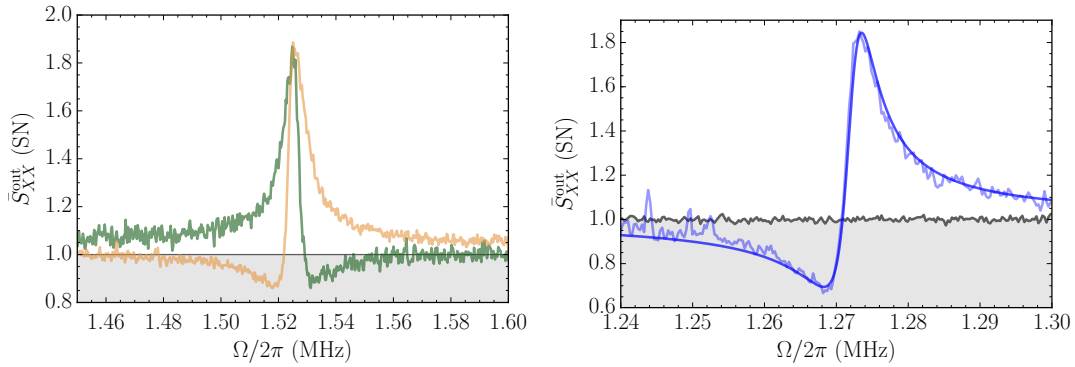

Figure 6.10: **Ponderomotive squeezing in hybrid system.** The full hybrid system displays significant ponderomotive squeezing in the optical amplitude quadrature for both the spin and mechanical subsystems. The optical shot noise (SN) level shown in black averaged over many spectra is verified to within 5 % by both balanced detection and comparison to a white light source. The sub shot noise region is shaded grey. **Left:** Spin system squeezing in final hybrid detection. Both positive (dark green) and negative (yellow) effective spin mass displays squeezing with an opposite sign due to the difference in their susceptibilities. The amount of squeezing is about 10 % below shot noise, which when correcting for the large detection losses gives about 25 % below shot noise (−1.3 dB). **Right:** Optomechanical squeezing in reflection (light blue). The fit (dark blue) is used to determine the mechanical bath temperature giving a cooperativity of $C_q^M = 2.6 \pm 0.3$. The amount of observed squeezing is −1.7 dB, equivalent to −2.6 dB correcting for the detection efficiency of 72 %.

A simplified infrastructure and operational experience allowed for a higher overall detection efficiency and a higher efficiency optical link between the two systems. This is particularly evident from fig. 6.10 where the detectable squeezing in the final hybrid detection is substantial for the spin system. The losses are however still far from negligible as the spins system has a total detection efficiency of only $\eta_{\text{total}} \simeq 40\,\%$ in the hybrid system.

This higher cooperativity now available implies that the quantum back-action contribution to the mechanical variance dominates the thermal contribution by a factor of 1.8, whilst this is 1.1 for the spins. Thus, in the hybrid system there is, in total, significantly more quantum back-action noise than classical noise. This is shown in fig. 6.11 as the dominating hatched contributions.

Once the total mechanical variance has been broken down into the thermal and back-action contributions, it is possible to calibrate the spectra in terms of mechanical displacement using eq. (4.47). The calibration is naturally cast in terms of mechanical zero point fluctuations x_{zpf}, one unit of which determines the motional variance of the ground state (with variance x_{zpf}^2). This displacement scale is shown as the right hand axis of fig. 6.11 and in all subsequent figures featuring measured mechanical motion in the optical phase quadrature. This includes hybrid system variances as the absolute scaled of displacement sensitivity enhancement resultant from any back-action evasion is of interest.

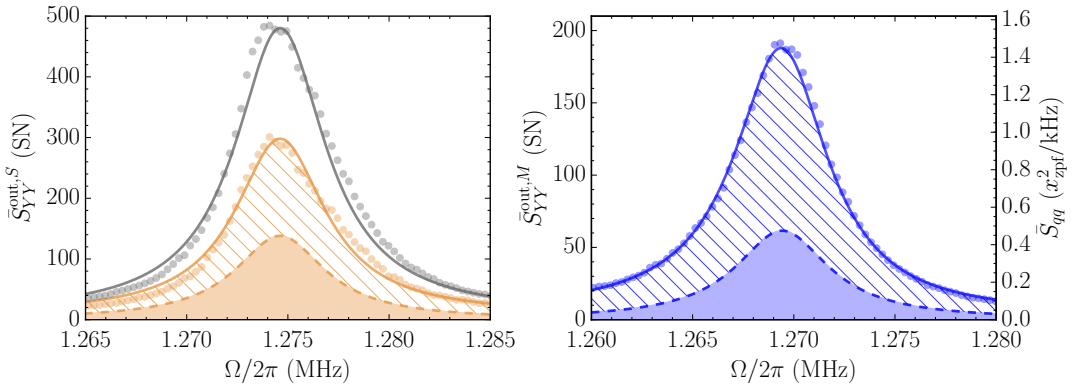

Figure 6.11: **Hybrid subsystems variance contributions.** Shown are the variance contributions to spin (**left**) and optomechanical (**right**) system variances (dots) along with the solid fit lines (yellow - spin, blue - mechanics) from the model described in section 6.4.1. The shaded region bounded by the dashed line indicates the thermal noise contribution to the variance, and the hatched region indicates the quantum back-action variance contribution. Both are determined from each systems cooperativity. For the spin system this is determined by the response (black) to a white noise drive of $\bar{n}^S_{\mathrm{WN}} = 1.2$ just as in fig. 6.5 and as described in appendix C. The mechanical cooperativity is determined from the ponderomotive squeezing shown in fig. 6.10.

This calibration relies on knowing the cooling factor $\gamma_m/\gamma_{\mathrm{eff}}$ and the thermal bath occupancy (temperature). The former is measured rather precisely. The intrinsic mechanical broadening γ_m through ringdowns and γ_{eff} by the observed broadening in the optical phase quadrature power spectral density. The latter underpins the calibration of the back-action to thermal noise fraction in the first place and carries the dominating uncertainty. Thus, the error in this calibration is on the order of the mechanical back-action to thermal noise measurement of $\simeq 10\,\%$.

Looking once more at the spectral responses of both systems in fig. 6.11 we see that with the now narrower cavity we are better able to match the systems. In particular, they now have very similar broadenings. Using the simple logic of fig. 6.4 we can, by comparing the spectral heights along with the thermal noise contribution, deduce that the readout rates are also similar.

Now that we will be dealing with *quantum* back-action there are a few important effects that must be addressed and accounted for. We will discuss these and the theoretical model incorporating them in section 6.4.1 as well as a very useful approximation in section 6.4.2. This allows for a deeper understanding of the limits of the employed scheme as well as a useful expectation as to the spectral structure of the evasion. As we shall see, in the case of large optical broadening of the mechanics, while needed to match the system responses, introduces an undesirable effect and complicates the back-action interference which underpins its evasion.

We will, then, discuss two cases of quantum back-action evasion. First, in section 6.4.3, the canonical case where the sub-systems have the same resonance frequency and are otherwise closely matched. Secondly, we will consider the case where the subsystems are slightly detuned from each other. This scheme can achieve a

higher degree of quantum back-action evasion if the input quadratures to the optomechanical cavity (output quadratures of the spin ensemble) are pre-rotated. The experimental parameters for each case are displayed in table 6.1.

Parameter	Symbol	Value (section 6.4.3, section 6.4.4)
Atomic spin oscillator		
Intrinsic damping rate	$\gamma_{S,0}$	$2\pi \times 1\,\mathrm{kHz}$
Total damping rate	γ_S	$2\pi\times$ (5.2, 4.6) kHz
LO_1 input driving power		(1.7, 1.5) mW
Readout rate	Γ_S	$2\pi\times$ (70, 60) kHz
Detuning from the D_2 $F = 4 \rightarrow F' = 5$ transition	Δ_S	3 GHz
Quantum cooperativity	C_q^S	1.10 ± 0.15
Spin Polarization	$\lvert P\rvert$	60 %
Microcell full transmission		13%
Microcell temperature		67.7 °C, 68.4 °C
Mechanical oscillator		
Effective mass	m_{eff}	14 ng
Zero point fluctuations	x_{zpf}	0.7 fm
Intrinsic mechanical frequency	$\Omega_{M,0}$	$2\pi \times 1.28\,\mathrm{MHz}$
Intrinsic damping rate	$\gamma_{M,0}$	$2\pi \times 0.1\,\mathrm{Hz}$
Optical damping rate	γ_{opt}	$2\pi\times$ (5.6, 5.36) kHz
Optical mechanical frequency shift	$\delta\Omega_m$	$2\pi\times$ (-12, -11) kHz
Cavity detuning	$\bar{\Delta}$	$-2\pi \times 4.7\,\mathrm{MHz}$
Total cavity linewidth (FWHM)	κ	$2\pi\times$ (17.4, 15.4) MHz
LO2 input drive power		(54, 38) µW
Intracavity photons	$\bar{n}$	$(5.8, 4.4)\times 10^6$
Single photon coupling rate	g_0	$2\pi\times$ 150 Hz
Thermal bath temperature	T_{bath}	7 K
Bath occupancy	$\bar{n}_{\mathrm{bath}}$	114×10^3
Mean thermal occupancy	$\bar{n}_M^{\mathrm{th}}$	2.0, 2.1
Quantum cooperativity	C_q^M	(2.6, 2.2)
Cavity mode-matching	η_{mm}	89%
Cavity incoupling efficiency	κ_1/κ	96 %
Hybrid & detection		
Quadrature mapping between systems	θ	0°, 6°
Efficiency outside cell to outside cavity		67 %
Efficiency inside cell to intracavity		45 %
Efficiency outside cavity to detector		82 %, 85 %
Detector quantum efficiency		90 %
Homodyning visibility	$\mathcal{V}$	89 %
Efficiency Intracavity to photoelectron		39 %
Model intrasystem efficiency	η_1	61 %
Model detection efficiency (ampl. quad.)	η_2	72 %, 75 %
Model detection efficiency (phase quad.)	η_2	54 %, 57 %

Table 6.1: **Summary of relevant experimental parameters.** Experimental parameters for the optomechanical, spin and hybrid systems relevant for the steady state quantum back-action measurements presented in section 6.4.

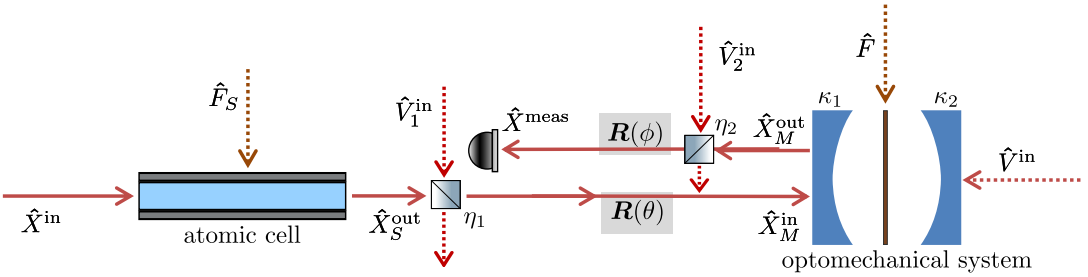

Figure 6.12: **Theoretical hybrid schematic.** The atomic spins (in the spin cell, blue box at left) are interrogated and driven by the light quadratures of $\hat{\boldsymbol{X}}^{\text{in}}$ and additionally driven by the spin noise $\hat{\boldsymbol{F}}_S$. Output light quadratures of the spin system $\hat{\boldsymbol{X}}_S^{\text{out}}$ are channeled to the optomechanical system. En route, it experiences losses characterized by a transmissivity η_1 associated with replaced vacuum noise $\hat{\boldsymbol{V}}_1^{\text{in}}$ and a phase rotation by an angle θ, resulting in a driving field $\hat{\boldsymbol{X}}_M^{\text{in}}$ for the optomechanical system. The optomechanical cavity has two ports with with decay rates κ_1 and κ_2. The optomechanical system is driven in addition by light noise $\hat{\boldsymbol{V}}^{in}$ from the unprobed port and a thermal force $\hat{\boldsymbol{F}}$. The output field of the optomechanical system $\hat{\boldsymbol{X}}_M^{\text{out}}$, in being detected, experiences further losses with transmissivity η_2 associated with additional light noise $\hat{\boldsymbol{V}}_2^{\text{in}}$. Before detection it rotated by an angle ϕ.

6.4.1 Detailed theoretical model

The most important experimental complexity, by far, not accounted for in the basic QND model described in section 6.1 is clearly the finite detuning of the optomechanical cavity. Including the effects of a detuned cavity into our hybrid model is straight forward and the full optomechanical model and input-output equations are given in appendix H. The spin input-output equations remain QND as described in eq. (6.14).

Next, the mapping of the output quadratures of the spin system to the input quadratures of the mechanical system need, in practice, not be exactly as described in eq. (6.3). In general the mapping will be related by a rotation matrix $\boldsymbol{R}(\theta)$ (defined in eq. (2.84)) by

$$\hat{\boldsymbol{X}}_M^{\text{in}} = \boldsymbol{R}(\theta)\hat{\boldsymbol{X}}_S^{\text{out}}, \tag{6.30}$$

where the quadratures are rotated by an amount given by the angle θ. Previously in the simple QND we had $\theta = \pi$, which will also be the case in section 6.4.3. However, in section 6.4.4 we will vary this angle. This can, in practice, be done since this quadrature filtering is done by locking the relative phase of two local oscillators to be $\pi/2$ out of phase. Deviating slightly from this lock point, by a controllable offset to the error signal, changes the quadrature rotation angle θ in eq. (6.30).

The two systems are linked via eq. (6.30), as shown schematically in fig. 6.12. Taking all these effects into account we can write the compound transfer matrix (in

Fourier space) for the hybrid optomechanical-spin system as

$$\begin{aligned}\hat{\boldsymbol{X}}^{\mathrm{out}}(\Omega) = &\underbrace{\sqrt{\eta_1\eta_2}\,\mathbb{M}(\Omega)\boldsymbol{R}(\theta)\mathbb{S}(\Omega)\hat{\boldsymbol{X}}^{\mathrm{in}}(\Omega)}_{\substack{\text{vacuum noise of light transduced}\\ \text{through spin and mechanics}}}\\ &+\underbrace{\sqrt{\eta_1\eta_2}\,\mathbb{M}(\Omega)\boldsymbol{R}(\theta)\sqrt{\Gamma_S\gamma_S}\,\chi_S(\Omega)\hat{\boldsymbol{F}}_S(\Omega)}_{\text{spin thermal noise transduced through mechanics}}+\underbrace{\sqrt{\eta_2}\,\mathbb{F}(\Omega)\hat{\boldsymbol{F}}(\Omega)}_{\text{mechanical thermal noise}}\\ &+\underbrace{\sqrt{(1-\eta_1)\eta_2}\,\mathbb{M}(\Omega)\hat{\boldsymbol{V}}_1^{\mathrm{in}}(\Omega)}_{\substack{\text{vacuum noise of light from}\\ \text{losses between spin and mechanics}}}+\underbrace{\sqrt{\eta_2}\,\mathbb{V}(\Omega)\hat{\boldsymbol{V}}^{\mathrm{in}}(\Omega)}_{\substack{\text{vacuum noise of light from}\\ \text{losses in optomechanical cavity}}}\\ &+\underbrace{\sqrt{1-\eta_2}\,\hat{\boldsymbol{V}}_2^{\mathrm{in}}(\Omega)}_{\substack{\text{vacuum noise from losses}\\ \text{between mechanics and detector}}}\end{aligned} \tag{6.31}$$

where η_1 and η_2 denote the transmission efficiencies from the spin system to the optomechanical cavity and from the optomechanical cavity to the detector, respectively. Vacuum noises incurred through these losses are described by $\hat{\boldsymbol{V}}_{1(2)}^{\mathrm{in}}(\Omega)$. An optional phase shift θ introduced deliberately in between the two systems is accounted for by the rotation matrix $\boldsymbol{R}(\theta)$.

The first term of eq. (6.31) is the input quadratures of light transduced through the spins by matrix $\mathbb{S}$, then rotated by the filter matrix $\boldsymbol{R}$, and then transduced through the optomechanical matrix $\mathbb{M}$. The second term is the spin thermal noise transduced through the optomechanical system and the third term is simply the read out mechanical thermal noise transduced according to the matrix $\mathbb{F}$. The final three terms are the contributions from vacuum introduced as a result of losses. The first of these three is the introduced vacuum between the spin and optomechanical system and then transduced by the mechanics. Next is the vacuum leaking in from the uncoupled port of the optomechanical cavity. This is transduced through the mechanics by the matrix $\mathbb{V}$. Finally, we have the vacuum introduced by the detection losses. In this model the finite cavity modematching is modeled as additional loss in the incoupling port as described in appendix B.5.3.

Finally, the homodyne detection is performed in the frame of the classical field after the optomechanical system where it has acquired a phase shift relative to the field before the optomechanical cavity. The acquired phase is described in section 2.5.2 and can be undone by rotating the output quadratures back. The measured quadratures are thus

$$\hat{\boldsymbol{X}}^{\mathrm{meas}} = \boldsymbol{R}(\phi)\hat{\boldsymbol{X}}^{\mathrm{out}}(\Omega), \tag{6.32}$$

where rotation angle ϕ is given in eq. (2.85).

6.4.2 Unresolved sideband regime approximation

We will now use the transfer matrix (1st line of eq. (6.31)) of the hybrid system to analyze the quantum back-action contribution to the optical output field in the

detuned cavity case. We do so neglecting the thermal noise contributions for simplicity and because their contributions are easy to add in and are well understood. In the sideband unresolved limit of $\Omega_M \ll \kappa$, which we find ourselves in[1], we can approximate optomechanical transfer matrix as described in appendix H.2. The approximation further assumes a one-sided cavity which we also easily meet. Using the resultant transfer matrix of eq. (H.2.23) and ignoring optical losses between the systems ($\eta_1 = \eta_2 = 0$) for simplicity the output optical phase quadrature is given by

$$\hat{Y}^{\mathrm{QBA}} \approx \left[\Gamma_M L_0^2 \chi_M(\Omega) + \Gamma_S \chi_S(\Omega)\left\{1 + i\Gamma_M \chi_M(\Omega) L_0 \delta L(\Omega)\right\}\right] \hat{X}^{\mathrm{in}}, \tag{6.33}$$

$$L_0 \equiv |L(\Omega = 0)| = \frac{\kappa/2}{\sqrt{(\kappa/2)^2 + \Delta^2}},\ \delta L(\Omega) = \frac{\Omega\Delta\kappa/2}{((\kappa/2)^2 + \Delta^2)^{3/2}} \tag{6.34}$$

where we have neglected an overall phase factor and have assumed the we set $\theta = \pi$ (standard mapping of quadratures between systems). In eq. (6.33) L_0 is the empty cavity Lorentzian response at $\Omega = 0$, the relevant zero order term since we will care about Fourier frequencies close to the mechanical, $\Omega \approx \Omega$, and we are operating in the unresolved sideband regime. The first order Lorentzian dependence on the Fourier sideband frequency is $\delta L(\Omega)$, which is approximately the difference in cavity response at $\pm\Omega$. One can easily relate the optical damping to the sideband asymmetry characterized by $\delta L(\Omega)$ by considering the mechanical effective susceptibility, where one finds the optical damping in this regime to be given by $\gamma_M \approx \gamma_{M,0} + \Gamma_M L_0 \delta L(\Omega_{M,0})$.

Immediately clear from eq. (6.33) is the appearance of a third term $\propto \chi_M \chi_S \delta L$ beyond the previous seen two terms of $\Gamma_M \chi_M$ and $\Gamma_S \chi_S$ seen in the QND case of eq. (6.8). This third term is only present for $\Delta \neq 0$ and has the same fundamental origin as optomechanical ponderomotive squeezing discussed in section 4.4, namely the partial mixing of the system response in the cavity optical phase quadratutre into the amplitude quadrature. In this hybrid case the mixing of the spin and mechanical responses occurs due to the finite cavity detuning and prevents perfect interference of the back-action responses spin and mechanical. It is particularly easy to see this in the case of strong optomechanical cooling $\gamma_M \gg \gamma_{M0}$, where there clearly is no back-action cancellation at the joint resonance frequency $\Omega = \Omega_M = |\Omega_S|$ since $i\chi_M(\Omega = \Omega_M)\gamma_M = -1$.

Interestingly however, at this particular Fourier frequency there seems to be no contribution from the spin system, even though this is at the peak of its response. It seems interference is going on and we will now probe deeper into this third term and the back-action evasion in this regime of a detuned optomechanical system.

Constituent phase responses

Additional insight can come from considering the phase response of each term in eq. (6.33). These are shown in fig. 6.13 for both cases of spin mass and with these

[1] For the back-action evading experiments described here we always have $\Omega/\kappa < 0.1$.

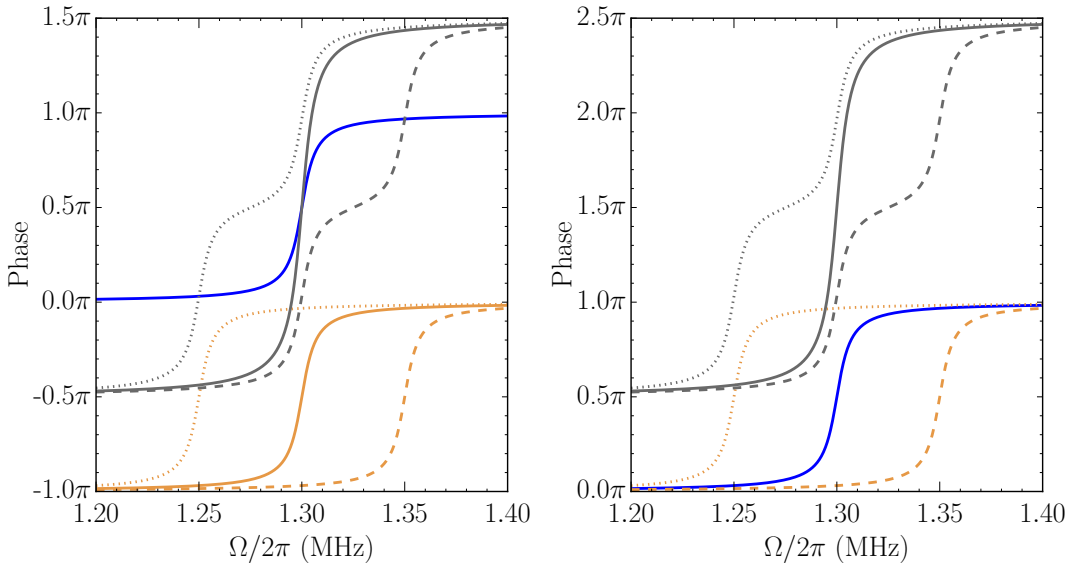

Figure 6.13: **Phases of the terms involved in hybrid QBAE.** Shown are the phases ($\mathrm{Arg}\,\chi$) of the terms comprising eq. (6.33), namely χ_M (blue), χ_S (yellow) and $i\chi_M\chi_S$ (grey). Dashed (dotted) curves are the phases with the spin resonance frequency blue (red) detuned from the mechanical resonance frequency (1.3 MHz) by 50 kHz. Both oscillators have the same broadening, $\gamma_M = \gamma_S = 2\pi \times 5\,\mathrm{kHz}$. **Left:** Negative mass spin ensemble. **Right:** Positive mass spin ensemble. When the two systems are degenerate they share the same phase response (blue).

we can discuss the phase of the back-action contributions arising from each term. In the negative mass case (left) it is clear that, in the degenerate case of $\Omega_m = |\Omega_S|$, the spin and mechanical susceptibilities are $-\pi$ out of phase everywhere meaning that these terms will destructively interfere at all frequencies[2]. However, the mixing term is clearly not perfectly out of phase anywhere. On the wings (far detuned from both systems) it is $\pi/2$ out of phase with of the contributions from both systems implying some cancellation. When the two systems are degenerate, the term is perfectly out of phase with spin system on mechanical resonance, thus, canceling the spin back-action contribution. This leaves only the mechanical contribution remaining meaning that we should expect no cancellation on mechanical resonance in case of degenerate oscillators.

When the spin oscillator is detuned from the mechanical resonance, the region between the two resonances displays no cancellation. This is a slightly more involved argument as one needs to account for the amplitude of each response at particular frequencies in addition to the phase. However, we simply note that in this region the mechanical and spin oscillator are in phase, and thus their contributions constructively interfere.

We can argue similarly in the case of a positive mass spin oscillator (right fig. 6.13). In the degenerate case, on resonance, the spin response is π out of phase

[2]These are the QND contributions discussed in the simplistic cases previously.

with the mixing term, and thus they destructively interfere leaving only the mechanical response. Thus, in this case, like in the negative mass case just discussed, there should be no back-action evasion on mechanical resonance. However, on the wings whilst the mixing term is $\pi/2$ out of phase with both contributions, both systems are in phase and thus we should expect the back-action contributions to constructively interfere.

In the case of non-degenerate positive mass oscillators the back-action contributions in the region between them can interfere destructive. The logic here is the same as in the negative mass case just discussed. Simply note that, disregarding the mixing term, the systems are π out of phase.

Spectral response

From the intuition gained from section 6.4.2 we now consider the power spectrum of the quantum back-action component of the measured optical phase quadrature for the hybrid system given by eq. (6.33). This is given by

$$\bar{S}_{YY}^{\mathrm{QBA}} = \frac{(\Gamma_M L_0^2 \delta_S \pm \Gamma_S \delta_M)^2 + \Gamma_M^2 L_0^4 \gamma_S^2}{(\delta_M^2 + \gamma_M^2)(\delta_S^2 + \gamma_S^2)} \bar{S}_{XX}^{\mathrm{in}}, \tag{6.35}$$

where $\delta_{M,S} = \Omega - |\Omega_{M,S}|$ and the $\pm$ indicate the choice of positive or negative spin mass respectively. $\bar{S}_{XX}^{\mathrm{in}}$ is the power spectral density of the input light amplitude fluctuations. The detuning of the spin system from the mechanical is given by $|\Omega_S| - \Omega_M = \delta_S - \delta_M$. The spectral response in the cases of positive and negative spin masses are shown in fig. 6.14 for the case of matched oscillators with $\Gamma_S = \Gamma_M L_0^2$, $\gamma_M = \gamma_S$ and $|\Omega_S| = \Omega_M$. Notice that the overall structure is as described in section 6.4.2.

For degenerate oscillators, $\Omega_M = |\Omega_S|$ (giving $\delta = \delta_S = \delta_M$), and matched readout rates, $\Gamma_S = \Gamma_M L_0^2$, the interference term completely cancels out in the negative spin mass hybrid setting! There is maximal interference in the positive mass setting. Under these conditions, the ratio of the hybrid quantum back-action to that of mechanics alone[3], at a particular Fourier frequency Ω, is given by

$$\frac{\bar{S}_{YY}^{\mathrm{QBA,Hybrid}}(\Omega)}{\bar{S}_{YY}^{\mathrm{QBA,Membrane}}(\Omega)} = \begin{cases} \frac{\gamma_M^2}{\delta^2 + \gamma_M^2}, & \text{for negative mass} \\ \frac{4\delta^2 + \gamma_M^2}{\delta^2 + \gamma_M^2}, & \text{for positive mass} \end{cases} \tag{6.36}$$

Thus, as explained in section 6.4.2, quantum back-action interference is indeed expected everywhere (to some extent), *except* for on joint resonance of $\delta = 0$. On the wings there will be destructive (constructive) interference in the negative (positive) mass case of the spins.

Additionally, the strength of the interference decreases approaching the system resonance frequency. Of course, the system variance has its biggest contribution in

[3] To retrieve the mechanics only simply set $\Gamma_S = \gamma_S = \Omega_S = 0$.

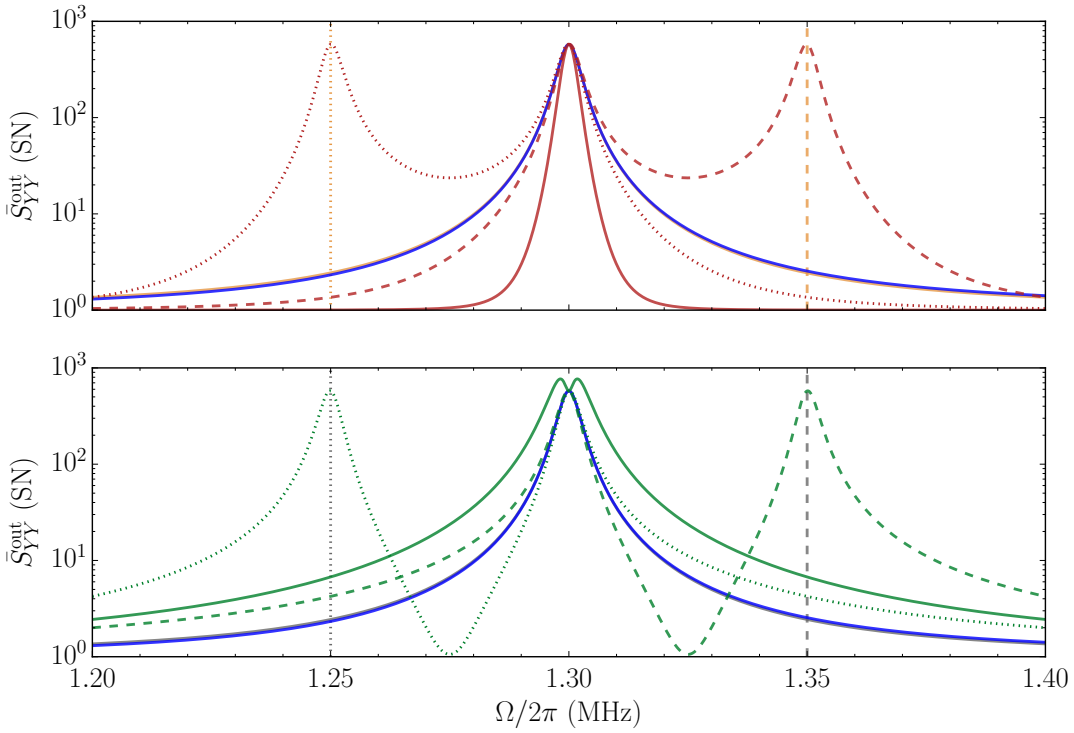

Figure 6.14: **Theoretical spectral response of hybrid quantum back-action evasion.** Spectral response expected according to eq. (6.35) with shot noise added also. The mechanical system alone is shown in blue, whereas the spin system alone is shown in yellow (negative mass) and grey (positive mass). Dashed (dotted) vertical lines indicate the resonance frequency of the spin ensemble when blue (red) detuned from mechanical resonance (1.3 MHz) by 50 kHz. The hybrid system is shown in red (negative spin mass) and green (positive spin mass). Both oscillators have the same broadening, $\gamma_M = \gamma_S = 2\pi \times 5\,\text{kHz}$ and have matched readout rates $\Gamma_S = \Gamma_M L_0^2$. **Top:** Negative mass spin ensemble. **Bottom:** Positive mass spin ensemble.

this region, and thus the fractional amount of achievable back-action evasion will be reduced accordingly. The total back-action variance is the spectral area, and thus can found by integration over the spectral response, i.e.

$$\text{Var}\left(\hat{Y}^{\text{QBA}}\right) = \int_{-\infty}^{\infty} \bar{S}_{YY}^{\text{QBA}}\, \mathrm{d}\delta. \tag{6.37}$$

In the degenerate case with matched readout rates, the variance of the hybrid quantum back-action compared to that of the mechanical oscillator alone is found to be

$$\frac{\text{Var}\left(\hat{Y}^{\text{QBA,Hybrid}}\right)}{\text{Var}\left(\hat{Y}^{\text{QBA,Membrane}}\right)} = \begin{cases} \frac{\gamma_S}{\gamma_S+\gamma_M}, & \text{for negative mass} \\ \frac{4\gamma_M+\gamma_S}{\gamma_S+\gamma_M}, & \text{for positive mass} \end{cases} \tag{6.38}$$

Whereas in the simple QND case the optimal back-action evasion occurs for perfectly matched systems, the penalty of the mixing term arising from the non-QND optomechanical interaction is not plain to see. In the case of perfectly matched

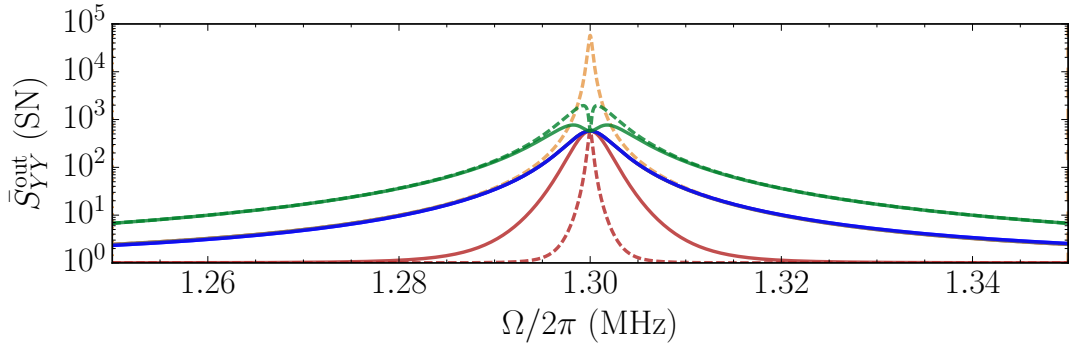

Figure 6.15: **Theoretical spectral response of degenerate hybrid quantum back-action evasion with a narrow spin oscillator.** Spectral response expected according to eq. (6.35) with shot noise added also. The mechanical system alone is shown in blue, whereas the degenerate spin system alone is shown in yellow (both positive and negative mass). Both systems are set to have the same readout rate. The hybrid system is shown in red (negative spin mass) and green (positive spin mass). The solid lines indicate the membrane and spins having the same linewidth $\gamma_M = \gamma_S = 2\pi \times 5\,\text{kHz}$, and the dashed lines indicate a narrower spin system with $\gamma_M = 10 \times \gamma_S = 2\pi \times 5\,\text{kHz}$. For the solid lines the spin system is identical to the mechanics only (blue curve) and is, thus, obscured. When the spin linewidth is reduced (dashed) it is clearly visible. In this case the reduction (increase) of the hybrid negative (positive) spin mass system back-action as compared to the membrane only is clearly greater than when $\gamma_M = \gamma_S$ in accordance with eq. (6.38).

oscillators ($\gamma_S = \gamma_M$, etc) the back-action evasion is limited to 1/2 in the negative hybrid spin mass case. In the positive mass case the back-action interference leads to an increase by a factor of 5/2. This 50 % limit in the negative mass case is far from the perfect (100 %) reduction in principle available in the QND case.

Fortunately, from eq. (6.38) we can see that the back-action evasion in the negative mass case approaches perfect evasion as $\gamma_M \to \infty$. In practice, having simply $\gamma_M \gg \gamma_S$ leads to an achievable back-action evasion approaching γ_S/γ_M! Likewise, the positive mass hybrid system approaches perfect constructive interference with 4 times the membrane only variance. Keeping the readout rates the same as in fig. 6.14 but simply reducing the broadening of the spins such that $\gamma_S/\gamma_M = 1 \to 1/10$ a much larger back-action cancellation (1/11) is seen in fig. 6.15. The desire is, thus, clearly for $\gamma_M \to \infty$ and $\gamma_S \to 0$, keeping the readout rates equal.

This noise filtering can be viewed through the lens of an OMIT type effect, where the cavity response is now replaced by the mechanical susceptibility. The phase sidebands are now the spin response and are partially projected onto, and thus drive, the mechanics. The response goes largely back into the phase quadrature where it interferes with the original spin sidebands. Notice the positive mass case of fig. 6.15 similarity to the features of fig. 4.20. The negative mass case appears to have the inverted effect.

This knowledge was not fully developed and appreciated at the time the experiments reported here were carried out. In practice, we were experimentally constrained from below to the spin broadening of $\simeq 5\,\text{kHz}$ by the necessity to be

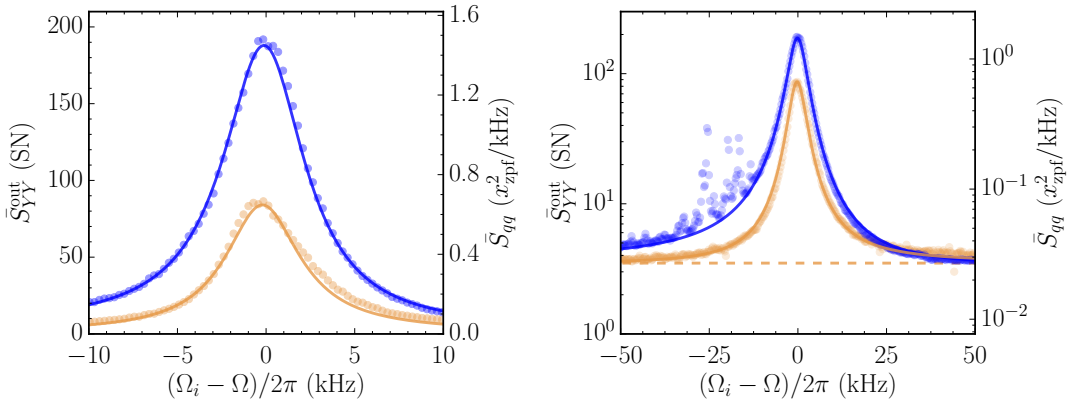

Figure 6.16: **Spectral comparison of the spin and mechanical systems under hybrid detection.** Spins system (yellow) detuned from mechanics (blue) and observed jointly in the optical phase quadrature. The response of the spins is offset manually to appear degenerate with the mechanics. This allows for a comparison of the two systems. Dots are measurement and solid lines are fits with the full hybrid model. The dashed yellow line is the broadband atomic spin noise (see section 5.11.2). Linear scale (**left**), logarithmic scale (**right**).

dominated by the optically power broadening and have a reasonable C_q^S. On the optomechanical side, our sideband assymmetry set the mechanical optical broadening for a given readout rate at the optimal cavity detuning. This limited the mechanical broadening as increasing it meant further mismatch of the readout rates. Thus, at the time, we were limited to the (still much improved compared to section 6.3) case of relatively matched systems as seen in fig. 6.11.

The conditions discussed so far apply to the case of degenerate subsystems and the canonical mapping of optical quadratures. It turns out that adjusting these knobs leads to more complicated behaviour, which as we shall see in section 6.4.4, can result in improvements upon the degenerate oscillator case. First, however, let us experimentally probe the case of matched degenerate oscillators.

6.4.3 Degenerate subsystems

Having fairly well matched, and quantum back-action dominated, systems as seen in fig. 6.11 we link the two with the standard mapping of the optical quadratures $\theta = \pi$ (see eq. (6.30)). Measuring the full hybrid system with the atoms far detuned from the mechanics we can compare the responses of both systems as seen in fig. 6.16. The spin system is noticably reduced by the losses between the systems.

Beyond the mechanical lorentzian feature seen in fig. 6.11 there are additionally some noise spikes on the blue side of resonance. These are likely a combination of hybridized modes, as described in section 3.10, or mirror modes of the cavity mirror substrates as described in section 4.5.7. They are thankfully many $\gamma_M/2$ away, thus their influence is minor and is not further treated.

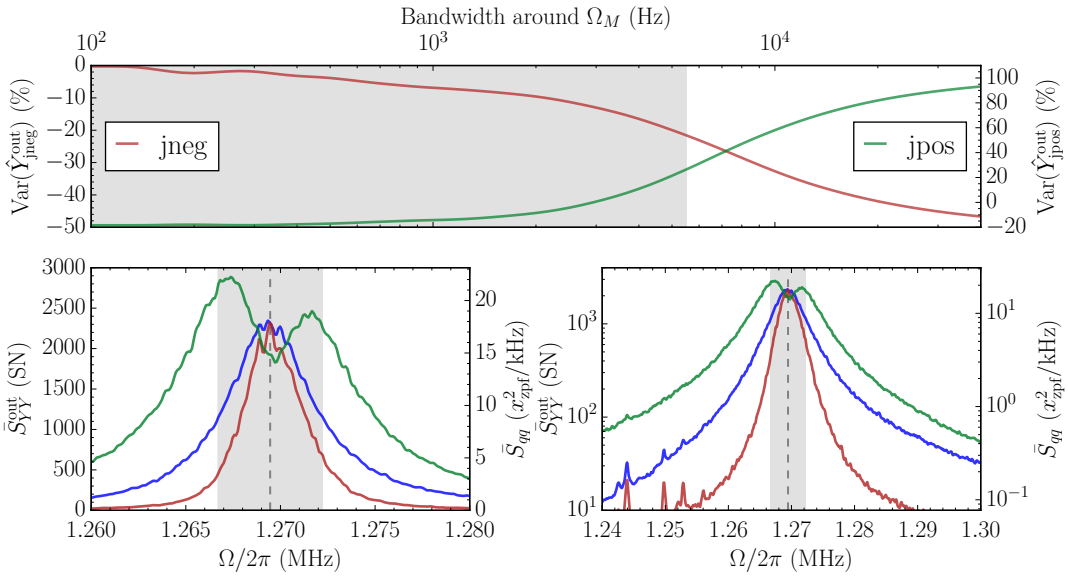

Figure 6.17: **Degenerate hybrid white noise back-action evasion.** Mechanics, shown in blue, has a resonance frequency at the dashed grey line as do the spins, thus degenerate. Hybrid system with spins as negative mass (red) and positive mass (green) clearly show significant back-action interference. The grey shaded region indicates the bandwidth corresponding to the full mechanical linewidth γ_M centered on the mechanical resonance. **Top:** Variance for hybrid system (spectral areas of the panels below, subtracting shot noise), relative to that of the membrane alone, in a variable bandwidth centered on mechanical resonance. Hybrid system with negative spin mass (joint negative: jneg) and with positive spin mass (joint positive: jpos) are shown together but on different axes, left and right, respectively. **Bottom left:** Power spectral density of hybrid system and membrane only as read out in the optical phase quadrature. **Bottom right:** Same as left, but on logarithmic scale and in a wider spectral window.

Added white noise

To see the back-action response of the total system clearly we apply lots of white noise ($\bar{n}_{\mathrm{WN}} \gtrsim 20$) and observe the resultant spectra shown in fig. 6.17. From the lower panels we see the features of the degenerate hybrid case just discussed in section 6.4.2. In particular, notice the features of reduced interference on resonance and large reduction on the wings in the hybrid negative mass case. This is as expected save for the small on resonance reduction. In the positive mass case back-action is not added on resonance – indeed actually a small reduction is observed. The large constructive interference on the wings is also clearly seen.

The total variances for the positive and negative mass systems, relative to the mechanics only variance, are 100 % and −46 %, respectively. These are within, and very close to, the limits[4] from eq. (6.38) of ≈ 155 % and ≈ −52 %, respectively.

[4]Here we using the fractional differences. Thus, limits for the negative and positive mass evasion (enhancement) of say $\frac{1}{2}$ and $\frac{5}{2}$ from section 6.4.2 expressed as fractional differences are simply $\frac{1}{2} - 1 = -\frac{1}{2}$ and $\frac{5}{2} - 1 = \frac{3}{2}$.

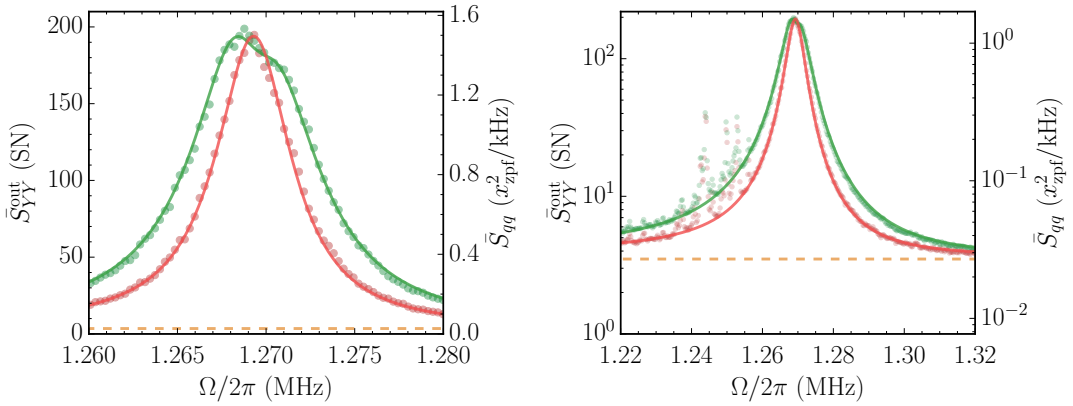

Figure 6.18: **Contrast between hybrid positive/negative spin mass.** Power spectral density of the hybrid system with a negative (red) and positive (green) spin mass. Dots are measurements and solid lines are fits from the full hybrid model. Dashed yellow line is the broadband atomic spin noise (see section 5.11.2). Linear scale (**left**), logarithmic scale (**right**).

Thus, we have prepared the hybrid system such that, under ideal conditions, the back-action contribution in the hybrid system could be reduced to nearly half that of mechanics alone.

Quantum back-action evasion

In the same experiment we now turn off the white noise modulation. The resulting power spectral density now contains non-negligible contributions from the thermal noise components of both systems. These, along with the losses between the systems, reduces the contrast of the back-action interference. Nonetheless, in fig. 6.18 we see clearly the contrast between the positive and negative mass hybrid system. The on resonance dip and larger wings in the positive mass case are clearly seen.

Compared to the membrane only, the hybrid system does not have as dramatic an impact as in the case of white noise. In the negative mass case the hybrid response is nearly identical to that of the membrane only, thus omitted for clarity. The evaded back-action has been nearly perfectly compensated for by the added spin thermal noise. Nonetheless, a statistically significant overall sensitivity improvement is observed with the total variance of the negative mass hybrid system being $(95 \pm 2)\,\%$ of the membrane only variance.

This is clear from the variance contribution breakdown seen in fig. 6.19. The total membrane only variance is $12.20 x_{\text{zpf}}^2$, of which the thermal motion constitutes $4.07 x_{\text{zpf}}^2$, equivalent to an effective thermal bath of $\bar{n}_{\text{M}}^{\text{th}} = 2.04$ thermal phonons[5]. The remaining $8.13 x_{\text{zpf}}^2$ is the variance due to the quantum back-action drive. The negative mass hybrid system has a total variance of $11.59 x_{\text{zpf}}^2$, only slightly less than

[5]The dynamical back-action cooling is indeed quite substantial reducing the thermal noise by a factor of 5.6×10^4.

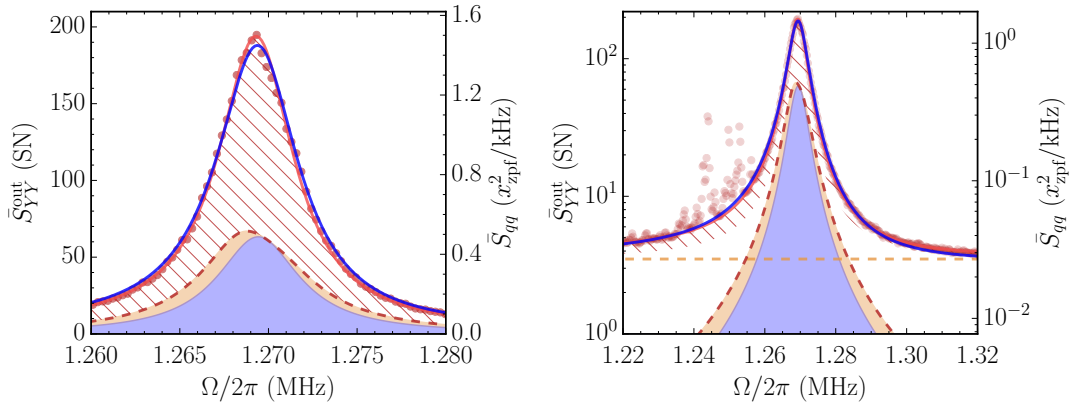

Figure 6.19: **Hybrid quantum back-action evasion in degenerate oscillator case.** Power spectral density of the hybrid system with a negative (red), and membrane alone (blue). Dots are measurements and solid lines are fits from the full hybrid model. Membrane only data omitted for clarity but can be seen in fig. 6.16. Red hatch is the quantum back-action contribution to the negative mass hybrid system. Shaded areas are thermal noise contributions of the membrane (blue) and spins (yellow). Dashed yellow line is the broadband atomic spin noise (see section 5.11.2). Linear scale (**left**), logarithmic scale (**right**).

that of the membrane only, as previously stated. The thermal noise contribution is increased to $5.15x^2_{\text{zpf}}$ by the now added spin thermal noise. The remaining $6.44x^2_{\text{zpf}}$ back-action variance is significantly less than that of the membrane alone.

Thus, we infer the amount of evaded quantum back-action to be $-24 \pm 5\,\%$ ($-1.0\,\text{dB}$) of the mechanics alone[6], quite a considerable amount! In the positive mass setting the hybrid system has a total variance of $17.62x^2_{\text{zpf}}$ and only a slightly higher thermal noise contribution. This it contains $50 \pm 8\,\%$ (1.9 dB) more quantum back-action noise than the membrane only. This is a quite sizeable interference contrast, only masked on the absolute scale by thermal noise.

We may further notice that the spin thermal noise has been processed by the optomechanical system as the added contribution on top of the mechanical thermal noise is reduced near resonance also. This is a consequence of the same mixing term discussed in section 6.4.2 limiting the back-action evasion to $\simeq 1/2$. Indeed all the spin noise is transduced through the transfer matrix, and in this case the optomechanical response reduces the spin thermal noise contribution by $-18\,\%$.

The back-action evasion makes the sensitivity to mechanical motion greater by reducing the back-action contribution. We define the sensitivity enhancement as the fraction of the membrane spectral response to that of the negative spin mass hybrid system. This, furthermore, provides a convenient way to view the quantum back-action cancellation experimentally realized in a wide bandwidth, since it is now normalized to the mechanical response.

In the left panel of fig. 6.20 we see this sensitivity enhancement as a fractional

[6]Once again these are fractional differences.

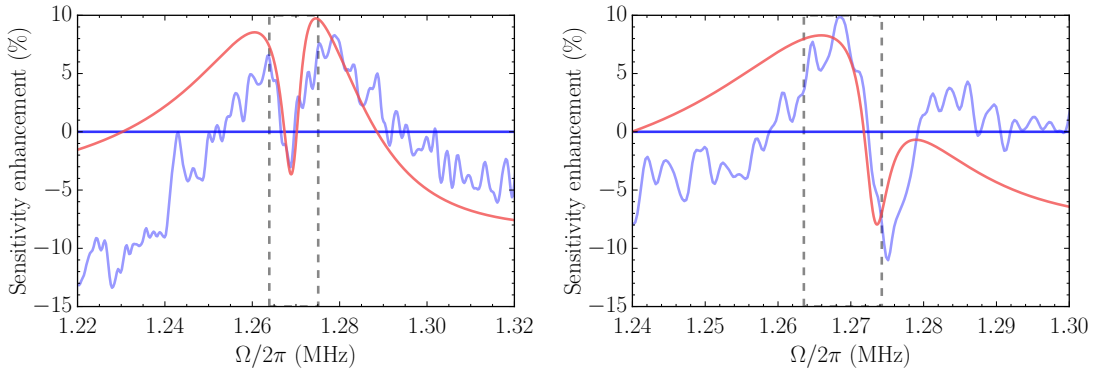

Figure 6.20: **Quantum back-action evasion sensitivity enhancement.** Blue line is the fractional difference of the membrane only and negative spin mass hybrid system. The red solid line is the same fractional difference of the individual fits of the hybrid model to each measurement, not a fit to the fractional difference. The solid blue line indicates the mechanical response to which the negative spin mass hybrid system is compared. Dashed black lines indicate a γ_M wide region around the mechanical resonance frequency. **Left:** The case of degenerate oscillators discussed in section 6.4.3. Data and fits are seen in figs. 6.16 and 6.19.. **Right:** The case of non-degenerate oscillators discussed in section 6.4.4. The data and associated fits are shown in fig. 6.23.

difference[7]. In the region near the mechanical resonance we see that the sensitivity enhancement is mostly positive, although small, except for on exact joint resonance, where there is not net gain. Initially, on the wings of the resonance, the gains are long lived spanning more than two full linewidths, but eventually become negligible and a loss.

Lastly, we notice that the sensitivity enhancement has qualitatively the same form as the positive spin mass hybrid system interference. This is, of course, no coincidence as the enhancement is a consequence of the destructive interference. This is itself like a inverted image of the constructive interference.

6.4.4 Non-degenerate subsystems

The limit of $\simeq -50\,\%$ back-action cancellation is specific to the case of degenerate, matched, oscillators. If, and we are, one is free to set the relative detuning and the quadrature mapping phase θ at will, then one can surpass the $\simeq -50\,\%$ mark without making the mechanical response broader. The trick is to detune the spin system whilst simultaneously rotating the optical quadratures input to the cavity. This combination shifts the point of no back-action cancellation away from mechanical resonance, where the response has the largest gain. How far from resonance is optimal depends on the gain factor of the spin ensemble. The detuning can be considerable since the back-action interference depends on differences in quadrature amplitudes, not power.

[7]Subtracting unity from the ratio of responses gives the fractional difference.

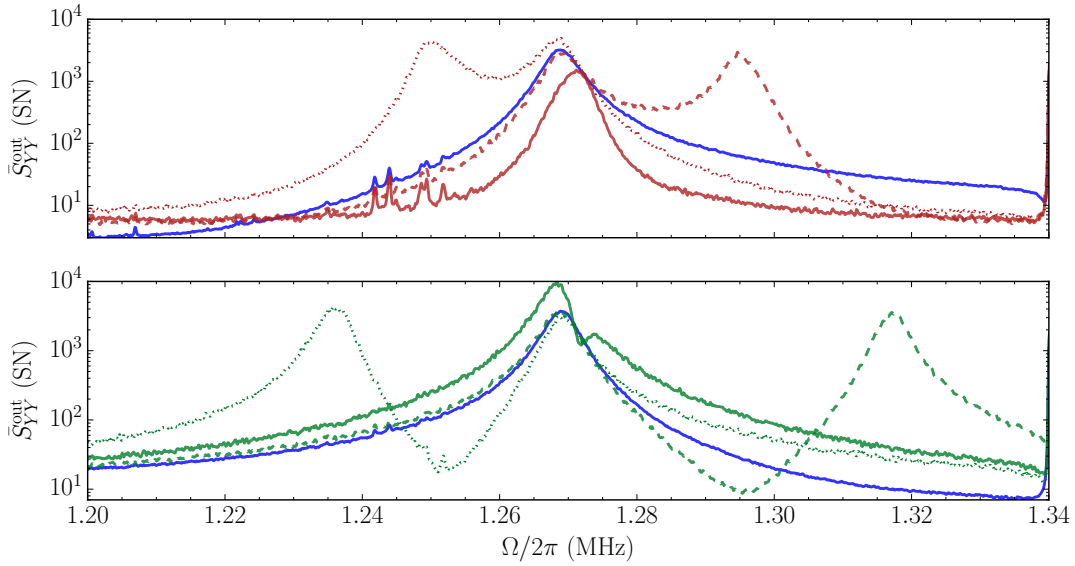

Figure 6.21: **White noise spectral response of non-degenerate hybrid system.** Spectral response of a non-degenerate hybrid system otherwise reasonably well matched. The mechanical system alone is shown in blue and the negative (positive) spin mass hybrid system in red (green). In the case of solid curves the spin system is set $|\Omega_S| - \Omega_M = 2\pi \times 4.2\,\mathrm{kHz}$ slightly blue detuned. As in fig. 6.14 the dashed (dotted) curves are for spins which are far blue (red) detuned from the mechanical resonance frequency (1.27 MHz) by $\geq 20\,\mathrm{kHz}$. Both oscillators have similar broadenings, $\gamma_M = 2\pi \times 5.4\,\mathrm{kHz}$ and $\gamma_S = 2\pi \times 4.6\,\mathrm{kHz}$ and similar readout rates. The spin system spectra are not shown for clarity. **Top:** Negative mass spin ensemble. **Bottom:** Positive mass spin ensemble.

In this scheme the back-action interference in the hybrid system has, to a large extent, the same general behaviour as the degenerate case, with only spectrally local differences. To appreciate this we compare the back-action response (to white noise) of the detuned system, fig. 6.21, with that expected from the degenerate case shown in fig. 6.14. The features characteristic of the negative and positive mass hybrid system are clear. There is a point of no back-action cancellation, still at the spin resonance frequency, and large interference in the wings of the hybrid response. Detuning the spin ensemble far into the blue or red we see the characteristic positive and negative hybrid spin mass interference features. Two positive mass systems has destructive interference between the oscillators and constructive outside, whereas for a positive (mechanical) and negative (spin) mass combination in the hybrid system yields constructive interference between them and destructive outside.

For the experiments which follow the mechanical cooperativity was slightly lower than in section 6.4.3, now $C_q^M = 2.2$, meaning an optomechanical quantum back-action to thermal noise ratio of 1.5. Despite this, as we shall see, greater quantum back-action cancellation was achieved. In detuning the spins from the mechanics by $|\Omega_S| - \Omega_M = 2\pi \times 4.2\,\mathrm{kHz}$ we rotated the quadrature mapping described by eq. (6.30) by $\theta = 6°$.

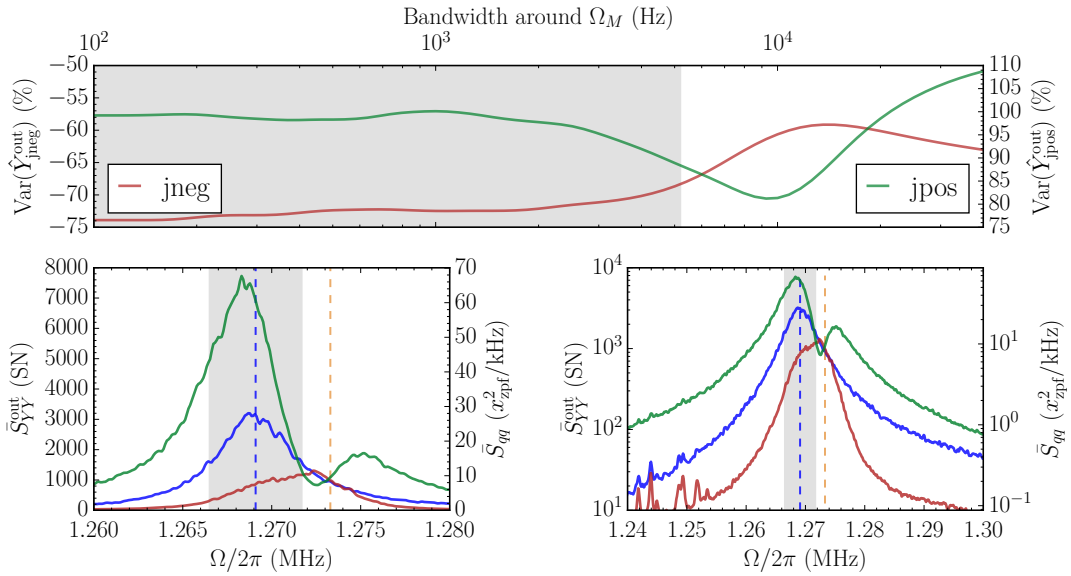

Figure 6.22: **Non-degenerate hybrid white noise back-action evasion.** Mechanics, shown in blue, has a resonance frequency at the dashed blue line. Likewise the spins have their resonance frequency at the dashed yellow line. Hybrid system with spins as negative mass (red) and positive mass (green) clearly show significant back-action interference. The grey shaded region indicates the bandwidth corresponding to the full mechanical linewidth γ_M centered on the mechanical resonance. **Top:** Variance for hybrid system (spectral areas of the panels below, subtracting shot noise), relative to that of the membrane alone, in a variable bandwidth centered on mechanical resonance. Hybrid system with negative spin mass (joint negative: jneg) and with positive spin mass (joint positive: jpos) are shown together but on different axes, left and right, respectively. **Bottom left:** Power spectral density of hybrid system and membrane only as read out in the optical phase quadrature. **Bottom right:** Same as left, but on logarithmic scale and in a wider spectral window.

Added white noise

Lets take a closer look at case where lots of white noise is added, as we did in the degenerate case. When the spin system is blue detuned from the mechanics as just described we have fig. 6.22. In this case the back-action evasion on mechanical resonance is very large, at $-74\,\%$. Enabled by the relocation of no interference point to the wings of the mechanical response.

As we look in a very wide bandwidth, the total back-action in the hybrid system is reduced by $-63\,\%$, considerably more than the maximum of $-54\,\%$ expected from eq. (6.38) had the systems been degenerate.

Likewise the positive mass hybrid system interference is very large, approaching $110\,\%$ of the membrane only. With such large interference we now switch off the white noise drive, as done previously, expecting the quantum-back action to display a similar interference profile.

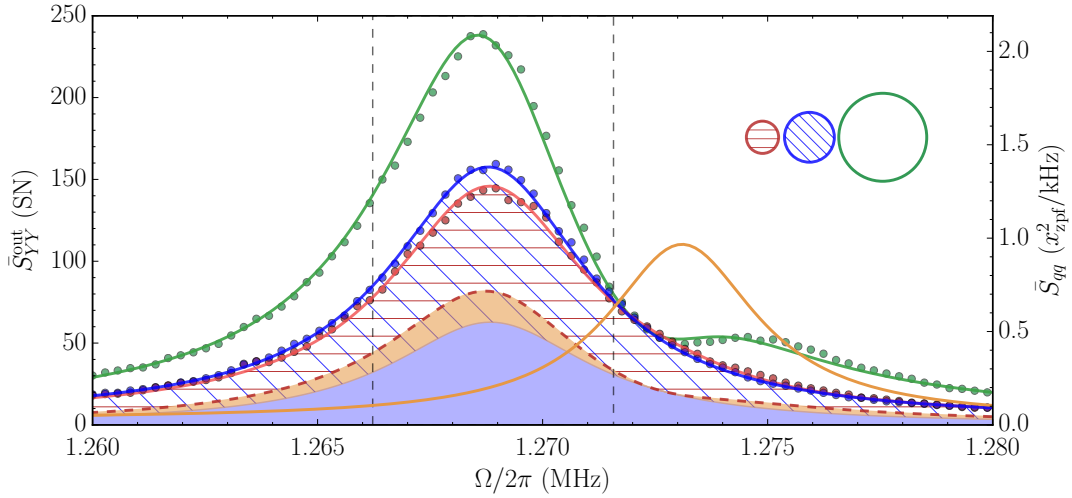

Figure 6.23: **Hybrid quantum back-action evasion in the non-degenerate case.** Power spectral density of the output optical phase quadrature for the hybrid system with a negative (red), and positive (green) spin mass. Also shown are the membrane only (blue) and spin only (yellow). Dots are measurements and solid lines are fits from the full hybrid model. The spin measurements are omitted here for clarity. The red hatched region is the quantum back-action contribution to the hybrid system whereas the blue hatched region is similarly the quantum back-action contribution from the membrane only. The region between the green solid line and the red dashed line is approximately the quantum back-action contribution to the positive spin mass hybrid system. The region contained between the dashed grey lines indicated a full mechanical linewidth γ_M around the resonance resonance. **Inset:** The areas of the circles are directly proportional to the quantum back-action variance contribution for each system.

Quantum back-action evasion

Now with no white noise we *clearly* see the interference of the quantum back-action in fig. 6.23. In particular we also see a significant noise reduction on mechanical resonance. The responses shown in fig. 6.23 display the same form as the white noise driven case shown in fig. 6.22 with the biggest interference on mechanical resonance, least near the spin resonance frequency, and again noticeably (in this figure however only in the positive mass case) above the spin resonance frequency.

The interference in the negative mass case is easily seen through the sensitivity enhancement shown in fig. 6.20. Notice the qualitative similarity in the enhancement profile of the degenerate case. In this case we have a significant sensitivity enhancement of 8 % near the mechanical resonance frequency. Indeed, there is a statistically significant net sensitivity improvement over the entire bandwidth. The full variance of the negative mass hybrid system, $10.4x_{\text{zpf}}^2$, is (94 ± 2) %, of the full membrane only variance $11.1x_{\text{zpf}}^2$. This improvement is as found in the degenerate case, but the spectral region of sensitivity improvement with respect to the mechanical susceptibility is quite different.

Let us now consider the contributions to the variances seen in fig. 6.23. The total variance for the mechanical oscillator is $11.10x_{\text{zpf}}^2$ and the thermal noise contributes

$4.26x^2_{\mathrm{zpf}}$ equivalent to an effective thermal bath of $\bar{n}^{\mathrm{th}}_{\mathrm{M}} = 2.13$ thermal phonons. The quantum back-action variance of $6.84x^2_{\mathrm{zpf}}$ dominates. Adding the negative mass spin system gives a total hybrid variance of $10.44x^2_{\mathrm{zpf}}$ of which $5.9x^2_{\mathrm{zpf}}$ is thermal noise and the remaining $4.54x^2_{\mathrm{zpf}}$ quantum back-action contribution, clearly reduced comparable the membrane only case. When the hybrid system is in the positive spin mass configuration the total variance is $17.7x^2_{\mathrm{zpf}}$ and the thermal contribution merely $5.61x^2_{\mathrm{zpf}}$. Thus the quantum back-action comprises $12.09x^2_{\mathrm{zpf}}$.

From these we infer that the quantum back-action variance of the negative spin mass hybrid system is $-34 \pm 5\,\%$ ($-1.8\,\mathrm{dB}$) below that of the membrane only. For the positive spin mass case the variance is increased $73 \pm 10\,\%$ ($2.4\,\mathrm{dB}$). Once again we note that the spin thermal noise is filtered by the optomechanical transfer matrix, in this case by $-17\,\%$.

The quantum back-action variance contributions to the membrane, as well as hybrid system in both mass configurations, are displayed in the inset of fig. 6.23 as the areas of the circles. By comparison of these, the contrast between the constructive and destructive interference is vividly clear, as well as the very appreciable amount of demonstrated quantum back-action evasion in the negative mass hybrid system.

Chapter 7

Summary and Outlook

, specifically and section 6.4,

7.1 Summary

In this thesis I have presented the two most important results of my experimental work conducted at the Niels Bohr Institute over the past 4 years. Initially the focus was on realizing a robust and versatile quantum enabled membrane-in-the-middle optomechanical system. These efforts, intimately linked with the development of highly coherent mechanical resonators Tsaturyan et al. (2014), ultimately succeeded for multiple mechanical modes simultaneously and was published in Nielsen et al. (2016). This laid the foundation for further developments enabling us to generate, and detect, even stronger ponderomotive squeezing of light, (-3.18 ± 0.18) dB below the shot noise level. This is, to the best of my knowledge, the largest degree of ponderomotive squeezing of light reported to date.

These results are discussed in section 4.4, and serve as a testament to the strength of the quantum correlations achievable in our optomechanical system. The simple design of this system, along with the implementation in a flow cryostat, enabled improvements in both the optical and mechanical components to be rapidly implemented. High detection efficiencies are also feasible with such a platform, which was crucial for subsequent endeavors where quantum correlations are of great importance.

Building on top of this quantum optomechanical platform, we proceeded to design and realize a hybrid spin-optomechanical system, combining the atomic spin ensemble and the aforementioned membrane-in-the-middle system. The spin ensemble consisted of a vapour cell with 10^9 spin polarized cesium atoms used to realize an effective negative mass oscillator. Measuring in the reference frame of this oscillator, it is possible to evade the back-action on the mechanical oscillator motion concomitant with quantum limited sensitivity. The experiment realized is based on a proposal by Hammerer et al. (2009), which will soon celebrate its decennial anniversary.

This hybrid system demonstrated the evasion, by $-1.8\,\mathrm{dB}$, of quantum back-action limiting the sensitivity to mechanical motion. This result was published in Møller et al. (2017) and marked the first time two different systems were optically linked in such a quantum enabled fashion. The nature of the hybrid system paves the way for entanglement generating as well as improved sensing of force, motion and gravity beyond the standard quantum limit.

7.2 Outlook

The encouraging results obtained and described in this work have led to new aspirations. One such idea is inspired by the dawn of gravitational wave-astronomy being ushered in by Abbott et al. (2016) as well as the fields recent entry into the multi-messenger astronomy community facilitated by the detection of the binary neutron star merger described in Abbott et al. (2017). As outlined in the pre-print by Khalili and Polzik (2017), the idea is to use a negative mass spin system to evade the quantum back-action on the motion of the mechanical interferometer mirrors comprising state-of-the-art gravitational wave detectors. This scheme, drawing on many of the same key concepts as the work presented here, promises to improve instrument sensitivity in a wide bandwidth.

As our understanding of the current spin-optomechanical hybrid system dynamics continues to improve, new insights and visions are likely to emerge. Although both systems comprise harmonic oscillators at heart, the hybrid system is vastly greater than the sum of its parts and has provided ample surprises throughout the work carried out so far. Going forward I expect nothing less.

7.2.1 Entanglement

The initial long term vision for this experiment, namely Einstein-Podolsky-Rosen (EPR) entanglement between the mechanical and spin systems, was laid out by Hammerer et al. (2009). I am not the first PhD student to have worked towards this ambitious goal and, clearly, I am not the last. The system realized thus far however, shows great potential towards this end. Demonstrating the evasion of the quantum back-action is an underlying feature of the desired EPR entanglement.

Towards this effort the recent pre-print by Huang et al. (2018) provides ample motivation as it details the details of how our hybrid system may generate, even unconditional, EPR entanglement. They define a generalized EPR variance, ξ_g, taking into account the relevant experimental realities of our hybrid system. These are the finite losses between our two systems, which may in general be read out at different rates and have a fundamentally different interactions with light. The spin ensemble is predominantly probed with a QND interaction, whereas for the mechanics we probe significantly off cavity resonance, realizing a manifestly non-QND interaction as seen by the significant dynamical back-action cooling present in

chapter 6.

They have shown that the misbalance of interaction types, and large dynamical back-action broadening of the mechanics as compared to the spins, may be used as a resource. We already saw in section 6.4.2 that this regime is also favourable from the perspective of back-action evasion.

Entering the desired regime of unconditional entanglement set by $\xi_g < 1$ is restrained by the thermal noises of both systems as well as the optical losses between the systems. Furthermore, if conditional entanglement is pursued, where the measurement record is included in our knowledge of the system evolution, the detection efficiency is of added importance. Thus, before concluding this work, we discuss some exciting new technical improvements diminishing the adverse effects of thermal noise and optical losses on future entanglement in the hybrid system.

In discussing these improvements it is worth keeping in mind the following results from Huang et al. (2018). The presence of a power loss ϵ between the systems bounds the entanglement to no less than

$$\xi_g \geq \sqrt{\frac{\epsilon}{4-3\epsilon}}. \tag{7.1}$$

The effect of thermal noise is harder to bound, but the achievable entanglement is enhanced by higher quantum cooperativities. The scaling with these are handwavingly, $\propto \sqrt{1/C_q^S}$ and $\propto \sqrt{1/C_q^M}$, thus the fraction of thermal noise compared to back-action is on the same square root footing as the optical losses.

The unconditional scheme relies on large dynamical back-action cooling to reduce the thermal variance. If sufficient optical broadening is not experimentally feasible, then conditional entanglement, where the thermal motion is measured and corrected for, may instead be the way to go.

7.2.2 Optomechanical improvements

On the optomechanical side, the new generation of "soft clamped" membrane resonators by Tsaturyan et al. (2017) are now realized in our optomechanical setup. These membranes do not show signs of hybridization and their much higher Q factors, even keeping thickness and resonance frequency fixed, enable quantum cooperativities at least an order of magnitude higher than the $C_q^M = 2.6$ described in section 6.4. The mechanical cooperativity can be further increased since the higher spin system cooperativity realizes a larger readout rate for the same probe induced broadening. These two factors will all but remove the mechanical thermal noise contribution realizing a hybrid system abundantly dominated by quantum back-action.

As thermal noise diminishes in importance, classical laser amplitude noise will take its spot as dominant factor for mechanical decoherence. In practice this limits the feasible mechanical frequency from below. Reducing the laser noise influence without going to a higher frequency can be achieved by introducing a filter cavity at the laser output. Since our back-action evasion scheme is fixed in absolute operating

frequency by the atomic D2 line, the added experimental complexity of such a cavity may not be too large of an inconvenience. Having less amplitude noise also means higher probe powers can be used, thereby increasing the achievable readout rate.

Mirror noise also constrains the choice of mechanical resonance frequency and limits the amount of dynamical back-action that is practically useful. An improved understanding and enhanced predictive capabilities in regards to where (spectrally) a particular cavity assembly produces cavity noise is sure to help. Additionally, physically smaller mirrors in conjunction with an updated cavity assembly should yield a significantly less dense spectrum of cavity noise. The deep valleys between Brownian noise peaks in such a spectrum may even allow for room temperature quantum optomechanics.

7.2.3 Spin system improvements

On the atomic side, a spin system with an improved quantum cooperativity of $C_q^S = 3.5$ has already been realized at 55 °C. Comparing this to the $C_q^S = 1.1$ achieved for the results of section 6.4, at 68 °C, the spin thermal noise contribution is now significantly diminished. Furthermore, the intrinsic damping rate of the spins in this vapour cell is more than two times less, at only 400 Hz, meaning this higher cooperativity can be reached for a smaller probe induced broadening. Indeed this higher cooperativity was reached already at a broadening of 1.5 kHz. This makes it significantly easier for the dynamical back-action affected mechanics to be significantly broader than the spins. This will allow for a greater degree of quantum back-action evasion, and likely also entanglement.

Furthermore, embedding the atomic ensemble in a low-finesse cavity may prove advantageous as it can boost the readout rate for the same optically induced broadening. Higher quantum cooperativities should therefore be expected. However, making high transmission vapour cells is a difficult task as it appears the spin-relaxation coating crucial for low decoherence negatively impacts the anti-reflection coating of the windows. Additionally the cavity must be largely one-sided towards the mechanics as the outcoupling efficiency will constitute an intrasystem loss.

The higher mechanical coherence times available with the new generation of membranes means possible improvements on the atomic ensemble. The length of the microchannel confining the atoms, 300 µm across, was designed such that the atomic motion would average out over the decoherence time of the mechanical oscillator. Now that this time is increased, by an order of magnitude, the microchannel may equally be made larger.

A larger channel width, keeping the length constant, would allow the waist of the optical probe to be made larger. Since the Rayleigh range is longer this probe could sample a larger fraction of the atoms, thus reducing the effect of the broadband noise. If instead the cavity is made longer, then the optical depth will increase as more atoms are sampled. This gives a larger readout rate and thus a higher spin

cooperativity. Similarly advantageous, the wider channel decreases an atoms wall collisions per unit time, thus decreasing the intrinsic spin decoherence rate.

7.2.4 Optical link and detection improvements

On the optical side, a severe reduction in the optical losses between the spin and mechanical systems, and in ultimate detection, has been made following the experiments of chapter 6. Before, the losses between the systems amounted to roughly 54 % of the quantum vacuum driving spin system being replaced before driving the mechanics as described in section 6.2.3. Clearly there was room for improvement.

The new vapour cell not only enables a higher cooperativity but also has lower optical losses, now only contributing 1.5 % to the intrasystem loss[1]. Furthermore, the optical layout has been simplified and fitted with low loss, high quality, waveplates, polarizing beam splitters, mirrors, and lenses. The loss from outside the cell to the input of the optomechanical cavity is now merely 7 %, a reduction by 26 percent points. The cavity one-sidedness remains unchanged, but the reduced number of optics, and a less distorted optical mode from the new vapour cell, now allows for mode matching losses of less than 3 %. Thus the total losses now only amount to roughly 15.5 %, a more than three-fold reduction! This will allow for even larger back-action interference and, using eq. (7.1), should limit the achievable unconditional entanglement to $\xi_g \geq .21$, which would be very respectable bearing in mind that $\xi_g = 1$ is the case of no entanglement.

The layout of the homodyne detection scheme needed for optical phase quadrature readout has not changed much. Previously, the losses in converting intracavity quantum fluctuations into photo-current fluctuations of was 70 %. Here there was certainly also room for improvement.

Just as with the optical link, the detection path has been fitted with low loss optics and benefits from an improved cavity mode matching. This has reduced the loss from outside the cavity to detector down to 5 % and the improved mode matching now results in losses of 3 %. The homodyning visilibilty is also helped by the improved spatial mode quality of the probe and can now reach 97 % thus responsible for 6 % loss. Thus the total detection loss is now < 20 %, again, a more than three-fold improvement! This not only greatly improves the sensitivity of our detection and allows for conditional entanglement to be considered.

The homodyne detector still uses glass encapsulated diodes with a quantum efficiency of 90 % responsible for a 10 % loss. Removing this protective glass leaves the bare diodes which are specified to have a quantum efficiency of 98 % at 852 nm. This would bring the losses from the diodes down to 2 % thus rendering it feasible that our detection losses may be still be significantly reduced. This will also remove the now most lossy single element in detecting spin or mechanical ponderomotive

[1] A full transmission of 3 %.

squeezing. The latter case, combined with the improved cooperativities, should thus be able to just about reach $-10\,\mathrm{dB}$ of observed squeezing.

7.2.5 Final remarks

The selection of hybrid system improvements just discussed have been carried out since the experiments of chapter 6. To me they highlight the ever improving and evolving nature of our experiments, achieved through hard work, improved understanding, and concerted effort. Taken together with the results obtained so far, the hybrid system constructed seems a promising candidate for, and inspiration to, future pioneering experiments. I hope our efforts here prove useful for experimentalists and theorists alike, at QUANTOP, and elsewhere.

This is the end, beautiful friend
This is the end, my only friend, the end.

Jim Morrison, The Doors

Bibliography

[Abbott et al., 2016] B. P. Abbott et al. Observation of gravitational waves from a binary black hole merger. *Phys. Rev. Lett.*, 116:061102, Feb 2016. doi: 10.1103/PhysRevLett.116.061102. URL https://link.aps.org/doi/10.1103/PhysRevLett.116.061102. ↑204

[Abbott et al., 2017] B. P. Abbott et al. Gw170817: Observation of gravitational waves from a binary neutron star inspiral. *Phys. Rev. Lett.*, 119:161101, Oct 2017. doi: 10.1103/PhysRevLett.119.161101. URL https://link.aps.org/doi/10.1103/PhysRevLett.119.161101. ↑204

[Arimondo et al., 1977] E. Arimondo, M. Inguscio, and P. Violino. Experimental determinations of the hyperfine structure in the alkali atoms. *Rev. Mod. Phys.*, 49:31–75, Jan 1977. doi: 10.1103/RevModPhys.49.31. URL https://link.aps.org/doi/10.1103/RevModPhys.49.31. ↑125

[Aspelmeyer et al., 2014] Markus Aspelmeyer, Tobias J. Kippenberg, and Florian Marquardt. Cavity optomechanics. *Rev. Mod. Phys.*, 86:1391–1452, Dec 2014. doi: 10.1103/RevModPhys.86.1391. URL https://link.aps.org/doi/10.1103/RevModPhys.86.1391. ↑3

[B. Alcock et al., 1984] C B. Alcock, V P. Itkin, and M K. Horrigan. Vapour pressure equations for the metallic elements: 298–2500k. 23:309–313, 07 1984. ↑142

[Bao et al., 2002] Minhang Bao, Heng Yang, Hao Yin, and Yuancheng Sun. Energy transfer model for squeeze-film air damping in low vacuum. *Journal of Micromechanics and Microengineering*, 12(3):341, 2002. URL http://stacks.iop.org/0960-1317/12/i=3/a=322. ↑54

[Bechhoefer, 2005] John Bechhoefer. Feedback for physicists: A tutorial essay on control. *Rev. Mod. Phys.*, 77:783–836, Aug 2005. doi: 10.1103/RevModPhys.77.783. URL https://link.aps.org/doi/10.1103/RevModPhys.77.783. ↑99

[Bernard et al., 2016] Simon Bernard, Christoph Reinhardt, Vincent Dumont, Yves-Alain Peter, and Jack C. Sankey. Precision resonance tuning and design of sin photonic crystal reflectors. *Opt. Lett.*, 41(24):5624–5627, Dec 2016. doi: 10.1364/OL.41.005624. URL http://ol.osa.org/abstract.cfm?URI=ol-41-24-5624. ↑83

[Black, 2001] Eric D. Black. An introduction to pound–drever–hall laser frequency stabilization. *American Journal of Physics*, 69(1):79–87, 2001. doi: 10.1119/1.1286663. URL https://doi.org/10.1119/1.1286663. ↑107

[Boller et al., 1991] K.-J. Boller, A. Imamoğlu, and S. E. Harris. Observation of electromagnetically induced transparency. *Phys. Rev. Lett.*, 66:2593–2596, May 1991. doi: 10.1103/PhysRevLett.66.2593. URL https://link.aps.org/doi/10.1103/PhysRevLett.66.2593. ↑93

[Borregaard et al., 2016] J. Borregaard, M. Zugenmaier, J. M. Petersen, H. Shen, G. Vasilakis, K. Jensen, E. S. Polzik, and A. S. Sørensen. Scalable photonic network architecture based on motional averaging in room temperature gas. *Nature Communications*, 7:11356, Apr 2016. URL http://dx.doi.org/10.1038/ncomms11356. Article. ↑150

[Bowen, 2016] Gerard J Bowen, Warwick P.; Milburn. *Quantum optomechanics*. CRC Press, 2016. ISBN 978-1-4822-5916-2,1482259168. ↑229, ↑233, ↑234

[Braginskii and Manukin, 1977] V. B. Braginskii and A. B. Manukin. *Measurement of weak forces in physics experiments*. 1977. ↑5

[Braginsky et al., 1985] V.B. Braginsky, V.P. Mitrofanov, V.I. Panov, K.S. Thorne, and C. Eller. *Systems with Small Dissipation*. University of Chicago Press, 1985. ISBN 9780226070735. URL https://books.google.dk/books?id=fkOIvXwrENcC. ↑50

[Braginsky et al., 1980] Vladimir B. Braginsky, Yuri I. Vorontsov, and Kip S. Thorne. Quantum nondemolition measurements. *Science*, 209(4456):547–557, August 1980. ISSN 00368075. ↑3, ↑5, ↑7

[Braginsky et al., 1992] Vladimir B. Braginsky, Farid Ya Khalili, and Kip S. Thorne. *Quantum Measurement*. Cambridge University Press, 1992. doi: 10.1017/CBO9780511622748. ↑5

[Breit and Rabi, 1931] G. Breit and I. I. Rabi. Measurement of nuclear spin. *Phys. Rev.*, 38:2082–2083, Dec 1931. doi: 10.1103/PhysRev.38.2082.2. URL https://link.aps.org/doi/10.1103/PhysRev.38.2082.2. ↑127

[Brooks et al., 2012a] Daniel W. C. Brooks, Thierry Botter, Sydney Schreppler, Thomas P. Purdy, Nathan Brahms, and Dan M. Stamper-Kurn. Non-classical light generated by quantum-noise-driven cavity optomechanics. *Nature*, 488:476, Aug 2012a. URL http://dx.doi.org/10.1038/nature11325. ↑6

[Brooks et al., 2012b] Daniel W. C. Brooks, Thierry Botter, Sydney Schreppler, Thomas P. Purdy, Nathan Brahms, and Dan M. Stamper-Kurn. Non-classical light generated by quantum-noise-driven cavity optomechanics. *Nature*, 488 (7412):476–480, Aug 2012b. ISSN 0028-0836. doi: 10.1038/nature11325. URL http://dx.doi.org/10.1038/nature11325. ↑101

[Budker and Kimball, 2013] D. Budker and D.F.J. Kimball. *Optical Magnetometry*. Optical Magnetometry. Cambridge University Press, 2013. ISBN 9781107010352. ↑4

[Budker and Romalis, 2007] Dmitry Budker and Michael Romalis. Optical magnetometry. *Nature Physics*, 3:227, Apr 2007. URL http://dx.doi.org/10.1038/nphys566. Review Article. ↑4

[Bui et al., 2012] Catvu H. Bui, Jiangjun Zheng, S. W. Hoch, Lennon Y. T. Lee, J. G. E. Harris, and Chee Wei Wong. High-reflectivity, high-q micromechanical membranes via guided resonances for enhanced optomechanical coupling. *Applied Physics Letters*, 100(2):021110, 2012. doi: 10.1063/1.3658731. URL https://doi.org/10.1063/1.3658731. ↑83

[Camerer et al., 2011] Stephan Camerer, Maria Korppi, Andreas Jöckel, David Hunger, Theodor W. Hänsch, and Philipp Treutlein. Realization of an optomechanical interface between ultracold atoms and a membrane. *Phys. Rev. Lett.*, 107:223001, Nov 2011. doi: 10.1103/PhysRevLett.107.223001. URL https://link.aps.org/doi/10.1103/PhysRevLett.107.223001. ↑7

[Caniard et al., 2007] T. Caniard, P. Verlot, T. Briant, P.-F. Cohadon, and A. Heidmann. Observation of back-action noise cancellation in interferometric and weak force measurements. *Phys. Rev. Lett.*, 99:110801, Sep 2007. doi: 10.1103/PhysRevLett.99.110801. URL https://link.aps.org/doi/10.1103/PhysRevLett.99.110801. ↑6

[Caves, 1980] Carlton M. Caves. Quantum-mechanical radiation-pressure fluctuations in an interferometer. *Phys. Rev. Lett.*, 45:75–79, Jul 1980. doi: 10.1103/PhysRevLett.45.75. URL https://link.aps.org/doi/10.1103/PhysRevLett.45.75. ↑6

[Caves et al., 1980] Carlton M. Caves, Kip S. Thorne, Ronald W. P. Drever, Vernon D. Sandberg, and Mark Zimmermann. On the measurement of a weak classical force coupled to a quantum-mechanical oscillator. i. issues of principle. *Rev. Mod. Phys.*, 52:341–392, Apr 1980. doi: 10.1103/RevModPhys.52.341. URL https://link.aps.org/doi/10.1103/RevModPhys.52.341. ↑3, ↑5

[Chakram et al., 2014] S. Chakram, Y. S. Patil, L. Chang, and M. Vengalattore. Dissipation in ultrahigh quality factor sin membrane resonators. *Phys. Rev. Lett.*, 112:127201, Mar 2014. doi: 10.1103/PhysRevLett.112.127201. URL https://link.aps.org/doi/10.1103/PhysRevLett.112.127201. ↑52

[Chan et al., 2011] Jasper Chan, T. P. Mayer Alegre, Amir H. Safavi-Naeini, Jeff T. Hill, Alex Krause, Simon Gröblacher, Markus Aspelmeyer, and Oskar Painter. Laser cooling of a nanomechanical oscillator into its quantum ground state. *Nature*, 478:89, Oct 2011. URL http://dx.doi.org/10.1038/nature10461. ↑5

[Chen et al., 2017] Xu Chen, Clément Chardin, Kevin Makles, Charles Caër, Sheon Chua, Rémy Braive, Isabelle Robert-Philip, Tristan Briant, Pierre-François Cohadon, Antoine Heidmann, Thibaut Jacqmin, and Samuel Deléglise. High-finesse fabry-perot cavities with bidimensional si3n4 photonic-crystal slabs. *Light: Science &Amp; Applications*, 6:e16190, Jan 2017. URL http://dx.doi.org/10.1038/lsa.2016.190. Original Article. ↑83, ↑111

[Christopher Gerry, 2005] Peter Knight Christopher Gerry. *Introductory quantum optics*. Cambridge University Press, 2005. ISBN 052152735X. ↑12, ↑233, ↑241

[Clark et al., 2017] Jeremy B. Clark, Florent Lecocq, Raymond W. Simmonds, José Aumentado, and John D. Teufel. Sideband cooling beyond the quantum back-action limit with squeezed light. *Nature*, 541:191, Jan 2017. URL http://dx.doi.org/10.1038/nature20604. ↑77

[Clerk et al., 2008] A A Clerk, F Marquardt, and K Jacobs. Back-action evasion and squeezing of a mechanical resonator using a cavity detector. *New Journal of Physics*, 10(9):095010, 2008. URL http://stacks.iop.org/1367-2630/10/i=9/a=095010. ↑7

[Colangelo et al., 2017] Giorgio Colangelo, Ferran Martin Ciurana, Lorena C. Bianchet, Robert J. Sewell, and Morgan W. Mitchell. Simultaneous tracking of spin angle and amplitude beyond classical limits. *Nature*, 543:525, Mar 2017. URL http://dx.doi.org/10.1038/nature21434. ↑4

[DeSalvo, 2012] Gregory M Harry; Timothy P Bodiya; Riccardo DeSalvo. *Optical coatings and thermal noise in precision measurement*. Cambridge University Press, 1 edition, 2012. ISBN 9781139206341,1139206346,9780511762314,0511762313,1139203363,9781139203364. ↑117

[Dorsel et al., 1983] A. Dorsel, J. D. McCullen, P. Meystre, E. Vignes, and H. Walther. Optical bistability and mirror confinement induced by radiation pressure. *Phys. Rev. Lett.*, 51:1550–1553, Oct 1983. doi: 10.1103/PhysRevLett.51.1550. URL https://link.aps.org/doi/10.1103/PhysRevLett.51.1550. ↑65

[E., 1998] Hecht E. *Optics*. AW, 3 edition, 1998. ISBN 0201838877, 9780201838879. ↑236

[Einstein et al., 1935] A. Einstein, B. Podolsky, and N. Rosen. Can quantum-mechanical description of physical reality be considered complete? *Phys. Rev.*, 47:777–780, May 1935. doi: 10.1103/PhysRev.47.777. URL https://link.aps.org/doi/10.1103/PhysRev.47.777. ↑2

[Faust et al., 2014] Thomas Faust, Johannes Rieger, Maximilian J. Seitner, Jörg P. Kotthaus, and Eva M. Weig. Signatures of two-level defects in the temperature-dependent damping of nanomechanical silicon nitride resonators. *Phys. Rev.*

B, 89:100102, Mar 2014. doi: 10.1103/PhysRevB.89.100102. URL https://link.aps.org/doi/10.1103/PhysRevB.89.100102. ↑51

[Fischer et al., 2016] R. Fischer, N. S. Kampel, G. G. T. Assumpção, P.-L. Yu, K. Cicak, R. W. Peterson, R. W. Simmonds, and C. A. Regal. Optical probing of mechanical loss of a si_3n_4 membrane below 100 mk. *Arxiv*, Nov 2016. URL arXiv:1611.00878. ↑116

[Foot, 2005] C.J. Foot. *Atomic physics*. Oxford master series in physics. Oxford University Press, 2005. ISBN 9780198506966. URL https://books.google.dk/books?id=kXYpAQAAMAAJ. ↑126

[Ford et al., 1988] G. W. Ford, J. T. Lewis, and R. F. O'Connell. Quantum langevin equation. *Phys. Rev. A*, 37:4419–4428, Jun 1988. doi: 10.1103/PhysRevA.37.4419. URL https://link.aps.org/doi/10.1103/PhysRevA.37.4419. ↑43

[Gardiner and Collett, 1985] C. W. Gardiner and M. J. Collett. Input and output in damped quantum systems: Quantum stochastic differential equations and the master equation. *Phys. Rev. A*, 31:3761–3774, Jun 1985. doi: 10.1103/PhysRevA.31.3761. URL https://link.aps.org/doi/10.1103/PhysRevA.31.3761. ↑26

[Gardiner, 2010] Crispin Gardiner. *Stochastic Methods: A Handbook for the Natural and Social Sciences (Springer Series in Synergetics)*. Springer Series in Synergetics. Springer, softcover reprint of hardcover 4th ed. 2009 edition, 2010. ISBN 3642089623,9783642089626. ↑229

[Geek3, 2014] Geek3. Poincare-sphere arrows.svg, 2014. URL https://commons.wikimedia.org/wiki/File:Poincare-sphere_arrows.svg. Computer graphic, viewed Dec 2017, (GNU Free Documentation license v. 1.2). ↑18, ↑137

[Genes and Dantan, 2017] Claudiu Genes and Aurélien Dantan. Light–matter interactions in multi-element resonators. *Journal of Physics B: Atomic, Molecular and Optical Physics*, 50(10):105502, 2017. URL http://stacks.iop.org/0953-4075/50/i=10/a=105502. ↑90

[Gerrard, 1975] J. M. Gerrard, A.; Burch. *Introduction to Matrix Methods in Optics*. Dover Publications, 1975. ISBN 978-1-62198-674-4,978-87-630-0005-5,0-486-68044-4. ↑238

[Giovannetti and Vitali, 2001] Vittorio Giovannetti and David Vitali. Phase-noise measurement in a cavity with a movable mirror undergoing quantum brownian motion. *Phys. Rev. A*, 63:023812, Jan 2001. doi: 10.1103/PhysRevA.63.023812. URL https://link.aps.org/doi/10.1103/PhysRevA.63.023812. ↑43

[Goldstein, 2003] Dennis H. Goldstein. *Polarized Light, Revised and Expanded (Optical Science and Engineering)*. CRC Press, 2 edition, 2003. ISBN 082474053X. ↑16, ↑17, ↑239

[Gorodetksy et al., 2010] M. L. Gorodetksy, A. Schliesser, G. Anetsberger, S. Deleglise, and T. J. Kippenberg. Determination of the vacuum optomechanical coupling rate using frequency noise calibration. *Opt. Express*, 18(22):23236–23246, Oct 2010. doi: 10.1364/OE.18.023236. URL http://www.opticsexpress.org/abstract.cfm?URI=oe-18-22-23236. ↑115

[Gröblacher et al., 2009a] Simon Gröblacher, Klemens Hammerer, Michael R. Vanner, and Markus Aspelmeyer. Observation of strong coupling between a micromechanical resonator and an optical cavity field. *Nature*, 460:724, Aug 2009a. URL http://dx.doi.org/10.1038/nature08171. ↑83

[Gröblacher et al., 2009b] Simon Gröblacher, Jared B. Hertzberg, Michael R. Vanner, Garrett D. Cole, Sylvain Gigan, K. C. Schwab, and Markus Aspelmeyer. Demonstration of an ultracold micro-optomechanical oscillator in a cryogenic cavity. *Nature Physics*, 5:485, Jun 2009b. URL http://dx.doi.org/10.1038/nphys1301. ↑83

[Hammerer et al., 2009] K. Hammerer, M. Aspelmeyer, E. S. Polzik, and P. Zoller. Establishing einstein-poldosky-rosen channels between nanomechanics and atomic ensembles. *Phys. Rev. Lett.*, 102:020501, Jan 2009. doi: 10.1103/PhysRevLett.102.020501. URL https://link.aps.org/doi/10.1103/PhysRevLett.102.020501. ↑xi, ↑3, ↑7, ↑203, ↑204

[Hammerer et al., 2010] Klemens Hammerer, Anders S. Sørensen, and Eugene S. Polzik. Quantum interface between light and atomic ensembles. *Rev. Mod. Phys.*, 82:1041–1093, Apr 2010. doi: 10.1103/RevModPhys.82.1041. URL https://link.aps.org/doi/10.1103/RevModPhys.82.1041. ↑3, ↑150

[Huang et al., 2018] X. Huang, E. Zeuthen, D. V. Vasilyev, Q. He, K. Hammerer, and E. S. Polzik. Unconditional steady-state entanglement in macroscopic hybrid systems by coherent noise cancellation. *Arxiv*, Jan 2018. URL arXiv:1801.02569. ↑204, ↑205

[Ismail et al., 2016] Nur Ismail, Cristine Calil Kores, Dimitri Geskus, and Markus Pollnau. Fabry-pérot resonator: spectral line shapes, generic and related airy distributions, linewidths, finesses, and performance at low or frequency-dependent reflectivity. *Opt. Express*, 24(15):16366–16389, Jul 2016. doi: 10.1364/OE.24.016366. URL http://www.opticsexpress.org/abstract.cfm?URI=oe-24-15-16366. ↑22

[Jayich et al., 2008] A M Jayich, J C Sankey, B M Zwickl, C Yang, J D Thompson, S M Girvin, A A Clerk, F Marquardt, and J G E Harris. Dispersive optomechanics: a membrane inside a cavity. *New Journal of Physics*, 10(9):095008, 2008. URL http://stacks.iop.org/1367-2630/10/i=9/a=095008. ↑24, ↑87, ↑90

[Jensen et al., 2016] Kasper Jensen, Rima Budvytyte, Rodrigo A. Thomas, Tian Wang, Annette M. Fuchs, Mikhail V. Balabas, Georgios Vasilakis, Lars D. Mosgaard, Hans C. Stærkind, Jörg H. Müller, Thomas Heimburg, Søren-Peter Olesen, and Eugene S. Polzik. Non-invasive detection of animal nerve impulses with an atomic magnetometer operating near quantum limited sensitivity. *Scientific Reports*, 6: 29638, Jul 2016. URL http://dx.doi.org/10.1038/srep29638. Article. ↑4

[Jöckel et al., 2014] Andreas Jöckel, Aline Faber, Tobias Kampschulte, Maria Korppi, Matthew T. Rakher, and Philipp Treutlein. Sympathetic cooling of a membrane oscillator in a hybrid mechanical-atomic system. *Nature Nanotechnology*, 10:55, Nov 2014. URL http://dx.doi.org/10.1038/nnano.2014.278. ↑8

[Julsgaard, 2003] Brian Julsgaard. *Entanglement and Quantum Interactions with Macroscopic Gas Samples*. PhD thesis, 2003. ↑15, ↑122, ↑128, ↑134, ↑147, ↑148, ↑150, ↑155

[Julsgaard et al., 2001] Brian Julsgaard, Alexander Kozhekin, and Eugene S. Polzik. Experimental long-lived entanglement of two macroscopic objects. *Nature*, 413:400, Sep 2001. URL http://dx.doi.org/10.1038/35096524. ↑xi, ↑4

[Kampel et al., 2017] N. S. Kampel, R. W. Peterson, R. Fischer, P.-L. Yu, K. Cicak, R. W. Simmonds, K. W. Lehnert, and C. A. Regal. Improving broadband displacement detection with quantum correlations. *Phys. Rev. X*, 7:021008, Apr 2017. doi: 10.1103/PhysRevX.7.021008. URL https://link.aps.org/doi/10.1103/PhysRevX.7.021008. ↑7

[Kasapi et al., 1995] A. Kasapi, Maneesh Jain, G. Y. Yin, and S. E. Harris. Electromagnetically induced transparency: Propagation dynamics. *Phys. Rev. Lett.*, 74:2447–2450, Mar 1995. doi: 10.1103/PhysRevLett.74.2447. URL https://link.aps.org/doi/10.1103/PhysRevLett.74.2447. ↑96

[Kaushik et al., 2005] A. Kaushik, H. Kahn, and A. H. Heuer. Wafer-level mechanical characterization of silicon nitride mems. *Journal of Microelectromechanical Systems*, 14(2):359–367, April 2005. ISSN 1057-7157. doi: 10.1109/JMEMS.2004.839315. ↑53

[Kemiktarak et al., 2012] Utku Kemiktarak, Mathieu Durand, Michael Metcalfe, and John Lawall. Cavity optomechanics with sub-wavelength grating mirrors. *New Journal of Physics*, 14(12):125010, 2012. URL http://stacks.iop.org/1367-2630/14/i=12/a=125010. ↑83

[Khalili and Polzik, 2017] F. Khalili and E. S. Polzik. Overcoming the sql in gravitational wave detectors using spin systems with negative effective mass. *Arxiv*, Oct 2017. URL arXiv:1710.10405. ↑204

[Kippenberg and Vahala, 2007] T.J. Kippenberg and K.J. Vahala. Cavity optomechanics. *Opt. Express*, 15(25):17172–17205, Dec 2007. doi: 10.1364/OE.15.017172. URL http://www.opticsexpress.org/abstract.cfm?URI=oe-15-25-17172. ↑63

[Kleckner et al., 2011] Dustin Kleckner, Brian Pepper, Evan Jeffrey, Petro Sonin, Susanna M. Thon, and Dirk Bouwmeester. Optomechanical trampoline resonators. *Opt. Express*, 19(20):19708–19716, Sep 2011. doi: 10.1364/OE.19.019708. URL http://www.opticsexpress.org/abstract.cfm?URI=oe-19-20-19708. ↑83

[Kohler et al., 2017] Jonathan Kohler, Justin Gerber, Emma Dowd, and Dan M. Stamper-Kurn. Negative-mass instability of the spin and motion of an atomic gas driven by optical cavity backaction. *Arxiv*, Sep 2017. URL arXiv:1709.04531. ↑8

[Kominis et al., 2003] I. K. Kominis, T. W. Kornack, J. C. Allred, and M. V. Romalis. A subfemtotesla multichannel atomic magnetometer. *Nature*, 422:596, Apr 2003. URL http://dx.doi.org/10.1038/nature01484. ↑4

[Koschorreck et al., 2010] M. Koschorreck, M. Napolitano, B. Dubost, and M. W. Mitchell. Sub-projection-noise sensitivity in broadband atomic magnetometry. *Phys. Rev. Lett.*, 104:093602, Mar 2010. doi: 10.1103/PhysRevLett.104.093602. URL https://link.aps.org/doi/10.1103/PhysRevLett.104.093602. ↑4

[Krauter et al., 2011] Hanna Krauter, Christine A. Muschik, Kasper Jensen, Wojciech Wasilewski, Jonas M. Petersen, J. Ignacio Cirac, and Eugene S. Polzik. Entanglement generated by dissipation and steady state entanglement of two macroscopic objects. *Phys. Rev. Lett.*, 107:080503, Aug 2011. doi: 10.1103/PhysRevLett.107.080503. URL https://link.aps.org/doi/10.1103/PhysRevLett.107.080503. ↑5

[Kuhn et al., 2014] A. G. Kuhn, J. Teissier, L. Neuhaus, S. Zerkani, E. van Brackel, S. Deléglise, T. Briant, P.-F. Cohadon, A. Heidmann, C. Michel, L. Pinard, V. Dolique, R. Flaminio, R. Taïbi, C. Chartier, and O. Le Traon. Free-space cavity optomechanics in a cryogenic environment. *Applied Physics Letters*, 104 (4):044102, 2014. doi: 10.1063/1.4863666. URL https://doi.org/10.1063/1.4863666. ↑83

[Landau L.D., 1986] Lifshitz E.M. Landau L.D. *Theory of elasticity*, volume 7. Butterworth-Heinemann, 3ed. edition, 1986. ISBN 9780750626330. ↑38

[Leissa, 1993] Arthur Leissa. *Vibration of Plates*. Asoa, 1993. ↑38

[Levin, 1998] Yu. Levin. Internal thermal noise in the ligo test masses: A direct approach. *Phys. Rev. D*, 57:659–663, Jan 1998. doi: 10.1103/PhysRevD.57.659. URL https://link.aps.org/doi/10.1103/PhysRevD.57.659. ↑118

[Levine and Wright, 1971] M. J. Levine and Jon Wright. Sixth-order magnetic moment of the electron. *Phys. Rev. Lett.*, 26:1351–1353, May 1971. doi: 10.1103/PhysRevLett.26.1351. URL https://link.aps.org/doi/10.1103/PhysRevLett.26.1351. ↑127

[Lifshitz and Roukes, 2000] Ron Lifshitz and M. L. Roukes. Thermoelastic damping in micro- and nanomechanical systems. *Phys. Rev. B*, 61:5600–5609, Feb 2000. doi: 10.1103/PhysRevB.61.5600. URL https://link.aps.org/doi/10.1103/PhysRevB.61.5600. ↑49

[Lukin, 2005] M.D. Lukin. Modern atomic and optical physics ii. Lecture Notes, 2005. http://docplayer.net/42357140-Modern-atomic-and-optical-physics-ii-lectures-by-m-d-lukin-notes-taken-and-typed-by-l-childress.html. ↑26

[Lyons, 2004] Richard G. Lyons. *Understanding Digital Signal Processing*. Pearson Education, second edition edition, 2004. ISBN 0131089897,9780131089891. ↑227

[Ma et al., 2017] Zhenyang. Ma, Xuhong. Liu, Xinhai. Yu, Chunlei. Shi, and Dayun. Wang. Mechanical, anisotropic, and electronic properties of xn (x = c, si, ge): Theoretical investigations. *Materials*, 10(912), 2017. doi: 10.3390/ma10080912. ↑50

[Marc André Meyers, 2008] Krishan Kumar Chawla Marc André Meyers. *Mechanical Behavior of Materials*. Cambridge University Press, 2 edition, 2008. ISBN 0521866758,9780521866750. ↑47

[Marquardt et al., 2007] Florian Marquardt, Joe P. Chen, A. A. Clerk, and S. M. Girvin. Quantum theory of cavity-assisted sideband cooling of mechanical motion. *Phys. Rev. Lett.*, 99:093902, Aug 2007. doi: 10.1103/PhysRevLett.99.093902. URL https://link.aps.org/doi/10.1103/PhysRevLett.99.093902. ↑74

[Milonni P.W., 2010] Eberly J.H. Milonni P.W. *Laser Physics*. Wiley, 2 edition, 2010. ISBN 0470387718,9780470387719. ↑253, ↑255

[Møller et al., 2017] Christoffer B. Møller, Rodrigo A. Thomas, Georgios Vasilakis, Emil Zeuthen, Yeghishe Tsaturyan, Mikhail Balabas, Kasper Jensen, Albert Schliesser, Klemens Hammerer, and Eugene S. Polzik. Quantum back-action-evading measurement of motion in a negative mass reference frame. *Nature*, 547(7662): 191–195, Jul 2017. ISSN 0028-0836. doi: 10.1038/nature22980. URL http://dx.doi.org/10.1038/nature22980. Letter. ↑xii, ↑7, ↑68, ↑157, ↑204

[Murch et al., 2008] Kater W. Murch, Kevin L. Moore, Subhadeep Gupta, and Dan M. Stamper-Kurn. Observation of quantum-measurement backaction with an ultracold atomic gas. *Nat Phys*, 4(7):561–564, Jul 2008. ISSN 1745-2473. doi: 10.1038/nphys965. URL http://dx.doi.org/10.1038/nphys965. ↑5, ↑101

[Neuhaus et al., 2013] L. Neuhaus, A. G. Kuhn, S. Zerkani, J. Teissier, D. García-Sánchez, S. Deléglise, T. Briant, P. F. Cohadon, and A. Heidmann. Fabry-perot cavity optomechanics with ultrahigh mechanical-q-factor quartz micropillars at cryogenic temperature. In *2013 Conference on Lasers Electro-Optics Europe International Quantum Electronics Conference CLEO EUROPE/IQEC*, pages 1–1, May 2013. doi: 10.1109/CLEOE-IQEC.2013.6801641. ↑83

[Nielsen, 2016] William Nielsen. *Quantum Cavity Optomechanics with Phononic Bandgap Shielded Silicon Nitride Membranes*. PhD thesis, Niels Bohr Institute, Copenhagen University, May 2016. ↑xii, ↑24, ↑85, ↑88, ↑96, ↑101, ↑110, ↑114, ↑115, ↑116

[Nielsen et al., 2016] William Hvidtfelt Padkær Nielsen, Yeghishe Tsaturyan, Christoffer Bo Møller, Eugene S. Polzik, and Albert Schliesser. Multimode optomechanical system in the quantum regime. *Proceedings of the National Academy of Sciences*, 114(1):62–66, Dec 2016. doi: 10.1073/pnas.1608412114. URL http://www.pnas.org/content/114/1/62.abstract. ↑xii, ↑6, ↑9, ↑85, ↑88, ↑98, ↑101, ↑103, ↑104, ↑203

[Norte et al., 2016] R. A. Norte, J. P. Moura, and S. Gröblacher. Mechanical resonators for quantum optomechanics experiments at room temperature. *Phys. Rev. Lett.*, 116:147202, Apr 2016. doi: 10.1103/PhysRevLett.116.147202. URL https://link.aps.org/doi/10.1103/PhysRevLett.116.147202. ↑83

[Ockeloen-Korppi et al., 2016] C. F. Ockeloen-Korppi, E. Damskägg, J.-M. Pirkkalainen, A. A. Clerk, M. J. Woolley, and M. A. Sillanpää. Quantum backaction evading measurement of collective mechanical modes. *Phys. Rev. Lett.*, 117:140401, Sep 2016. doi: 10.1103/PhysRevLett.117.140401. URL https://link.aps.org/doi/10.1103/PhysRevLett.117.140401. ↑7

[Ockeloen-Korppi et al., 2017] C. F. Ockeloen-Korppi, E. Damskagg, J.-M. Pirkkalainen, A. A. Clerk, F. Massel, M. J. Woolley, and M. A. Sillanpaa. Entangled massive mechanical oscillators. *Arxiv*, Nov 2017. URL arXiv:1711.01640. ↑7

[O'Connell et al., 2010] A. D. O'Connell, M. Hofheinz, M. Ansmann, Radoslaw C. Bialczak, M. Lenander, Erik Lucero, M. Neeley, D. Sank, H. Wang, M. Weides, J. Wenner, John M. Martinis, and A. N. Cleland. Quantum ground state and single-phonon control of a mechanical resonator. *Nature*, 464:697, Mar 2010. URL http://dx.doi.org/10.1038/nature08967. Article. ↑5

[Ou and Mandel, 1989] Z. Y. Ou and L. Mandel. Derivation of reciprocity relations for a beam splitter from energy balance. *American Journal of Physics*, 57(1):66–67, 1989. doi: 10.1119/1.15873. URL http://dx.doi.org/10.1119/1.15873. ↑241

[Peterson et al., 2016a] R. W. Peterson, T. P. Purdy, N. S. Kampel, R. W. Andrews, P.-L. Yu, K. W. Lehnert, and C. A. Regal. Laser cooling of a micromechanical

membrane to the quantum backaction limit. *Phys. Rev. Lett.*, 116:063601, Feb 2016a. doi: 10.1103/PhysRevLett.116.063601. URL https://link.aps.org/doi/10.1103/PhysRevLett.116.063601. ↑6

[Peterson et al., 2016b] R. W. Peterson, T. P. Purdy, N. S. Kampel, R. W. Andrews, P.-L. Yu, K. W. Lehnert, and C. A. Regal. Laser cooling of a micromechanical membrane to the quantum backaction limit. *Phys. Rev. Lett.*, 116:063601, Feb 2016b. doi: 10.1103/PhysRevLett.116.063601. URL https://link.aps.org/doi/10.1103/PhysRevLett.116.063601. ↑74

[Pierson, 2000] Hugh O. Pierson. *Handbook Of Chemical Vapor Deposition*. Materials Science and Process Technology. William Andrew, 2 edition, 2000. ISBN 9780815514329,0815514328. ↑37

[Polzik and Hammerer, 2015] Eugene S. Polzik and Klemens Hammerer. Trajectories without quantum uncertainties. *Annalen der Physik*, 527(1-2):A15–A20, 2015. ISSN 1521-3889. doi: 10.1002/andp.201400099. URL http://dx.doi.org/10.1002/andp.201400099. ↑1, ↑3

[Purdy et al., 2013a] T. P. Purdy, R. W. Peterson, and C. A. Regal. Observation of radiation pressure shot noise on a macroscopic object. *Science*, 339(6121):801–804, 2013a. ISSN 0036-8075. doi: 10.1126/science.1231282. URL http://science.sciencemag.org/content/339/6121/801. ↑5, ↑101

[Purdy et al., 2013b] T. P. Purdy, P.-L. Yu, R. W. Peterson, N. S. Kampel, and C. A. Regal. Strong optomechanical squeezing of light. *Phys. Rev. X*, 3:031012, Sep 2013b. doi: 10.1103/PhysRevX.3.031012. URL https://link.aps.org/doi/10.1103/PhysRevX.3.031012. ↑6, ↑101

[Reiter and Sørensen, 2012] Florentin Reiter and Anders S. Sørensen. Effective operator formalism for open quantum systems. *Phys. Rev. A*, 85:032111, Mar 2012. doi: 10.1103/PhysRevA.85.032111. URL https://link.aps.org/doi/10.1103/PhysRevA.85.032111. ↑140, ↑259

[Ressler et al., 1969] N. W. Ressler, R. H. Sands, and T. E. Stark. Measurement of spin-exchange cross sections for cs^{133}, rb^{87}, rb^{85}, k^{39}, and na^{23}. *Phys. Rev.*, 184:102–118, Aug 1969. doi: 10.1103/PhysRev.184.102. URL https://link.aps.org/doi/10.1103/PhysRev.184.102. ↑154

[Robinson et al., 1958] H. G. Robinson, E. S. Ensberg, and H. G. Dehmelt. Preservation of a spin state in free atom-inert surface collisions. *Bulletin of the American Physical Society*, 3, 1958. ↑154

[Safavi-Naeini et al., 2011] A. H. Safavi-Naeini, T. P. Mayer Alegre, J. Chan, M. Eichenfield, M. Winger, Q. Lin, J. T. Hill, D. E. Chang, and O. Painter. Electromagnetically induced transparency and slow light with optomechanics. *Nature*, 472:69 EP, Mar 2011. URL http://dx.doi.org/10.1038/nature09933. ↑6

[Safavi-Naeini et al., 2013] Amir H. Safavi-Naeini, Simon Groblacher, Jeff T. Hill, Jasper Chan, Markus Aspelmeyer, and Oskar Painter. Squeezed light from a silicon micromechanical resonator. *Nature*, 500(7461):185–189, Aug 2013. ISSN 0028-0836. URL http://dx.doi.org/10.1038/nature12307. Letter. ↑6, ↑101

[Saulson, 1994] P.R. Saulson. *Fundamentals of Interferometric Gravitational Wave Detectors*. World Scientific, 1994. ISBN 9789810218201. URL https://books.google.dk/books?id=4JyGQgAACAAJ. ↑230

[Savukov et al., 2006] I. M. Savukov, S.-K. Lee, and M. V. Romalis. Optical detection of liquid-state nmr. *Nature*, 442:1021, Aug 2006. URL http://dx.doi.org/10.1038/nature05088. ↑4

[Schleier-Smith, 2016] Monika Schleier-Smith. Editorial: Hybridizing quantum physics and engineering. *Phys. Rev. Lett.*, 117:100001, Aug 2016. doi: 10.1103/PhysRevLett.117.100001. URL https://link.aps.org/doi/10.1103/PhysRevLett.117.100001. ↑3

[Schliesser et al., 2008] A. Schliesser, R. Riviere, G. Anetsberger, O. Arcizet, and T. J. Kippenberg. Resolved-sideband cooling of a micromechanical oscillator. *Nat Phys*, 4(5):415–419, May 2008. ISSN 1745-2473. doi: 10.1038/nphys939. URL http://dx.doi.org/10.1038/nphys939. ↑64

[Schmid and Hierold, 2008] S. Schmid and C. Hierold. Damping mechanisms of single-clamped and prestressed double- clamped resonant polymer microbeams. *Journal of Applied Physics*, 104(9):093516, 2008. doi: 10.1063/1.3008032. URL http://dx.doi.org/10.1063/1.3008032. ↑52

[Schmid et al., 2016] Silvan Schmid, Luis Guillermo Villanueva, and Michael Lee Roukes. *Fundamentals of Nanomechanical Resonators*. Springer International Publishing, 1 edition, 2016. ISBN 978-3-319-28689-1, 978-3-319-28691-4. ↑40, ↑47, ↑53

[Schmidt et al., 1994] O. Schmidt, K. M. Knaak, R. Wynands, and D. Meschede. Cesium saturation spectroscopy revisited: How to reverse peaks and observe narrow resonances. *Applied Physics B*, 59(2):167–178, Aug 1994. ISSN 1432-0649. doi: 10.1007/BF01081167. URL https://doi.org/10.1007/BF01081167. ↑152

[Seltzer and Romalis, 2009] S. J. Seltzer and M. V. Romalis. High-temperature alkali vapor cells with antirelaxation surface coatings. *Journal of Applied Physics*, 106 (11):114905, 2009. doi: 10.1063/1.3236649. URL https://doi.org/10.1063/1.3236649. ↑154

[Seltzer et al., 2010] S. J. Seltzer, D. J. Michalak, M. H. Donaldson, M. V. Balabas, S. K. Barber, S. L. Bernasek, M.-A. Bouchiat, A. Hexemer, A. M. Hibberd, D. F. Jackson Kimball, C. Jaye, T. Karaulanov, F. A. Narducci, S. A. Rangwala, H. G.

Robinson, A. K. Shmakov, D. L. Voronov, V. V. Yashchuk, A. Pines, and D. Budker. Investigation of antirelaxation coatings for alkali-metal vapor cells using surface science techniques. *The Journal of Chemical Physics*, 133(14):144703, 2010. doi: 10.1063/1.3489922. URL https://doi.org/10.1063/1.3489922. ↑154

[Seltzer, 2008] Scott J. Seltzer. *Developments in alkali -metal atomic magnetometry*. PhD thesis, 2008. URL https://search.proquest.com/docview/275671021?accountid=13607. ↑153

[Serra et al., 2012] E. Serra, A. Borrielli, F. S. Cataliotti, F. Marin, F. Marino, A. Pontin, G. A. Prodi, and M. Bonaldi. Ultralow-dissipation micro-oscillator for quantum optomechanics. *Phys. Rev. A*, 86:051801, Nov 2012. doi: 10.1103/PhysRevA.86.051801. URL https://link.aps.org/doi/10.1103/PhysRevA.86.051801. ↑83

[Serra et al., 2013] E Serra, A Bagolini, A Borrielli, M Boscardin, F S Cataliotti, F Marin, F Marino, A Pontin, G A Prodi, M Vannoni, and M Bonaldi. Fabrication of low loss moms resonators for quantum optics experiments. *Journal of Micromechanics and Microengineering*, 23(8):085010, 2013. URL http://stacks.iop.org/0960-1317/23/i=8/a=085010. ↑83

[Sewell et al., 2012] R. J. Sewell, M. Koschorreck, M. Napolitano, B. Dubost, N. Behbood, and M. W. Mitchell. Magnetic sensitivity beyond the projection noise limit by spin squeezing. *Phys. Rev. Lett.*, 109:253605, Dec 2012. doi: 10.1103/PhysRevLett.109.253605. URL https://link.aps.org/doi/10.1103/PhysRevLett.109.253605. ↑4

[Spethmann et al., 2015] Nicolas Spethmann, Jonathan Kohler, Sydney Schreppler, Lukas Buchmann, and Dan M. Stamper-Kurn. Cavity-mediated coupling of mechanical oscillators limited by quantum back-action. *Nature Physics*, 12:27, Oct 2015. URL http://dx.doi.org/10.1038/nphys3515. ↑7

[Steck, 2010] D. A. Steck. Cesium d line data. *online reference*, 2010. doi: http://steck.us/alkalidata. URL http://steck.us/alkalidata. ↑126, ↑127

[Suh et al., 2014] J. Suh, A. J. Weinstein, C. U. Lei, E. E. Wollman, S. K. Steinke, P. Meystre, A. A. Clerk, and K. C. Schwab. Mechanically detecting and avoiding the quantum fluctuations of a microwave field. *Science*, 344(6189):1262–1265, 2014. ISSN 0036-8075. doi: 10.1126/science.1253258. URL http://science.sciencemag.org/content/344/6189/1262. ↑7

[Teufel et al., 2011] J. D. Teufel, T. Donner, Dale Li, J. W. Harlow, M. S. Allman, K. Cicak, A. J. Sirois, J. D. Whittaker, K. W. Lehnert, and R. W. Simmonds. Sideband cooling of micromechanical motion to the quantum ground state. *Nature*, 475:359, Jul 2011. URL http://dx.doi.org/10.1038/nature10261. ↑5

[Teufel et al., 2016] J. D. Teufel, F. Lecocq, and R. W. Simmonds. Overwhelming thermomechanical motion with microwave radiation pressure shot noise. *Phys. Rev. Lett.*, 116:013602, Jan 2016. doi: 10.1103/PhysRevLett.116.013602. URL https://link.aps.org/doi/10.1103/PhysRevLett.116.013602. ↑101

[Treutlein et al., 2014] Philipp Treutlein, Claudiu Genes, Klemens Hammerer, Martino Poggio, and Peter Rabl. *Hybrid Mechanical Systems*, pages 327–351. Springer Berlin Heidelberg, Berlin, Heidelberg, 2014. ISBN 978-3-642-55312-7. doi: 10.1007/978-3-642-55312-7_14. URL https://doi.org/10.1007/978-3-642-55312-7_14. ↑3

[Tsang and Caves, 2012] Mankei Tsang and Carlton M. Caves. Evading quantum mechanics: Engineering a classical subsystem within a quantum environment. *Phys. Rev. X*, 2:031016, Sep 2012. doi: 10.1103/PhysRevX.2.031016. URL https://link.aps.org/doi/10.1103/PhysRevX.2.031016. ↑3

[Tsaturyan et al., 2017] Y. Tsaturyan, A. Barg, E.S. Polzik, and A. Schliesser. Ultracoherent nanomechanical resonators via soft clamping and dissipation dilution. *Nat. Nano.*, 12:776–783, August 2017. doi: 10.1038/nnano.2017.101. URL http://www.nature.com/nnano/journal/v12/n8/abs/nnano.2017.101.html. ↑xii, ↑39, ↑40, ↑53, ↑58, ↑59, ↑112, ↑113, ↑205

[Tsaturyan, 2016] Yeghishe Tsaturyan. Ultra-high Q micromechanical resonators for cavity optomechanics, 2016. Master's Thesis. ↑57

[Tsaturyan et al., 2014] Yeghishe Tsaturyan, Andreas Barg, Anders Simonsen, Luis Guillermo Villanueva, Silvan Schmid, Albert Schliesser, and Eugene S. Polzik. Demonstration of suppressed phonon tunneling losses in phononic bandgap shielded membrane resonators for high-q optomechanics. *Opt. Express*, 22(6):6810–6821, Mar 2014. doi: 10.1364/OE.22.006810. URL http://www.opticsexpress.org/abstract.cfm?URI=oe-22-6-6810. ↑xii, ↑56, ↑58, ↑203

[Vacher et al., 2005] René Vacher, Eric Courtens, and Marie Foret. Anharmonic versus relaxational sound damping in glasses. ii. vitreous silica. *Phys. Rev. B*, 72:214205, Dec 2005. doi: 10.1103/PhysRevB.72.214205. URL https://link.aps.org/doi/10.1103/PhysRevB.72.214205. ↑51

[Vasilakis et al., 2011] G. Vasilakis, V. Shah, and M. V. Romalis. Stroboscopic backaction evasion in a dense alkali-metal vapor. *Phys. Rev. Lett.*, 106:143601, Apr 2011. doi: 10.1103/PhysRevLett.106.143601. URL https://link.aps.org/doi/10.1103/PhysRevLett.106.143601. ↑4, ↑146

[Vasilakis et al., 2015] G. Vasilakis, H. Shen, K. Jensen, M. Balabas, D. Salart, B. Chen, and E. S. Polzik. Generation of a squeezed state of an oscillator by stroboscopic

back-action-evading measurement. *Nature Physics*, 11:389, Mar 2015. URL http://dx.doi.org/10.1038/nphys3280. ↑4

[Vasilyev et al., 2012] D. V. Vasilyev, K. Hammerer, N. Korolev, and A. S. Sørensen. Quantum noise for faraday light–matter interfaces. *Journal of Physics B: Atomic, Molecular and Optical Physics*, 45(12):124007, 2012. URL http://stacks.iop.org/0953-4075/45/i=12/a=124007. ↑140

[Verbridge et al., 2006] Scott S. Verbridge, Jeevak M. Parpia, Robert B. Reichenbach, Leon M. Bellan, and H. G. Craighead. High quality factor resonance at room temperature with nanostrings under high tensile stress. *Journal of Applied Physics*, 99 (12):124304, 2006. doi: 10.1063/1.2204829. URL http://dx.doi.org/10.1063/1.2204829. ↑52

[Verbridge et al., 2007] Scott S. Verbridge, Daniel Finkelstein Shapiro, Harold G. Craighead, and Jeevak M. Parpia. Macroscopic tuning of nanomechanics: Substrate bending for reversible control of frequency and quality factor of nanostring resonators. *Nano Letters*, 7(6):1728–1735, 2007. doi: 10.1021/nl070716t. URL http://dx.doi.org/10.1021/nl070716t. PMID: 17497822. ↑52

[Villanueva and Schmid, 2014] L. G. Villanueva and S. Schmid. Evidence of surface loss as ubiquitous limiting damping mechanism in sin micro- and nanomechanical resonators. *Phys. Rev. Lett.*, 113:227201, Nov 2014. doi: 10.1103/PhysRevLett.113.227201. URL https://link.aps.org/doi/10.1103/PhysRevLett.113.227201. ↑55, ↑113

[Wallquist et al., 2009] M Wallquist, K Hammerer, P Rabl, M Lukin, and P Zoller. Hybrid quantum devices and quantum engineering. *Physica Scripta*, 2009(T137):014001, 2009. URL http://stacks.iop.org/1402-4896/2009/i=T137/a=014001. ↑3

[Wang et al., 1996] Chong Min Wang, Xiaoqing Pan, M. Rühle, F. L. Riley, and M. Mitomo. Silicon nitride crystal structure and observations of lattice defects. *Journal of Materials Science*, 31(20):5281–5298, Oct 1996. ISSN 1573-4803. doi: 10.1007/BF01159294. URL https://doi.org/10.1007/BF01159294. ↑51

[Wasilewski et al., 2010] W. Wasilewski, K. Jensen, H. Krauter, J. J. Renema, M. V. Balabas, and E. S. Polzik. Quantum noise limited and entanglement-assisted magnetometry. *Phys. Rev. Lett.*, 104:133601, Mar 2010. doi: 10.1103/PhysRevLett.104.133601. URL https://link.aps.org/doi/10.1103/PhysRevLett.104.133601. ↑4

[Weaver et al., 2016] M. J. Weaver, B. Pepper, F. Luna, F. M. Buters, H. J. Eerkens, G. Welker, B. Perock, K. Heeck, S. de Man, and D. Bouwmeester. Nested trampoline resonators for optomechanics. *Applied Physics Letters*, 108(3):033501, 2016. doi: 10.1063/1.4939828. URL https://doi.org/10.1063/1.4939828. ↑83

[Weis et al., 2010] Stefan Weis, Rémi Rivière, Samuel Deléglise, Emanuel Gavartin, Olivier Arcizet, Albert Schliesser, and Tobias J. Kippenberg. Optomechanically induced transparency. *Science*, 330(6010):1520–1523, 2010. ISSN 0036-8075. doi: 10.1126/science.1195596. URL http://science.sciencemag.org/content/330/6010/1520. ↑6, ↑96

[Wilson et al., 2009] D. J. Wilson, C. A. Regal, S. B. Papp, and H. J. Kimble. Cavity optomechanics with stoichiometric sin films. *Phys. Rev. Lett.*, 103:207204, Nov 2009. doi: 10.1103/PhysRevLett.103.207204. URL https://link.aps.org/doi/10.1103/PhysRevLett.103.207204. ↑56, ↑84

[Wilson, 2012] Dalziel Joseph Wilson. *Cavity optomechanics with high-stress silicon nitride films*. PhD thesis, California Institute of Technology, 2012. URL http://resolver.caltech.edu/CaltechTHESIS:06122012-123343193. Dissertation (Ph.D.). ↑39, ↑56, ↑87, ↑90

[Wilson-Rae, 2008] I. Wilson-Rae. Intrinsic dissipation in nanomechanical resonators due to phonon tunneling. *Phys. Rev. B*, 77:245418, Jun 2008. doi: 10.1103/PhysRevB.77.245418. URL https://link.aps.org/doi/10.1103/PhysRevB.77.245418. ↑55

[Wilson-Rae et al., 2011] I. Wilson-Rae, R. A. Barton, S. S. Verbridge, D. R. Southworth, B. Ilic, H. G. Craighead, and J. M. Parpia. High-q nanomechanics via destructive interference of elastic waves. *Phys. Rev. Lett.*, 106:047205, Jan 2011. doi: 10.1103/PhysRevLett.106.047205. URL https://link.aps.org/doi/10.1103/PhysRevLett.106.047205. ↑55

[Wolfgramm et al., 2010] Florian Wolfgramm, Alessandro Cerè, Federica A. Beduini, Ana Predojević, Marco Koschorreck, and Morgan W. Mitchell. Squeezed-light optical magnetometry. *Phys. Rev. Lett.*, 105:053601, Jul 2010. doi: 10.1103/PhysRevLett.105.053601. URL https://link.aps.org/doi/10.1103/PhysRevLett.105.053601. ↑4

[Woolley and Clerk, 2013] M. J. Woolley and A. A. Clerk. Two-mode back-action-evading measurements in cavity optomechanics. *Phys. Rev. A*, 87:063846, Jun 2013. doi: 10.1103/PhysRevA.87.063846. URL https://link.aps.org/doi/10.1103/PhysRevA.87.063846. ↑7

[Woolley and Clerk, 2014] M. J. Woolley and A. A. Clerk. Two-mode squeezed states in cavity optomechanics via engineering of a single reservoir. *Phys. Rev. A*, 89:063805, Jun 2014. doi: 10.1103/PhysRevA.89.063805. URL https://link.aps.org/doi/10.1103/PhysRevA.89.063805. ↑27

[Yu et al., 2012] P.-L. Yu, T. P. Purdy, and C. A. Regal. Control of material damping in high-q membrane microresonators. *Phys. Rev. Lett.*, 108:083603, Feb 2012. doi:

10.1103/PhysRevLett.108.083603. URL https://link.aps.org/doi/10.1103/PhysRevLett.108.083603. ↑52

[Yu et al., 2014] P.-L. Yu, K. Cicak, N. S. Kampel, Y. Tsaturyan, T. P. Purdy, R. W. Simmonds, and C. A. Regal. A phononic bandgap shield for high-q membrane microresonators. *Applied Physics Letters*, 104(2):023510, 2014. doi: 10.1063/1.4862031. URL http://dx.doi.org/10.1063/1.4862031. ↑56

[Yuan et al., 2015] Mingyun Yuan, Vibhor Singh, Yaroslav M. Blanter, and Gary A. Steele. Large cooperativity and microkelvin cooling with a three-dimensional optomechanical cavity. *Nature Communications*, 6:8491, Oct 2015. URL http://dx.doi.org/10.1038/ncomms9491. Article. ↑116

[Zener, 1937] Clarence Zener. Internal friction in solids. i. theory of internal friction in reeds. *Phys. Rev.*, 52:230–235, Aug 1937. doi: 10.1103/PhysRev.52.230. URL https://link.aps.org/doi/10.1103/PhysRev.52.230. ↑49

[Zener, 1938] Clarence Zener. Internal friction in solids ii. general theory of thermoelastic internal friction. *Phys. Rev.*, 53:90–99, Jan 1938. doi: 10.1103/PhysRev.53.90. URL https://link.aps.org/doi/10.1103/PhysRev.53.90. ↑49

[Zener, 1948] Clarence Zener. *Elasticity and Anelasticity of Metals*. University of Chicago Press, 1 edition, 1948. ↑48

[Zwickl et al., 2008] B. M. Zwickl, W. E. Shanks, A. M. Jayich, C. Yang, A. C. Bleszynski Jayich, J. D. Thompson, and J. G. E. Harris. High quality mechanical and optical properties of commercial silicon nitride membranes. *Applied Physics Letters*, 92 (10):103125, 2008. doi: 10.1063/1.2884191. URL http://dx.doi.org/10.1063/1.2884191. ↑84

[Zwickl, 2011] Benjamin Zwickl. *Progress Toward Observation of Radiation Pressure Shot Noise*. PhD thesis, Yale University, 2011. ↑52

Appendix A

Fourier Analysis

In this appendix we discuss the basics of Fourier analysis as it pertains to time varying signals as they are most relevant for this work. We will discuss the mathematical Fourier transform, the discrete analogue used in practice as an estimator, and finally the power spectral density as it relates to signals of interest.

A.1 Fourier Transform

Suppose we have a time varying signal $X(t)$. We define its Fourier transform (FT) as

$$X(\Omega) = \mathcal{F}[X(t)](\Omega) \equiv \int_{-\infty}^{\infty} X(t) e^{-i\Omega t} dt. \tag{A.1.1}$$

This signal $X(\Omega)$ quantifies the strength of the constituent frequency components at Ω present in $X(t)$. Likewise, if we had a signal already in the Fourier domain, say $X(\Omega)$, or wanted to undo our previous transformation, we could simply apply the inverse FT defined here as

$$X(t) = \mathcal{F}^{-1}[X(\Omega)](t) \equiv \int_{-\infty}^{\infty} X(\Omega) e^{i\Omega t} \frac{d\Omega}{2\pi}. \tag{A.1.2}$$

Notice here we are integrating over both positive and negative frequency components. This is often seen as confusing, but is in fact a perfectly consistent and useful tool in signal analysis – and is crucial for understanding the signals that we detect and analyze. That both negative and positive frequency components are important and not at all mystical as explained well in Lyons (2004, Chapter 8.3-4). For now consider the simple example of a real time varying sinuosoid

$$X(t) = \cos \omega t = \frac{e^{i\omega t} + e^{-i\omega t}}{2}, \tag{A.1.3}$$

which when written as complex exponentials clearly indicates – looking at eq. (A.1.1) – that the signal $X(\Omega)$ will have two equal amplitude components at $\Omega = \pm\omega$. One can think of these two components as counter-rotating at the same frequency ω

leaving only a real component, namely $\cos \omega t$. Extending this logic to real signals with multiple frequency components is trivial. From there to complex signals one can further imagine the effect of having a phase difference between the counter rotating components.

For complex signals in general and operators in particular it is important to note the relationship between Hermitian conjugates, namely

$$[X(\Omega)]^\dagger = X^\dagger(-\Omega), \tag{A.1.4}$$

$$X^\dagger(\Omega) = X(\Omega). \tag{A.1.5}$$

We are often concerned with the Fourier transform of time derivatives. By considering the time derivative of eq. (A.1.2) it is clear that

$$\frac{\mathrm{d}}{\mathrm{d}t}X(t) = \frac{\mathrm{d}}{\mathrm{d}t}\mathcal{F}^{-1}[X(\Omega)](t) = \mathcal{F}^{-1}[i\Omega X(\Omega)](t), \tag{A.1.6}$$

$$\therefore \mathcal{F}\left[\frac{\mathrm{d}}{\mathrm{d}t}X(t)\right] = i\Omega X(\Omega). \tag{A.1.7}$$

This logic also applies to spatial derivatives. To see this simply relabel the frequency Ω with a wavenumber k and $\frac{\mathrm{d}}{\mathrm{d}t}$ with $\frac{\mathrm{d}}{\mathrm{d}x}$.

A.2 Discrete Fourier Transform

The use of the Fourier domain is particularly relevant when we care about a particular frequency component of a continuous time trace, e.g. the voltage time trace on a detector. In real life we don't have infinite time traces and so the finite time FT is more relevant,

$$X_T(\Omega) = \int_{-T/2}^{T/2} X(t)e^{-i\Omega t}dt, \tag{A.2.8}$$

where T is the total duration of the time trace.

In practice the FT is often implemented digitally. This involves first digitizing an analogue signal. This digitizes the analogue signal at a sampling rate of f_s for some time T producing an array x total of $N = f_s T$ samples. We then implement a discretized version of the FT known as the Discrete Fourier Transform (DFT), which is defined as

$$X(m) = \sum_{n=0}^{N-1} x(n)e^{-i2\pi nm/N}. \tag{A.2.9}$$

Here the DFT output array $X(m)$ has $m \in \{0, N-1\}$ and maps to a particular component of frequency

$$\Omega(m) = 2\pi m f_s/N = 2\pi m/T. \tag{A.2.10}$$

Clearly the finite length of the time trace sets the spectral resolution, known as the resolution bandwidth (RBW). This is the frequency difference between adjacent bins of $X(m)$ and is given simply by

$$\mathrm{RBW} = f_s/N = 1/T. \tag{A.2.11}$$

Now we can estimate the finite time FT of an continuous $X(t)$ (eq. (A.2.8)) with using the DFT of the sampled array $x(n)$(eq. (A.2.9)) as

$$X_T(\Omega) \approx X(m)/f_s. \tag{A.2.12}$$

A.3 Power Spectral Density

In this section we draw broadly from Bowen (2016) and Gardiner (2010, Chapter 1.5).

The type of signals of interest here are stochastic and will always have the same statistical properties, i.e. they are "stationary". We will also consider the time average of the signals, as described in eq. (A.3.15), as equivalent to the ensemble average. This is known as ergodicity and is tantamount to saying the long time average of a single realization is equivalent to the averaging of many – shorter time – realizations. When considering the stochastic signals relevant in this work, these assumptions are to our knowledge justified.

For such signals, we are typically interested in at particular Fourier frequencies. Considering just a single signal, this is conveniently quantified by the so called power spectral density, which distributes the total power of the system into its constituent frequency components.

We can define the so called power spectral density[1] of a signal $X(t)$ through its finite time Fourier transform as

$$S_{XX}(\Omega) \equiv \lim_{T\to\infty} \frac{1}{T} \left|X_T(\Omega)\right|^2. \tag{A.3.13}$$

In practice of course we do not measure the power spectral density as defined above, but can merely estimate it. The estimator of choice for this work is the so-called Periodogram. It – rather unsurprisingly – uses the discrete Fourier transform approximation of the Fourier transform (eq. (A.2.12)) to give

$$P_{XX} = \frac{1}{T} \left|X(m)/f_s\right|^2 \approx \frac{1}{T} \left|X(\Omega)/f_s\right|^2 = S_{XX}(\Omega). \tag{A.3.14}$$

We can extend the notion of the power spectral density to correlations between two signals. This along with a more detailed description of the power spectral density is given in the subsection below.

[1] This is sometimes also referred to as the spectrum of $X(t)$

A.3.1 Power and cross spectral density theory

Suppose we have two complex signals $X(t)$ and $Y(t)$, we can define the cross correlation function of the signals by (Saulson, 1994, Chapter 4)

$$(X \star Y)(\tau) = G_{XY}(\tau) = \lim_{T\to\infty} \frac{1}{T} \int_{-T/2}^{T/2} X^*(t) Y(t+\tau)\, \mathrm{d}\tau, \tag{A.3.15}$$

where the notational shorthand G_{XY} stands for the application of the $\star$ operation of Y on X. This operation measures the correlations between the signals X and Y at a lag time of τ. It may already be clear how this type of correlation would be of relevant for a signals that are periodically correlated, as the function would have deviations on intervals given by the period.

On the assumption that our signals are ergodic and stationary as discussed above, we can re-write eq. (A.3.15) in terms of the ensemble average as

$$G_{XY}(\tau) = \langle X^*(t) Y(t+\tau) \rangle = \langle X^*(0) Y(\tau) \rangle, \tag{A.3.16}$$

where we have set $t = 0$ for convenience since the signals statistical properties are independent of time (stationary).

Although cross spectral density of two complex signals $X(t)$ and $Y(t)$ is generally defined through their finite time Fourier transforms,

$$S_{XY}(\Omega) \equiv \lim_{T\to\infty} \frac{1}{T} \langle X_T^*(\Omega) Y_T(\Omega') \rangle, \tag{A.3.17}$$

it can be shown via the Weiner-Khincin theorem that the cross spectral density is the Fourier transform of the correlation function, i.e.

$$S_{XY}(\Omega) \equiv \int_{-\infty}^{\infty} G_{XY}(\tau) e^{-i\Omega\tau}\, \mathrm{d}\tau. \tag{A.3.18}$$

This is a very useful result as we can often specify the statistics of a variable through its correlation function.

We can, and it is often more useful for us to, evaluate eq. (A.3.18) in terms of the signals in Fourier space,

$$S_{XY}(\Omega) = \int_{-\infty}^{\infty} \langle X^*(\Omega) Y(\Omega') \rangle \frac{\mathrm{d}\Omega}{2\pi}. \tag{A.3.19}$$

Recall that the power spectral density is simply the cross spectral density when $X = Y$ and will always be a real quantity. On the other hand it is clear that the cross spectral density – in general – is a complex quantity and it can be shown that

$$S_{XY}(\Omega) = S_{YX}^*(\Omega). \tag{A.3.20}$$

As the reader may have been guessed, the case most relevant for us is where the complex variables are in fact operators, i.e. $X \to \hat{X}$ and $Y \to \hat{Y}$ (and replace * with † of course). The definitions and results above are still valid, where the ensemble

averaging now implies the expectation value. There is, however, a key difference in that operators may not always commute. This can lead to differences in the power spectral density, $S_{XX}(\Omega) \neq S_{XX}(-\Omega)$, that cannot occur classically. Thus we define the symmetrized power spectral density as the weighted sum of the negative and positive frequency contributions,

$$\bar{S}_{XX}(\Omega) \equiv \frac{S_{XX}(\Omega) + S_{XX}(-\Omega)}{2} \tag{A.3.21}$$

which is akin to the single sided power spectral density defined classically and is what is actually measured and presented throughout this thesis. That we really measure the symmetrized power spectral density is discussed in appendix B.

Appendix B

Detection and losses

B.1 Direct detection

In this section we will follow Bowen (2016) closely. In direct detection we direct a light field onto a single linear detector as illustrated in fig. B.1. The photons produce electrons in proportion with detectors quantum efficiency, which for the diodes used in this thesis is $\sim 90\,\%$. The statistics of the field detected is therefore carried over into the resultant photo-current.

Let us for simplicity assume the detection is $100\,\%$ efficient. The way to treat losses is described in appendix B.5.1. Suppose the input field is described by some mode $\hat{a}(t)$, then the photo-current operator $\hat{I}$ will be directly related to the photon number flux $\hat{n}(t)$. Taking them to be directly related for simplicity we have

$$\hat{I}(t) = \hat{a}^\dagger(t)\hat{a}(t) = \hat{n}(t). \tag{B.1.1}$$

The detection is comprised of an absorption induced photo-current which goes through the detector electronics and is boosted - irreversibly - to a large classical signal with photo-current $I(t)$. The power spectral density of this classical variable is given by a second order correlation function (see eq. (A.3.18))

$$S_{II}(\Omega) \equiv \int_{-\infty}^{\infty} G_{II}(\tau)e^{-i\Omega\tau}d\tau = \int_{-\infty}^{\infty} \langle I^*(0)I(\tau)\rangle e^{-i\Omega\tau}d\tau \tag{B.1.2}$$

which, when related to the field operator $\hat{a}$ that produced it, should be normal and time ordered[1] (Christopher Gerry, 2005, Chapter 5). This means that the power spectral density of the classical photo-current can be written as

$$S_{II}(\Omega) = \int_{-\infty}^{\infty} \langle :\hat{I}^\dagger(0)\hat{I}(\tau):\rangle e^{-i\Omega\tau}d\tau \tag{B.1.3}$$

$$= \int_{-\infty}^{\infty} \langle \hat{a}^\dagger(0)\hat{a}^\dagger(\tau)\hat{a}(\tau)\hat{a}(0)\rangle e^{-i\Omega\tau}d\tau. \tag{B.1.4}$$

[1] since we are actually annihilating photons by absorption

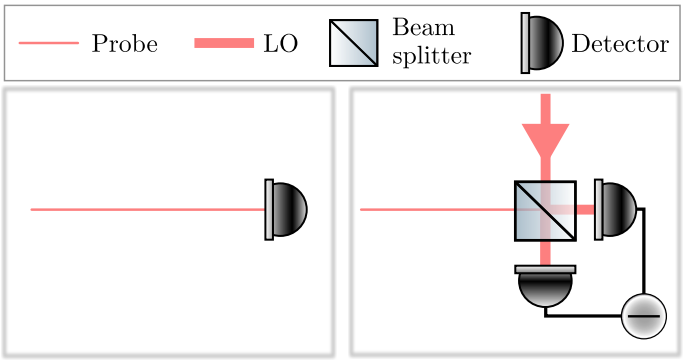

Figure B.1: **Direct and homodyne detection schemes. Left:** In direct direction a probe field is sent directly onto a detector. **Right:** In homodyne detection the probe field is interfered on a 50:50 beamsplitter with a strong field of the same frequency and polarization. This serves as a phase reference for the probe.

Suppose the detected field has a large classical component α (which it often does) then we can write the field in the a linearized fashion as $\hat{a}(t) \to \alpha + \hat{a}(t),\ \alpha \in \mathbb{C}$. We can then see in eq. (B.1.5) below that the photo-current operator measures a particular quadrature $\hat{X}^\theta \equiv \left(\hat{a}^\dagger e^{i\theta} + \hat{a}e^{-i\theta}\right)/\sqrt{2}$ of the quantum field given by the phase θ of the classical component.

$$\hat{I}(t) = \hat{a}^\dagger(t)\hat{a}(t) \to |\alpha|^2 + \sqrt{2}\,|\alpha|\,\hat{X}^\theta(t) + \hat{a}^\dagger(t)\hat{a}(t). \tag{B.1.5}$$

It is clear that the large classical component produces a large DC (i.e. constant in time) value $|\alpha|^2$. The Hermitian quadrature $\hat{X}^\theta(t)$ will dominate the time varying part of $I(t)$ since it is boosted by the amplitude of the large coherent field α. It can further be shown that the power spectral density (without the DC component) will be given by (Bowen, 2016, Chapter 3)

$$S_{II}(\Omega) \approx |\alpha|^2\, \bar{S}_{X^\theta X^\theta}(\Omega), \tag{B.1.6}$$

where the $\bar{S}$ indicates the symmetrized PSD, see eq. (A.3.21). This important result shows that we measure a quadrature of the light field in direct detection by simply investigating the single-sided PSD of the classical photocurrent[2]. Exactly which field quadrature is measured (i.e. what value θ takes) is in direct detection not a free parameter as it is determined by the phase of the coherent component. To access the full range of available quadrature phases we can (and do) use the technique of homodyning.

B.2 Homodyne detection

In this section we also follow Bowen (2016). With homodyning – unlike direct detection – a particular phase quadrature of the field $\hat{a}$ can be measured. We will

[2]to highlight this the operator hat was left on the quadrature $\hat{X}^\theta$ in the subscript of the PSD. This is not done throughout this thesis as it needlessly complicates the notation.

treat this field with a large coherent component, as in appendix B.1, as it is typically the relevant case. The detection scheme is draw in fig. B.1 and simply injects a constant large (degenerate) coherent field α_{LO} with a tunable phase into a 50/50 beam splitter. This field is typically called a local oscillator (LO) as it provides a phase. The photo-current operators on each diode (+ and −) are $\hat{I}_{\pm}(t) = \hat{n}_{\pm}(t)$ neglecting losses (i.e. assuming a unit quantum efficiency).

Looking at the difference current $\hat{I}(t) \equiv \hat{I}_{+}(t) - \hat{I}_{-}(t)$, it can easily be shown that the we will in general measure

$$\hat{I}(t) = (\alpha_{LO}^{*} + \alpha^{*})\,\hat{a}(t) + (\alpha_{LO} + \alpha)\,\hat{a}^{\dagger}(t) \tag{B.2.7}$$

$$\approx \sqrt{2}\,|\alpha_{LO}|\,\hat{X}^{\theta_{LO}}(t),\ \forall\,|\alpha_{LO}| \gg |\alpha|\,, \tag{B.2.8}$$

$$\hat{X}^{\theta_{LO}}(t) \equiv \frac{1}{\sqrt{2}}\left(\hat{a}^{\dagger}e^{i\theta_{LO}} + \hat{a}e^{-i\theta_{LO}}\right). \tag{B.2.9}$$

The phase θ_{LO} is now the phase of the LO, and as such the measured phase quadrature is tunable. In practice this may not always be so easy of course. This freedom is an advantage of homodyning and if the coherent part of the homodyned field, α, is not too large, then it is easy to compensate the LO phase for the phase rotation it causes.

Additionally it is clear that the shot noise level is dominated by the LO, but only be a fraction of α_{LO}/α, i.e. by the fraction of their amplitudes, the square root of the ratio of powers.

Lastly, it is an implicit assumption here that the fields mixed on the BS are in the same spatial mode. This is not true in general, and their mismatch is a source of effective loss. This is described in appendix B.5.2.

B.3 Measuring Stokes components

The polarization quadratures, which are relevant for the atomic spin system, can be completely described by the Stokes operators defined in eq. (2.23d). To measure these quadratures will need to do some polarimetry involving phase retarders, a polarizer and a differential detector.

Let us work in the basis of a field propagating along the z direction while linearly polarized light in the horizontal and vertical (x and y) directions. Let these two polarization modes be described by $\hat{a}_x$ and $\hat{a}_y$. To see the effects of various optical elements on these polarization modes we will adapt the mathematical infrastructure of Jones calculus. This language is expressed in terms of linearly polarized light aligned along x and y (horizontal and vertical), e.g. a horizontally polarized state is given by

$$\hat{a}_x\,|0\rangle = |{\leftrightarrow}\rangle = \begin{pmatrix} 1 \\ 0 \end{pmatrix}. \tag{B.3.10}$$

Operator	State	Stokes vector	Jones vector
$\hat{a}_x$, $\hat{a}_y$	$\|\updownarrow\rangle$, $\|\leftrightarrow\rangle$	$\begin{pmatrix} 1 \\ \pm 1 \\ 0 \\ 0 \end{pmatrix}$	$\begin{pmatrix} 1 \\ 0 \end{pmatrix}$, $\begin{pmatrix} 0 \\ 1 \end{pmatrix}$
$\hat{a}_{\pm 45}$	$\|\nearrow\rangle$, $\|\nwarrow\rangle$	$\begin{pmatrix} 1 \\ 0 \\ \pm 1 \\ 0 \end{pmatrix}$	$\frac{1}{\sqrt{2}}\begin{pmatrix} 1 \\ \pm 1 \end{pmatrix}$
$\hat{a}_{\pm}$	$\|\circlearrowright\rangle$, $\|\circlearrowleft\rangle$	$\begin{pmatrix} 1 \\ 0 \\ 0 \\ \pm 1 \end{pmatrix}$	$\frac{1}{\sqrt{2}}\begin{pmatrix} 1 \\ \mp i \end{pmatrix}$

Table B.1: **Stokes and Jones vectors for a selection of polarization states**. Table inspired by E. (1998).

A right hand circularly polarized state has the y component simply lagging the x component by $\pi/2$, which is reflected in the Jones vector of

$$\hat{a}_+ |0\rangle = |\circlearrowright\rangle = \begin{pmatrix} 1 \\ -i \end{pmatrix}. \tag{B.3.11}$$

The Jones vectors for all the polarization basis states are shown in table B.1 where they are also related to the Stokes vector given by,

$$\boldsymbol{S} = \begin{pmatrix} S_0 \\ S_x \\ S_y \\ S_z \end{pmatrix}. \tag{B.3.12}$$

They can be visualizing on the Poincaré sphere fig. 2.3.

B.3.1 S_x

The Stokes component S_x is simply the difference in the number x and y polarized photons. Suppose we have a detection scheme comprising of a polarizer (PBS) aligned in the x, y polarization basis and a detector at each of the two outputs. Taking the difference clearly will be a measure of S_x. This is shown in fig. B.2. This sounds almost trivial; the input light will simply be split by the PBS it into horizontally linearly polarized light in one output, and vertically polarized in the other. Looking at this more formally, however, will aid in understanding how to measure the remaining Stokes components.

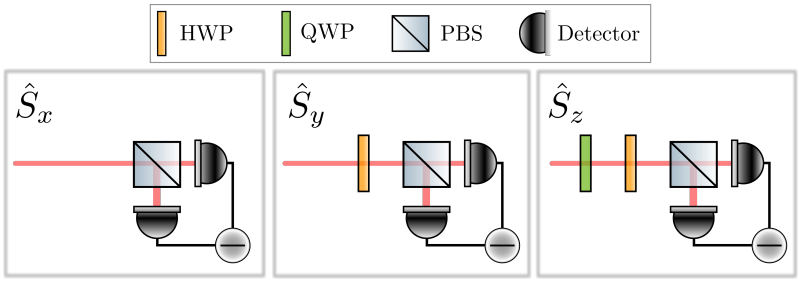

Figure B.2: **Detection of Stokes components.** To detect $\hat{S}_x$ (**left**) we only need a polarizing beamsplitter (PBS) and balanced detection. To measure $\hat{S}_y$ (**middle**) we need to add a half-wave plate (HWP). To measure $\hat{S}_z$ (**right**) we need to add a quarter-wave plate (QWP). The half-wave plate is optional.

The polarizer is the crucial element which performs the projection of the input light. The eigenstates of this projection are what allow us to measure the light components in the basis of x, y. This projection is (in the Jones calculus language) described by the linear polarizer (LP) operator with $\theta = 0$ ($\theta = \pi/2$) where $|\updownarrow\rangle$ ($|\leftrightarrow\rangle$) is the eigenstate. This is trivially checked and is shown below for clarity.

$$\begin{pmatrix} 1 & 0 \\ 0 & 0 \end{pmatrix} |\updownarrow\rangle = |\updownarrow\rangle \,. \tag{B.3.13}$$

This type of measurement is useful for measuring the amount of horizontally vs vertically polarized light which was in our input state. By looking at the variance of the photo-current we will also learn fluctuations of this difference.

The logic just described can be extended to that of S_y and S_z. To measure these we can simply rotate the basis onto which we project.

B.3.2 S_y

Recall that Sy could be seen in the eq. (2.23d) to be simply measuring the difference in photon number operators in the $\pm 45°$ basis. This basis is easily related to the x, y basis through

$$\hat{a}_{\pm 45} = \frac{\hat{a}_x \pm \hat{a}_y}{\sqrt{2}} = \begin{pmatrix} \hat{a}_x & \hat{a}_y \end{pmatrix} \frac{1}{\sqrt{2}} \begin{pmatrix} 1 \\ \pm 1 \end{pmatrix} \tag{B.3.14}$$

which is also clearly seen from the Jones vector in the x,y basis.

In analogy with appendix B.3.1 we simply need to project onto the basis of light polarized along $\pm 45°$ basis. This can be done using a half waveplate retarder (HWP) set at an angle of $\theta = \pi/8$ wrt to the fast axis as shown in fig. B.2. We can think of this in two ways, either we change the polarizer basis or we convert the states in the $\pm 45°$ basis to the x,y basis. Let us simply consider the projection operator due to this basis rotation of the HWP. Again, let us only look at the x output of the PBS,

	LP	QWP	HWP
θ	$\begin{pmatrix} C_1^2 & C_1S_1 \\ C_1S_1 & S_1^2 \end{pmatrix}$	$\begin{pmatrix} C_1^2 - iS_1^2 & C_1S_1(1+i) \\ C_1S_1(1+i) & S_1^2 - iC_1^2 \end{pmatrix}$	$\begin{pmatrix} C_2 & S_2 \\ S_2 & -C_2 \end{pmatrix}$
$\theta = 0$	$\begin{pmatrix} 1 & 0 \\ 0 & 0 \end{pmatrix}$	$\begin{pmatrix} 1 & 0 \\ 0 & -i \end{pmatrix}$	$\begin{pmatrix} 1 & 0 \\ 0 & -1 \end{pmatrix}$
$\theta = \pm\pi/2$	$\begin{pmatrix} 0 & 0 \\ 0 & 1 \end{pmatrix}$	$\begin{pmatrix} -i & 0 \\ 0 & 1 \end{pmatrix}$	$\begin{pmatrix} -1 & 0 \\ 0 & 1 \end{pmatrix}$
$\theta = \pm\pi/4$	$\frac{1}{2}\begin{pmatrix} 1 & \pm 1 \\ \pm 1 & 1 \end{pmatrix}$	$\frac{\sqrt{2}}{2}e^{-i\pi/4}\begin{pmatrix} 1 & \pm i \\ \pm i & 1 \end{pmatrix}$	$\begin{pmatrix} 0 & \pm 1 \\ \pm 1 & 0 \end{pmatrix}$
$\theta = \pm\pi/8$	$\frac{1}{2\sqrt{2}}\begin{pmatrix} 1+\sqrt{2} & \pm 1 \\ \pm 1 & -1+\sqrt{2} \end{pmatrix}$	$\frac{1}{2}e^{-i\pi/4}\begin{pmatrix} \sqrt{2}+i & \pm i \\ \pm i & \sqrt{2}-i \end{pmatrix}$	$\frac{\sqrt{2}}{2}\begin{pmatrix} 1 & \pm 1 \\ \pm 1 & -1 \end{pmatrix}$

Table B.2: **Overview of Jones matrices for the common optical elements** Jones matrices for a linear polarizer (LP), have-wave plate (HWP), and a quarter-wave plate (QWP). θ is the angle with respect to x for the LP, and with respect to the fast axis for the HWP and QWP. $C_1 = \cos\theta$, $C_2 = \cos 2\theta$, $S_1 = \sin\theta$ and $S_2 = \sin 2\theta$. Inspired by Gerrard (1975).

which will now be

$$\begin{aligned} \mathrm{HWP}^\dagger(\theta = \pi/8)\,\mathrm{LP}(\theta = 0)\,\mathrm{HWP}(\theta = \pi/8) = \\ \frac{1}{2}\begin{pmatrix} 1 & 1 \\ 1 & 1 \end{pmatrix} = \mathrm{LP}(\theta = \pi/4)\,. \end{aligned} \tag{B.3.15}$$

The eigenstate is $|\swarrow\nearrow\rangle$ and if we were to look at the other PBS output (LP $(\theta = \pi/2)$ we would find $|\nwarrow\searrow\rangle$ as the eigenstate. The Jones matrices of the HWP and LP are shown in table B.2 along with that of the QWP.

Notice that the use of the HWP $\theta = \pi/8$ is the same as simply rotating the PBS by $45° = \pi/4$. This is no real surprise as rotating the PBS would trivially change the projection to the desired basis, and the HWP at angle θ rotates the polarization by 2θ. The two outputs of the PBS thus describe $\hat{a}_{\pm 45}$ and the detector difference signal will thus be a measure of $\hat{S}_y$, see fig. B.2.

B.3.3 S_z

To measure $\hat{S}_z$ we can apply the same logic as described above in appendix B.3.2. Suppose we inserted a QWP at $\theta = -\pi/4$ instead of the HWP introduced to measure $\hat{S}_y$. The effective x output of the PBS (eigenstate of new projection operator) will be that of right handed circularily polarized light. This can be seen by the projection

operator of (just like in eq. (B.3.15)) as follows,

$$\mathrm{QWP}^{\dagger}\left(\theta=-\pi/4\right)\mathrm{LP}\left(\theta=0\right)\mathrm{QWP}\left(\theta=-\pi/4\right)=\frac{1}{2}\begin{pmatrix}1 & -i\\ i & 1\end{pmatrix}, \tag{B.3.16}$$

which has $|\circlearrowleft\rangle$ as an eigenstate. Just like before the projection operator associated with the other PBS output ($\mathrm{LP}\left(\theta=\pi/2\right)$) will have $|\circlearrowright\rangle$ as an eigenstate.

Thus we now measure circularly polarized photons in the basis of $\hat{a}_{\pm}$ at the two PBS outputs and the difference signal will be a measure of $\hat{S}_z$. We could just as well have introduced the QWP in conjuction with the HWP (albeit with the choice of a different angle). In fact this is typically done out of convenience. Since these operators do not commute, one will not measure the same quadrature with a QWP followed by a HWP or vice versa. However a combination of angles can always be found[1] measures S_z.

B.3.4 Mueller Calculus

While the Jones calculus detailed above is simple and useful in cases where the input light is polarized – which is always the case for work presented in this thesis – there is Mueller calculus for the general case. Visualizing the rotations on the Poincaré sphere of fig. 2.3 are best done with the Mueller matrices. These are defined as

QWP	HWP
$\begin{pmatrix}1 & 0 & 0 & 0\\ 0 & C_2 & S_2C_2 & -S_2\\ 0 & S_2C_2 & S_2^2 & C_2\\ 0 & S_2 & -C_2 & 0\end{pmatrix}$	$\begin{pmatrix}1 & 0 & 0 & 0\\ 0 & C_4 & S_4 & 0\\ 0 & S_4 & -C_4 & 0\\ 0 & 0 & 0 & -1\end{pmatrix}$

Table B.3: **Mueller matrices for a QWP and a HWP.** See Goldstein (2003) for details. For compactness we write $C_n=\cos n\theta, S_n=\sin n\theta$.

In the case of measuring S_y and S_z it is clear that the effect of the HWP and QWP in both cases was simply to swap roles with S_x, which we measure with our linear polarizer in the absence of any polarization rotation. This is seen by

$$\mathrm{HWP}\left(\theta=\pi/8\right)\begin{pmatrix}S_0\\ S_x\\ S_y\\ S_z\end{pmatrix}=\begin{pmatrix}S_0\\ S_y\\ S_x\\ -S_z\end{pmatrix}, \tag{B.3.17}$$

$$\mathrm{QWP}\left(\theta=-\pi/4\right)\begin{pmatrix}S_0\\ S_x\\ S_y\\ S_z\end{pmatrix}=\begin{pmatrix}S_0\\ S_z\\ S_y\\ -S_x\end{pmatrix}. \tag{B.3.18}$$

[1] $\mathrm{QWP}\left(\theta=0\right)$ followed by $\mathrm{HWP}\left(\theta=\pi/8\right)$, or $\mathrm{HWP}\left(\theta=\pi/8\right)$ followed by $\mathrm{QWP}\left(\theta=\pi/4\right)$

B.4 Stokes operators relation to Pauli matrices.

The Stokes operators can be neatly expressed in in terms of the Hermitian Pauli matrices given by

$$\begin{aligned} \boldsymbol{\sigma_0} &= \begin{pmatrix} 1 & 0 \\ 0 & 1 \end{pmatrix}, \qquad \boldsymbol{\sigma_x} = \begin{pmatrix} 0 & 1 \\ 1 & 0 \end{pmatrix}, \\ \boldsymbol{\sigma_y} &= i\begin{pmatrix} 0 & -1 \\ 1 & 0 \end{pmatrix}, \qquad \boldsymbol{\sigma_z} = \begin{pmatrix} 1 & 0 \\ 0 & -1 \end{pmatrix}. \end{aligned} \tag{B.4.19}$$

and obey the commutation relations of $[\sigma_i, \sigma_j] = 2\epsilon_{ijk}\sigma_k,\ \forall i,j,k \in \{x,y,z\}$. From them we can easily define the Stokes operators in light bases of either linear x, y, $\pm 45°$ linear, or left (L) and right (R) hand circularly polarized like. These bases are written as

$$\boldsymbol{a} = \begin{pmatrix} \hat{a}_x \\ \hat{a}_y \end{pmatrix}, \begin{pmatrix} \hat{a}_{+45} \\ \hat{a}_{-45} \end{pmatrix}, \begin{pmatrix} \hat{a}_R \\ \hat{a}_L \end{pmatrix}, \tag{B.4.20}$$

respectively. We can then write the Stokes operators, for propagation along z, in the horizontal and vertically linear polarization basis as

$$\hat{S}_0 = \frac{1}{2}\hat{\boldsymbol{a}}^\dagger \boldsymbol{\sigma_x} \hat{\boldsymbol{a}} = \frac{1}{2}(\hat{a}_x^\dagger \hat{a}_x + \hat{a}_y^\dagger \hat{a}_y), \tag{B.4.21a}$$

$$\hat{S}_x = \frac{1}{2}\hat{\boldsymbol{a}}^\dagger \boldsymbol{\sigma_z} \hat{\boldsymbol{a}} = \frac{1}{2}(\hat{a}_x^\dagger \hat{a}_x - \hat{a}_y^\dagger \hat{a}_y), \tag{B.4.21b}$$

$$\hat{S}_y = \frac{1}{2}\hat{\boldsymbol{a}}^\dagger \boldsymbol{\sigma_x} \hat{\boldsymbol{a}} = \frac{1}{2}(\hat{a}_y^\dagger \hat{a}_x + \hat{a}_x^\dagger \hat{a}_y), \tag{B.4.21c}$$

$$\hat{S}_z = \frac{1}{2}\hat{\boldsymbol{a}}^\dagger \boldsymbol{\sigma_y} \hat{\boldsymbol{a}} = \frac{i}{2}(\hat{a}_y^\dagger \hat{a}_x - \hat{a}_x^\dagger \hat{a}_y). \tag{B.4.21d}$$

In the $\pm 45°$ linearly polarized basis,

$$\hat{S}_0 = \frac{1}{2}\hat{\boldsymbol{a}}^\dagger \boldsymbol{\sigma_0} \hat{\boldsymbol{a}} = \frac{1}{2}(\hat{a}_{+45}^\dagger \hat{a}_{+45} + \hat{a}_{-45}^\dagger \hat{a}_{-45}), \tag{B.4.22a}$$

$$\hat{S}_x = \frac{1}{2}\hat{\boldsymbol{a}}^\dagger \boldsymbol{\sigma_y} \hat{\boldsymbol{a}} = \frac{i}{2}(\hat{a}_{-45}^\dagger \hat{a}_{+45} - \hat{a}_{+45}^\dagger \hat{a}_{-45}), \tag{B.4.22b}$$

$$\hat{S}_y = \frac{1}{2}\hat{\boldsymbol{a}}^\dagger \boldsymbol{\sigma_z} \hat{\boldsymbol{a}} = \frac{1}{2}(\hat{a}_{+45}^\dagger \hat{a}_{+45} - \hat{a}_{-45}^\dagger \hat{a}_{-45}), \tag{B.4.22c}$$

$$\hat{S}_z = \frac{1}{2}\hat{\boldsymbol{a}}^\dagger \boldsymbol{\sigma_x} \hat{\boldsymbol{a}} = \frac{1}{2}(\hat{a}_{+45}^\dagger \hat{a}_{-45} + \hat{a}_{-45}^\dagger \hat{a}_{+45}), \tag{B.4.22d}$$

and finally in the circularly polarized basis,

$$\hat{S}_0 = \frac{1}{2}\hat{\boldsymbol{a}}^\dagger \boldsymbol{\sigma_0} \hat{\boldsymbol{a}} = \frac{1}{2}(\hat{a}_R^\dagger \hat{a}_R + \hat{a}_L^\dagger \hat{a}_L), \tag{B.4.23a}$$

$$\hat{S}_x = \frac{1}{2}\hat{\boldsymbol{a}}^\dagger \boldsymbol{\sigma_x} \hat{\boldsymbol{a}} = \frac{1}{2}(\hat{a}_R^\dagger \hat{a}_L + \hat{a}_L^\dagger \hat{a}_R), \tag{B.4.23b}$$

$$\hat{S}_y = \frac{1}{2}\hat{\boldsymbol{a}}^\dagger \boldsymbol{\sigma_y} \hat{\boldsymbol{a}} = \frac{i}{2}(\hat{a}_L^\dagger \hat{a}_R - \hat{a}_R^\dagger \hat{a}_L), \tag{B.4.23c}$$

$$\hat{S}_z = \frac{1}{2}\hat{\boldsymbol{a}}^\dagger \boldsymbol{\sigma_z} \hat{\boldsymbol{a}} = \frac{1}{2}(\hat{a}_R^\dagger \hat{a}_R - \hat{a}_L^\dagger \hat{a}_L). \tag{B.4.23d}$$

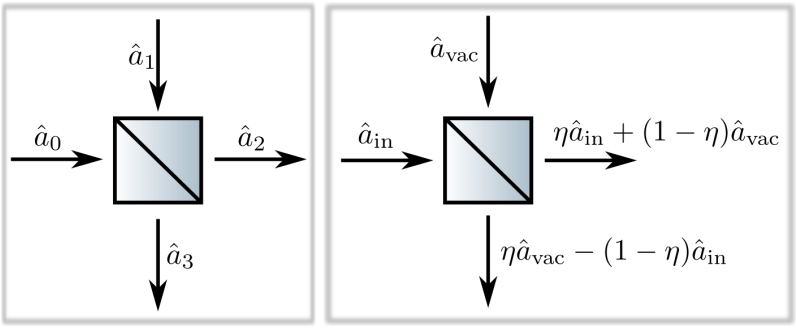

Figure B.3: **Input output field operators from a beam splitter**. Inspired by Christopher Gerry (2005). Shown **left** is the general case of two input modes $\hat{a}_0$, $\hat{a}_1$ and two output modes $\hat{a}_2$, $\hat{a}_3$ related via the reflection $(r,\ r')$ and transmission $(t,\ t')$ amplitudes of the beam splitter. Shown **right** is the case relevant for losses where an input mode $\hat{a}_{\text{in}}$ is combined with vacuum $\hat{a}_{\text{vac}}$ on a beamsplitter with power transmission η.

B.5 Losses

Loss is traditionally modelled by the use of a beamsplitter, where a percentage of your signal is reflected and transmitted, see fig. B.3. In general the input mode $\hat{a}_0$ is reflected and transmitted with amplitude coefficients (r, t). In order to preserve the commutation relations the splitting of this mode must include the addition of some other mode $\hat{a}_1$ with reflection and amplitude coefficients (r', t'). The two output modes will be related by a unitary matrix $\boldsymbol{U}$ according to

$$\begin{pmatrix}\hat{a}_2\\ \hat{a}_3\end{pmatrix} = \boldsymbol{U}\begin{pmatrix}\hat{a}_2\\ \hat{a}_3\end{pmatrix}, \tag{B.5.24}$$

$$\boldsymbol{U} = \begin{pmatrix}t' & r\\ r' & t\end{pmatrix}. \tag{B.5.25}$$

The reflection and transmission coefficients are constrained by the reciprocity relations, see Ou and Mandel (1989), basically describing energy conservation, which are simply,

$$|r| = |r'|\,, |t| = |t'|\,, \tag{B.5.26a}$$

$$|r|^2 + |t|^2 = |r'|^2 + |t'|^2 = 1, \tag{B.5.26b}$$

$$r^* t' + t^* r' = 0. \tag{B.5.26c}$$

One could more formally write this transformation in terms of the unitary transformation given by

$$\begin{pmatrix}\hat{a}_2\\ \hat{a}_3\end{pmatrix} = \hat{U}^\dagger\begin{pmatrix}\hat{a}_0\\ \hat{a}_1\end{pmatrix}\hat{U}, \tag{B.5.27}$$

$$\hat{U} = e^{\frac{\theta}{2}\left(\hat{a}_0^\dagger \hat{a}_1 - \hat{a}_q^\dagger \hat{a}_0\right)}. \tag{B.5.28}$$

B.5.1 Inefficiency

Reflecting part of the signal of interest away to a unobserved port, is clearly a loss of information. The transmitted portion is joined by uncorrelated vacuum in replacement for what was lost. Typically we give the loss of signal in terms of its equivalent power loss η, i.e. how much light power was lost from A to B. The transformation matrix $\boldsymbol{U}$ is then given simply by

$$\boldsymbol{U} = \begin{pmatrix} \sqrt{\eta} & \sqrt{1-\eta} \\ -\sqrt{1-\eta} & \sqrt{\eta} \end{pmatrix}. \tag{B.5.29}$$

This is illustrated in fig. B.3, where the relation to power loss is apparent by simply noting that the power is proportional to the mean excitation in the field (where vacuum has a zero mean occupation), i.e.

$$\langle n_{\text{out}} \rangle = \eta \langle n_{\text{in}} \rangle. \tag{B.5.30}$$

Loss of a particular quadrature is modeled in exactly the same way, i.e. some general quadrature $\hat{X}$ experiencing a power loss of η will have the input-output relation

$$\hat{X}_{\text{out}} = \sqrt{\eta}\,\hat{X}_{\text{in}} + \sqrt{1-\eta}\,\hat{X}_{\text{vac}}. \tag{B.5.31}$$

Similarly the power spectral density will be modified accordingly,

$$S_{XX}^{\text{out}} = \eta S_{XX}^{\text{in}} + (1-\eta)\, S_{XX}^{\text{vac}}. \tag{B.5.32}$$

B.5.2 Homodyning visibility

In homodyning a field the finite overlap of the LO field will manifest itself as an effective loss. The spatial overlap of two fields is typically measured by their visibility $\mathcal{V}$. The modematching efficiency turns out to be equivalent to a power loss and is related to the visibility by

$$\eta = \mathcal{V}^2. \tag{B.5.33}$$

To see how this comes about consider fig. B.4. Lets assume we have an input field[1] E_1', which is being homodyned with an LO of field E_{LO}. We can think of E_1' as being comprised of two orthogonal fields E_1 and E_2 where the former is in the same spatial mode as E_{LO}, whilst the latter in an orthogonal one. Thus E_1 and E_{LO} will interfere perfectly when mixed equally on a 50:50 BS. If we detect a single output of the BS on a diode the intensity we will measure will be given by,

$$I = \left| \frac{1}{\sqrt{2}} \left(E_{\text{LO}} + E_1' \right) \right|^2 \tag{B.5.34}$$

$$= \left(I_{\text{LO}} + \eta I_1 + (1-\eta) I_2 + \sqrt{\eta}\, |E_{\text{LO}} E_1^*|\, 2\cos\varphi \right)/2, \tag{B.5.35}$$

[1] Here we will simply assume classical electric fields since the visibility is typically measured with large classical fields. The results are directly transferable.

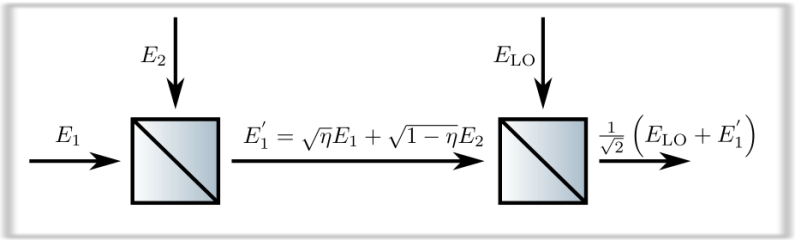

Figure B.4: **Spatial mismatch in homodyning.** Theoretical representation of finite modematching in the case of homodyne detection. A field $E_1^{'}$ is homodyned by the local oscillator field E_{LO}. We write the input field $E_1^{'}$ as composed of two spatially orthogonal fields, E_1 and E_2, the former being in the spatial mode of E_{LO}. The amount of power each E_1 and E_2 fields contribute to the total field $E_1^{'}$ is given by η.

where we have written the intensities of the fields as $I_i = |E_i E_i^*|$. Furthermore we have let the phase difference between fields E_1 and E_2 be given by φ. Note that there are no interference terms between E_{LO} and E_2 since they are in different spatial modes.

The interesting contribution in a homodyning signal is the interference term $|E_{\mathrm{LO}} E_1^*|$, which clearly is reduced by $\sqrt{\eta}$. This reduction is the same you would get given a power loss of η in the relevant field E_1, see eq. (B.5.31). To measure this loss factor we can simply measure the visibility, where one typically uses equal power in both fields to maximize the contrast. Thus if we let, $I_1^{'} = I_{\mathrm{LO}}$ we find that

$$I = I_{\mathrm{LO}} \left(1 + \sqrt{\eta}\cos\varphi\right) \tag{B.5.36}$$

and thus the visibility is given by

$$\mathcal{V} \equiv \frac{I_{\max} - I_{\min}}{I_{\max} + I_{\min}} \tag{B.5.37}$$

$$= \sqrt{\eta}, \tag{B.5.38}$$

as was initially stated in eq. (B.5.33).

B.5.3 Cavity mode matching

The degree to which two modes, with time and spatially varying electric fields given by E_1 and E_2, are similar, is given by the field overlap integral,

$$\eta = \frac{\left|\int E_1^* E_2 \,\mathrm{d}A\right|^2}{\int |E_1|^2 \,\mathrm{d}A \int |E_2|^2 \,\mathrm{d}A}, \tag{B.5.39}$$

over some plane A. If E_1 is a gaussian beam with field distribution given by eq. (D.1.1) and E_2 a cavity mode given by eq. (D.3.31), then we can consider eq. (B.5.39) to be the degree of cavity mode matching. To gauge the impact this mode matching has on the cavity dynamics we present here an argument based on a note by Klemens Hammerer.

Suppose the intracavity field $\hat{a}$ is coupled to input mode $\hat{a}_{\text{in}}$ with through port 1 with rate κ_1. The residual extraneous cavity losses are associated with losses to a single general field $\hat{a}_{\text{ex}}$ with rate κ_{ex}. The full cavity decay rate is given by $\kappa = \kappa_1 + \kappa_{\text{ex}}$. Thus the cavity mode evolution is given by

$$\dot{\hat{a}} = -\frac{\kappa}{2}\hat{a} + \sqrt{\kappa_1}\hat{a}_{\text{in}} + \sqrt{\kappa_{\text{ex}}}\hat{a}_{\text{in}}. \tag{B.5.40}$$

Suppose our we wish to probe this cavity mode with an experimental input field, $\hat{s}_{\text{in}}$, which is not exactly mode matched to mode $\hat{a}_{\text{in}}$ that couples to the cavity due to a spatial mismatch as just described in eq. (B.5.39). We can think of $\hat{a}_{\text{in}}$ as being in a superposition of the input mode $\hat{s}_{\text{in}}$ and an orthogonal mode $\hat{s}_{\text{in}}^{\perp}$ with the fraction of each given by η, i.e.

$$\hat{a}_{\text{in}} = \sqrt{\eta}\,\hat{s}_{\text{in}} + \sqrt{1-\eta}\,\hat{s}_{\text{in}}^{\perp}. \tag{B.5.41}$$

This means that we can rewrite the cavity evolution equation as

$$\dot{\hat{a}} = -\frac{\kappa}{2}\hat{a} + \sqrt{\eta\kappa_1}\hat{s}_{\text{in}} + \sqrt{(1-\eta)\kappa_1}\,\hat{s}_{\text{in}}^{\perp} + \sqrt{\kappa_{\text{ex}}}\hat{a}_{\text{ex}} \tag{B.5.42}$$

$$= -\frac{\kappa}{2}\hat{a} + \sqrt{\eta\kappa_1}\hat{s}_{\text{in}} + \sqrt{\kappa'_{\text{ex}}}\hat{a}'_{\text{ex}} \tag{B.5.43}$$

where we collect the orthogonal input mode together with the extraneous losses by defining a new mode

$$\hat{a}'_{\text{ex}} = \sqrt{(1-\eta)\kappa_1/\kappa'_{\text{ex}}}\,\hat{s}_{\text{in}}^{\perp} + \sqrt{\kappa_{\text{ex}}/\kappa'_{\text{ex}}}\,\hat{a}_{\text{ex}} \tag{B.5.44}$$

coupled to the cavity mode with rate $\kappa'_{\text{ex}} = \kappa - \eta\kappa_1 = (1-\eta)\kappa_1 + \kappa_{\text{ex}}$.

From the point of view of the cavity mode dynamics of eq. (B.5.43) the mode matching reduces the importance of input field just as reduced incoupling efficiency would. This is seen by expressing the cavity incoupling rate as a fraction η_c of the total decay rate as $\kappa_1 = \eta_c\kappa$. Then the term coupling to our input field of interest reads $\sqrt{\eta\eta_c\kappa}$.

To determine the input-output relations for our input field we note that we can define a mode orthogonal to $\hat{a}_{\text{in}}$ as

$$\hat{a}_{\text{in}}^{\perp} = \sqrt{1-\eta}\,\hat{s}_{\text{in}} - \sqrt{\eta}\,\hat{s}_{\text{in}}^{\perp} \tag{B.5.45}$$

and thus express our input field as

$$\hat{s}_{\text{in}} = \sqrt{\eta}\,\hat{a}_{\text{in}} + \sqrt{1-\eta}\,\hat{a}_{\text{in}}^{\perp}. \tag{B.5.46}$$

Similarly, we can write the output mode of interest as having contributions from the cavity output mode $\hat{a}_{\text{out}}$ and some orthogonal output mode $\hat{a}_{\text{out}}$, i.e.

$$\hat{s}_{\text{out}} = \sqrt{\eta}\,\hat{a}_{\text{out}} + \sqrt{1-\eta}\,\hat{a}_{\text{out}}^{\perp}. \tag{B.5.47}$$

The cavity output mode has the expected input-output relation $\hat{a}_{\mathrm{out}} = \hat{a}_{\mathrm{in}} - \sqrt{\kappa_1}\hat{a}$ whereas the orthogonal input mode is completely reflected off the cavity such that $\hat{a}^{\perp}_{\mathrm{out}} = \hat{a}^{\perp}_{\mathrm{in}}$. Thus we can write eq. (B.5.47) as

$$\begin{aligned}\hat{s}_{\mathrm{out}} &= \sqrt{\eta}\,\hat{a}_{\mathrm{in}} + \sqrt{1-\eta}\,\hat{a}^{\perp}_{\mathrm{out}} - \sqrt{\eta\eta_c\kappa}\,\hat{a} \\ &= \sqrt{\eta}\,\hat{a}_{\mathrm{in}} + \sqrt{1-\eta}\,\hat{a}^{\perp}_{\mathrm{in}} - \sqrt{\eta\eta_c\kappa}\,\hat{a} \\ &= \hat{s}_{\mathrm{in}} - \sqrt{\eta\eta_c\kappa}\,\hat{a}. \end{aligned} \tag{B.5.48}$$

So, from the point of view of the output field of interest reflected off the cavity, the intracavity field is read out with a reduced efficiency equivalent to a less onesided cavity.

A hasty interpretation may lead to the conclusion that the mode matching is equivalent to intracavity losses from the point of the view of the input field. This is not the case as highlighted by considering the two fundamentally different cases $\eta = 1/2,\ \eta_c = 1$ and $\eta = 1,\ \eta_c = 1/2$. In the former case the cavity is perfectly onesided and the mode matching is only 50 %, whereas in the latter case the mode matching is perfect and the cavity is critically coupled.

To make use of our classical intuition, we consider the mean fields and take the only relevant field to be our input field $\bar{s}_{\mathrm{in}} = \sqrt{\eta}\,\bar{a}_{\mathrm{in}} + \sqrt{1-\eta}\,\bar{a}^{\perp}_{\mathrm{in}}$. The reflected power is given by

$$|\bar{s}_{\mathrm{out}}|^2 = \eta|\bar{a}_{\mathrm{in}}|^2\,(1-2\eta_c)^2 + (1-\eta)|\bar{a}^{\perp}_{\mathrm{in}}|^2, \tag{B.5.49}$$

and thus the cases just discussed give

$$|\bar{s}_{\mathrm{out}}|^2 = \begin{cases} \frac{1}{2}|\bar{a}_{\mathrm{in}}|^2 + \frac{1}{2}|\bar{a}^{\perp}_{\mathrm{in}}|^2, & \text{for } \eta = 1/2,\ \eta_c = 1, \\ 0, & \text{for } \eta = 1,\ \eta_c = 1/2. \end{cases} \tag{B.5.50}$$

In the first case, half of the input mode is reflected and the remaining half interacts with the cavity eventually being completely reflected. In the latter case the entire input field interacts with the critically coupled cavity, being lost in the process.

Appendix C

Measuring quantum cooperativity with classical white noise

The method detailed here gives the fraction of quantum back-action comprising the detected optical phase quadrature variance. This fraction is directly related to the quantum cooperativity, by definition. Knowing the quantum back-action fraction further allows one to infer the system readout rates through the logic shown in fig. 6.4.

From the optical output quadratures of eq. (6.2), combined with a detection efficiency of η we can write the power spectral densities of the detected quadratures $\hat{X}$ and $\hat{Y}$, be they from homodyning or direct detection, as

$$\begin{aligned} \bar{S}_{XX} &= \eta \bar{S}^{\text{in}}_{XX} + (1-\eta)\bar{S}^{\text{vac}}_{XX} \\ \bar{S}_{YY} &= \eta \bar{S}^{\text{in}}_{YY} + (1-\eta)\bar{S}^{\text{vac}}_{YY} + \eta\Gamma\bar{S}_{QQ} \end{aligned} \tag{C.1.1}$$

where we have dropped the subscript i differentiating each system since eq. (C.1.1) applies to each system in the same fashion. The fluctuations of the input optical amplitude quadrature $\hat{X}^{\text{in}}$ are given by eq. (6.18) and the optical phase quadrature $\hat{Y}^{\text{in}}$ is taken to be vacuum.

We can write the variance contribution from the system motion, $\Gamma\bar{S}_{QQ}$, in terms of the fraction coming from the back-action (BA) $\bar{S}^{\text{BA}}_{YY}$ and that coming from thermal noise (TN) $\bar{S}^{\text{TN}}_{YY}$,

$$\Gamma\bar{S}_{QQ} = \bar{S}^{\text{BA}}_{YY}(\bar{n}_{\text{WN}}) + \bar{S}^{\text{TN}}_{YY}, \tag{C.1.2}$$

$$\bar{S}^{\text{BA}}_{YY}(\bar{n}_{\text{WN}}) = 2\bar{S}^{\text{BA}}_{YY}(0)\left(\bar{n}_{\text{WN}} + 1/2\right), \tag{C.1.3}$$

The back-action contribution is driven by $\bar{S}^{L,\text{in}}_{XX}$ and thus $\bar{n}_{\text{WN}} + 1/2$ as seen from eq. (6.18). The fraction of this that is the quantum back-action we can write as $\bar{S}^{\text{BA}}_{YY}(0)$, where the implication it that this is for $\bar{n}_{\text{WN}} = 0$.

If the input optical phase quadrature is only vacuum, $\bar{S}^{\text{in}}_{YY} = 1/2$, then input-output relations of eq. (C.1.1) can be written as

$$\bar{S}_{XX}(\bar{n}_{WN}) = \eta\bar{n}_{WN} + 1/2, \tag{C.1.4a}$$

$$\bar{S}_{YY}(\bar{n}_{WN}) = \eta\left[2\bar{S}^{\text{BA}}_{YY}(0)(\bar{n}_{WN} + 1/2) + \text{TN}\right] + 1/2. \tag{C.1.4b}$$

From eq. (C.1.4) it is clear that experimentally, to be able to calculate the back action to thermal noise ratio under a particular set of operating conditions, one needs only to measure the

i) response of the system to SN drive (i.e. vacuum),

ii) response of the system to some modulation $\bar{n}_{WN}$,

iii) used modulation $\bar{n}_{WN}$.

However, typically, at least for this work, the detection efficiency η is needed to accurately determine $\bar{n}_{WN}$. Since $\bar{S}_{XX}(\bar{n}_{WN}) - \bar{S}_{XX}(\bar{n}_{WN} = 0) = \eta\bar{n}_{WN}$ we simply measure $\bar{S}_{XX}$ with and without added white noise. If we then divide out the measured detection efficiency we are left with $\bar{n}_{WN}$ to within the detection efficiency error given the spectral measurements are appropriately averaged.

If we measure $\bar{S}_{YY}(\bar{n}_{WN})$ and subtract the constant shot noise factor (1/2) we are left with two equations defined here as A and B, given by

$$\bar{S}_{YY}(\bar{n}_{WN}) - 1/2 \equiv B = \eta\left[2\bar{S}^{\mathrm{BA}}_{YY}(0)(\bar{n}_{WN} + 1/2) + \mathrm{TN}\right], \tag{C.1.5a}$$

$$\bar{S}_{YY}(\bar{n}_{WN} = 0) - 1/2 \equiv A = \eta\left[\bar{S}^{\mathrm{BA}}_{YY}(0) + \mathrm{TN}\right]. \tag{C.1.5b}$$

From this set of equations the ratio of quantum back-action (QBA) to thermal noise (TN) can be found as

$$\frac{\mathrm{QBA}}{\mathrm{TN}} = \frac{\bar{S}^{\mathrm{BA}}_{YY}(0)}{\bar{S}^{\mathrm{TN}}_{YY}} = \frac{B - A}{(2\bar{n}_{WN} + 1)A - B}. \tag{C.1.6}$$

This fraction can – since we can always subtract the shot noise contribution – be measured at any Fourier frequency. However in practice the best signal to noise is found on-resonance with the system being probed, or by comparing spectral areas.

Appendix D

Gaussian beams and cavity formulae

D.1 Basic formulae Gaussian beam

A generic radially symmetric Gaussian beam travelling along z is described by the electric field profile given by,

$$E(r,z) = E_0 \frac{w_0}{w(z)} \exp\left(\frac{-r^2}{w^2(z)}\right) \exp\left(ik\frac{r^2}{2R(z)}\right) \exp(i\left[kz - \phi(z)\right]) \tag{D.1.1}$$

where the waist (radius) $w(z)$, wavefront curvature $R(z)$ and Gouy Phase $\phi(z)$ are given at distance of z from the focus by,

$$w(z) = w_0\sqrt{1 + \left(\frac{z}{z_R}\right)^2}, \tag{D.1.2}$$

$$R(z) = z + \frac{z_R^2}{z}, \tag{D.1.3}$$

$$\phi(z) = \arctan(z/z_R). \tag{D.1.4}$$

At beam focus $z = 0$ the waist is minimal and denoted by $w_0 \equiv w(0)$. The wavefront curvature is infinite, i.e. plane. Common to both eqs. (D.1.2) and (D.1.3) is the rayleigh length z_R. This is the characteristic length scale over which the Gaussian beam parameters change. It is related to the waist and the light wavelength λ via,

$$z_R = \frac{\pi w_0^2}{\lambda}. \tag{D.1.5}$$

Clear from this relationship is the fact that if we wish to focus a beam to a small waist it will diverge over a very short distance. The divergence angle is given by

$$\theta = \frac{w_0}{z_R} = \frac{\lambda}{\pi w_0}. \tag{D.1.6}$$

The intensity of a Gaussian beam averaged over an optical period is given by

$$I(r,z) = \frac{\epsilon_0 c}{2} |E(r,z)|^2 = \frac{2P}{\pi w^2(z)} \exp\left(\frac{-2r^2}{w^2(z)}\right), \tag{D.1.7}$$

where the total power P through plane A perpendicular to the direction of propagation z is given by,

$$P = \int_A I(r,z)\, \mathrm{d}A. \tag{D.1.8}$$

D.2 Aperture effects.

In general the effect of a Gaussian beam passing through a 2D aperture is a complex diffraction problem. Here we will give an oversimplified treatment, which is nonetheless still valuable to estimate the order of magnitude of a potential issue.

The optimal waist for minimal clipping loss in any cell, which is l long, can be easily shown to be given by the requirement that $z_R = l/2$. It is independent of the aperture size and whether it is square or circular. For a cell of 10 mm this is a waist of $w_0 \simeq 116\,\mu\mathrm{m}$. This sets the natural relevant scale of waists to consider, but may not represent the practical optimal. Some amount of clipping losses are always tolerable and a larger waist may be desirable, for example if a large filling factor, described in appendix D.2.3, is required.

Probing a membrane motion is best done at an anti-node of modal motion. The wavelength of a, say, $(1,2)$ mode on a $L = 500\,\mu\mathrm{m}$ sized membrane is $\sim L$. We wish to probe the motion ideally at a point of maximum displacement. In practice that means we need a spot size on the membrane roughly $L/10$. This gives the natural scale for the relevant cavity waist of $\sim 50\,\mu\mathrm{m}$.

D.2.1 Circular aperture

Mention clipping radial aperture, power in given radius. relevant for light on mirror. has to be good over some distance. With high finesse this is a necessary consideration

Passing a Gaussian beam of waist radius w concentrically through a circular aperture or radius R results in beam clipping and diffraction. The power transmitted can be easily calculated from eq. (D.1.8) in the general case as

$$P_{\mathrm{out}} = \int_0^{2\pi} \int_0^R I(r,z) r\, \mathrm{d}r\, \mathrm{d}\theta \tag{D.2.9}$$

$$= P_{\mathrm{in}} \left(1 - \exp\left(\frac{-2R^2}{w^2}\right)\right). \tag{D.2.10}$$

This also describes the amount of power which is contained within a given radius. For example, the power contained within a single waist $R = w$ is $1 - e^{-2} \simeq 86\,\%$. This is known as the $1/e^2$ waist for obvious reasons and is a good measure for the extent of a beam.

This consideration is important when considering high finesse mirrors. In such mirrors we typically are concerned with losses on the order of $\sim 10\,\text{ppm}$, but in some circumstances care about $\sim 1\,\text{ppm}$. Loss on these orders correspond to being concerned about the condition of a mirror on the scales of $R \simeq 2.4w$ and $R \simeq 2.6w$ respectively. This corresponds to a region of about 105 µm in radius (210 µm diameter) for a cavity waist (radius) of 40 µm. From the perspective of added losses this small, but non-negligible, region must be devoid of major defects and distortions. If the waist is larger, as it would be for any mirror not placed at the cavity waist, this region is bigger.

D.2.2 Square aperture

The passage of a Gaussian beam through a square aperture is also of interest. This is relevant for both the membrane and the atomic spins. The membrane is square and suspended from an opaque Si frame. This creates a naturally sharp aperture; sharp and very ($\ll \lambda$) thin.

The clipping of a beam through a point (x_0, y_0) on a square aperture centered on $(0, 0)$, is given by

$$P_{\text{out}} = \int_{-L_x/2}^{L_x/2} \int_{-L_y/2}^{L_y/2} I(x, y)\,\mathrm{d}x\,\mathrm{d}y \tag{D.2.11}$$

$$= P_{\text{in}} \operatorname{erf}\left(\frac{L_x - 2x_0}{\sqrt{2}\,w(z)}\right) \operatorname{erf}\left(\frac{L_y - 2y_0}{\sqrt{2}\,w(z)}\right). \tag{D.2.12}$$

where the error function $\operatorname{erf}(\cdot)$ is defined as,

$$\operatorname{erf}(x) = \frac{2}{\sqrt{\pi}} \int_0^x \exp\left(-t^2\right) \mathrm{d}x. \tag{D.2.13}$$

Membrane aperture

Let us first see the effect from the frame aperture of a square membrane of side length $L \simeq 500\,\mu\text{m}$. Note first that since the membrane is embedded in a high finesse cavity where the relevant loss scale is $\sim 1\,\text{ppm}$ to $10\,\text{ppm}$ like that of appendix D.2.1.

The plano-concave cavity used for the work here had a cavity waist[1] of 40 µm, which would mean that we would not see additional losses due to this effect, if we probed right in the center. This clipping as a function of the cavity waist is shown in fig. D.1 for a selection of aperture side lengths.

However, if we were to move away from the center this effect becomes important. In practice we probed the $(1, 2)$ mode at an antinode. This entails an offset of $\sim L/4$ in either x or y. This also adds negligible (but much less so) loss as can be seen in fig. D.1.

[1] corresponding to a Rayleigh length of $z_R \sim 6\,\text{mm}$ and our membrane was always placed close to this waist in units of z_R.

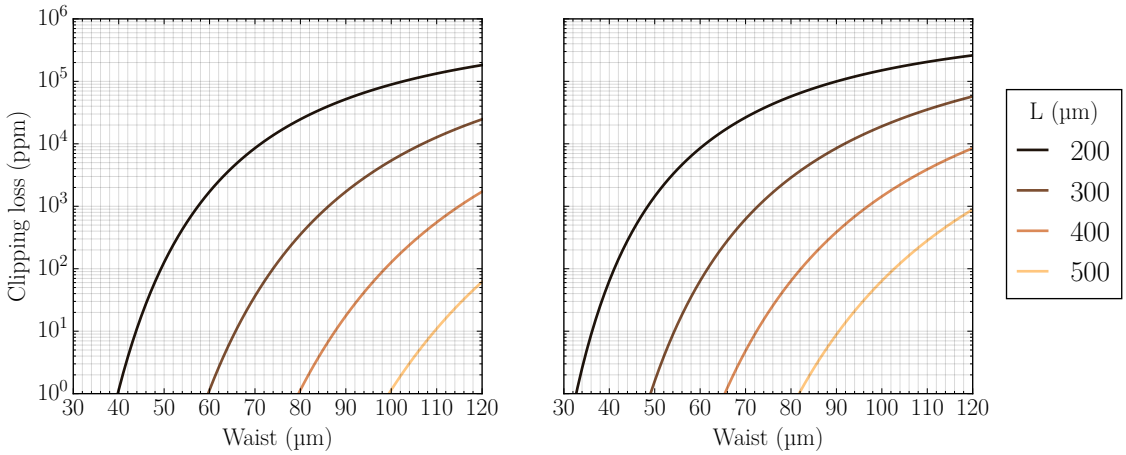

Figure D.1: Power clipping loss for a beam of varying waist (radius) through a square aperture of side length L. The aperture is assumed to be opaque outside the aperture. Diffraction is not taken into account. **Left**: Beam passing through the middle of the square. **Right**: Beam passing through the square with an offset (parallel to edge) of 10 % of the side length L from the center.

Cell aperture

For the spin cell the clipping loss is of much less importance as it is not embedded in a cavity, let alone a high finesse one. For the cell clipping is more a question of competing interests. The trade-off is between the filling fraction – i.e. how much of the cell volume your optical mode sees – and the losses due to clipping. The former is discussed in appendix D.2.3. These obviously scale inversely with the beam waist.

For the experiments reported in this thesis a beam waist through the cell of 55 µm was used. The clipping loss resulting from this choice is negligible as is clear from fig. D.1.

Waist characterization

The predictable power clipping of a Gaussian beam by a straight edge is experimentally used to characterize the beam waist. This is easy to see from eq. (D.2.12), where we could simply just choose to clip the beam only from one side.

$$P_{\text{out}} = \int_{-\infty}^{\infty}\int_{-\infty}^{X} I(x,y)\,\mathrm{d}x\,\mathrm{d}y \tag{D.2.14}$$

Doing this with, say, a razor blade (or something with a well defined edge compared to the expected waist size) allows one to measure the waist along a particular axis. This is known as the knife-edge technique and it can be shown using eq. (D.2.14) that the distance δX_{10-90} between blocking 10 % and 90 % of the beam is related to the waist (radius) via,

$$w_x(z) = \frac{\delta X_{10-90}}{1.28}. \tag{D.2.15}$$

D.2.3 Filling factor

Consider a probing beam passing through the atomic cell microchannel. If we define the filling fraction FF to be proportional to the volume of the beam V_{beam}, truncated at a waist on either side, probing the channel of volume V_{channel} we have

$$\text{FF} \equiv \frac{V_{\text{beam}}}{V_{\text{channel}}} \tag{D.2.16}$$

If we consider a rectangular channel of length l and opening side length L, probed by a Gaussian beam whose extent is approximated by the beam waist $w(z)$, this filling fraction defined in eq. (D.2.16) is given by,

$$\text{FF} = \frac{1}{L^2 l}\int_{-l/2}^{l/2} \pi w^2(z)\,\mathrm{d}z = \frac{\pi w_0^2}{L^2}\left(\frac{1}{2}+\frac{a^2}{6}\right), \tag{D.2.17}$$

$$a = \frac{l/2}{z_R}. \tag{D.2.18}$$

The point $z = 0$ is chosen to be the center of the channel and the focal point of the beam.

Had we chosen to work with a cylindrical channel the filling factor would simply be $4/\pi \simeq 1.27$ times larger. This extra 27 % is quite significant and the feasibility of a cylindrical cell is currently being considered.

In principle one could reshape the beam to more efficiently fill the channel. Reshaping the beam into a top hat shape is one such possibility.

D.3 Cavity formulae

Here we state simple results about the spatial nature of cavity modes. A larger overview, and derivations, can be found in Milonni P.W. (2010).

For a basic two mirror Fabry-Pérot cavity we define a useful parameter g_i for each mirror i. If each mirror has radius of curvature given by R_i and the cavity is L long, then

$$g_i = 1 - \frac{L}{R_i}. \tag{D.3.19}$$

A stable cavity requires that $0 \leq g_1 g_2 \leq 1$, and concave mirrors are defined to have positive radius of curvature whilst convex mirrors have negative radius of curvature. Flat mirrors have a infinite radius of curvature.

The waist of the TEM00 mode, see eq. (D.3.31), defined by the cavity mirrors will in general be,

$$w_0 = \sqrt{\frac{\lambda L}{\pi}}\left[\frac{g_1 g_2\,(1-g_1 g_2)}{(g_1+g_2-2g_1 g_2)}\right]^{1/4} \tag{D.3.20}$$

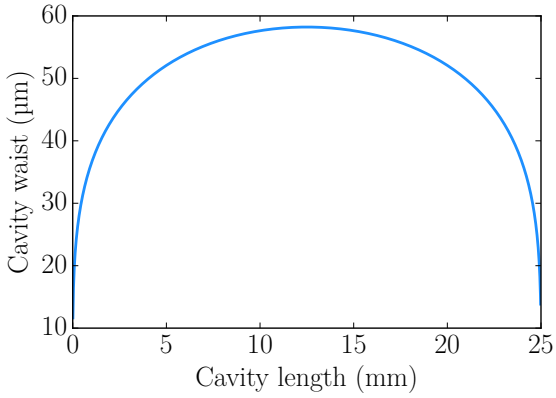

Figure D.2: **Cavity waist with cavity length.** Plano-concave cavity waist according to eq. (D.3.21) for a curved mirror with a 25 mm radius of curvature and a varied cavity length.

Where λ is the wavelength of light. In the specific (and very relevant) case of a plano-concave cavity we have $g_1 = 1$ (plano) and $g_2 = 1 - L/R$ (concave with radius of curvature R). Thus eq. (D.3.20) simplifies to,

$$w_0 = \sqrt{\frac{\lambda L}{\pi}} \left(\frac{R}{L} - 1\right)^{1/4}, \tag{D.3.21}$$

and is shown for a fig. D.2 as a function of cavity length.

For cavity lengths much smaller than radius of curvature (or lengths very close to R), we can make the following approximation for the cavity waist,

$$w_0 \approx 36.45\,\mu\text{m} \left(\frac{L}{1\,\text{mm}}\right)^{1/4} \left(\frac{R}{25\,\text{mm}}\right)^{1/4} \left(\frac{\lambda}{852\,\text{nm}}\right)^{1/2}. \tag{D.3.22}$$

Since the cavity waist is symmetric around $L = R/2$, eq. (D.3.22) also describes the cavity waist for very long cavities where $L = R - \Delta L$, $\forall \Delta L \ll L$. In this case simply replace the L in eq. (D.3.22) with ΔL.

What about the size of the spot on the cavity mirrors? These are given by

$$w_1 = \sqrt{\frac{\lambda L}{\pi}} \left[\frac{g_2}{g_1\left(1 - g_1 g_2\right)}\right]^{1/4}, \tag{D.3.23}$$

$$w_2 = \sqrt{\frac{\lambda L}{\pi}} \left[\frac{g_1}{g_2\left(1 - g_1 g_2\right)}\right]^{1/4}. \tag{D.3.24}$$

In the case of a plano-concave cavity $w_1 = w_0$ and the waist on the concave mirror is given by

$$w_2 = \sqrt{\frac{\lambda L}{\pi}} \left[\frac{L}{R}\left(1 - \frac{L}{R}\right)\right]^{-1/4}. \tag{D.3.25}$$

In the very short cavity regime, $L \ll R$, we simply have $w_2 \approx w_1$. In the regime of a very long $L \approx R$ cavity, just as above in eq. (D.3.22), we can approximately write

$L = R - \Delta L$. The spot size on the mirror is then

$$w_2 = 182.25\,\mu\text{m}\left(\frac{\Delta L}{1\,\text{mm}}\right)^{1/4}\left(\frac{R}{25\,\text{mm}}\right)^{1/4}\left(\frac{\lambda}{852\,\text{nm}}\right)^{1/2}. \tag{D.3.26}$$

In general, the position of the waist wrt to each mirror i is given by z_i, which is given by

$$z_1 = \frac{-Lg_2(1-g_1)}{g_1+g_2-2g_1g_2} \tag{D.3.27}$$

$$z_2 = z_1 + L. \tag{D.3.28}$$

The location of the waist for a plano-concave cavity will always be on the plano mirror, as is easily checked from eq. (D.3.28). In a confocal cavity where the mirrors are identical, $g_1 = g_2$, the cavity waist is located at $L/2$, as would naively be expected.

The TEM00 modes of the cavity have a frequency given by

$$\nu_q = \text{FSR}\left(q + \frac{\arccos(g_1g_2)}{\pi}\right) \tag{D.3.29}$$

where the free spectral range FSR $\equiv c/2L$ gives the frequency difference between two consecutive longitudinal modes q and $q+1$.

The remaining TEM modes, denoted by indexes m, n see eq. (D.3.31), have frequencies given by,

$$\nu_{qmn} = \text{FSR}\left[q + \frac{1}{\pi}(m+n+1)\arccos(\sqrt{g_1g_2})\right]. \tag{D.3.30}$$

Clearly the spacing between difference transverse modes depends on g_1 and g_2. One can use this fact to determine these if required.

Modes of the Fabry-Pérot cavity are given by the Hermite-Gaussian modes. These TEM modes have electric field distributions given by Milonni P.W. (2010) as

$$E_{\text{mn}}(x,y,z) = E_0\frac{w(0)}{w(z)}H_m\left(\frac{\sqrt{2}x}{w(z)}\right)H_n\left(\frac{\sqrt{2}y}{w_y(z)}\right)\exp\left(\frac{-(x^2+y^2)}{w^2(z)}\right)$$
$$\exp\left(ik\frac{x^2+y^2}{2R(z)}\right)\exp\left(i\left[kz-(m+n+1)\arctan\left(\frac{z}{z_0}\right)\right]\right) \tag{D.3.31}$$

Appendix E

Mathematical methods

E.1 Rotating Frame

Moving to the rotating frame consists of making a unitary transformation of the full Hamiltonian $\hat{\mathcal{H}}$ according to the matrix $\hat{U}$ by

$$\hat{\mathcal{H}} \rightarrow \hat{U}^{\dagger}\hat{\mathcal{H}}\hat{U} - \hat{A}, \hat{U} = \exp\Big(-i\hat{A}t/\hbar\Big) \tag{E.1.1}$$

To do this in practice it is useful to know the Baker-Hausdorf lemma, which by Taylor expansion, states

$$e^{i\lambda\hat{A}}\hat{B}e^{-i\lambda\hat{A}} = \hat{B} + i\lambda\left[\hat{A},\hat{B}\right] + \frac{(i\lambda)^2}{2!}\left[\hat{A},\left[\hat{A},\hat{B}\right]\right] + ... \tag{E.1.2}$$

An very relevant example is the effect of a transforming into a rotating frame (RF) at the laser frequency ω_L. Suppose we are interested in the effect of this transformation on a hamiltonian of the form

$$\hat{\mathcal{H}} = \hbar\omega_c\hat{a}^{\dagger}(t)\hat{a}(t) + i\hbar\Big(\hat{a}(t) - \hat{a}^{\dagger}(t)\Big) \tag{E.1.3}$$

where the mode has the time dependence $\hat{a}(t)$. This time dependence can often conveniently be broken down into a fast oscillatory dynamic and a (typically much slower) residual time depedence. For this mode $\hat{a}^{\dagger}(t)$ it is very clear that is will have dynamics on a timescale of $1/\omega_c$. With this intuition in mind we can write $\hat{a}(t) = \tilde{\hat{a}}(t)e^{-i\omega_c t}$ where we have pulled out the fast dynamics and write the remaining slow dynamics as $\tilde{\hat{a}}(t)$.

Thus using $\hat{A} = \hbar\omega_L\hat{a}^{\dagger}(t)\hat{a}(t)$ gives

$$\hat{\mathcal{H}} \rightarrow -\hbar\Delta\hat{a}^{\dagger}\hat{a} + i\hbar\Big(\hat{a} - \hat{a}^{\dagger}\Big) \tag{E.1.4}$$

where we have written $\hat{a} \equiv \tilde{\hat{a}}(t)$. This notation of neglecting the tilde and residual time dependence symbol (t) is a notational shorthand that can sometimes be confusing, but allows for more easily digestible equations. When calculating the

dynamics of the operator it should be clear from which hamiltonian is being used which operator is being considered. If we have

$$\dot{\hat{a}} = \frac{i}{\hbar}[\hat{\mathcal{H}}, \hat{a}] \tag{E.1.5}$$

then if $\hat{\mathcal{H}}$ is the original hamiltonian then $\dot{a}$ means $\dot{\hat{a}}(t)$. Whereas if $\hat{\mathcal{H}}$ is the hamiltonian in the rotating frame, then $\dot{a}$ means $\dot{\tilde{\hat{a}}}(t)$.

E.2 Useful algebraic relations

Cavity lorentzian

In calculations of cavity dynamics the real and imaginary components of the cavity lorentzian given by

$$L(\Omega) = \frac{\kappa/2}{(\bar{\Delta} - \Omega) + i\kappa/2} \tag{E.2.6}$$

often appear. The following relations are useful in simplifying expressions

$$\frac{2\bar{\Delta}}{(i\Omega + \kappa/2)^2 + \bar{\Delta}^2} = \frac{1}{\kappa/2}\left(L(\Omega) + L^*(-\Omega)\right) \tag{E.2.7a}$$

$$\frac{i\Omega + \kappa/2}{(i\Omega + \kappa/2)^2 + \bar{\Delta}^2} = \frac{i}{\kappa}\left(L(\Omega) - L^*(-\Omega)\right). \tag{E.2.7b}$$

Atomic operators

When manipulating atomic operators the following relations are very handy to keep in mind.

$$\begin{aligned} \hat{\sigma}_{ij}\hat{\sigma}_{kl} &= \hat{\sigma}_{il}\delta_{jk} \\ [\hat{\sigma}_{ij}, \hat{\sigma}_{kl}] &= \hat{\sigma}_{il}\delta_{jk} - \hat{\sigma}_{kj}\delta_{li}. \end{aligned} \tag{E.2.8}$$

Jacobi-Anger expansion

The Jacobi-Anger expansion is given by

$$e^{i\beta\sin\theta} = \sum_{n=-\infty}^{\infty} J_n(\beta)e^{in\theta}, \tag{E.2.9}$$

where J_n is the nth Bessel function of the first kind.

Parsevals Theorem

Parsevals theorem links the energy in a time domain signal to that contained in the spectral domain. For some time domain signal $\hat{Q}(t)$ we have

$$\lim_{\tau\to\infty}\int_{-\tau/2}^{\tau/2}\langle\hat{Q}^\dagger(t)\hat{Q}(t)\rangle\,\mathrm{d}t = \frac{1}{2\pi}\int_{-\infty}^{\infty} S_{QQ}(\Omega)\frac{\mathrm{d}\Omega}{2\pi} \tag{E.2.10}$$

Appendix F

Effective atomic Hamiltonian and decay

Here we will use the effective operator formalism described in Reiter and Sørensen (2012) to derive the effective Hamiltonian and decay rates for the spin 1/2 toy model of section 5.5 used to describe the atomic spin ensemble. This formalism is employed since it readily generalizable to the case of many atomic levels, which our cesium atoms indeed have. The extended structure our cesium ground state manifold is not treated in (nor is it within the scope of) this work, but currently appears to be relevant for future work.

F.1 Effective operator formalism

Suppose there are various processes responsible for decay from the excited state manifold to the ground state. Associating a Lindblad operator $\hat{L}_k$ to each such a process we can write the dynamics of the system through the master equation,

$$\dot{\hat{\rho}} = -\frac{i}{\hbar}[\hat{\mathcal{H}}, \hat{\rho}] + \sum_k \left[\hat{L}_k \hat{\rho} \hat{L}_k^\dagger - \frac{1}{2}\left(\hat{L}_k^\dagger \hat{L}_k \hat{\rho} + \hat{\rho} \hat{L}_k^\dagger \hat{L}_k\right)\right], \tag{F.1.1}$$

where the systems density matrix is given $\hat{\rho}$ and the system Hamiltonian is $\hat{\mathcal{H}}$. We have assumed (as is so often the case) that the dynamics of the system is Markovian.

Eliminating the excited states, as described and justified in section 5.5, and through perturbation theory of $\hat{\rho}$, one finds an effective master equation of the form

$$\dot{\hat{\rho}} = -\frac{i}{\hbar}[\hat{\mathcal{H}}_{\text{eff}}, \hat{\rho}] + \sum_k \left[\hat{L}_{k,\text{eff}} \hat{\rho} \hat{L}_{k,\text{eff}}^\dagger - \frac{1}{2}\left(\hat{L}_{k,\text{eff}}^\dagger \hat{L}_{k,\text{eff}} \hat{\rho} + \hat{\rho} \hat{L}_{k,\text{eff}}^\dagger \hat{L}_{k,\text{eff}}\right)\right], \tag{F.1.2}$$

where the effective Hamiltonian $\hat{\mathcal{H}}_{\text{eff}}$ will given some effective coherent coupling rate g_{eff} and the effective Lindblad operators $\hat{L}_{k,\text{eff}}$ will yield some effective dissipation

rate γ_{eff}. These operators are given by

$$\hat{\mathcal{H}}_{\text{eff}} = -\frac{1}{2}\hat{V}_{-}\left(\hat{\mathcal{H}}_{\text{NH}}^{-1} + \hat{\mathcal{H}}_{\text{NH}}^{-1,\dagger}\right)\hat{V}_{+} + \hat{\mathcal{H}}_{g}, \tag{F.1.3a}$$

$$\hat{\mathcal{H}}_{\text{NH}} = \hat{\mathcal{H}}_{e} - \frac{i}{2}\sum_{k}\hat{L}_{k}^{\dagger}\hat{L}_{k}, \tag{F.1.3b}$$

$$\hat{L}_{k,\text{eff}} = \hat{L}_{k}\hat{\mathcal{H}}_{\text{NH}}^{-1}\hat{V}_{+}, \tag{F.1.3c}$$

where $\hat{\mathcal{H}}_{\text{NH}}$ is the non-Hermitian part of the Hamiltonian responsible for decay.

Theoretically we construct our Hamiltonian from the subspaces of the ground, $\hat{\mathcal{H}}_{g}$, and excited state, $\hat{\mathcal{H}}_{e}$, manifolds. Then we add perturbative excitation $\hat{V}_{+}$ and de-excitation $\hat{V}_{-}$ operators. Our Hamiltonian is then given by

$$\hat{\mathcal{H}} = \hat{\mathcal{H}}_{g} + \hat{\mathcal{H}}_{e} + \hat{V}_{+} + \hat{V}_{-}. \tag{F.1.4}$$

These subspace Hamiltonians are given by projection operators acting on the full Hamiltonian. For example, the ground state subspace is given by $\hat{\mathcal{H}}_{g} \equiv \hat{P}_{g}\hat{\mathcal{H}}\hat{P}_{g}$, with $\hat{P}_{g} = \hat{\sigma}_{11} + \hat{\sigma}_{22}$. Similarly for the excited state we define $\hat{P}_{e} = \hat{\sigma}_{33} + \hat{\sigma}_{44}$. The perturbative excitation operator $\hat{V}_{+} \equiv \hat{P}_{e}\hat{\mathcal{H}}\hat{P}_{g}$ and de-excitation operator $\hat{V}_{-} \equiv \hat{P}_{g}\hat{\mathcal{H}}\hat{P}_{e}$ couple the ground and excited subspaces.

F.2 Modified spin half toy model

The coherent coupling and dissipation desired in a modified spin half model can be motivated through terms of eq. (F.1.3) in the following handwaving fashion. In eq. (F.1.3a) the coherent interaction $\hat{V}_{+}$ brings us into the excited state manifold, in which we undergo evolution before being coherently brought back by $\hat{V}_{-}$. The competing process leading to decay happens when, following the evolution in the excited state manifold, we are brought back to the ground state manifold by decay via $\hat{L}_{k,\text{eff}}$.

Recalling our toy model Hamiltonian from section 5.5, which was given by

$$\hat{\mathcal{H}} = \hbar\Delta\left(\hat{\sigma}_{33} + \hat{\sigma}_{44}\right) + \hbar g\left(\hat{a}_{R}^{\dagger}\hat{\sigma}_{14} + \hat{a}_{L}^{\dagger}\hat{\sigma}_{23} + \text{h.c.}\right) \tag{F.2.5}$$

we can thus easily identify the following mapping (letting $\hbar = 1$).

$$\hat{\mathcal{H}}_{g} = 0, \tag{F.2.6a}$$

$$\hat{\mathcal{H}}_{e} = \Delta\left(\hat{\sigma}_{33} + \hat{\sigma}_{44}\right), \tag{F.2.6b}$$

$$\hat{V}_{+} = g\left(\hat{a}_{R}\hat{\sigma}_{41} + \hat{a}_{L}\hat{\sigma}_{32}\right), \tag{F.2.6c}$$

$$\hat{V}_{-} = g\left(\hat{a}_{R}^{\dagger}\hat{\sigma}_{14} + \hat{a}_{L}^{\dagger}\hat{\sigma}_{23}\right). \tag{F.2.6d}$$

$$\tag{F.2.6e}$$

Now let us consider the situation where the excited states decay due to spontaneous emission at a rate given by γ. Lets assume that occurs at the same rate for

all levels. In that case we write our Lindblad operators as,

$$\hat{L}_{14} = \sqrt{\gamma}\,\hat{\sigma}_{14}, \tag{F.2.7a}$$
$$\hat{L}_{13} = \sqrt{\gamma}\,\hat{\sigma}_{13}, \tag{F.2.7b}$$
$$\hat{L}_{24} = \sqrt{\gamma}\,\hat{\sigma}_{24}, \tag{F.2.7c}$$
$$\hat{L}_{23} = \sqrt{\gamma}\,\hat{\sigma}_{23}. \tag{F.2.7d}$$

We can now readily calculate the effective operators of eq. (F.1.3)[1]. First off, the non–Hermitian part of the Hamiltonian is,

$$\begin{aligned}\hat{\mathcal{H}}_{\text{NH}} &= \Delta(\hat{\sigma}_{33}+\hat{\sigma}_{44}) - \frac{i\gamma}{2}(\hat{\sigma}_{33}+\hat{\sigma}_{44}) \\ &= (\Delta - i\gamma/2)(\hat{\sigma}_{33}+\hat{\sigma}_{44}), \qquad \text{(F.2.8a)}\\ \hat{\mathcal{H}}_{\text{NH}}^{-1} &= \frac{\hat{\sigma}_{33}+\hat{\sigma}_{44}}{\Delta - i\gamma/2}, \qquad \text{(F.2.8b)}\\ \therefore \hat{\mathcal{H}}_{\text{NH}}^{-1} + (\hat{\mathcal{H}}_{\text{NH}}^{-1})^\dagger &= (\hat{\sigma}_{33}+\hat{\sigma}_{44})\left(\frac{1}{\Delta - i\gamma/2} + \frac{1}{\Delta + i\gamma/2}\right) \\ &= (\hat{\sigma}_{33}+\hat{\sigma}_{44})\frac{2\Delta}{\Delta^2 + (\gamma/2)^2}. \qquad \text{(F.2.8c)}\end{aligned}$$

The effective Hamiltonian is then

$$\begin{aligned}\hat{\mathcal{H}}_{\text{eff}} &= -\frac{1}{2}\hat{V}_-\left(\hat{\mathcal{H}}_{\text{NH}}^{-1} + \hat{\mathcal{H}}_{\text{NH}}^{-1,\dagger}\right)\hat{V}_+ + \hat{\mathcal{H}}_g \\ &= \frac{g^2\Delta}{\Delta^2 + (\gamma/2)^2}(\hat{a}_R^\dagger\hat{\sigma}_{14} + \hat{a}_L^\dagger\hat{\sigma}_{23})(\hat{\sigma}_{33}+\hat{\sigma}_{44})(\hat{a}_R\hat{\sigma}_{41} + \hat{a}_L\hat{\sigma}_{32}) \\ &= g_{\text{eff}}(\hat{a}_R^\dagger\hat{a}_R\hat{\sigma}_{11} + \hat{a}_L^\dagger\hat{a}_L\hat{\sigma}_{22}), \\ &= g_{\text{eff}}(\hat{S}_0\hat{J}_0 - \hat{S}_z\hat{J}_z)\end{aligned} \tag{F.2.9}$$

where we defined the effective coupling rate

$$g_{\text{eff}} \equiv \frac{g^2\Delta}{\Delta^2 + (\gamma/2)^2}, \tag{F.2.10}$$

and used the relation of the spin operators defined in eq. (5.21) for a quantization axis along z.

Similarly, we also calculate the effective Lindblad operators using eq. (F.1.3) which are,

$$\begin{aligned}\hat{L}_{14}^{\text{eff}} &= \frac{\sqrt{\gamma}\,g}{\Delta - i\gamma/2}\hat{\sigma}_{14}(\hat{\sigma}_{33}+\hat{\sigma}_{44})(\hat{a}_R\hat{\sigma}_{41} + \hat{a}_L\hat{\sigma}_{32}) \\ &= \sqrt{\gamma_{\text{eff}}}\,\hat{\sigma}_{11}\hat{a}_R \qquad \text{(F.2.11a)}\\ \hat{L}_{13}^{\text{eff}} &= \sqrt{\gamma_{\text{eff}}}\,\hat{\sigma}_{12}\hat{a}_L \qquad \text{(F.2.11b)}\\ \hat{L}_{24}^{\text{eff}} &= \sqrt{\gamma_{\text{eff}}}\,\hat{\sigma}_{21}\hat{a}_R \qquad \text{(F.2.11c)}\\ \hat{L}_{23}^{\text{eff}} &= \sqrt{\gamma_{\text{eff}}}\,\hat{\sigma}_{22}\hat{a}_L. \qquad \text{(F.2.11d)}\end{aligned}$$

[1] Particularly useful expressions in this exercise are those of eq. (E.2.8).

Above we have written the effective dissipation rate due to spontaneous emission as

$$\sqrt{\gamma_{\text{eff}}} = \frac{\sqrt{\gamma}\, g}{\Delta - i\gamma/2}. \tag{F.2.12}$$

The above mathematical acrobatics followed from density matrix approach in the Schrödinger picture. For the dynamics of the system, we would like to convert this to the Heisenberg picture. We can relate the effective parameters found to the Heisenberg–Langevin equation of eq. (2.62), which in terms of these Lindblad operators is given by (written here in terms of the atomic system operators),

$$\dot{\hat{\sigma}}_{ij} = \frac{i}{\hbar}[\hat{\mathcal{H}}, \hat{\sigma}_{ij}] + \sum_k (\hat{L}_k^\dagger/2 + \hat{F}_k^\dagger)[\hat{\sigma}_{ij}, \hat{L}_k] - [\hat{\sigma}_{ij}, \hat{L}_k^\dagger](\hat{L}_k/2 + \hat{F}_k) \tag{F.2.13}$$

$$= \frac{i}{\hbar}[\hat{\mathcal{H}}, \hat{\sigma}_{ij}] + \sum_k \underbrace{\frac{1}{2}(2\hat{L}_k^\dagger \hat{\sigma}_{ij} \hat{L}_k - \hat{L}_k^\dagger \hat{L}_k \hat{\sigma}_{ij} - \hat{\sigma}_{ij} \hat{L}_k^\dagger \hat{L}_k)}_{\text{dissipation}} + \underbrace{\hat{F}_k^\dagger [\hat{\sigma}_{ij}, \hat{L}_k] - [\hat{\sigma}_{ij}, \hat{L}_k^\dagger]\hat{F}_k}_{\hat{F}_{ij}} \tag{F.2.14}$$

Here $\hat{F}_k$ is the Langevin force as a result of dissipation through channel $\hat{L}_k$.

In practice it is easier to calculate the dissipation using the terms grouped in the second expression of eq. (F.2.13) and simply ignore the detailed dependence of the effective Langevin force $\hat{F}_{ij}$. In the end of the day we will anyway care about the Langevin force correlator of eq. (2.59), which can be conveniently calculated from the fluctuation dissipation theorem of eq. (2.60). The dissipation part for each atomic operator is given by,

$$\dot{\hat{\sigma}}_{11} : \gamma_{\text{eff}}(\hat{a}_L^\dagger \hat{a}_L \hat{\sigma}_{22} - \hat{a}_R^\dagger \hat{a}_R \hat{\sigma}_{11}), \tag{F.2.15a}$$

$$\dot{\hat{\sigma}}_{22} : \gamma_{\text{eff}}(\hat{a}_R^\dagger \hat{a}_R \hat{\sigma}_{11} - \hat{a}_L^\dagger \hat{a}_L \hat{\sigma}_{22}), \tag{F.2.15b}$$

$$\dot{\hat{\sigma}}_{12} : -2\gamma_{\text{eff}} \hat{\sigma}_{12} \hat{S}_0, \tag{F.2.15c}$$

$$\dot{\hat{\sigma}}_{21} : -2\gamma_{\text{eff}} \hat{\sigma}_{21} \hat{S}_0, \tag{F.2.15d}$$

which means that the contributions to the spin operators in our chosen quantization axis (along our probe) along z are

$$\dot{\hat{J}}_x : -2\gamma_{\text{eff}} \hat{S}_0 \hat{J}_x, \tag{F.2.16a}$$

$$\dot{\hat{J}}_y : -2\gamma_{\text{eff}} \hat{S}_0 \hat{J}_y, \tag{F.2.16b}$$

$$\dot{\hat{J}}_z : -2\gamma_{\text{eff}} (\hat{S}_0 \hat{J}_z + \hat{S}_z \hat{J}_0), \tag{F.2.16c}$$

$$\dot{\hat{J}}_0 : 0. \tag{F.2.16d}$$

F.3 Probe induced broadening

We now change our quantization axis to the x direction while keeping the probe direction to be along z. This is the experimentally relevant case for the setup in

section 5.1. Cyclically permuting the spin operators as in section 5.7, we now have dissipation contributions of

$$\dot{\hat{J}}_x : -2\gamma_{\text{eff}}(\hat{S}_0\hat{J}_x + \hat{S}_z\hat{J}_0), \tag{F.3.17a}$$

$$\dot{\hat{J}}_y : -2\gamma_{\text{eff}}\hat{S}_0\hat{J}_y, \tag{F.3.17b}$$

$$\dot{\hat{J}}_z : -2\gamma_{\text{eff}}\hat{S}_0\hat{J}_z, \tag{F.3.17c}$$

$$\dot{\hat{J}}_0 : 0. \tag{F.3.17d}$$

If we make the Holstein-Primakoff approximation, as described in section 5.10.1, we can write the effective spin quadratures as

$$\dot{\hat{Q}}_S : -2\gamma_{\text{eff}}S_0\hat{Q}_S = \frac{\gamma_{\text{probe}}}{2}\hat{Q}_S, \tag{F.3.18a}$$

$$\dot{\hat{P}}_S : -2\gamma_{\text{eff}}S_0\hat{P}_S = \frac{\gamma_{\text{probe}}}{2}\hat{P}_S, \tag{F.3.18b}$$

where we have also taken the probe field to have a large classical nature, writing the optical Stokes component $\hat{S}_0 = S_0$ and absorbing it into γ_{probe}.

These equations are within the rotating wave approximation thus why the dissipation is shared between the spin quadratures instead of collected in $\hat{P}_S$ at the full rate γ_{probe}. The S_0 Stokes component is related to the mean probe flux α^2 by $S_0 = \alpha^2$.

Appendix G

Pulsed oscillator response and optical readout

G.1 Demodulated oscillator response

Since the only quantity connecting the oscillators is the common back-action driving force, their dynamics can be solved for separately as implied by their uncoupled equations of motion, eq. (6.11). Since all local oscillators are running continuously, the time-domain solution of each oscillator i is

$$\boldsymbol{Q}_i(t) = \int_{-\infty}^{t} \mathrm{d}t' e^{\boldsymbol{M}_i(t-t')} \boldsymbol{F}_i(t'). \tag{G.1.1}$$

Demodulating this time domain response according to its harmonic components $q(\Omega, t) \in \{\cos(\Omega t), \sin(\Omega t)\}$ over the finite interval $t \in [0, T]$ gives

$$\boldsymbol{\mathcal{Q}}_{q,i}(\omega) \equiv \frac{2}{\sqrt{T}} \int_0^T \mathrm{d}t q(\Omega, t) \boldsymbol{Q}_i(t) = \frac{2}{\sqrt{T}} \int_{-\infty}^{T} \mathrm{d}t' \boldsymbol{u}_{q,i}(\Omega, t') \boldsymbol{F}_i(t'), \tag{G.1.2}$$

where the subscript indicates the harmonic component $q = \cos(\sin)$. Note that in the second equality of eq. (G.1.2) we reversed the order of integration $\mathrm{d}t\,\mathrm{d}t' \to \mathrm{d}t'\,\mathrm{d}t$, and introduced the oscillator filter functions

$$\boldsymbol{u}_{q,i}(\Omega, t') \equiv \int_{\max\{t',0\}}^{T} \mathrm{d}t q(\Omega, t) e^{\boldsymbol{M}_i(t-t')}. \tag{G.1.3}$$

These mode functions reflect the point of view that the oscillator dynamics filters the output quadrature $q(\Omega, t)$ resulting in (a matrix of) effective oscillator filter functions $\boldsymbol{u}_{q,i}(\Omega, t')$. To determine these, it is useful to note that the matrix of response functions in eq. (G.1.3) can be evaluated using eq. (6.12) to find,

$$e^{\boldsymbol{M}_i \tau} = e^{-\gamma_i \tau/2} \begin{pmatrix} \cos(\Omega_i \tau) & \sin(\Omega_i \tau) \\ -\sin(\Omega_i \tau) & \cos(\Omega_i \tau) \end{pmatrix}. \tag{G.1.4}$$

The (1,2) element of the matrix eq. (G.1.4) is the response function that maps the optical back-action force into oscillator position response and is related to the oscillator susceptibility χ_i.

Thus, being an important example, we explicitly evaluate the (1,2) matrix element of $\boldsymbol{u}_{q,i}(\Omega, t')$. Choosing the output harmonic cosine quadrature $q(\Omega, t) = \cos(\Omega t)$ as an example gives

$$\begin{aligned}[\boldsymbol{u}_{\cos,i}(\Omega, t')]_{1,2} &= \int_{\max\{t',0\}}^{T} \mathrm{d}t \cos(\Omega t) e^{-\gamma_i (t-t')/2} \sin(\Omega_i (t-t')) \\ &= g_i(\Omega, t') + g_i(-\Omega, t'),\end{aligned} \tag{G.1.5}$$

where we have defined

$$\begin{aligned} g_i(\Omega, t') \equiv & -\frac{1}{2} \frac{1}{(\gamma_i/2)^2 + (\Omega - \Omega_i)^2} \cdot \\ & \Bigg[e^{\gamma_i \min\{t',0\}/2} \Bigg(\frac{\gamma_i}{2} \sin\left(\Omega t' - [(\Omega - \Omega_i) \min\{t', 0\}]\right) \\ & \qquad + (\Omega - \Omega_i) \cos(\Omega t' - [(\Omega - \Omega_i) \min\{t', 0\}]) \Bigg) \\ & - e^{-\gamma_i (T - t')/2} \Bigg(\frac{\gamma_i}{2} \sin([\Omega - \Omega_i] T + \Omega_i t') \\ & \qquad + (\Omega - \Omega_i) \cos([\Omega - \Omega_i] T + \Omega_i t') \Bigg) \Bigg]. \end{aligned} \tag{G.1.6}$$

From eqs. (G.1.5) and (G.1.6) we note that if $\Omega_M = -\Omega_S, \gamma_M = \gamma_S$, then

$$\Rightarrow [\boldsymbol{u}_{\mathrm{c},M}(\Omega, t')]_{1,2} = -[\boldsymbol{u}_{\mathrm{c},S}(\Omega, t')]_{1,2}, \tag{G.1.7}$$

as expected for two identical oscillators in the positive-negative (mechanics-spins) mass configuration, $\Omega_S = -\Omega_M$. If on the other hand $\gamma_M \neq \gamma_S$, the property of eq. (G.1.7) will fail to hold for a general (Ω, t'). In the relevant regime of large quality factors $Q_i \equiv |\Omega_i|/\gamma_i \gg 1$ we have

$$[\boldsymbol{u}_{\mathrm{c},i}(\Omega, t')]_{1,2} \approx g_i(\mathrm{sgn}(\Omega_i)|\Omega|, t'). \tag{G.1.8}$$

If we evaluate eq. (G.1.8) for on mechanical resonance with both systems, i.e. at $\Omega = \Omega_M = |\Omega_S|$, we find that

$$[\boldsymbol{u}_{\mathrm{c},i}(|\Omega_i|, t')]_{1,2} \approx -\frac{1}{\gamma_i} \left[e^{\gamma_i \min\{t',0\}/2} - e^{-\gamma_i (T-t')/2} \right] \sin(\Omega_i t'). \tag{G.1.9}$$

G.2 Optical readout of the oscillator cascade

We now consider the optical readout of the oscillator cascade, which can be determined by combining the solution for the oscillator responses (G.1.2) with the input-output relation (6.17). Defining cosine and sine quadratures of $\hat{Y}^{\mathrm{out}}$ analogously to (G.1.2),

$$\hat{Y}^{\mathrm{out(in)}}_{(q)}(\Omega) \equiv \frac{2}{\sqrt{T}} \int_0^T \mathrm{d}t q(\Omega, t) \hat{Y}^{\mathrm{out(in)}}(t), \tag{G.2.10}$$

which is normalized to shot noise units when considering variances, we find for the phase quadrature of light that

$$\begin{aligned}\hat{Y}^{\mathrm{out}}_{(q)}(\Omega) = -\hat{Y}^{\mathrm{in}}_{(q)}(\Omega) + \frac{2}{\sqrt{T}} \begin{pmatrix} 1 \\ 0 \end{pmatrix}^T \cdot \\ \int_{-\infty}^{T} \mathrm{d}t' \Bigg(\sqrt{\eta_1\eta_2}\sqrt{\Gamma_S}\, \boldsymbol{u}_{q,S}(\Omega,t') \left[-\sqrt{\gamma_S}\, \hat{\boldsymbol{F}}_S^{\mathrm{th,in}}(t') - \sqrt{\Gamma_S}\, \hat{\boldsymbol{F}}_S^{\mathrm{L,in}}(t') \right] \\ - \sqrt{\eta_2}\sqrt{\Gamma_M}\, \boldsymbol{u}_{q,M}(\Omega,t') \Big[-\sqrt{\gamma_M}\, \hat{\boldsymbol{F}}_M^{\mathrm{th,in}} \\ - \sqrt{\Gamma_M} \left(-\sqrt{\eta_1}\, \hat{\boldsymbol{F}}_S^{\mathrm{L,in}}(t') + \sqrt{1-\eta_1}\, \hat{\boldsymbol{F}}^{\mathrm{v,in}}(t') \right) \Big] \Bigg).\end{aligned} \tag{G.2.11}$$

eq. (G.2.11) is the desired solution of the equations considered here, and all moments of $\hat{Y}^{\mathrm{out}}_{(q)}(\Omega)$ can be calculated from it once the state of the input operators has been specified.

Appendix H

General optomechanical model

H.1 Derivation

The optomechanical quantum Heisenberg-Langevin equations of eq. (4.26) in the Fourier domain can in general be solved for a particular cavity input port quadratures. Re-writing eq. (4.26) in terms of block matrices then we find

$$\begin{pmatrix} \boldsymbol{R}^{\intercal}(\phi) & 0 \\ 0 & 1 \end{pmatrix} \begin{pmatrix} \boldsymbol{A} & \boldsymbol{B} \\ \boldsymbol{B}^{\intercal} & \chi(\Omega) \end{pmatrix} \begin{pmatrix} \boldsymbol{R}(\phi) & 0 \\ 0 & 1 \end{pmatrix} \begin{pmatrix} \hat{\mathbf{X}}(\Omega) \\ \hat{Q}_M(\Omega) \end{pmatrix} = \begin{pmatrix} \sqrt{\kappa_1}\hat{\mathbf{X}}^{\text{in}}_M(\Omega) + \sqrt{\kappa_2}\hat{\boldsymbol{V}}^{\text{in}}(\Omega) \\ \sqrt{\gamma_{M0}}\hat{f}(\Omega) \end{pmatrix} \tag{H.1.1}$$

where $\boldsymbol{R}(\phi)$ is the 2D rotation matrix defined in eq. (2.84). The remaining elements are

$$\boldsymbol{A} = \begin{pmatrix} i\Omega + \kappa/2 & \bar{\Delta} \\ -\bar{\Delta} & i\Omega + \kappa/2 \end{pmatrix}, \qquad \boldsymbol{B} = \begin{pmatrix} 0 \\ -2g \end{pmatrix}, \tag{H.1.2}$$

$$\hat{\boldsymbol{X}}^{\text{in}}_M(\Omega) = \begin{pmatrix} \hat{X}^{\text{in}}_M(\Omega) \\ \hat{Y}^{\text{in}}_M(\Omega) \end{pmatrix}, \qquad \hat{\boldsymbol{X}}(\Omega) = \begin{pmatrix} \hat{X}(\Omega) \\ \hat{Y}(\Omega) \end{pmatrix}. \tag{H.1.3}$$

This equation is easily inverted from which we find that the intracavity field quadratures $\hat{\boldsymbol{X}}$ and mechanical position quadrature $\hat{Q}_M$ are given by

$$\begin{pmatrix} \hat{\boldsymbol{X}}(\Omega) \\ \hat{Q}_M(\Omega) \end{pmatrix} = \begin{pmatrix} \boldsymbol{R}^{\intercal}(\phi) & 0 \\ 0 & 1 \end{pmatrix} \begin{pmatrix} \boldsymbol{A} & \boldsymbol{B} \\ \boldsymbol{B}^{\intercal} & \chi^{-1}(\Omega) \end{pmatrix}^{-1} \begin{pmatrix} \boldsymbol{R}(\phi) & 0 \\ 0 & 1 \end{pmatrix} \begin{pmatrix} \sqrt{\kappa_1}\hat{\boldsymbol{X}}^{M}_{L,in}(\Omega) + \sqrt{\kappa_2}\hat{\boldsymbol{V}}^{in}(\Omega) \\ \sqrt{\gamma_{M0}}\hat{f}(\Omega). \end{pmatrix} \tag{H.1.4}$$

The inverse Block matrix can be expressed in two equivalent forms, namely

$$\begin{pmatrix} \boldsymbol{A} & \boldsymbol{B} \\ \boldsymbol{B}^{\intercal} & \chi^{-1}(\Omega) \end{pmatrix}^{-1} = \begin{pmatrix} \boldsymbol{A}^{-1} + \boldsymbol{A}^{-1}\boldsymbol{B}S^{-1}\boldsymbol{B}^{\intercal}A^{-1} & -\boldsymbol{A}^{-1}\boldsymbol{B}S^{-1} \\ -S^{-1}\boldsymbol{B}^{\intercal}A^{-1} & S^{-1} \end{pmatrix} \tag{H.1.5}$$

$$= \begin{pmatrix} \boldsymbol{T}^{-1} & -\boldsymbol{T}^{-1}\boldsymbol{B}\chi(\Omega) \\ -\chi(\Omega)\boldsymbol{B}^{\intercal}\boldsymbol{T}^{-1} & \chi(\Omega) + \chi(\Omega)\boldsymbol{B}^{\intercal}\boldsymbol{T}^{-1}\boldsymbol{B}\chi(\Omega), \end{pmatrix} \tag{H.1.6}$$

where we have made use of the Schur complements S and T. These are given by

$$S = \chi(\Omega) - \boldsymbol{B}^{\intercal}\boldsymbol{A}^{-1}\boldsymbol{B} = \chi^{-1}(\Omega) + \Omega_{M,0}\frac{\kappa\Gamma_M\bar{\Delta}}{(i\Omega+\kappa/2)^2+\bar{\Delta}^2} \equiv \chi_{\text{eff}}^{-1}(\Omega), \tag{H.1.7}$$

$$\boldsymbol{T} = \boldsymbol{A} - \boldsymbol{B}\chi(\Omega)\boldsymbol{B}^{\intercal} = \begin{pmatrix} i\Omega+\kappa/2 & \bar{\Delta} \\ -\bar{\Delta}-\kappa\Gamma_M\chi(\Omega) & i\Omega+\kappa/2 \end{pmatrix}, \tag{H.1.8}$$

where the effective susceptibility χ_{eff} is modified by dynamical back-action. The additional term is defined in eq. (4.30) and discussed in sections 4.1.4 and 4.1.4. The effective mechanical susceptibility now includes optically induced mechanical frequency shift and additional damping.

The intracavity light quadratures now follow directly from eqs. (H.1.5) and (H.1.6) and are

$$\begin{aligned}\hat{\boldsymbol{X}}(\Omega) = {}& \boldsymbol{R}(\phi)T^{-1}\boldsymbol{R}^{\intercal}(\phi)\left(\sqrt{\kappa_1}\hat{\boldsymbol{X}}_M^{\text{in}}(\Omega) + \sqrt{\kappa_2}\hat{\boldsymbol{V}}_{in}(\Omega)\right) \\ & + \sqrt{\gamma_{M0}\kappa\Gamma_M}\,\chi_{\text{eff}}(\Omega)\frac{\Omega_{M,0}}{\Omega_M}\boldsymbol{R}(\phi)\boldsymbol{A}^{-1}\hat{\boldsymbol{F}}(\Omega),\end{aligned} \tag{H.1.9}$$

$$\hat{\boldsymbol{F}}(\Omega) \equiv \left(0, \hat{f}(\Omega)\right)^{\intercal}. \tag{H.1.10}$$

Using the cavity input-output equation for the field quadratures reflecting off port 1 of the cavity we have

$$\begin{aligned}\hat{\boldsymbol{X}}_M^{\text{out}}(\Omega) &= -\hat{\boldsymbol{X}}_M^{\text{in}}(\Omega) + \sqrt{\kappa_1}\hat{\boldsymbol{X}}(\Omega) \\ &= \boldsymbol{R}(\phi)(\kappa_1\boldsymbol{T}^{-1} - \mathbb{1})\boldsymbol{R}^{\intercal}(\phi)\hat{\boldsymbol{X}}_M^{\text{in}}(\Omega) + \sqrt{\kappa_1\kappa_2}\boldsymbol{R}(\phi)T^{-1}\boldsymbol{R}^{\intercal}(\phi)\hat{\boldsymbol{V}}_{in}(\Omega) \\ &\quad + \sqrt{\kappa\Gamma_M\kappa_1\gamma_{M0}}\,\chi_{\text{eff}}(\Omega)\frac{\Omega_{M,0}}{\Omega_M}\boldsymbol{R}(\phi)\boldsymbol{A}^{-1}\hat{\boldsymbol{F}}(\Omega) \\ &\equiv \mathbb{M}(\Omega)\hat{\boldsymbol{X}}_M^{\text{in}}(\Omega) + \mathbb{V}(\Omega)\hat{\boldsymbol{V}}_{in}(\Omega) + \mathbb{F}(\Omega)\hat{\boldsymbol{F}}(\Omega).\end{aligned} \tag{H.1.11}$$

This is the general input-output relation used for the optomechanical mechanical subsystem and allows for a general intracavity field phase. Through eq. (H.1.11) we define the transfer matrices for the optomechanics $\mathbb{M}(\Omega)$, vacuum fields introduced due to loss $\mathbb{V}(\Omega)$, and the thermal noise driving the mechanics $\mathbb{F}(\Omega)$.

The optomechanical transfer matrix $\mathbb{M}(\Omega)$ filtering the input quadratures in eq. (H.1.11) is given by

$$\begin{aligned}\mathbb{M}(\Omega) &= \frac{\kappa_1}{D_c(\Omega)}\frac{\chi(\Omega)}{\chi_{\text{eff}}(\Omega)}\frac{\Omega_{M,0}}{\Omega_M}\boldsymbol{R}(\phi)\begin{pmatrix} i\Omega+\kappa/2 & -\bar{\Delta} \\ \bar{\Delta}+\kappa\Gamma_M\chi(\Omega) & i\Omega+\kappa/2 \end{pmatrix}\boldsymbol{R}^{\intercal}(\phi) - \mathbb{1} \\ &= \frac{\kappa_1}{\kappa}\frac{\chi(\Omega)}{\chi_{\text{eff}}(\Omega)}\frac{\Omega_{M,0}}{\Omega_M}\boldsymbol{R}(\phi)\left[2\begin{pmatrix} v & u \\ -u & v \end{pmatrix} + \begin{pmatrix} 0 & 0 \\ \frac{\kappa^2\Gamma_M\chi(\Omega)}{D_c(\Omega)} & 0 \end{pmatrix}\right]\boldsymbol{R}^{\intercal}(\phi) - \mathbb{1}\end{aligned} \tag{H.1.12}$$

where $D_c(\Omega) = (i\Omega+\kappa/2)^2 + \bar{\Delta}^2$ and, as in eq. (4.111), we define $u(\Omega) = -[L(\Omega) + L^*(-\Omega)]/2$ and $v(\Omega) = i\left[L(\Omega) - L^*(-\Omega)\right]/2$. This latter formulation makes clear the contributions of the cavity rotation of optical quadratures and the optomechanical response. The complex cavity Lorentzian L is defined in eq. (4.32) and also described below in eq. (H.2.15).

H.2 Unresolved sideband approximation

For a broadband, one-sided cavity with $\kappa \gg \bar{\Delta},\ \Omega_M,\ \Omega$ and $\kappa_2 = 0$ eq. (H.1.11) simplifies to the simple QND optomechanical input-output relation described ineq. (6.14), namely

$$\hat{\boldsymbol{X}}_M^{\text{out}}(\Omega) = \mathbb{M}(\Omega)\hat{\boldsymbol{X}}_M^{\text{in}}(\Omega) + \sqrt{\Gamma_M \gamma_{M,0}}\,\chi_M(\Omega)\hat{\boldsymbol{F}}_M^{\text{th,in}}(\Omega), \tag{H.2.13}$$

$$\mathbb{M}(\Omega) = \begin{pmatrix} 1 & 0 \\ \Gamma_M \chi_M(\Omega) & 1 \end{pmatrix}. \tag{H.2.14}$$

In this regime there is no dynamical back-action and the system responds according to its bare susceptibility.

For a nonzero detuning we, in general, need to take the finite cavity linewidth into account by way of the more detailed input-output relations of eq. (H.1.11). However, in the unresolved-sideband regime ($\kappa \gg \Omega_M, \Omega$) we may obtain an approximate expression for the optomechanical transfer matrix eq. (H.1.12). To see how we first write out the amplitude and phase of the complex Lorentzian as

$$L(\Omega) = \frac{\kappa/2}{(\Delta - \Omega) + i\kappa/2} = |L(\Omega)|e^{i\theta(\Omega)}, \tag{H.2.15}$$

$$|L(\Omega)| = \frac{\kappa/2}{\sqrt{(\kappa/2)^2 + (\Delta - \Omega)^2}}, \tag{H.2.16}$$

$$\theta(\Omega) = \arctan\left(\frac{\kappa/2}{\Delta - \Omega}\right). \tag{H.2.17}$$

Writing the u and v components as

$$u = -\frac{1}{2}\left[|L(\Omega)|e^{i\theta(\Omega)} + |L(-\Omega)|e^{-i\theta(-\Omega)}\right], \tag{H.2.18a}$$

$$v = \frac{i}{2}\left[|L(\Omega)|e^{i\theta(\Omega)} + |L(-\Omega)|e^{-i\theta(-\Omega)}\right], \tag{H.2.18b}$$

we notice that the rotation matrix $\boldsymbol{R}\left([\theta(\Omega) + \theta(-\Omega)]/2\right)$ can be pulled out. We can thus can re-express eq. (H.1.12) as

$$\begin{aligned}\mathbb{M}(\Omega) = e^{i[\theta(\Omega)-\theta(-\Omega)]}&\boldsymbol{R}\left(\phi + [\theta(\Omega) + \theta(-\Omega)]/2\right) \times \\ &\left(\left[1 + i\frac{\Gamma_M\chi_M(\Omega)}{4}\left(|L(\Omega)|^2 - |L(-\Omega)|^2\right)\right]\mathbb{1}\right. \\ &\left. + \frac{\Gamma_M\chi_M(\Omega)}{4}\begin{pmatrix} 0 & -(|L(\Omega)| - |L(-\Omega)|)^2 \\ (|L(\Omega)| + |L(-\Omega)|)^2 & 0 \end{pmatrix}\right)\times \\ &\boldsymbol{R}^{\intercal}\left(\phi - [\theta(\Omega) + \theta(-\Omega)]/2\right),\end{aligned} \tag{H.2.19}$$

where $\phi = \pi/2 - \theta(0)$ is the phase acquired by the on local oscillator field.

We can further simplify eq. (H.2.19) in the regime of $\kappa \gg \Omega_M, \Omega$ by expanding $|L(\Omega)|$ and $\theta(\Omega)$ to first order in Ω around the carrier frequency of $\Omega = 0$. This gives

$$|L(\Omega)| \approx L_0 + \delta L(\Omega), \tag{H.2.20}$$

$$L_0 \equiv |L(0)| = \frac{\kappa/2}{\sqrt{(\kappa/2)^2 + \Delta^2}}, \; \delta L(\Omega) = \frac{\Omega\Delta\kappa/2}{((\kappa/2)^2 + \Delta^2)^{3/2}}, \tag{H.2.21}$$

$$\theta(\Omega) \approx \phi + \delta\theta(\Omega), \quad \delta\theta(\Omega) = \Omega\frac{\kappa/2}{(\kappa/2)^2 + \Delta^2}, \tag{H.2.22}$$

which results in the approximate optomechanical scattering matrix of

$$\begin{aligned}\mathbb{M}(\Omega) \approx e^{2i\delta\theta(\Omega)}\boldsymbol{R}(2\phi)\Bigg(&[1 + i\Gamma_M L_0 \delta L(\Omega)\chi_M(\Omega)]\,\mathbb{1} \\ &+ \Gamma_M L_0^2 \chi_{\text{eff}}(\Omega)\begin{pmatrix} 0 & 0 \\ 1 & 0 \end{pmatrix}\Bigg),\end{aligned} \tag{H.2.23}$$

to first order in $\delta\theta$ and δL. The phase prefactor can be omitted whenever the end result is a power spectrum as it will cancel out in any correlation function.

This transfer matrix of eq. (H.2.23) provides a useful middle ground between the simplistic QND result of eq. (H.2.14), valid in the limit $\kappa \to \infty$, and the general – but complicated – result of eq. (H.1.12).